AN ABSTRACT OF THE THESIS OF

Robert Henry Kraus, Jr. for the degree of Doctor of Philosophy in Chemistry presented on 27. June 1985.

Title: HOLMIUM TARGET FRAGMENTATION INDUCED BY INTERMEDIATE ENERGY ^{12}C AND ^{16}O IONS

Redacted for Privacy

Abstract approved: _____
Walter D. Loveland

Target fragment ($40 < A < 180$) production cross sections were measured using off-line gamma-ray spectroscopy for the interaction of 208 MeV ^{12}C, 272 MeV ^{16}O, 442 MeV ^{12}C, 1020 MeV ^{12}C, and 1635 MeV ^{16}O with ^{165}Ho. Target fragment isobaric yields were deduced from these measurements. Trans-target nuclides were identified for all reaction systems. Nuclides up to 4 Z-units above the target were identified for 208 MeV ^{12}C and 272 MeV ^{16}O induced reactions, to 3 Z-units above the target for 442 MeV ^{12}C and 1020 MeV ^{12}C induced reactions, and to 2 Z-units above the target for 1635 MeV ^{16}O induced reactions. Fission was observed to decrease between 17 MeV/A and 37 MeV/A from 13% of the reaction cross section to 4% for ^{12}C induced reactions. No fission contribution was observed for 1020 MeV ^{12}C and 1635 MeV ^{16}O induced interactions.

Fission yields were observed to decrease above 17 MeV/A. The decrease in the fission yield with increasing projectile energy was observed to correlate with the deduced average angular momentum of the primary system, $\langle l_{sys} \rangle$. Fission yields predicted by the

Wilczynski generalized sum-rule and firestreak models were less than observed quantities by more than 200% and 400%, respectively. The small predicted fission yields were caused by calculated primary fragment angular momentum distributions which were unrealistic (and/or calculated angular momentum transfers which in at least a fraction of events were too small).

The observed heavy fragment (A > 100) distributions for 442 MeV ^{12}C + ^{165}Ho, 1020 MeV ^{12}C + ^{165}Ho, and 1635 MeV ^{16}O + ^{165}Ho reaction systems were predicted relatively well by the firestreak model, however, trans-target product yields were underestimated. Heavy fragment distributions calculated by computer codes based on the firestreak and Wilczynski sum-rule models underestimated the width of the observed distributions for 208 MeV ^{12}C and 272 MeV ^{16}O induced reactions.

HOLMIUM TARGET FRAGMENTATION INDUCED BY INTERMEDIATE ENERGY ^{12}C AND ^{16}O IONS

by
Robert Henry Kraus, Jr.

A THESIS
submitted to
Oregon State University

the requirements for the
degree of

Doctor of Philosophy

Completed: 27. June 1985

Commencement: June 1986

APPROVED:

Redacted for Privacy

Professor of Chemistry, in charge of major

Redacted for Privacy

Head of the Department of Chemistry

Redacted for Privacy

Dean of the Graduate School

Date thesis is presented: 27. June 1985

DEDICATION

I could not have possibly maintained the energy and persistence to complete this work were it not for the support, prodding, and especially the love contributed by my very special wife, Debbie. This work is truly our joint effort. My parents have also given endlessly of their love and support during my graduate career and throughout my entire life.

I, therefore, dedicate this thesis to my parents, my most loved and appreciated wife and to our child-to-be!

ACKNOWLEDGEMENTS

The list of people who played a role in this research effort is quite long and the contributions of each individual can only briefly be summarized, but suffice it to say that each person listed below played an invaluable part in the successful completion of this work.

The first and foremost contributor in more ways than can possibly be mentioned in this short space is Dr. Walter D. Loveland, my advising professor. Arranging beam time at the various accelerator facilities, assisting in irradiation preparations, assisting in spectroscopic measurements, and running some of the modeling computer codes number as only a few of his contributions. Dr. G.T. Seaborg at the Lawrence Berkeley Laboratory was instrumental in providing beam time and computer facilities at LBL for our use as well as financial assistance. Dr. K. Aleklett from the Studsvik Scientific Laboratory and Dr. P.L. McGaughey from Los Alamos National Laboratory, along with Dr. Loveland, performed irradiations at the CERN laboratory and arranged shipment of samples to the U.S. for spectroscopic analysis. Dr. K. Moody performed one of the LBL cyclotron irradiations and arranged for sample shipment to OSU. Dr. M. Smith, Mr. C. Oertel and Mr. K. Keasler were among the people assisting in the arduous task of making spectroscopic measurements. Mr. Chan and Mr. Rosenberg from the Lawrence Berkeley Laboratory assisted Dr. Loveland in the completion of many of the deexcitation calculations performed at LBL.

The United States Department of Energy was the primary source of financial assistance for this work, either through Dr. Loveland or Dr. Seaborg. Without the grants from the USDOE, this work would never have been completed. Other sources of financial assistance crucial to the completion of this research were the OSU computer center and the OSU Department of Chemistry.

TABLE OF CONTENTS

I. INTRODUCTION.....1

II. EXPERIMENTAL.....10

A. Targetry and Irradiations.....10

B. Gamma-ray Spectroscopy.....18

1. Spectroscopic System Calibration.....18

2. Data Acquisition and Analysis.....23

3. Decay Half-life Determination.....26

C. Yield Determination.....29

1. Cross Section Calculation.....29

2. Charge Dispersion and Mass Yield Calculation....39

III. RESULTS AND DISCUSSION.....66

A. Yields.....66

1. Experimental Production Cross Sections.....66

2. Experimental Mass Yields.....72

2a. Heavy Fragment Yields.....75

2b. Fission Yields.....79

B. Phenomenological Model Predictions.....87

1. Deexcitation Parameters and Procedures.....88

2. Reaction Yield Comparison.....93

3. Fission Yield Comparison.....95

4. Heavy Fragment Yield Comparisons.....101

IV. SUMMARY AND CONCLUSIONS.....113

V. REFERENCES.....117

VI. APPENDICES.....125

A. Sampo-80.....126

B. Theoretical Models.....130

1. Introduction.....130

2. Firestreak Model.....131

3. Sum-Rule Model.....137

4. Deexcitation.....142

C. High Energy Data.....146

D. Charge Dispersions.....195

LIST OF FIGURES

Figure	Description	Page
1.	A simple schematic representation of an high energy peripheral nuclear interaction.	5
2.	Holmium target and catcher arrangement used at the CERN SC accelerator.	12
3.	Holmium target and catcher arrangement used at the LBL 88-inch cyclotron.	13
4.	Schematic representation of the spectroscopic system design.	19
5.	Flow diagram of the procedure used to calibrate the spectroscopic system.	21
6.	Flow diagram of the procedure used to analyze spectroscopic data.	25
7.	Fragment isobaric yield distribution for the reaction system 208 MeV ^{12}C + ^{165}Ho.	54
8.	Fragment isobaric yield distribution for the reaction system 265 MeV ^{16}O + ^{165}Ho.	55
9.	Fragment isobaric yield distribution for the reaction system 442 MeV ^{12}C + ^{165}Ho.	56
10.	Fragment isobaric yield distribution for the reaction system 1020 MeV ^{12}C + ^{165}Ho.	57
11.	Fragment isobaric yield distribution for the reaction system 1635 MeV ^{16}O + ^{165}Ho.	58
12.	Plot of the most probable Z-value (from charge dispersion fit) relative to valley of beta stability for the reaction system 208 MeV ^{12}C + ^{165}Ho.	60
13.	Plot of the most probable Z-value (from charge dispersion fit) relative to valley of beta stability for the reaction system 1635 MeV ^{16}O + ^{165}Ho.	61
14.	Trans-target nuclidic production cross sections plotted as a function of total projectile kinetic energy.	70
15.	Combined isobaric yield distributions for all five systems studied.	73

16. Plot of most probable Z-value (from charge dispersion fit) relative to valley of beta stability for the fission fragment region of all reaction systems studied. 74

17. Fission yields plotted as a function of E_{CM}-V. 83

18. Angular momentum probability distributions for two typical primary products resulting form the interaction of 265 MeV ^{16}O + ^{165}Ho. 97

19. Heavy fragment isobaric yields calculated using various combinations of interaction and deexcitation codes for reactions induced by 442 MeV carbon. 103

20. Comparative deexcitation results of ^{177}Ta with 182 MeV excitation energy and $\langle l \rangle = 44\hbar$ and with 345 MeV excitation energy and $\langle l \rangle = 40\hbar$. 105

21. Comparison plot of measured heavy fragment isobaric yields and an average calculated heavy fragment distribution for the reaction system 208 MeV ^{12}C + ^{165}Ho. 107

22. Comparison plot of measured heavy fragment isobaric yields and an average calculated heavy fragment distribution for the reaction system 265 MeV ^{16}O + ^{165}Ho. 108

23. Comparison plot of measured heavy fragment isobaric yields and calculated heavy fragment distributions for the reaction system 442 MeV ^{12}C + ^{165}Ho. 109

24. Comparison plot of measured heavy fragment isobaric yields and a calculated heavy fragment distribution for the reaction system 1020 MeV ^{12}C + ^{165}Ho. 110

25. Comparison plot of measured heavy fragment isobaric yields and a calculated heavy fragment distribution for the reaction system 1635 MeV ^{16}O + ^{165}Ho. 111

APPENDICES:

B-1. A simple schematic representation of an high energy peripheral nuclear interaction. 132

B-2. Schematic representation of colliding tubes concept used in the firestreak model. 134

C-1. Fragment isobaric yield distribution for the reaction system 2.9 GeV ^{12}C + ^{165}Ho. 173

C-2. Fragment isobaric yield distribution for the reaction system 7.7 GeV ^{20}Ne + ^{165}Ho. 174

C-3. Fragment isobaric yield distribution for the reaction system 12.5 GeV ^{12}C + ^{165}Ho. 175

C-4. Fragment isobaric yield distribution for the reaction system 12.5 GeV ^{12}C + ^{152}Sm. 176

C-5. Fragment isobaric yield distribution for the reaction system 12.5 GeV ^{12}C + ^{144}Sm. 177

C-6. Fragment isobaric yield distribution for the reaction system 20.8 GeV ^{20}Ne + ^{165}Ho. 178

C-7. Fragment isobaric yield distribution for the reaction system 20.8 GeV ^{20}Ne + ^{nat}Ce. 179

C-8. Fragment isobaric yield distribution for the reaction system 33.8 GeV ^{40}Ar + ^{165}Ho. 180

D-1. Calculated fragment charge dispersion plots for the reaction system 208 MeV ^{12}C + ^{165}Ho 196

D-2. Calculated fragment charge dispersion plots for the reaction system 265 MeV ^{16}O + ^{165}Ho 201

D-3. Calculated fragment charge dispersion plots for the reaction system 442 MeV ^{12}C + ^{165}Ho 206

D-4. Calculated fragment charge dispersion plots for the reaction system 1020 MeV ^{12}C + ^{165}Ho 209

D-5. Calculated fragment charge dispersion plots for the reaction system 1635 MeV ^{16}O + ^{165}Ho 213

LIST OF TABLES

Table	Description	Page
1.	A tabulation of irradiation conditions and targetry data for the indicated experiments.	11
2.	A tabulation of the minimum number of gamma-rays used to identify any given nuclide tabulated in table 3.	31
3.	A tabulation of all measured nuclidic cross sections for the reaction systems studied.	35
4.	Tabulation of the measured and calculated independent and mass yields for the nuclides produced by the interaction of 208 MeV ^{12}C and ^{165}Ho.	40
5.	Tabulation of the measured and calculated independent and mass yields for the nuclides produced by the interaction of 265 MeV ^{16}O and ^{165}Ho.	42
6.	Tabulation of the measured and calculated independent and mass yields for the nuclides produced by the interaction of 442 MeV ^{12}C and ^{165}Ho.	45
7.	Tabulation of the measured and calculated independent and mass yields for the nuclides produced by the interaction of 1020 MeV ^{12}C and ^{165}Ho.	47
8.	Tabulation of the measured and calculated independent and mass yields for the nuclides produced by the interaction of 1635 MeV ^{16}O and ^{165}Ho.	49
9.	A tabulation of the measured trans-target nuclidic yields.	67
10.	A tabulation of heavy fragment and fission yields and parameters describing general aspects of the yield distributions.	80
11.	A tabulation of the deduced fractional linear momentum transfer, P_{par}/P_{CN}, and angular momentum transfer, $\langle l_{sys} \rangle$, to the target nucleus for the interactions studied.	86
12.	A tabulation of calculated and measured fission yields as a function of fission barrier and level density parameters.	91
13.	A comparison of measured and calculated fission and reaction cross sectons.	94

APPENDICES

A-1. A tabulation of the analysis time of the SAMPO-80 computer code implemented on the OSU ND-6600. 129

C-1. A tabulation of irradiation conditions and targetry data for the high energy experiments. 148

C-2. A tabulation of the total thickness of targets, catchers, and monitor foils which preceded the target assemblies discussed in the text. 149

C-3. A tabulation of observed gamma-ray photopeak energies and associated branching ratios required to identify nuclides tabulated in table C-4. 150

C-4. A tabulation of measured nuclidic yields and calculated independent and mass yields for the reaction system 2.9 GeV ^{12}C + ^{165}Ho. 154

C-5. A tabulation of measured nuclidic yields and calculated independent and mass yields for the reaction system 7.7 GeV ^{20}Ne + ^{165}Ho. 156

C-6. A tabulation of measured nuclidic yields and calculated independent and mass yields for the reaction system 12.5 GeV ^{12}C + ^{165}Ho. 158

C-7. A tabulation of measured nuclidic yields and calculated independent and mass yields for the reaction system 12.5 GeV ^{12}C + ^{152}Sm. 160

C-8. A tabulation of measured nuclidic yields and calculated independent and mass yields for the reaction system 12.5 GeV ^{12}C + ^{144}Sm. 163

C-9. A tabulation of measured nuclidic yields and calculated independent and mass yields for the reaction system 20.8 GeV ^{20}Ne + ^{165}Ho. 166

C-10. A tabulation of measured nuclidic yields and calculated independent and mass yields for the reaction system 20.8 GeV ^{20}Ne + ^{nat}Ce. 168

C-11. A tabulation of measured nuclidic yields and calculated independent and mass yields for the reaction system 33.8 GeV ^{40}Ar + ^{165}Ho. 170

C-12. A tabulation of the Z_p function and Gaussian width parameters of the respective mass regions used for calculation of independent and mass yields for the reaction system 2.9 GeV ^{12}C + ^{165}Ho. 181

C-13. A tabulation of the Z_p function and Gaussian width parameters of the respective mass regions used for calculation of independent and mass yields for the reaction system 7.7 GeV ^{20}Ne + ^{165}Ho. 182

C-14. A tabulation of the Z_p function and Gaussian width parameters of the respective mass regions used for calculation of independent and mass yields for the reaction system 12.5 GeV ^{12}C + ^{165}Ho. 183

C-15. A tabulation of the Z_p function and Gaussian width parameters of the respective mass regions used for calculation of independent and mass yields for the reaction system 12.5 GeV ^{12}C + ^{152}Sm. 184

C-16. A tabulation of the Z_p function and Gaussian width parameters of the respective mass regions used for calculation of independent and mass yields for the reaction system 12.5 GeV ^{12}C + ^{144}Sm. 185

C-17. A tabulation of the Z_p function and Gaussian width parameters of the respective mass regions used for calculation of independent and mass yields for the reaction system 20.8 GeV ^{20}Ne + ^{165}Ho. 186

C-18. A tabulation of the Z_p function and Gaussian width parameters of the respective mass regions used for calculation of independent and mass yields for the reaction system 20.8 GeV ^{20}Ne + ^{nat}Ce. 187

C-19. A tabulation of the Z_p function and Gaussian width parameters of the respective mass regions used for calculation of independent and mass yields for the reaction system 33.8 GeV ^{40}Ar + ^{165}Ho. 188

C-20. A tabulation of the measured kinematical quantities, for nuclides identified in the target and both catcher foils resulting from the interaction of 2.9 GeV ^{12}C + ^{165}Ho. 189

C-21. A tabulation of the measured kinematical quantities, for nuclides identified in the target and both catcher foils resulting from the interaction of 12.5 GeV ^{12}C + ^{165}Ho. 190

C-22. A tabulation of the measured kinematical quantities, for nuclides identified in the target and both catcher foils resulting from the interaction of 33.8 GeV ^{40}Ar + ^{165}Ho. 191

C-23. A tabulation of kinematical quantities deduced following the two-step formalism implemented by Winsberg [110] for nuclides resulting from the interaction of 2.9 GeV ^{12}C + ^{165}Ho. 192

C-24. A tabulation of kinematical quantities deduced following the two-step formalism implemented by Winsberg [110] for nuclides resulting from the interaction of 12.5 GeV ^{12}C + ^{165}Ho. 193

C-25. A tabulation of kinematical quantities deduced following the two-step formalism implemented by Winsberg [110] for nuclides resulting from the interaction of 33.8 GeV ^{40}Ar + ^{165}Ho. 194

D-1. Table of Z_p for the reaction system 208 MeV ^{12}C and ^{165}Ho. 218

D-2. Table of Z_p for the reaction system 265 MeV ^{16}O and ^{165}Ho. 219

D-3. Table of Z_p for the reaction system 442 MeV ^{12}C and ^{165}Ho. 220

D-4. Table of Z_p for the reaction system 1020 MeV ^{12}C and ^{165}Ho. 221

D-5. Table of Z_p for the reaction system 1635 MeV ^{16}O and ^{165}Ho. 222

HOLMIUM TARGET FRAGMENTATION INDUCED BY INTERMEDIATE ENERGY ^{12}C AND ^{16}O IONS

I. INTRODUCTION

Considerable interest in recent years has been devoted to the study of intermediate energy heavy-ion collisions. The sudden and recent interest in this region of projectile kinetic energy was predominantly a matter of "technological fate" and partially a result of "theoretical fancy". Prior to 1974, heavy-ion research was generally limited to the investigation of interactions induced by heavy ion projectiles with a maximum kinetic energy of 10-20 MeV/A. The ingenious concept to use the Lawrence Berkeley Laboratory HILAC as an injector for the Bevatron led to an hundredfold increase in attainable kinetic energy for heavy-ion beams. This turn of technological fate had, in one giant step, opened a completely new frontier of nuclear science (relativistic heavy-ion, RHI, interactions) while, for practical purposes, entirely skipping over the intermediate region.

The low energy realm of nuclear reactions has been actively studied for approximately four decades. The realm of low energy reactions extends from an energy sufficient to induce nuclear reactions up to about 20 MeV/A. Reactions observed at low energies are often categorized into four groups: elastic scattering, quasi-elastic scattering, deep inelastic (strongly damped) collisions, and compound nuclear (complete fusion) reactions [1-12].

These reactions are associated with impact parameter or angular momentum windows. Lefort [4] extended the sharp cut-off l-window picture of Blair [5] (originally proposed for elastic scattering reactions) to describe the entire reaction cross section. Systems with incident angular momentum between 0 and $l_{crit}(CF)$ would result in complete fusion events. Those systems with angular momentum between $l_{crit}(CF)$ and $l_{crit}(DI)$ would result in a deep inelastic (DI) event, etc. Lefort's concept has more recently been extended to represent a smooth cut-off transition between l-windows leading to a given reaction mechanism [11-13].

Elastic scattering is the simplest interaction of nuclear potential fields. This type of interactions results in no net transmutations of the nuclei. The differential cross section data ($d\sigma/d\Omega$, as a function of angle) for elastic events has a signature similar to purely Coulombic (Rutherford or Mott) interactions combined with oscillations characteristic of diffraction [14,15]. The overall structure has been successfully described using semi-classical optical models. The very grazing or peripheral interactions involve small overlaps of the nuclear surfaces resulting in short interaction times, small mass, energy, and momentum transfers, and scattering characteristics similar to elastic events [16,17]. Deep inelastic (strongly damped) collisions involve substantial energy and mass transfer [8,18-20]. The interaction is interpreted in terms of the projectile experiencing strong frictional forces [21]. The frictional forces convert kinetic energy to internal excitation energy and transform the angular momentum of the system to intrinsic spin. Large angle scattering events have been

inter-preted in te rms of a "sticking" deep-inelastic (DI) mechanism causing the ions to rotate through some relatively large angle (thus reducing the relative angular momentum of the reaction partners) before separating [10]. If the angular momentum of the system is sufficiently low the ions will fuse to form a compound nucleus.

The kinetic energies of low energy reactions are small compared to the kinetic energies of the Fermi motion. The time scale in which internal degrees of freedom change is, therefore, expected to be fast compared to typical collision times for all but the most grazing collisions. During the reaction the transformation of kinetic energy and angular momentum to internal excitation energy and spin can be described in terms of frictional forces. The exchange of nucleons and further equilibration processes can be described in terms of a nucleon-diffusion mechanism [22]. These concepts connect, in a continuous way, the domains of quasielastic transfer, deep inelastic transfer, and compound nucleus formation to describe nuclear reactions at low energies.

Relativistic heavy ion (RHI) induced interactions have only been extensively studied since the Princeton-Pennsylvania accelerator (PPA) and Lawrence Berkeley Laboratory Bevalac became operational in the mid-1970's. The LBL Bevalac accelerator is capable of accelerating heavy ions to approximately 2.1 GeV/A producing intense (relative to cosmic rays) beams. The realm of high energy (RHI induced) interactions is typically assumed to extend from approximately 200 MeV/A to the maximum attainable energy (currently $\leq$2.1 GeV/A). Very simplistically, interactions observed at high energies have often been categorized as either peripheral or central

collisions. The central collision, in this simplistic picture, results in the total or near total obliteration of projectile and target nuclei yielding a tremendous shower with a multiplicity on the order of 100 particles [23-26]. The peripheral interaction is, by comparison, a relatively gentle grazing collision resulting in two relatively cold spectator nuclei, and a group of highly excited nucleons.

Peripheral collisions constitute the majority of the total reaction cross section [27]. Theorists have proposed models to aid the understanding of RHI induced fragmentation interactions. The abrasion-ablation [28] concept was the forerunner of the models which envisioned the RHI induced reaction in terms of a two-step process. Such a peripheral interaction is depicted in figure 1 where the projectile nucleus is shown with initial velocity β. The fast interaction step (abrasion) is governed purely by geometrical constraints. The projectile slices out a chunk from the target nucleus corresponding to the volume of overlap between the target and projectile assuming straight line trajectory. This process is described by a "clean-cut" interaction in which the projectile spectator retains its initial velocity, β, no kinetic energy or angular momentum are transferred to the target spectator, and the highly excited nuclear matter from the overlap volume travels at an intermediate velocity. The slower second stage is the equilibration and deexcitation of the deformed residual fragment. The abrasion-ablation concept was subsequently refined into the fireball [29] and firestreak [30] models (the latter is described further in appendix B).

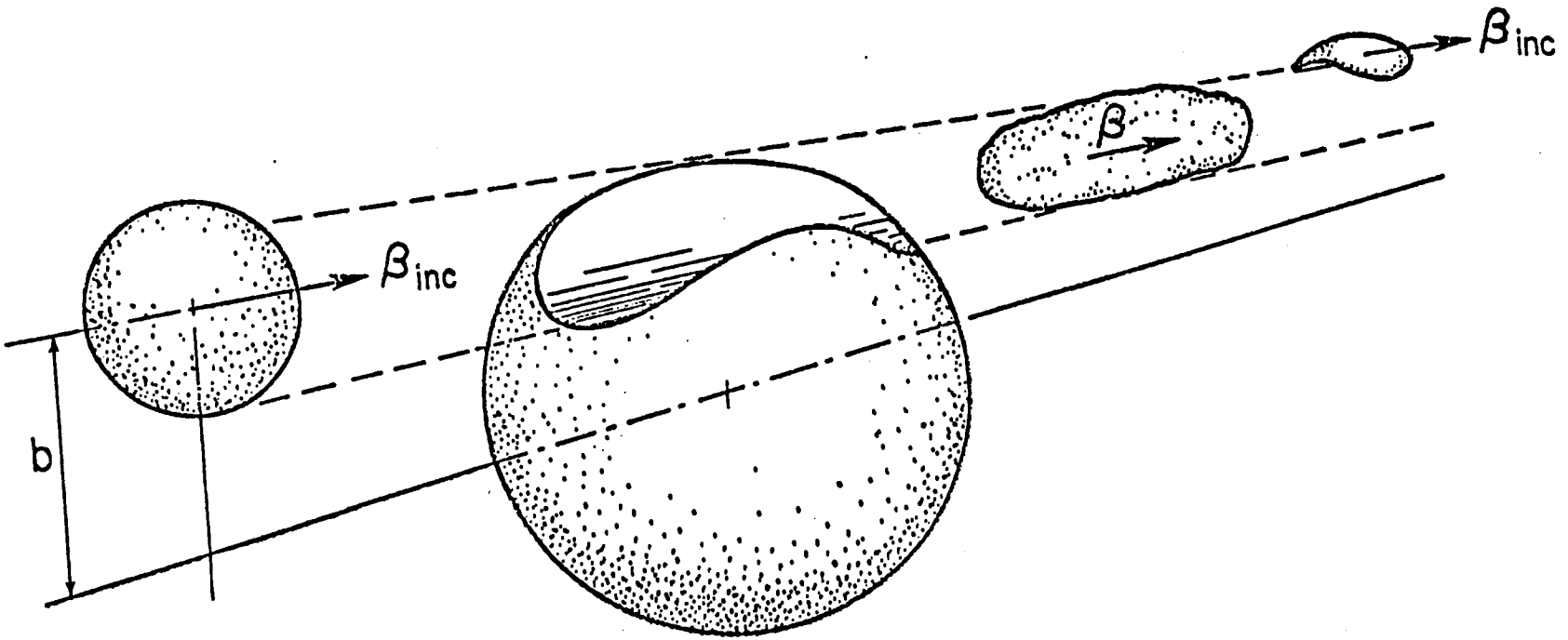

A simple schematic representation of an high energy peripheral nuclear interaction. This figure is borrowed from reference 29.

Figure 1

Nuclear fragments resulting from very peripheral interactions are envisioned to be relatively undisturbed with little transfer of excitation energy (with the exception of the deformation caused by the removed volume) and angular momentum. The overlap region is an extremely excited volume of nuclear matter which has been modeled by a hot expanding ideal gas [29] and the coalescing [31,32] (or condensing) of small particles within a given volume. The theoretical treatment of the central collision can successfully incorporate similar concepts used to describe the overlap region for peripheral collisions [33] to reproduce observations.

The conceptual differences between the RHI induced reactions and low energy reactions are dramatic. Reactions described by transfer processes and complete fusion evolve into fragmentation, or spallation type processes and total nuclear disintegration. The reaction exit channel changes from containing almost exclusively one or two fragments at low energies to interactions where a few or 100 or more fragments may be observed for a single high energy event. Large momentum transfers associated with fusion reactions are not observed for any heavy target residues resulting from RHI induced interactions. Similarly, reactions at low energy are often associated with high angular momentum, whereas, at high energy the degree of overlap (geometry) is the major factor determining the violence of the interaction. The extremely short interaction times at high energies do not allow nucleon diffusion, energy equilibration or angular momentum dissipation processes to occur during the interaction of projectile and target. Systems in which the

trajectory of a high energy projectile significantly (or completely) overlaps a target are not expected to survive.

Intermediate energy heavy ion induced nuclear reactions have recently become an extremely active field of investigation as more accelerators become available to produce intense heavy ion beams with energies between 20 MeV/A and 100 MeV/A. Considerable information and insight has been gained in recent years about this region of transition between phenomena observed at low and high energies. The linear momentum transferred to the target nucleus by light-heavy ions (A<40) has been widely studied. Viola, et al. [34] and Stokstad et al. [35] have developed systematics of fractional momentum transfer for light projectiles ($A \leq 20$) that show the fraction of the beam momentum transferred to the target nucleus decreases approximately linearly with increasing relative velocity of the colliding nuclei. Viola et al. [36] and Chan et al. [37] report these systematics are evidence of a decreasing role of complete fusion in the total reaction cross section between 7 and 20 MeV/A. Their interpretation predicts the fraction of the cross section resulting in complete fusion decreases slowly above 20 MeV/A until around 70 MeV/A where no complete fusion is observed. Blachot et al. [38] have reported observing small (1%), however significant, "quasi-compound" nucleus formation in the reaction of 84 MeV/A ^{12}C with Sn and Ag targets.

While momentum transfer and fusion mechanisms are decreasing with increasing energy, Natowitz et al. [39] observe significant signatures of projectile fragmentation, a traditional high energy mechanism, in 43 MeV/A ^{20}Ne induced reactions. Natowitz also noted the observation of light fragments characteristic of fusion reactions

and nonequilibrium processes. Lynen et al. [40] studied target fragmentation of ^{181}Ta, ^{197}Au, and ^{238}U induced by 86 MeV/A ^{12}C. They assigned significant fractions of the reaction cross section to high energy processes such as spallation and "deep" spallation; however, they also observed the production of light fragments ($10<A<40$) as low multiplicity binary events in sharp contrast to relativistic heavy-ion induced interactions for which light fragments are produced in high multiplicity events (central collisions) [25,26].

The above observations clearly demonstrate the transitional nature of the intermediate energy regime of nuclear reactions. Interactions described by low energy mechanisms are observed over a large portion of this region but diminishing with increasing projectile kinetic energy. Reactions induced by projectiles at the high end of the intermediate energy regime show characteristics similar to high energy mechanisms. This energy region is, in general, characterized by the slowly diminishing role of low energy mechanisms followed by (or overlapped with) the onset of high energy mechanisms.

Researchers have observed other important features of intermediate energy interactions, not necessarily transitional in nature. Complete and incomplete fusion and deep-inelastic scattering have been observed for reactions induced by projectiles with kinetic energies above 10 MeV/A [20,41,64,68]. The fraction of the observed cross section that is associated with complete fusion reactions has been reported to decrease as the projectile energy increases (from 93% for the interaction of 8.5 MeV/A ^{16}O + ^{154}Sm to <5% for 35 MeV/A

^{12}C + ^{154}Sm [68]). Incomplete fusion reactions involve the "fusion" of a portion of the projectile nucleus with the target while the remainder of the projectile travels at near 0 degrees with near beam velocity. The fraction of the observed cross section that is associated with incomplete fusion has been reported to increase dramatically between 8.5 MeV/A and 86 MeV/A projectile energies [68].

There are many questions about the nature of intermediate energy heavy ion induced interactions that remain unanswered. Radioanalytical techniques allow us to address the more general aspects of these reactions. The questions which this work addresses are:

1. How does the fission cross section evolve with increasing projectile energy?
2. How does the general shape of the target fragment mass yield curve evolve? What can we learn from the mass yield curves?
3. How does projectile energy affect the excitation functions of observed nuclides, particularly trans-target species?
4. How well do the Wilczynski sum-rule and firestreak models predict the observables?

II. EXPERIMENTAL

A. TARGETRY AND IRRADIATIONS

Interactions were induced in holmium targets by 208 MeV ^{12}C and 272 MeV ^{16}O beams from the Lawrence Berkeley Laboratory 88-inch cyclotron; and 442 MeV ^{12}C, 1020 MeV ^{12}C, and 1635 MeV ^{16}O beams supplied by the CERN SC synchro-cyclotron. All beams were undegraded primary beams with the exception of the 442 MeV ^{12}C beam which was degraded from 1020 MeV. An aluminum degrader block was placed upstream from the experimental station. The degraded beam was bent twice prior to entering the experimental station removing secondaries produced in the degrader block. The beam characteristics for each system studied and the accelerator at which the experiments were conducted are tabulated in table 1. Target and catcher material specifications are also given in table 1.

Each holmium target assembly consisted of an elemental ^{165}Ho metal foil target surrounded by forward and backward catcher foils. Catchers used for 208 MeV ^{12}C, 442 MeV ^{12}C, and 1635 MeV ^{16}O induced interactions were sufficiently thick to stop all fragments heavier than A=25. Catcher foils used for 272 MeV ^{16}O and 1020 MeV ^{12}C induced interactions were only thick enough to stop fragments with A60. A schematic of the experimental arrangements used at the CERN SC synchrocyclotron and the LBL 88-inch cyclotron for the holmium target assemblies are shown in figures 2 and 3, respectively. The target assemblies used at CERN were mounted on frames which were

IRRADIATION INFORMATION

ION	PROJECTILE ENERGY INIT. (MeV)	-COT- (MeV)	(MeV/A)	TOTAL FLUX (IONS)	IRRAD. LENGTH (MIN)	TARGET THICKNESS (mg/cm^2)	CATCHER THICKNESS (mg/cm^2)	TAEI to COUNTING (hours)	ACCEL.
$^{16}O^{6+}$	1712	1635	102.	7.76×10^{13}	515.	114.0	20.3 (C)	86.0	CERN SC
$^{12}C^{4+}$	1032	1020	85.0	1.17×10^{15}	60.	123.3	5.55 (Al)	130.0	CERN SC
$^{12}C^{4+}$	588	442	36.8	1.37×10^{14}	130.	229.1	33.2 (C)	127.0	CERN SC
$^{16}O^{6+}$	315	272	17.2	1.97×10^{14}	326.	26.4	20.3 (C,Fwd) 6.7 (Al,Bkd)	4.5	LBL 88"
$^{12}C^{5+}$	236	208	17.3	1.53×10^{15}	583.	26.4	20.3 (C)	96.0	LBL 88"

The above is a tabulation of irradiation conditions and targetry data for the indicated experiments. Projectile energies are tabulated for the extracted beam and at the center-of-target. The TAEI to counting column shows approximate lapsed times between the end-of-irradiation and the first gamma spectroscopic measurement for each experiment.

Table 1

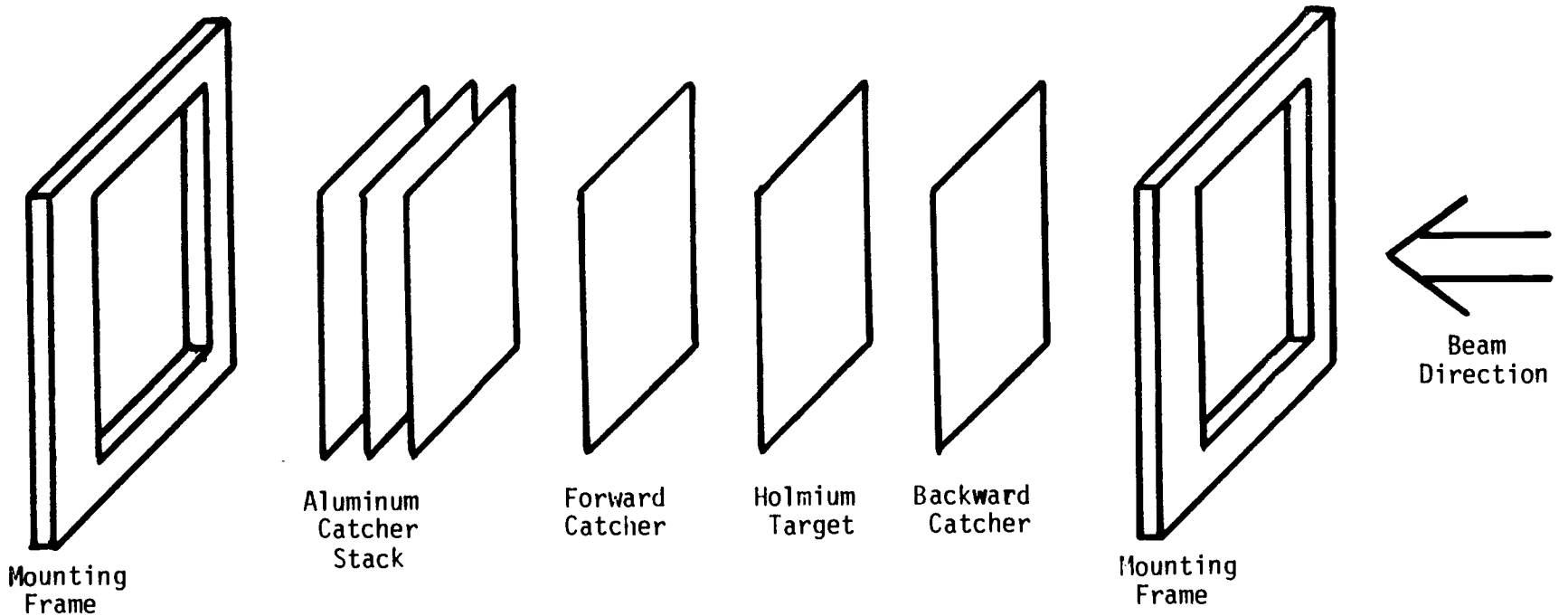

Holmium target and catcher arrangement used at the CERN SC accelerator. Target and catcher materials preceding holmium target stack are discussed in the text.

Figure 2

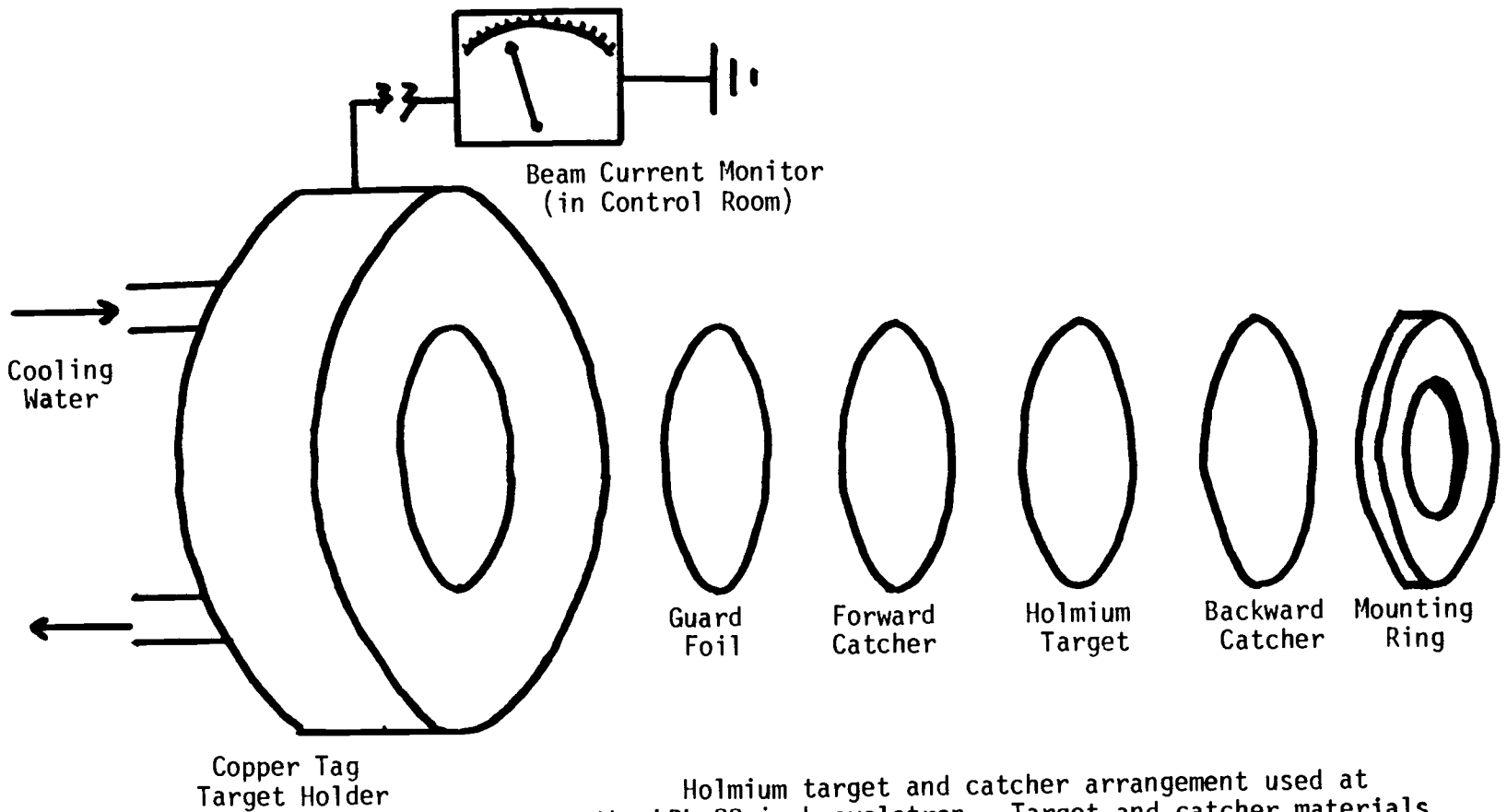

Holmium target and catcher arrangement used at the LBL 88-inch cyclotron. Target and catcher materials preceding holmium target stack are discussed in the text.

Figure 3

attached to a fast-access vacuum chamber provided by the ISOLDE research collaboration. The target assemblies at LBL were mounted to a tag-target holder which provided quick access, water cooling, and charge collection to monitor beam intensity.

Multiple target assembiles were often mounted in the beam to obtain the greatest use for any given irradiation. A gold target stack consisting of two 6.24 mg/cm^2 Al catcher folis, one 5.16 mg/cm^2 Au foil and a 2.6 mg/cm^2 Al guard foil preceeded the holmium target stack in the 208 MeV ^{12}C irradiation. A 4.65 mg/cm^2 Be foil supporting 0.97 mg/cm^2 Sm followed by a 2.5 mg/cm^2 Al catcher foil preceeded the holmium target stack in the 315 MeV ^{16}O irradiation. A monitor stack followed by a uranium target stack followed by another monitor stack preceeded the holmium target stack in the 588 MeV ^{12}C irradiation. Each of the monitor stacks consisted of one 20.3 mg/cm^2 C foil, one 8.65 mg/cm^2 Al foil, and three 20.3 mg/cm^2 C foils. The uranium stack consists of one 20.3 mg/cm^2 C foil, one 46.4 mg/cm^2 U foil, and one 20.3 mg/cm^2 C foil. The holmium target stack in the 1032 MeV ^{12}C irradiation had no other preceeding foils. A monitor stack and uranium target stack preceeded the holmium target stack in the 1635 MeV ^{16} irradiation. The monitor stack consisted of two 20.3 mg/cm^2 C foils, one 6.9 mg/cm^2 Al foil, and one 20.3 mg/cm^2 C foil. The uranium target stack consisted of one 20.3 mg/cm^2 C foil, one 46.8 mg/cm^2 U foil, and one 20.3 mg/cm^2 C foil.

Holmium targets irradiated by 208 MeV ^{12}C, 272 MeV ^{16}O, 1020 MeV ^{12}C, and 1635 MeV ^{16}O projectiles were 99.99% pure supplied by the Goodfellow Ltd. company. The holmium target irradiated by 442 MeV ^{12}C ions was 99.9% pure supplied by the Alfa Inc. company. The

target thicknesses used in the experiments are indicated in table 1. Carbon or aluminum catcher foils were used in all of the experiments. The foils used in the five experiments were 99.8% pure light-tight carbon sheets supplied by the Goodfellow, Ltd. company. The specifications for catcher materials and thicknesses used in each experiment are tabulated in table 1.

The integral particle intensities are tabulated as a part of table 1. Beam intensities at the LBL 88-inch cyclotron were monitored continuously and tabulated periodically by the operations staff. The beam intensity was calculated from absolute charge collection of beam ions in the tag target holder used in all of the irradiations at LBL and the known ionic charge state. The integral beam intensities at the CERN SC synchrocyclotron were determined using Al foil monitors and known monitor cross sections. The cross section used for the 1020 MeV ^{12}C irradiation was 34.1 ± 0.6 mb [43] for the ^{27}Al(85 MeV/A ^{12}C,X)^{22}Na monitor reaction. The same value was used to approximate the 102 MeV/A ^{16}O monitor reaction cross section (the true value for this energy and projectile is not known). A cross section of 32. ± 2. mb [44] for the ^{27}Al(49 MeV/A ^{12}C,X)^{22}Na monitor reaction was used to approximate the 37 MeV/A ^{12}C value. These monitor cross sections enable us to calculate absolute cross sections only for the 85 MeV/A ^{12}C induced reactions for experiments conducted at the CERN laboratory. The monitor cross sections used for 37 MeV/A ^{12}C and 102 MeV/A ^{16}O induced interactions are not explicitly known thus the cross sections tabulated for these experiments must be considered only as relative quantities. The 1020 MeV/A ^{12}C beam intensity calculated from the ^{27}Al(85 MeV/A ^{12}C,X)^{22}Na

monitor cross section disagree with the intensity calculated from the $^{27}Al(85\ MeV/A\ ^{12}C,X)^{24}Na$ monitor cross section reported elsewhere for the same bombardment [91].

Beam intensity histories were kept for all of the bombardments at LBL and CERN. An accurate knowledge of fluctuations in beam intensity is necessary to accurately calculate production cross sections when the time scale of the fluctuations are on the order of half-lives of the observed nuclides. The time delay from end-of-bombardment (EOB) to the initial gamma-ray spectroscopic measurements (due to shipping of targets from the accelerator facility to the laboratory where measurements were made) are included in table 1 (designated as TAEI, the time after end-of-irradiation). The delay times for all experiments, with the exception of the 272 MeV ^{16}O irradiation, were significantly longer than the irradiation period. The delay time for the 272 MeV ^{16}O irradiation was relatively short and inclusion of beam intensity fluctuations in calculation of the cross sections for the shorter-lived nuclides became important. The beam intensity histories were supplied by the operations staffs of the accelerators at LBL and CERN. The beam histories obtained from the CERN SC synchrocyclotron operations staff were scaled to the monitor cross sections (above).

Table 1 lists two different beam energies, the first being the projectile energy entering the irradiation station and the second the beam energy at the center of the holmium target. The projectile energy degradation is caused by passage through various target assemblies and the backward catcher preceeding the holmium target. The center-of-target energy, E_{cot}, is calculated by iteratively

determining the projectile energy after each foil, $E_{proj}(i)$. $E_{proj}(i)$ is determined by subtracting the thickness of foil i, T_i, from the total range of the projectile in that foil material:

$$R_{fin} = R_{init} - T_i \qquad \text{[eqn 1]}$$

and converting the resultant range, R_{fin}, to an energy. The ranges and projectile energies are approximated by using the tables of Hubert, et al. [49].

B. GAMMA-RAY SPECTROSCOPY

1. Spectroscopic System Calibration

Gamma-ray spectroscopic measurements were made using a system schematically depicted in figure 4. A gamma-ray detector unit is comprised of a coaxial lithium drifted germanium, Ge(Li), diode DC - coupled to a charge sensitive preamplifier. The preamplifier was connected to a high-rate linear amplifier adjusted to match the input signal rise-time. The amplifier output was AC - coupled to an analogue-to-digital converter (ADC). An active baseline restorer was used to produce consistent amplifier output pulse shapes over a wide range of counting rates to improve photopeak resolution. Digital output from the ADC was transferred directly to random access memory (RAM) through the direct memory access channel (DMA) of the minicomputer controlled multichannel analyzer system. Data was acquired into 4096 channel spectra for preset periods of time and permanently stored with identifying header data, on at least one of the magnetic storage media available. Systems were adjusted for approximately 0.5 keV per channel energy calibration with roughly 0.0 keV offset, and lower level discriminators were adjusted to eliminate noise and X-rays below 80 keV. This calibration allowed the observation of gamma-rays over an approximate range of 80 to 2000 keV.

An experimental spectra may contain more than 300 resolvable photopeaks. Determination of accurate photopeak intensities is dependent upon obtaining and maintaining extremely good spectroscopic

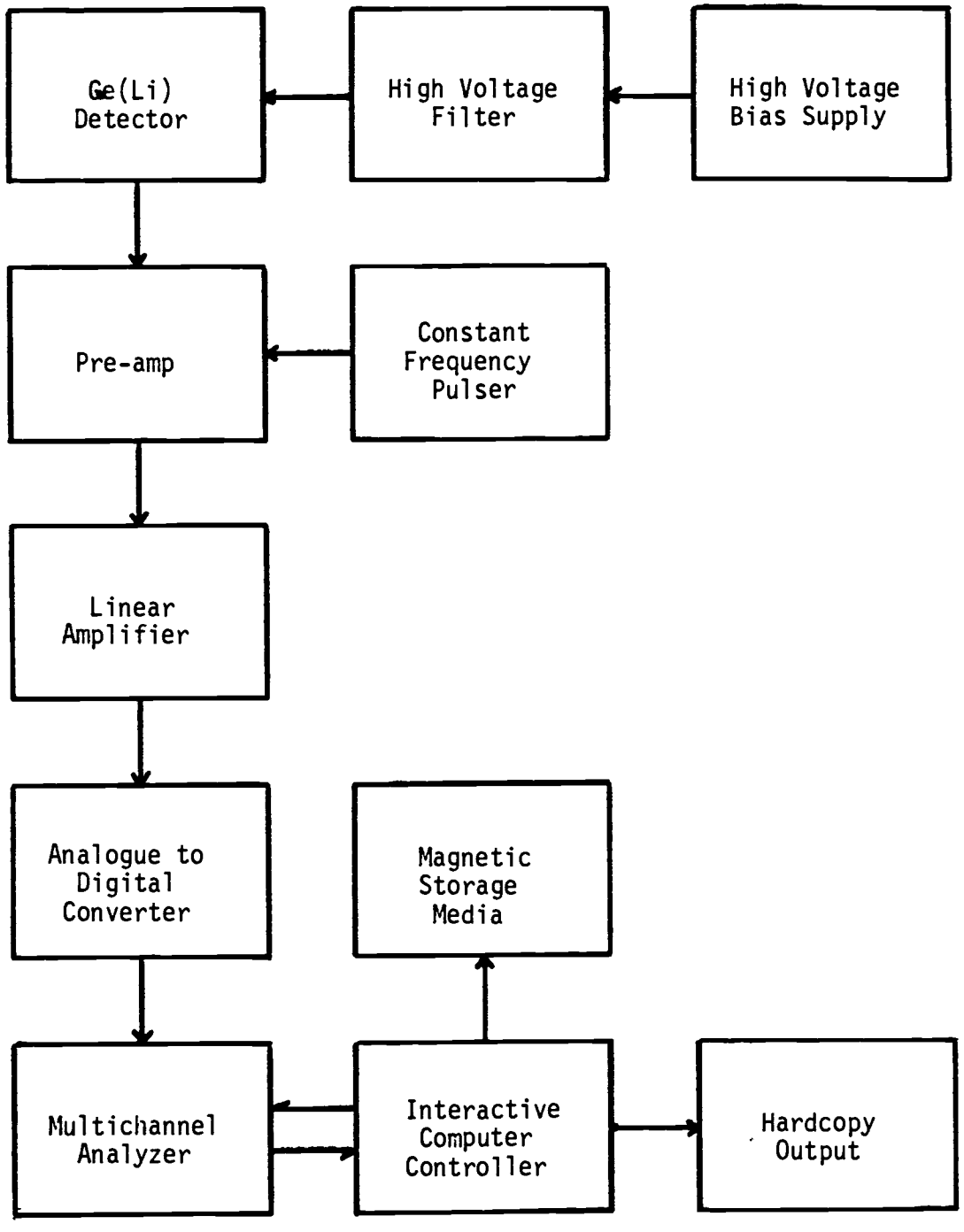

Schematic representation of the spectroscopic system design.

Figure 4

resolution. The full-width at half-maximum (FWHM) and tailing of spectral peaks were minimized by carefully matching amplifier and preamplifier rise-times. Active baseline restoration of the amplified signal output was adjusted to minimize signal oscillation about the baseline. Stability and electronic signal to noise ratio were greatly enhanced by linking all system components to an absolute ground. The measured FWHM value for the ^{60}Co 1332.5 keV gamma-ray line was approximately 1.9 keV for all spectroscopic systems used.

Absolute efficiency and energy calibrations for each detection system were generated using techniques outlined previously [46]. A flow diagram of the calibration procedure is shown in figure 5. The calibration source was the National Bureau of Standards mixed radionuclide gamma-ray emission-rate standard reference material, SRM-4275/15. Several calibration spectra of varying acquisition time were taken at each geometry used during the experiments. The calibration spectra provided a database from which to generate energy, efficiency and photopeak shape calibrations.

The computer program, SAMPO-80 [47,48], has been modified and adapted to the LSI-11 based Nuclear Data Inc. model 6660 (ND-6660) multiparameter gamma-ray spectroscopy system. A brief description the modifications and implementation of SAMPO-80 on the ND-6660 are given in Appendix A. SAMPO-80 has two primary modes of operation, a calibration mode and an analysis mode. The calibration mode was used to determine photopeak shape characteristics. This was accomplished through the use of a functional form that can be linearly fit to the photopeak energy (or channel number). The shape of a photopeak was assumed to be the sum of a Gaussian and two independent exponential

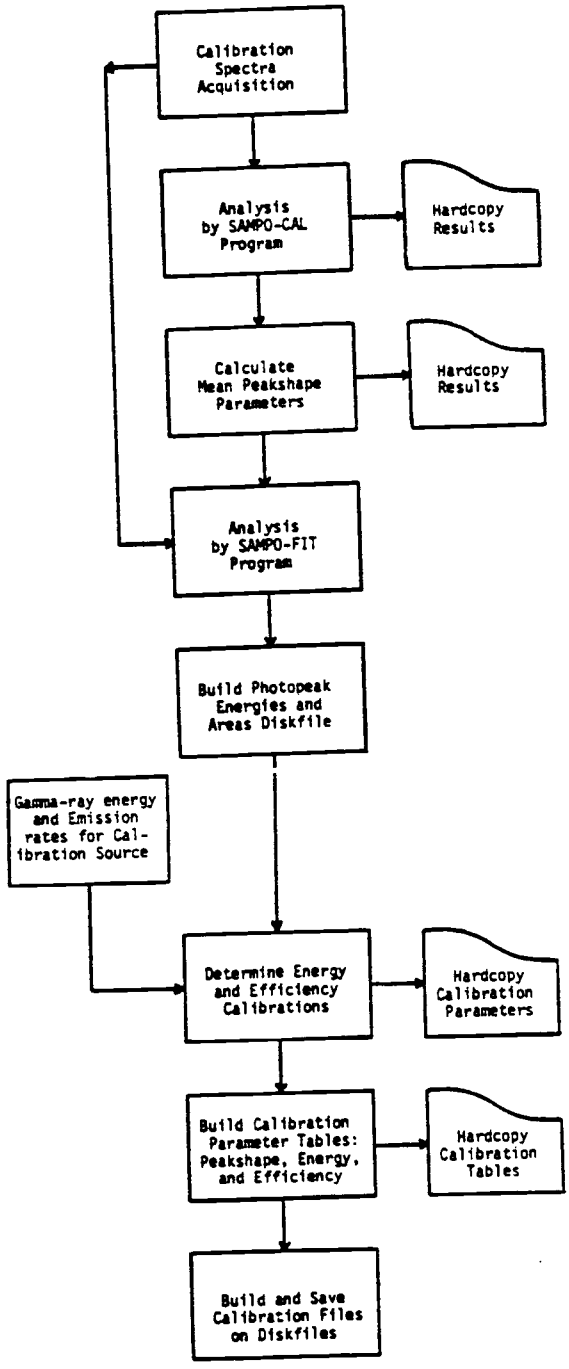

Flow diagram of the procedure used to calibrate the spectroscopic system.

Figure 5

tails smoothly joined to each side of the Gaussian. Four parameters were used to describe the shape of a photopeak: the Gaussian centroid, the Gaussian width parameter, and the distances from the centroid where each exponential tail joins the Gaussian. These parameters varied as a function of photopeak energy. A set of four parameters was generated for each photopeak in a calibration spectra. Photopeak shape parameters were determined for all calibration spectra. Weighted averages of each shape parameter for each photopeak energy comprised the final shape calibration table used by the analysis mode of SAMPO-80. During the analysis mode, SAMPO-80 generates shape parameters for any part of the spectrum by linear interpolation between calibration values. The effects of electronic dead time on the shape of the photopeak parameters were carefully examined. Photopeak broadening and increased tailing were measurable in spectra acquired at greater than 15% dead time, thus, the counting geometry was adjusted to maintain dead time below 15%.

Calibration spectra photopeak areas and centroids calculated by the SAMPO-80 analysis mode were used to generate the energy and efficiency calibration parameters. The energy calibration for each detector system was obtained by fitting peak centroids to the quadratic function:

$$E_\gamma(x) = a(1) + a(2)*x + a(3)* x^2 \qquad \text{[eqn 2]}$$

where $E_\gamma(x)$ and x are the peak centroid energy (keV) and channel

number, respectively. A least squares fitting routine was used to determine the coefficients, a(i). The amplifier gain and ADC zero-level offset were used to attempt to calibrate the parameters $a(1) \simeq a(3) \simeq 0.0$ keV and $a(2) \simeq 0.5$ keV.

Absolute detector efficiency functions were determined for all geometries used during an experiment. The photopeak efficiency was calculated by dividing the photopeak activity (from SAMPO) by the known gamma-ray emission rate. Calculated efficiencies for each geometry were fit to the function:

$$\varepsilon(E) = P(1) * \{E^{P(2)} + P(3) * \exp^{P(4)*E}\} \qquad \text{[eqn 3]}$$

where ε is the detector efficiency at a gamma-ray energy E. The coefficients, P(i), were obtained by least squares fitting. Nominal efficiency at 1332.5 keV of the Ge(Li) detec-tors used varied between 17% and 21%, relative to NaI at 35cm.

The shape calibration table, energy and efficiency calibration function coefficients were used by the analysis mode of SAMPO to locate peaks and assign absolute energies and activities.

2. Data Acquisition and Analysis

Post irradiation gamma spectroscopic measurements of induced activities were made at Oregon State University and the Lawrence Berkeley Laboratory using a strategy outlined in reference 46. All

target assemblies irradiated at CERN were shipped via air transportation to OSU. The target assembly irradiated by 208 MeV ^{12}C ions at the LBL 88-inch cyclotron was also shipped by air freight to OSU. The target assembly irradiated by 272 MeV ^{16}O ions at LBL was assayed after the end-of-bombardment at LBL. The times after EOB at which gamma-ray spectroscopic measurements began for the various experiments are tabulated in table 1.

The irradiated samples were disassembled into forward catcher, backward catcher, and target. Each catcher sample and the target were separately mounted on counting cards designed for the respective system on which the sample was to be assayed. The counting cards were supported on detector racks designed for reproducibility of the geometries at which samples were counted. The counting geometry for a sample was chosen to maintain electronic dead time below 15% for reasons discussed above. Spectra of the various samples were iteratively collected over a period of 90 to 120 days to allow half-life determination of most nuclides produced in the interaction.

A flow diagram of the procedure used to analyze spectral data is shown in figure 6. The block lettered names in the flowchart are the names of computer codes used in the analysis procedure; these programs are discussed below. The analysis mode of SAMPO-80 was used to locate and fit peaks in gamma-ray spectra. The version of SAMPO-80 implemented on the ND-6660 system (see Appendix A) is capable of identifying up to 350 peaks in a single spectra and will deconvolute multiplets containing up to 6 individual peaks. SAMPO-80 output consists of a detailed analysis for each assignment directed to hardcopy and fit results directed to magnetic storage media for

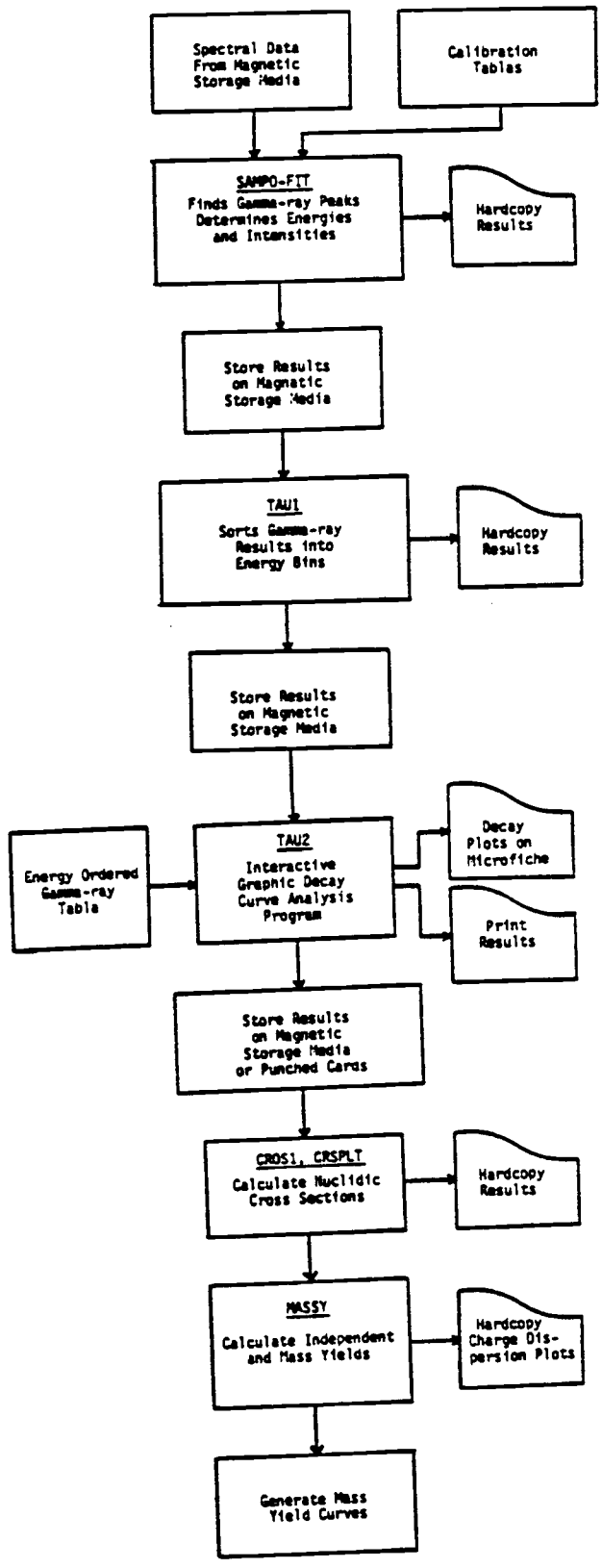

Flow diagram of the procedure used to analyze spectroscopic data.

Figure 6

subsequent analysis. The summary results consist of an identifying tagword, the time after the end-of-irradiation (TAEI) that the spectra were acquired, and photopeak energy, intensity, and associated uncertainties for each accepted peak.

3. Decay Half-Life Determination

After the spectral analysis was complete, the code TAU1 [46] sorts the observed gamma-ray peak assignments by spectrum tagword and gamma-ray energy so that decay curves may be constructed. The first pass sorts the data by the tagword which identifies the sample of which the spectrum was taken. The energy sorting algorithm was designed to group assignments for the same peak together in a single bin. An average energy and energy window were associated with each bin. The algorithm iteratively searches through a spectrum, determines if a peak energy falls within the bounds of a bin window, and adds the new datum to the bin if it does. New bins were initialized by assignments not falling within the window of an existing bin. When a new datum is added, the average bin energy and window bounds were recalculated. A bin window is defined by the bounds $\langle E \rangle + \delta$ and $\langle E \rangle - \delta$, where

$$\delta = \log(\langle E \rangle) - 1.5 \qquad \text{[eqn 4]}$$

and all values are expressed in terms of keV. The final sorted data consisted of one file per sample (tagword) comprised of records of

energy ordered decay results (bins). Each final bin consisted of an average energy and a time ordered list of activities. Bins consisting of a single assignment were automatically deleted.

The next stage of the analysis was to bring the measured decay curves for each gamma-ray line together with a compilation of known gamma-ray transitions obtained from a recent compilation [49] in order to identify the radionuclides present in the samples. The computer code TAU2 [46] (an interactive decay curve analysis program) constructed decay curves and presented relevant data on the nearest known gamma-ray transitions to facilitate the identification. The input data required by TAU2 was the sorted gamma-ray data from TAU1 and a version of the gamma-ray table [49], obtained most recently from the Gesellschaft für Schwerionenforschung (GSI). The data is stored on the permanent storage system (PSS) at LBL. Prior to 1982 the Binder-Kraus [50] version of the gamma-ray table of the isotopes was used. Results obtained with errant branching ratios from this table were corrected to agree with the more recent GSI data.

Once the decay data and twenty nearest gamma-ray transitions were displayed on the terminal the operator chose from a list of several options to fit the measured decay curve. Half-lives are held constant and activity at end-of-irradiation (A_0) values are calculated by the least squares method. When an acceptable identification of the decay curve was made, the graphics display was recorded on microfiche and the A_0 value, associated uncertainties, energy, and radionuclide identification was output to punched card and line printer. The A_0 value has units of decays per minute, having been corrected for transition abundance and parent branching

ratio when necessary. Resolution of multiple identifications is discussed below.

C. YIELD DETERMINATION

1. Cross Section Calculation

An energy ordered list of cross sections was calculated for each component of every decay curve. A computer code uses the A_0 and half-life information from TAU2 and calculates the nuclidic cross section with the formula:

$$\sigma = \frac{A_0}{N \sum_{i=1}^{n} \Phi_i (1-\exp[-\lambda t_{bi}]) \{\exp[-\lambda (\sum_{j=i+1}^{n} t_{bj})]\}} \qquad \text{[eqn 5]}$$

which incorporates the effects of nonuniform beam intensity on the cross sections. N is the number of target atoms and λ is the nuclide decay constant. The beam intensity history was used to divide the bombardment into intervals during which the beam intensity was relatively constant. Variables t_{bi} and t_{bj} represent intervals in the beam intensity period defined by the respective summation indicies, i and j. The intensity for the i-th interval is defined by Φ_i. Large fluctuations in the beam intensity and occasional interruptions in the bombardment of the target material necessitated the use of this expanded form of the cross section formula in the interaction of 272 MeV ^{16}O with holmium due to the short TAEI at which spectroscopy began (see section A of this chapter). Beam histories and the expanded form of the cross section calculation

also used in analysis of the other experiments for consistency. Identifications where the calculated uncertainty exceeded the value were discarded at this stage of the analysis.

The TAU2 identifications were sorted by isotope and a second calculation of the cross section was performed for each observed gamma transition and weighted average cross sections are calculated for each isotope. The computer output lists the nuclide, all gamma transitions used in the calculation and the final weighted average cross section for the isotope. At this point all identifications were screened by hand using the following rules:

a) The energy of each observed gamma-ray transition was within a maximum window of (log<E>-1.5) keV of published values [49].

b) Each identification is the result of a unique decay curve fit. If no resolution of a multiple assignment is attainable, the identification is discarded.

c) No gamma-ray lines with intensities stronger than the weakest observed transition can be missing unless they can be shown to be masked by a more intense gamma-ray or the product of an unresolvable multiple identification.

Table 2 lists all nuclides identified in the various experiments contained in this study along with the gamma-rays used for identification (only gamma-rays necessary for accepting a given identification are tabulated), their energies and branching ratios used to identify the given nuclide. This list represents gamma ray energies observed for all identifications of that particular nuclide. The resultant set of identifications was used for the final calculation of nuclidic production cross sections. Total nuclidic production cross sections were obtained by summing the observed cross sections for each nuclide in the target and forward

NUCLIDE IDENTIFICATION GAMMA-RAYS

NUCLIDE	MINIMUM GAMMA-RAYS TO IDENTIFY (ENERGY (keV)--BRANCHING RATIO (%))		
^{22}Na	1274.6-- 99.9		
^{24}Na	1368.5--100.		
^{28}Mg	400.6-- 35.9	941.7-- 35.9	1778.9--100.
^{43}K	372.8-- 88.3		
^{44m}Sc	271.2-- 77.8	1157.0--108.3	
^{46g}Sc	889.2--100.	1120.5--100.	
^{47}Ca	1297.1-- 74.9		
^{47}Sc	159.4-- 68.0		
^{48}Sc	983.5--100.	1037.5-- 97.5	1312.1--100.
^{48}V	983.5--100.	1312.1-- 97.5	
^{51}Cr	320.1-- 9.83		
^{52g}Mn	935.5-- 94.5	1434.1--100.	
^{54}Mn	834.8--100.		
^{56}Co	846.8-- 99.9	1238.3-- 67.0	
^{58g}Co	810.8-- 99.4		
^{59}Fe	1099.3-- 56.5	1291.6-- 43.2	
^{65}Zn	1115.5-- 50.7		
^{69}Ge	1106.4-- 36.0		
^{71}As	174.9-- 83.6		
^{72}Zn	144.7-- 83.0	834.0-- 95.6	
^{72}Ga	629.9-- 25.2	834.0-- 95.6	
^{72}As	834.0-- 80.1		
^{72}Se	834.0-- 91.3		
^{74}As	595.8-- 60.3	634.8-- 15.1	
^{75}Se	136.0-- 55.6	264.6-- 58.2	279.5-- 24.6
	400.4-- 11.1		
^{76}As	559.1-- 44.7		
^{77g}Br	239.0-- 23.1	520.7-- 22.4	
^{82}Sr	776.5-- 13.4		
^{83}Rb	520.4-- 46.1	529.5-- 30.0	
^{84g}Rb	881.6-- 67.8		
^{85g}Sr	514.0--100.		
^{86g}Y	627.7-- 32.6	1076.6-- 82.5	
^{87g}Y	388.4-- 85.3	484.9-- 92.2	
^{87m}Y	381.1-- 78.5		
^{88}Y	898.0-- 94.0	1836.0-- 99.4	
^{88}Zr	392.9-- 97.3	898.0-- 94.0	1836.0-- 99.4
^{89g}Zr	909.2-- 99.9		
^{92m}Nb	934.0-- 99.2		

Table 2

NUCLIDE	MINIMUM GAMMA-RAYS TO IDENTIFY (ENERGY (keV)--BRANCHING RATIO (%))			
^{95}Zr	724.2-- 43.7	756.7-- 55.4		
^{95g}Nb	765.8-- 99.9			
^{95m}Nb	235.7-- 25.1			
^{95g}Tc	765.8-- 93.9			
^{96g}Tc	778.2--100.	849.9-- 97.8		
^{97}Ru	215.7-- 85.8			
^{99}Mo	140.5-- 99.9			
^{100g}Rh	539.6-- 78.4	822.5-- 20.1	1553.4-- 20.5	
	1929.7-- 12.2			
^{100}Pd	539.6--103.0	822.5-- 26.5	1107.1-- 17.4	
	1553.4-- 27.0	1929.7-- 16.0		
^{101g}Rh	127.0-- 73.0	198.0-- 70.8		
^{101m}Rh	306.8-- 86.8			
^{102g}Rh	475.1-- 94.0	631.3-- 55.5		
^{103}Ru	497.1-- 89.5			
^{105g}Ag	280.4-- 29.5	344.5-- 40.9		
^{106m}Ag	451.0-- 28.4	616.2-- 21.7	717.3-- 29.1	
	748.4-- 20.7	1045.8-- 29.7	1527.7-- 16.4	
^{110m}Ag	657.7-- 94.4	763.9-- 22.3	884.7-- 72.8	
	937.5-- 34.3	1384.3-- 24.6		
^{111g}In	171.3-- 90.3	245.4-- 94.0		
^{119g}Te	644.0-- 84.4			
^{119m}Te	153.6-- 67.1	1212.7-- 67.0		
^{121g}Te	573.1-- 79.7			
^{121m}Te	212.2-- 82.6	573.1-- 79.5		
^{123m}Te	159.0-- 83.6			
^{125g}Xe	188.4-- 55.1	243.4-- 28.9		
^{127g}Xe	202.8-- 68.1			
^{128}Ba	442.9-- 25.8			
^{131g}Ba	123.8-- 29.2	216.1-- 19.9	373.2-- 14.1	
	493.3-- 47.1			
^{135g}Ce	265.6-- 42.4	606.8-- 19.5		
^{139g}Ce	165.8-- 78.9			
^{143}Pm	742.0-- 38.3			
^{144}Ce	133.5-- 10.8			
^{144}Pm	618.0-- 98.6	696.5-- 99.5		
^{145}Eu	653.6-- 16.0	893.8-- 63.9	1658.7-- 15.4	
^{146}Eu	747.2-- 98.0			
^{146}Gd	154.6-- 43.0	633.2-- 48.0	1297.6-- 6.24	
	1408.8-- 3.61	1534.2-- 6.80		
^{147}Eu	121.3-- 22.7	197.3-- 25.8		
^{147}Gd	229.2-- 57.3	928.3-- 18.0	396.5-- 26.2	

Table 2 (cont.)

NUCLIDE	MINIMUM GAMMA-RAYS TO IDENTIFY (ENERGY (keV)--BRANCHING RATIO (%))		
^{148m}Pm	550.2-- 92.9	629.9-- 89.2	725.6-- 32.8
	1013.7-- 20.4		
^{148}Eu	413.9-- 18.6	550.3-- 99.0	611.3-- 19.3
	629.9-- 70.9	725.7-- 13.0	1621.5-- 4.6
^{149}Gd	149.6-- 41.7	298.5-- 22.6	
^{151}Gd	153.6-- 5.10	174.7-- 2.45	243.2-- 4.59
^{151g}Tb	108.3-- 25.0	251.7-- 26.0	287.0-- 25.0
	479.0-- 16.0	731.1-- 9.1	
^{152g}Tb	344.3-- 67.2	778.9-- 5.96	
^{153}Gd	97.4-- 30.1	103.2-- 21.8	
^{153}Tb	211.9-- 32.5		
^{155}Tb	105.3-- 23.0	180.1-- 6.83	
^{155}Dy	227.0-- 68.0		
^{156g}Tb	199.2-- 40.2	534.3-- 67.0	1222.4-- 31.2
	1421.6-- 11.6		
^{160}Tb	298.6-- 27.4	879.4-- 30.0	962.3-- 10.0
	966.2-- 25.2	1177.9-- 15.5	
^{160}Er	197.0-- 15.0	645.5-- 17.0	728.1-- 36.0
	879.1-- 23.0	961.9-- 21.0	965.8-- 21.0
^{165}Tm	242.9-- 35.5	297.4-- 13.8	806.8-- 8.4
^{166}Yb	184.4-- 21.3	705.3-- 14.3	1273.4-- 20.1
^{167}Tm	207.8-- 41.0		
^{168}Tm	184.3-- 16.4	198.2-- 50.0	447.5-- 21.9
	815.9-- 46.3		
^{169g}Yb	109.8-- 18.0	130.5-- 11.5	177.2-- 22.0
	198.0-- 36.0	307.7-- 11.1	
^{169g}Lu	191.3-- 17.9	960.3-- 20.3	1449.7-- 8.6
^{170}Lu	1054.3-- 4.6	1225.6-- 4.84	1280.2-- 7.93
	1364.6-- 4.48	1428.1-- 3.38	1512.5-- 2.48
^{171g}Lu	667.5-- 10.9	739.8-- 47.6	840.0-- 3.0

A tabulation of the minimum number of gamma-rays used to identify any given nuclide tabulated in table 3.

Table 2 (cont.)

and backward catcher foils. No corrections of the total production cross sections were attempted for nuclides which were not observed in either catcher foil (usually the backward catcher). In the event no recoils for a given nuclide were observed in either catcher foil, the data were omitted. The measured cross sections obtained by this procedure are tabulated in table 3 for each of the interactions studied. Values calculated for 442 MeV ^{12}C and 1635 MeV ^{16}O experiments are tabulated as "arbitrary units" representing measured cross sections relative to $^{27}Al(^{12}C,X)^{22}Na$ = 32.0 mb and 34.1 mb, respectively.

Two major factors contributed to the uncertainties in the measured cross sections. The uncertainties due to counting statistics and decay curve fitting were calculated by standard methods discussed elsewhere [46,47]. The random and systematic errors due to the experimental procedure are less well known. The major source of uncertainty is the degree to which the counting geometry for each sample can be precisely reproduced. The uncertainty introduced by not exactly reproducing the initial geometry has been measured to be less than 4% at the smallest detectorsource distance [46]. A second source of uncertainty would arise from the lack of knowledge about precise size of the active sample area and the activity gradient (if any). The minimum uncertainties in the experimental procedure are conservatively estimated at 10%. Calculated uncertainties resulting in values less than 10% are assigned this minimum value.

MEASURED PRODUCTION CROSS SECTIONS FOR INTERACTIONS INDUCED IN HOLMIUM TARGETS BY VARIOUS PROJECTILES

NUCLIDE	208 MeV ^{12}C (mb)	272 MeV ^{16}O (mb)	442 MeV ^{12}C (a.u.)	1020 MeV ^{12}C (mb)	1635 MeV ^{16}O (a.u.)
^{22}Na					2.3 ± 0.7
^{24}Na					8.4 ± 0.9
^{28}Mg					1.8 ± 0.2
^{43}K		1.2 ± 0.1			
^{44m}Sc		0.5 ± 0.1			1.5 ± 0.2
^{46g}Sc	0.86 ± 0.09	2.0 ± 0.2	1.4 ± 0.2	1.5 ± 0.2	3.5 ± 0.4
^{47}Ca		0.48 ± 0.04			
^{47}Sc		2.2 ± 0.2		1.0 ± 0.2	1.8 ± 0.8
^{48}Sc	1.6 ± 0.2	1.0 ± 0.1	0.9 ± 0.1	0.48 ± 0.05	1.0 ± 0.1
^{48}V		0.48 ± 0.05	0.23 ± 0.03	0.62 ± 0.06	1.1 ± 0.1
^{51}Cr				2.0 ± 0.2	4.3 ± 0.6
^{52g}Mn		0.55 ± 0.06			0.61 ± 0.06
^{54}Mn	2.1 ± 0.2	4.1 ± 0.4	1.8 ± 0.2	2.3 ± 0.2	5.0 ± 0.5
^{56}Co					0.34 ± 0.03
^{58g}Co	1.3 ± 0.1	2.9 ± 0.3	1.4 ± 0.2	1.1 ± 0.1	3.0 ± 0.3
^{59}Fe	4.6 ± 0.5	6.8 ± 0.7	1.9 ± 0.2	0.65 ± 0.07	1.3 ± 0.1
^{65}Zn	1.6 ± 0.2	4.3 ± 0.4			4.2 ± 0.4
^{69}Ge		1.5 ± 0.2			
^{71}As		1.0 ± 0.1	1.9 ± 0.4		1.7 ± 0.2
^{72}Zn	0.58 ± 0.06	0.43 ± 0.05			
^{72}Ga		6.0 ± 0.6			
^{72}As		5.7 ± 0.6			
^{72}Se		0.12 ± 0.03			
^{74}As	9.2 ± 0.9	14. ± 1.	3.3 ± 0.4	1.0 ± 0.1	2.1 ± 0.2
^{75}Se	3.8 ± 0.4	9.7 ± 1.0	3.9 ± 0.4	1.2 ± 0.1	3.8 ± 0.4

Table 3

MEASURED PRODUCTION CROSS SECTIONS FOR INTERACTIONS INDUCED IN HOLMIUM TARGETS BY VARIOUS PROJECTILES

NUCLIDE	208 MeV ^{12}C (mb)	272 MeV ^{16}O (mb)	442 MeV ^{12}C (a.u.)	1020 MeV ^{12}C (mb)	1635 MeV ^{16}O (a.u.)
^{76}As	8.3 ± 0.8	10. ± 1.			
^{77g}Br	2.9 ± 0.3	5.8 ± 0.6	2.9 ± 0.3	2.5 ± 0.5	
^{82}Sr				0.6 ± 0.2	
^{83}Rb	12. ± 1.	24. ± 2.	5.5 ± 0.6	2.0 ± 0.2	7.9 ± 0.8
^{84g}Rb	15. ± 2.	9. ± 1.	1.6 ± 0.2		1.8 ± 0.2
^{85g}Sr	8.3 ± 0.8	12. ± 2.	3.1 ± 0.3	2.4 ± 0.6	6.2 ± 0.6
^{86g}Y					5.5 ± 2.6
^{87g}Y	8.8 ± 0.9	18. ± 2.	4.7 ± 0.5	2.1 ± 0.2	7.3 ± 0.8
^{87m}Y		12. ± 1.			6.5 ± 0.7
^{88}Y	11. ± 1.	17. ± 2.	2.8 ± 0.3	0.64 ± 0.06	1.9 ± 0.3
^{88}Zr	2.0 ± 0.2	6.3 ± 0.6	2.0 ± 0.2	2.0 ± 0.2	6.2 ± 0.6
^{89g}Zr	5.6 ± 0.6	12. ± 1.	3.6 ± 0.4	1.7 ± 0.2	6.7 ± 0.7
^{92m}Nb		0.8 ± 0.1			
^{95}Zr	1.5 ± 0.2	1.4 ± 0.1			
^{95g}Nb	4.8 ± 0.5	4.6 ± 0.5	1.0 ± 0.1	0.27 ± 0.03	0.7 ± 0.1
^{95m}Nb		0.22 ± 0.04			
^{95g}Tc		8.7 ± 0.9			
^{96g}Tc	1.9 ± 0.2	4.9 ± 0.5	1.1 ± 0.2		
^{97}Ru		4.9 ± 1.5			3.8 ± 0.4
^{99}Mo	2.0 ± 0.2	2.0 ± 0.2			
^{100}Pd					1.6 ± 0.2
^{100g}Rh					6.9 ± 0.7
^{101g}Rh		1.3 ± 0.3	1.1 ± 0.2		0.8 ± 0.1
^{101m}Rh	1.1 ± 0.2	3.9 ± 0.4	1.3 ± 0.2	1.8 ± 0.2	9.4 ± 0.9
^{102g}Rh		4.0 ± 0.4			1.7 ± 0.3

Table 3 (cont.)

MEASURED PRODUCTION CROSS SECTIONS FOR INTERACTIONS INDUCED IN HOLMIUM TARGETS BY VARIOUS PROJECTILES

NUCLIDE	208 MeV ^{12}C (mb)	272 MeV ^{16}O (mb)	442 MeV ^{12}C (a.u.)	1020 MeV ^{12}C (mb)	1635 MeV ^{16}O (a.u.)
^{103}Ru	3.1 ± 0.3	3.7 ± 0.4			
^{105g}Rh		2.4 ± 0.2			
^{105g}Ag	0.82 ± 0.08	3.4 ± 0.3		3.3 ± 0.3	13. ± 1.
^{106m}Ag	1.0 ± 0.1	2.6 ± 0.3		1.1 ± 0.1	0.33 ± 0.06
^{110m}Ag	0.9 ± 0.2	1.1 ± 0.1			
^{111g}In	0.85 ± 0.09	3.1 ± 0.3	0.9 ± 0.2	5.0 ± 0.5	14. ± 1.
^{119m}Te	0.49 ± 0.05	1.2 ± 0.2	0.33 ± 0.04	2.1 ± 0.4	3.4 ± 0.3
^{121g}Te	0.38 ± 0.04	1.9 ± 0.2	1.4 ± 0.2	14. ± 1.	29. ± 3.
^{121m}Te	0.56 ± 0.06	0.9 ± 0.1	0.27 ± 0.03	0.7 ± 0.1	1.4 ± 0.1
^{123m}Te	1.5 ± 0.2	0.16 ± 0.02			0.6 ± 0.1
^{125g}Xe					26. ± 3.
^{127g}Xe	0.57 ± 0.06	1.8 ± 0.2	2.5 ± 0.3	28. ± 3.	33. ± 3.
^{128}Ba		1.4 ± 0.2		25. ± 3.	24. ± 17.
^{131g}Ba		1.0 ± 0.1	2.7 ± 0.8	36. ± 4.	42. ± 4.
^{135g}Ce					30. ± 3.
^{139g}Ce	0.38 ± 0.04	1.3 ± 0.1			50. ± 5.
^{143}Pm			54. ± 6.	54. ± 5.	
^{144}Ce	0.22 ± 0.02				
^{144}Pm			1.0 ± 0.2	1.1 ± 0.1	
^{145}Eu		2.4 ± 0.2	63. ± 7.	40. ± 4.	35. ± 4.
^{146}Eu	0.32 ± 0.06		14. ± 2.		10. ± 1.
^{146}Gd	0.11 ± 0.01	0.8 ± 0.2	71. ± 8.	43. ± 4.	33. ± 3.
^{147}Eu	0.44 ± 0.07	8. ± 3.	111. ± 11.	61. ± 6.	44. ± 4.
^{147}Gd		1.0 ± 0.1	72. ± 7.	54. ± 5.	35. ± 4.
^{148}Eu	0.23 ± 0.02	0.73 ± 0.07			

Table 3 (cont.)

MEASURED PRODUCTION CROSS SECTIONS FOR INTERACTIONS INDUCED IN HOLMIUM TARGETS BY VARIOUS PROJECTILES

NUCLIDE	208 MeV ^{12}C (mb)	272 MeV ^{16}O (mb)	442 MeV ^{12}C (a.u.)	1020 MeV ^{12}C (mb)	1635 MeV ^{16}O (a.u.)
^{148m}Pm				2.2 ± 0.3	6.1 ± 0.7
^{149}Gd	0.46 ± 0.05	2.6 ± 0.3	122. ± 12.	53. ± 5.	49. ± 5.
^{151}Gd		6.8 ± 0.7	124. ± 13.	59. ± 6.	66. ± 7.
^{151}Tb		3.3 ± 0.3			31. ± 3.
^{152g}Tb		4.3 ± 0.4			48. ± 5.
^{153}Gd		12. ± 1.	95. ± 10.	54. ± 5.	52. ± 5.
^{153}Tb	4.1 ± 0.4	8.9 ± 0.9	123. ± 13.		
^{155}Tb	16. ± 2.	23. ± 4.	114. ± 12.	46. ± 5.	52. ± 5.
^{155}Dy				57. ± 6.	
^{156g}Tb	1.2 ± 0.1		4.3 ± 0.5	7.3 ± 0.8	10. ± 1.
^{160}Tb	1.0 ± 0.1		2.5 ± 0.3	3.8 ± 0.4	4.2 ± 0.4
^{160}Er	186. ± 19.	97. ± 10.	97. ± 10.	32. ± 3.	27. ± 3.
^{165}Tm	431. ± 43.	149. ± 23.	5. ± 2.		
^{166}Yb	214. ± 21.	82. ± 8.		1.3 ± 0.4	
^{167}Tm	124. ± 12.	116. ± 12.	3.1 ± 0.3		0.83 ± 0.08
^{168}Tm	0.90 ± 0.09	0.55 ± 0.06			
^{169g}Yb	6.6 ± 0.7	13. ± 1.	1.0 ± 0.2		
^{169g}Lu	3.5 ± 0.6	10. ± 1.			
^{170}Lu		4.5 ± 0.5			
^{171g}Lu		1.6 ± 0.2			

A tabulation of all measured nuclidic cross sections for the reaction systems studied. Cross sections for 442 MeV ^{12}C and 1635 MeV ^{16}O data are tabulated as arbitrary units, (a.u.), resulting from the unknown monitor reaction cross sections used (see experimental chapter, section A).

Table 3 (cont.)

2. Charge Dispersion and Mass Yield Calculation

The nuclidic cross sections calculated by the method described above were usually cumulative yield cross sections. A measured cumulative yield is the result of direct production of the observed nuclide by nuclear reactions followed by deexcitation and contributions from "fast" beta decay. Fast beta decay contributions result from nuclides produced in the reaction which decay to the observed nuclide between the time of the reaction and the time of detection. A small fraction ($\leq$10%) of the observed nuclides are completely shielded from precursor decay. These independent yields are a measure of only deexcited primary products. The tabulation of cross sections, tables 4-8, include a column specifying the tabulated yields as cumulative (C) or independent (I). All cross sections reported for 442 MeV ^{12}C and 1635 MeV ^{16}O induced interactions are relative values.

Independent yield cross sections are calculated from the observed cumulative values to determine the distribution and absolute quantity of nuclides produced directly by the nucleus-nucleus interactions. Cumulative yields are corrected for precursor decay to obtain independent ("primary") yields of observed nuclides. Once corrected, these values of independent production cross sections, $\sigma_{IY}(Z,A)$, can be used to calculate the mass and charge yields, $\sigma(A)$ and $\sigma(Z)$, and to estimate the fission and total reaction cross sections.

Special attention was given yields of isotopes with two or more isomers. Isomeric pairs were examined on a case-by-case basis and were included in the calculation of charge dispersions and

208 MeV ^{12}C + ^{165}Ho
MASS YIELD TABLE (mb)

NUCLIDE	MEASURED YIELD	CALCULATED INDEPENDENT YIELD	MASS YIELD	YIELD TYPE
^{46g}Sc	0.86 ± 0.09	0.86 ± 0.09	2.3 ± 0.2	I
^{48}Sc	1.6 ± 0.2	1.6 ± 0.2	2.6 ± 0.3	I
^{54}Mn	2.1 ± 0.2	2.1 ± 0.2	7.2 ± 0.7	I
^{58g}Co	1.3 ± 0.1	-	-	C
^{59}Fe	4.6 ± 0.5	4.4 ± 0.4	9.0 ± 0.9	C
^{65}Zn	1.6 ± 0.2	1.6 ± 0.2	24. ± 2.	C
^{72}Zn	0.58 ± 0.06	0.58 ± 0.06	27. ± 3.	C
^{74}As	9.2 ± 0.9	9.2 ± 0.9	18. ± 2.	I
^{75}Se	3.8 ± 0.4	3.7 ± 0.4	17. ± 2.	C
^{76}As	8.3 ± 0.8	8.3 ± 0.8	18. ± 2.	I
^{77g}Br	2.9 ± 0.3	2.9 ± 0.3	17. ± 2.	C
^{83}Rb	12. ± 1.	10. ± 1.	20. ± 2.	C
^{84g}Rb	15. ± 2.	15. ± 2.	23. ± 2.	I
^{85g}Sr	8.3 ± 0.8	7.5 ± 0.8	17. ± 2.	C
^{87g}Y	8.8 ± 0.9	-	-	C
^{88}Y	11. ± 1.	11. ± 1.	19. ± 2.	C
^{88}Zr	2.0 ± 0.2	2.0 ± 0.2	18. ± 2.	C
^{89g}Zr	5.6 ± 0.6	5.4 ± 0.5	19. ± 2.	C
^{95}Zr	1.5 ± 0.2	1.5 ± 0.2	18. ± 2.	C
^{95g}Nb	4.8 ± 0.5	4.7 ± 0.5	11. ± 1.	C
^{96g}Tc	1.9 ± 0.2	1.9 ± 0.2	11. ± 1.	I
^{99}Mo	2.0 ± 0.2	1.9 ± 0.2	9.1 ± 0.9	C
^{101m}Rh	1.1 ± 0.2	-	-	C
^{103}Ru	3.1 ± 0.3	2.6 ± 0.3	8.8 ± 0.9	C
^{105g}Ag	0.82 ± 0.08	0.78 ± 0.08	7.9 ± 0.8	C
^{106m}Ag	1.0 ± 0.1	-	-	I
^{110m}Ag	0.9 ± 0.2	-	-	I
^{111g}In	0.85 ± 0.09	0.79 ± 0.08	7.0 ± 0.7	C
^{119m}Te	0.49 ± 0.05	-	-	I
^{121g}Te	0.38 ± 0.04	0.17 ± 0.02	2.2 ± 0.2	C
^{121m}Te	0.56 ± 0.06	0.56 ± 0.06	-	I
^{123m}Te	1.5 ± 0.2	-	-	I
^{127g}Xe	0.57 ± 0.06	0.51 ± 0.05	1.1 ± 0.1	C
^{139g}Ce	0.38 ± 0.04	0.36 ± 0.04	1.0 ± 0.1	C
^{144}Ce	0.22 ± 0.02	0.21 ± 0.02	1.0 ± 0.1	C
^{146}Eu	0.32 ± 0.06	-	-	C
^{146}Gd	0.11 ± 0.01	-	-	C
^{147}Eu	0.44 ± 0.07	0.26 ± 0.04	0.47 ± 0.07	C
^{148}Eu	0.23 ± 0.02	0.23 ± 0.02	0.51 ± 0.05	C
^{149}Gd	0.46 ± 0.05	0.38 ± 0.04	0.64 ± 0.07	C

Table 4

208 MeV ^{12}C + ^{165}Ho
YIELD TABLE (cont.)

NUCLIDE	MEASURED YIELD	CALCULATED INDEPENDENT YIELD	MASS YIELD	YIELD TYPE
^{153}Tb	4.1 ± 0.4	4.0 ± 0.4	12. ± 1.	C
^{155}Tb	16. ± 2.	15. ± 2.	20. ± 2.	C
^{156g}Tb	1.2 ± 0.1	-	-	C
^{160}Tb	1.0 ± 0.1	1.0 ± 0.1	8.1 ± 0.8	I
^{160}Er	186. ± 19.	157. ± 16.	202. ± 20.	C
^{165}Tm	431. ± 43.	199. ± 20.	436. ± 44.	C
^{166}Yb	214. ± 21.	-	-	C
^{167}Tm	124. ± 12.	8.9 ± 0.9	150. ± 15.	C
^{168}Tm	0.90 ± 0.09	0.90 ± 0.09	82. ± 21.	I
^{169g}Yb	6.6 ± 0.7	-	-	C
^{169g}Lu	3.5 ± 0.6	-	-	C

Tabulation of the measured and calculated independent and mass yields for nuclides produced by the interaction of 208 MeV ^{12}C and ^{165}Ho. "I" and "C" designate whether the measured yield is an independent or cumulative yield. Independent and mass yields were not calculated for Yb and Lu nuclides due to insufficient data points.

Table 4 (cont.)

272 MeV ^{16}O + ^{165}Ho
MASS YIELD TABLE (mb)

NUCLIDE	MEASURED YIELD	CALCULATED INDEPENDENT YIELD	MASS YIELD	YIELD TYPE
^{43}K	1.2 ± 0.1	1.0 ± 0.1	2.4 ± 0.2	C
^{44m}Sc	0.5 ± 0.1	-	-	I
^{46g}Sc	2.0 ± 0.2	2.0 ± 0.2	3.9 ± 0.4	I
^{47}Ca	0.48 ± 0.04	0.46 ± 0.05	4.0 ± 0.4	C
^{47}Sc	2.2 ± 0.2	2.0 ± 0.2	4.2 ± 0.4	C
^{48}Sc	1.0 ± 0.1	1.0 ± 0.1	3.3 ± 0.3	I
^{48}V	0.48 ± 0.05	0.46 ± 0.05	3.2 ± 0.3	C
^{52g}Mn	0.55 ± 0.06	0.53 ± 0.05	5.9 ± 0.6	C
^{54}Mn	4.1 ± 0.4	4.1 ± 0.4	13. ± 1.	I
^{58g}Co	2.9 ± 0.3	-	-	C
^{59}Fe	6.8 ± 0.7	6.5 ± 0.7	14. ± 1.	C
^{65}Zn	4.3 ± 0.4	4.3 ± 0.4	15. ± 2.	C
^{69}Ge	1.5 ± 0.2	1.5 ± 0.2	9. ± 1.	C
^{71}As	1.0 ± 0.1	1.0 ± 0.1	14. ± 1.	C
^{72}Zn	0.43 ± 0.05	0.42 ± 0.04	18. ± 2.	C
^{72}Ga	6.0 ± 0.6	4.8 ± 0.5	18. ± 2.	C
^{72}As	5.7 ± 0.6	5.5 ± 0.6	31. ± 3.	C
^{72}Se	0.12 ± 0.03	0.12 ± 0.03	12. ± 3.	C
^{74}As	14. ± 1.	14. ± 1.	29. ± 3.	I
^{75}Se	9.7 ± 1.0	8.9 ± 0.9	32. ± 3.	C
^{76}As	10. ± 1.	10. ± 1.	26. ± 3.	I
^{77g}Br	5.8 ± 0.6	5.4 ± 0.5	25. ± 2.	C
^{83}Rb	24. ± 2.	16. ± 2.	27. ± 3.	C
^{84g}Rb	9. ± 1.	9. ± 1.	32. ± 3.	I
^{85g}Sr	12. ± 2.	-	-	C
^{87g}Y	18. ± 2.	11. ± 1.	36. ± 4.	C
^{87m}Y	12. ± 1.	9. ± 1.	-	C
^{88}Y	17. ± 2.	17. ± 2.	29. ± 3.	C
^{88}Zr	6.3 ± 0.6	6.0 ± 0.6	21. ± 2.	C
^{89g}Zr	12. ± 1.	11. ± 1.	23. ± 2.	C
^{92m}Nb	0.8 ± 0.1	-	-	C
^{95}Zr	1.4 ± 0.1	1.4 ± 0.1	59. ± 6.	C
^{95g}Nb	4.6 ± 0.5	4.6 ± 0.5	22. ± 2.	C
^{95g}Tc	8.7 ± 0.9	-	-	C
^{96g}Tc	4.9 ± 0.5	-	-	C
^{97}Ru	4.9 ± 1.5	4.4 ± 1.3	24. ± 7.0	C
^{99}Mo	2.0 ± 0.2	1.9 ± 0.2	24. ± 2.	C

Table 5

272 MeV ^{16}O + ^{165}Ho
YIELD TABLE (cont)

NUCLIDE	MEASURED YIELD	CALCULATED INDEPENDENT YIELD	MASS YIELD	YIELD TYPE
^{101g}Rh	1.3 ± 0.3	1.3 ± 0.3	11. ± 2.	C
^{101m}Rh	3.9 ± 0.4	3.4 ± 0.4	-	C
^{102g}Rh	4.0 ± 0.4	-	-	I
^{103}Ru	3.7 ± 0.4	3.4 ± 0.3	28. ± 3.	C
^{105g}Rh	2.4 ± 0.2	2.1 ± 0.2	10. ± 1.	C
^{105g}Ag	3.4 ± 0.3	2.9 ± 0.3	11. ± 1.	C
^{106m}Ag	2.6 ± 0.3	-	-	I
^{110m}Ag	1.1 ± 0.1	-	-	I
^{111g}In	3.1 ± 0.3	2.6 ± 0.3	8.4 ± 0.8	C
^{119g}Te	2.6 ± 0.5	1.8 ± 0.3	5.5 ± 0.9	C
^{119m}Te	1.2 ± 0.1	1.2 ± 0.1	-	I
^{121g}Te	1.9 ± 0.2	0.85 ± 0.09	5.2 ± 0.7	C
^{121m}Te	0.9 ± 0.1	0.9 ± 0.1	-	I
^{123g}Te	0.16 ± 0.04	-	-	C
^{127g}Xe	1.8 ± 0.2	0.59 ± 0.06	2.6 ± 0.3	C
^{128}Ba	1.4 ± 0.2	1.2 ± 0.2	3.2 ± 0.3	C
^{131g}Ba	1.0 ± 0.1	0.46 ± 0.05	1.2 ± 0.1	C
^{139g}Ce	1.3 ± 0.1	0.37 ± 0.04	2.0 ± 0.2	C
^{145}Eu	2.4 ± 0.2	2.4 ± 0.2	11. ± 1.	C
^{146}Gd	0.8 ± 0.2	-	-	C
^{147}Eu	8. ± 3.	7.2 ± 2.6	16. ± 6.	C
^{147}Gd	1.0 ± 0.1	1.0 ± 0.1	12. ± 1.	C
^{148}Eu	0.73 ± 0.07	0.73 ± 0.07	1.4 ± 0.1	I
^{149}Gd	2.6 ± 0.3	2.5 ± 0.3	11. ± 1.	C
^{151}Gd	6.8 ± 0.7	5.8 ± 0.6	14. ± 1.	C
^{151g}Tb	3.3 ± 0.3	3.3 ± 0.3	47. ± 5.	C
^{152g}Tb	4.3 ± 0.4	4.2 ± 0.4	34. ± 3.	C
^{153}Gd	12. ± 1.	8.8 ± 0.9	17. ± 2.	C
^{153}Tb	8.9 ± 0.9	5.4 ± 0.5	27. ± 3.	C
^{155}Tb	23. ± 4.	21. ± 4.	51. ± 9.	C
^{160}Er	97. ± 10.	95. ± 10.	149. ± 15.	C
^{165}Tm	149. ± 23.	101. ± 16.	152. ± 24.	C
^{166}Yb	82. ± 8.	-	-	C
^{167}Tm	116. ± 12.	16. ± 2.	127. ± 13.	C
^{168}Tm	0.55 ± 0.06	0.55 ± 0.06	24. ± 2.	I

Table 5 (cont.)

272 MeV ^{16}O + ^{165}Ho
YIELD TABLE (cont)

NUCLIDE	MEASURED YIELD	CALCULATED INDEPENDENT YIELD	MASS YIELD	YIELD TYPE
^{169g}Yb	13. ± 1.	-	-	C
^{169g}Lu	10. ± 1.	-	-	C
^{170}Lu	4.5 ± 0.5	-	-	C
^{171g}Lu	1.6 ± 0.2	-	-	C

Tabulation of the measured and calculated independent and mass yields for nuclides produced by the interaction of 272 MeV ^{16}O and ^{165}Ho. "I" and "C" designate whether the measured yield is an independent or cumulative yield. Independent and mass yields were not calculated for Yb and Lu nuclides due to insufficient data points.

Table 5 (cont.)

442 MeV ^{12}C + ^{165}Ho
MASS YIELD TABLE (arb. units)

NUCLIDE	MEASURED YIELD	CALCULATED INDEPENDENT YIELD	MASS YIELD	YIELD TYPE
^{46g}Sc	1.4 ± 0.2	1.4 ± 0.2	2.9 ± 0.3	I
^{48}Sc	0.9 ± 0.1	0.9 ± 0.1	2.4 ± 0.3	I
^{48}V	0.23 ± 0.03	0.23 ± 0.03	2.5 ± 0.3	C
^{54}Mn	1.8 ± 0.2	1.8 ± 0.2	5.7 ± 0.6	I
^{58g}Co	1.4 ± 0.2	-	-	C
^{59}Fe	1.9 ± 0.2	1.6 ± 0.2	3.7 ± 0.4	C
^{71}As	1.9 ± 0.4	1.9 ± 0.4	7. ± 1.	C
^{74}As	3.3 ± 0.4	3.3 ± 0.4	6.7 ± 0.7	I
^{75}Se	3.9 ± 0.4	3.1 ± 0.3	6.2 ± 0.6	C
^{77g}Br	2.9 ± 0.3	2.4 ± 0.3	5.2 ± 0.6	C
^{83}Rb	5.5 ± 0.6	3.7 ± 0.4	5.9 ± 0.6	C
^{84g}Rb	1.6 ± 0.2	1.6 ± 0.2	8.2 ± 0.8	I
^{85g}Sr	3.1 ± 0.3	-	-	C
^{87g}Y	4.7 ± 0.5	-	-	C
^{88}Y	2.8 ± 0.3	2.4 ± 0.3	4.3 ± 0.4	C
^{88}Zr	2.0 ± 0.2	1.9 ± 0.2	4.8 ± 0.5	C
^{89g}Zr	3.6 ± 0.4	3.1 ± 0.3	4.8 ± 0.5	C
^{95g}Nb	1.0 ± 0.2	-	-	C
^{96g}Tc	1.1 ± 0.2	-	-	C
^{101g}Rh	1.1 ± 0.2	1.0 ± 0.1	7. ± 1.	C
^{101m}Rh	1.3 ± 0.2	1.2 ± 0.2	-	C
^{111g}In	0.9 ± 0.2	0.9 ± 0.2	3.1 ± 0.7	C
^{119m}Te	0.33 ± 0.04	-	-	I
^{121g}Te	1.4 ± 0.2	0.7 ± 0.1	2.3 ± 0.3	C
^{121m}Te	0.27 ± 0.03	0.27 ± 0.03	-	I
^{127g}Xe	2.5 ± 0.3	0.82 ± 0.09	2.8 ± 0.3	C
^{131g}Ba	2.7 ± 0.8	1.7 ± 0.5	3.1 ± 0.9	C
^{143}Pm	54. ± 6.	3.3 ± 0.4	146. ± 30.	C
^{144}Pm	1.0 ± 0.2	1.0 ± 0.2	120. ± 40.	I
^{145}Eu	63. ± 7.	42. ± 5.	74. ± 8.	C
^{146}Eu	14. ± 2.	-	-	C
^{146}Gd	71. ± 8.	-	-	C
^{147}Eu	111. ± 11.	46. ± 5.	119. ± 12.	C
^{147}Gd	72. ± 7.	63. ± 6.	124. ± 13.	C
^{149}Gd	122. ± 12.	86. ± 9.	145. ± 15.	C
^{151}Gd	124. ± 13.	59. ± 7.	138. ± 15.	C

Table 6

442 MeV ^{12}C + ^{165}Ho
YIELD TABLE (cont.)

NUCLIDE	MEASURED YIELD	CALCULATED INDEPENDENT YIELD	MASS YIELD	YIELD TYPE
^{153}Gd	95. ± 10.	45. ± 5.	96. ± 10.	C
^{153}Tb	123. ± 13.	57. ± 6.	110. ± 11.	C
^{155}Tb	114. ± 12.	100. ± 10.	128. ± 13.	C
^{156g}Tb	4.3 ± 0.5	-	-	C
^{160}Tb	2.5 ± 0.3	2.5 ± 0.3	38. ± 4.	I
^{160}Er	97. ± 10.	90. ± 9.	98. ± 10.	C
^{165}Tm	5. ± 2.	-	-	C
^{167}Tm	3.1 ± 0.3	-	-	C
^{169g}Yb	1.0 ± 0.2	-	-	C

Tabulation of the measured and calculated independent and mass yields for nuclides produced by the interaction of 272 MeV ^{16}O and ^{165}Ho. Yields are tabulated as "arbitrary units" relative to a monitor cross section $^{27}Al(^{12}C,X)^{22}Na$ equal to 32.0 mb. "I" and "C" designate whether the measured yield is an independent or cumulative yield. Independent and mass yields were not calculated for Tm and Yb nuclides due to insufficient data points.

Table 6 (cont.)

1020 MeV ^{12}C + ^{165}Ho
MASS YIELD TABLE (mb)

NUCLIDE	MEASURED YIELD	CALCULATED INDEPENDENT YIELD	MASS YIELD	YIELD TYPE
^{46g}Sc	1.7 ± 0.2	1.5 ± 0.2	2.8 ± 0.3	I
^{47}Sc	1.0 ± 0.2	1.0 ± 0.2	2.7 ± 0.4	C
^{48}Sc	0.48 ± 0.05	0.48 ± 0.05	2.9 ± 0.3	I
^{48}V	0.62 ± 0.06	0.59 ± 0.06	2.7 ± 0.3	C
^{51}Cr	2.0 ± 0.2	2.0 ± 0.2	4.7 ± 0.5	C
^{54}Mn	2.3 ± 0.2	2.3 ± 0.2	4.2 ± 0.4	I
^{58g}Co	1.1 ± 0.1	-	-	C
^{59}Fe	0.65 ± 0.07	0.6 ± 0.07	2.7 ± 0.3	C
^{74}As	1.0 ± 0.1	1.0 ± 0.1	3.1 ± 0.3	I
^{75}Se	1.2 ± 0.1	0.86 ± 0.09	1.5 ± 0.2	C
^{77g}Br	2.5 ± 0.5	1.8 ± 0.4	3.0 ± 0.6	C
^{82}Sr	0.6 ± 0.2	0.6 ± 0.2	1.8 ± 0.6	C
^{83}Rb	2.0 ± 0.2	0.71 ± 0.07	2.2 ± 0.2	C
^{85g}Sr	2.4 ± 0.6	-	-	C
^{87g}Y	2.1 ± 0.2	-	-	C
^{88}Y	0.64 ± 0.06	0.52 ± 0.06	2.1 ± 0.2	C
^{88}Zr	2.0 ± 0.2	1.7 ± 0.2	2.8 ± 0.3	C
^{89g}Zr	1.7 ± 0.2	1.1 ± 0.1	1.9 ± 0.2	C
^{95g}Nb	0.27 ± 0.03	-	-	C
^{101m}Rh	1.8 ± 0.3	-	-	C
^{105g}Ag	3.3 ± 0.3	2.9 ± 0.3	7.7 ± 0.8	C
^{106m}Ag	1.1 ± 0.2	-	-	I
^{111g}In	5.0 ± 0.5	4.2 ± 0.4	7.6 ± 0.8	C
^{119m}Te	2.1 ± 0.4	-	-	I
^{121g}Te	14. ± 1.	4.7 ± 0.5	19. ± 2.	C
^{121m}Te	0.7 ± 0.1	0.7 ± 0.1	-	I
^{127g}Xe	28. ± 3.	5.0 ± 0.5	46. ± 5.	C
^{128}Ba	25. ± 3.	18. ± 2.	38. ± 4.	C
^{131g}Ba	36. ± 4.	12. ± 1.	43. ± 4.	C
^{143}Pm	54. ± 5.	8.6 ± 0.9	63. ± 6.	C
^{144}Pm	1.1 ± 0.1	1.1 ± 0.1	26. ± 3.	I
^{145}Eu	40. ± 4.	37. ± 4.	64. ± 6.	C
^{146}Gd	43. ± 4.	-	-	C
^{147}Eu	61. ± 6.	41. ± 4.	65. ± 7.	C
^{147}Gd	54. ± 5.	52. ± 5.	177. ± 18.	C
^{148m}Pm	2.2 ± 0.3	-	-	I
^{149}Gd	53. ± 5.	47. ± 5.	71. ± 7.	C

Table 7

1020 MeV ^{12}C + ^{165}Ho
YIELD TABLE (cont.)

NUCLIDE	MEASURED YIELD	CALCULATED INDEPENDENT YIELD	MASS YIELD	
^{151}Gd	59. ± 6.	31. ± 3.	62. ± 6.	C
^{153}Gd	54. ± 5.	27. ± 3.	64. ± 6.	C
^{155}Tb	46. ± 5.	34. ± 3.	69. ± 7.	C
^{155}Dy	57. ± 6.	40. ± 4.	67. ± 8.	C
^{156g}Tb	7.3 ± 0.8	-	-	C
^{160}Tb	3.8 ± 0.4	3.8 ± 0.4	47. ± 5.	I
^{160}Er	32. ± 3.	31. ± 3.	47. ± 5.	C
^{166}Yb	1.3 ± 0.4	1.2 ± 0.4	20. ± 6.	C

Tabulation of the measured and calculated independent and mass yields for nuclides produced by the interaction of 1020 MeV ^{12}C and ^{165}Ho. "I" and "C" designate whether the measured yield is an independent or cumulative yield.

Table 7 (cont.)

1635 MeV ^{16}O + ^{165}Ho
MASS YIELD TABLE
(arbitrary units)

NUCLIDE	MEASURED YIELD	CALCULATED INDEPENDENT YIELD	MASS YIELD	YIELD TYPE
^{22}Na	2.3 ± 0.7	2.3 ± 0.7	11. ± 3.	C
^{24}Na	8. ± 1.	7. ± 1.	10. ± 2.	C
^{28}Mg	1.8 ± 0.2	1.7 ± 0.2	6.8 ± 0.7	C
^{44m}Sc	1.5 ± 0.2	-	-	I
^{46g}Sc	3.5 ± 0.4	3.5 ± 0.4	5.9 ± 0.6	I
^{47}Sc	1.8 ± 0.8	1.7 ± 0.8	4.2 ± 1.9	C
^{48}Sc	1.0 ± 0.1	1.0 ± 0.1	5.6 ± 0.6	I
^{48}V	1.1 ± 0.1	1.1 ± 0.1	5.2 ± 0.5	C
^{51}Cr	4.3 ± 0.6	3.9 ± 0.6	9.9 ± 1.5	C
^{52g}Mn	0.61 ± 0.06	0.59 ± 0.06	4.5 ± 0.5	C
^{54}Mn	5.0 ± 0.5	5.0 ± 0.5	9.0 ± 0.9	I
^{56}Co	0.34 ± 0.03	0.33 ± 0.03	4.4 ± 0.4	C
^{58g}Co	3.0 ± 0.3	-	-	C
^{59}Fe	1.3 ± 0.1	1.3 ± 0.1	6.4 ± 0.6	C
^{65}Zn	4.2 ± 0.4	3.6 ± 0.4	6.8 ± 0.7	C
^{71}As	1.7 ± 0.2	1.6 ± 0.2	4.8 ± 0.8	C
^{74}As	2.1 ± 0.2	2.1 ± 0.2	5.0 ± 0.5	I
^{75}Se	3.8 ± 0.4	2.9 ± 0.3	4.8 ± 0.5	C
^{83}Rb	7.9 ± 0.8	3.1 ± 0.3	8.8 ± 0.9	C
^{84g}Rb	1.8 ± 0.2	1.8 ± 0.2	12. ± 1.	I
^{85g}Sr	6.2 ± 0.6	2.9 ± 0.3	6.8 ± 0.7	C
^{86g}Y	5.5 ± 2.6	2. ± 1.	3.6 ± 1.7	C
^{87g}Y	7.3 ± 0.8	2.7 ± 0.3	17. ± 2.	C
^{87m}Y	6.5 ± 0.7	5.5 ± 0.6	-	C
^{88}Y	1.9 ± 0.3	1.5 ± 0.2	5.4 ± 0.8	C
^{88}Zr	6.2 ± 0.6	5.1 ± 0.5	8.8 ± 0.9	C
^{89g}Zr	6.7 ± 0.7	4.3 ± 0.4	7.6 ± 0.8	C
^{95g}Nb	0.07 ± 0.01	0.06 ± 0.01	11. ± 3.	C
^{95m}Nb	0.6 ± 0.1	0.6 ± 0.1	-	I
^{97}Ru	3.8 ± 0.4	3.6 ± 0.4	11. ± 1.	C
^{100}Pd	1.6 ± 0.2	1.6 ± 0.2	47. ± 5.	C
^{100g}Rh	6.9 ± 0.7	5.5 ± 0.6	13. ± 1.	C
^{101g}Rh	0.8 ± 0.1	0.8 ± 0.1	14. ± 2.	I
^{101m}Rh	9.4 ± 0.9	7.6 ± 0.8	-	C
^{102g}Rh	1.7 ± 0.3	-	-	C
^{105g}Ag	13. ± 1.	11. ± 1.	31. ± 3.	C
^{106m}Ag	0.33 ± 0.06	-	-	I
^{111g}In	14. ± 1.	12. ± 1.	22. ± 2.	C
^{119m}Te	3.4 ± 0.5	-	-	I

Table 8

1635 MeV ^{16}O + ^{165}Ho
YIELD TABLE (cont.)
(arbitrary units)

NUCLIDE	MEASURED YIELD	CALCULATED INDEPENDENT YIELD	MASS YIELD	YIELD TYPE
^{121g}Te	29. ± 3.	13. ± 1.	39. ± 4.	C
^{121m}Te	1.4 ± 0.1	1.4 ± 0.1	-	I
^{123m}Te	0.6 ± 0.1	-	-	I
^{125g}Xe	26. ± 3.	19. ± 2.	35. ± 4.	C
^{127g}Xe	33. ± 3.	15. ± 2.	38. ± 4.	C
^{128}Ba	24. ± 17.	22. ± 15.	50. ± 36.	C
^{131g}Ba	42. ± 4.	23. ± 2.	46. ± 5.	C
^{135g}Ce	30. ± 3.	26. ± 3.	48. ± 5.	C
^{139g}Ce	50. ± 5.	13. ± 1.	62. ± 6.	C
^{145}Eu	35. ± 4.	18. ± 2.	38. ± 4.	C
^{146}Eu	10. ± 1.	-	-	C
^{146}Gd	33. ± 3.	-	-	C
^{147}Eu	44. ± 4.	14. ± 1.	50. ± 5.	C
^{147}Gd	35. ± 4.	28. ± 3.	49. ± 5.	C
^{148m}Pm	6.1 ± 0.7	-	-	I
^{149}Gd	49. ± 5.	32. ± 3.	56. ± 6.	C
^{151}Gd	66. ± 7.	28. ± 3.	74. ± 7.	C
^{151g}Tb	31. ± 3.	28. ± 3.	62. ± 6.	C
^{152g}Tb	48. ± 5.	40. ± 4.	74. ± 7.	C
^{153}Gd	52. ± 5.	14. ± 1.	58. ± 6.	C
^{155}Tb	52. ± 5.	30. ± 3.	57. ± 6.	C
^{156g}Tb	10. ± 1.	-	-	C
^{160}Tb	4.2 ± 0.4	4.2 ± 0.1	60. ± 6.	I
^{160}Er	27. ± 3.	17. ± 2.	27. ± 3.	C
^{167}Tm	0.83 ± 0.08	0.014 ± 0.002	1.5 ± 0.2	C

Tabulation of the measured and calculated independent and mass yields for nuclides produced by the interaction of 1635 MeV ^{16}O and ^{165}Ho. Yields are tabulated as "arbitrary units" relative to a monitor cross section $^{27}Al(^{12}C,X)^{22}Na$ equal to 34.1 mb. "I" and "C" designate whether the measured yield is an independent or cumulative yield.

Table 8 (cont.)

independent yields only if satisfactory decay corrections using the following rules could be made:

1) If both members of an isomeric pair with known decay scheme are observed, the individual independent yield corrections and mass yield contributions are calculated. The mass yield contributions are summed and tabulated with the ground state entry for the nuclide in tables 4-8.

2) Ground state isomers for which all (or nearly all) of the metastable state decays to the ground state by isomeric transition (IT) or internal conversion (IC) with a short half-life, relative to the time-of-irradiation, are treated as non-isomeric nuclides. The parent is assumed to be the next nuclide in the isobaric chain (not the metastable state) for calculating independent yield corrections and mass yields. The maximum error introduced by this procedure was calculated to be less than 4.3% for all such cases.

3) Independent yield corrections and mass yields are not calculated for isomers which do not fit either of the above criterion. Only measured yields are tabulated for these nuclides in tables 4-8.

Correction for precursor decay was based on the assumption that independent yield cross sections could be represented by a histogram that lies along a Gaussian probability function [51,52], commonly referred to as a charge dispersion. The procedure to determine the independent yields, $\sigma_{IY}(Z,A)$, was to fit the experimental nuclidic yields to the Gaussian charge distributions using the functional form:

$$\sigma_{IY}(Z,A) = \sigma(A)\ \{2\pi S_Z(A)^2\}^{-1/2}\ \exp\left(\frac{Z-Z_p(A)^2}{-2S_Z(A)^2}\right) \qquad \text{[eqn 6]}$$

$S_Z(A)$ is the Gaussian "width" and $Z_p(A)$ determines the centroid of

the Gaussian. The centroid of an isobaric Gaussian is the most probable (non-integer) Z for the given A of the isobar. The Gaussian described by equation 6 was fit to the data by iteratively varying the Gaussian width and centroid parameters, $S_Z(A)$ and $Z_p(A)$, respectively.

Unique determination of the three variables, $\sigma(A)$, $S_Z(A)$ and $Z_p(A)$ required the measurement of at least three independent yield cross sections for each isobar. This requirement could not be met since no isobaric chain contains three shielded nuclei. These studies measured many radioactivities spanning the entire periodic table accessible by the nuclear reaction under investigation. In general, however, the nature of radioanalytical studies (such as this one) do not lend themselves to the measurement of isobaric members. The important assumption that $\sigma(A)$ varies smoothly and slowly as a function of the mass number, A, must be made to correct for precursor decay with equation 6. A restatement of this assumption is that the charge dispersion curves for neighboring isobaric chains are very similar, thus, radionuclide yields from a small group of isobars can be used to determine a single charge dispersion curve applicable to that small mass region. Extreme care was used in the near-target mass region where $\sigma(A)$ varied more rapidly. No cumulative or independent yields are reported for several of the heaviest nuclides observed since there was insufficient data to unambiguously determine the charge dispersion for that mass region.

A computer code was used to iteratively fit the Gaussian width and centroid parameters, $S_Z(A)$ and $Z_p(A)$ respectively, to the measured data over small A bins. The width parameter was found to vary slowly with A, thus, for a group of nuclides spanning a small mass interval a constant $S_Z(A)$ was used. The Gaussian centroid was usually described by a linear function in A for each mass bin. Near target mass regions occasionally necessitated the addition of an A^2 term in the $Z_p(A)$ expression. The independent yields and isobaric cross sections calculated in the manner discussed above are tabulated in tables 4-8 along with the measured production cross sections. The plotted mass distributions for the systems studied are shown in figures 7-11. (The plotted mass yield represents an averaged value for cases where measured yields of two nuclides from the same isobar existed.) These results are discussed in the following chapter. Width parameters and $Z_p(A)$ coefficients used for each data set are given in tables D-1 to D-5 of appendix D. These parameters are viewed as a consistent set of parameters to describe an individual experiment. The parameters do not uniquely describe the charge dispersions; therefore, they can not be used as a reliable mode of comparison of experimental conditions or mechanisms between different data. The results of this procedure, the charge dispersions are shown in appendix D where the calculated independent yield cross sections are plotted versus $Z-Z_p(A)$, the distance in Z units from the center of the isobaric charge dispersion. The constraint that only small A-bins are allowed occasionally resulted in bins with only two data points. These data points were fit with Gaussian width and centroid

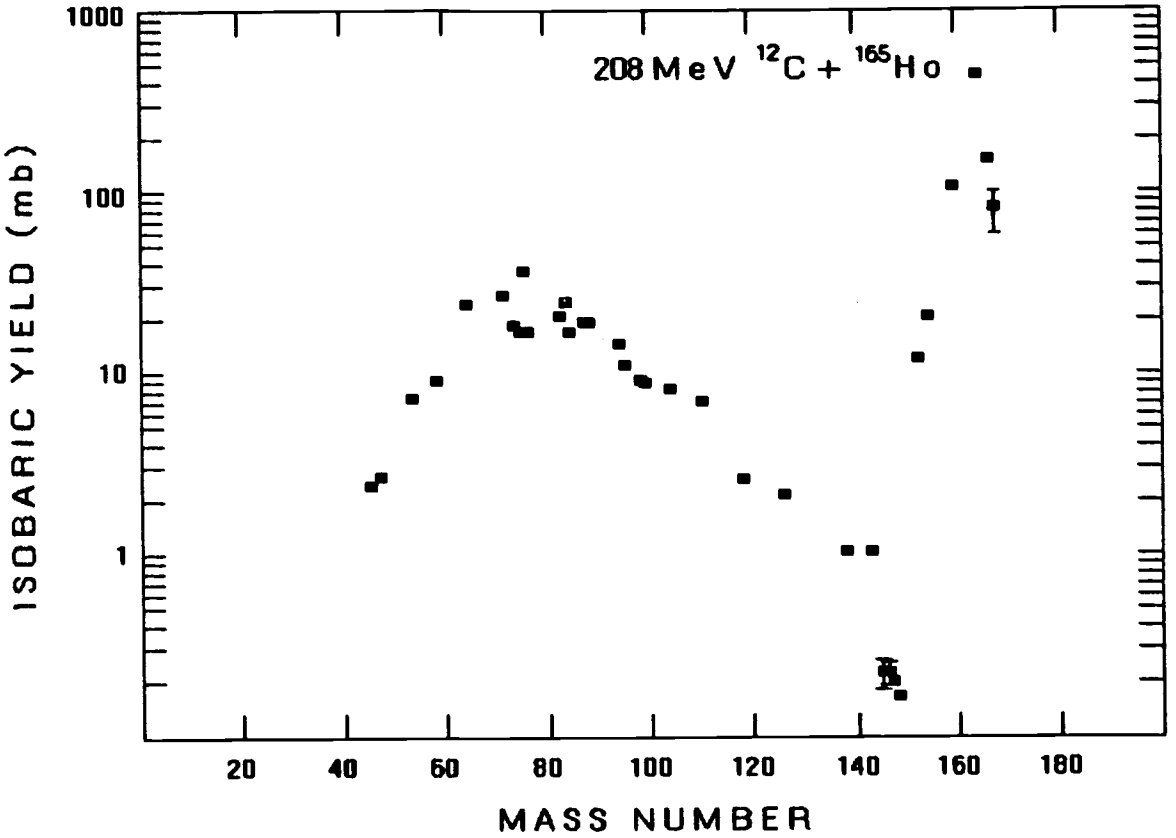

Fragment isobaric yield distribution for the reaction system 208 MeV $^{12}C + ^{165}Ho$.

Figure 7

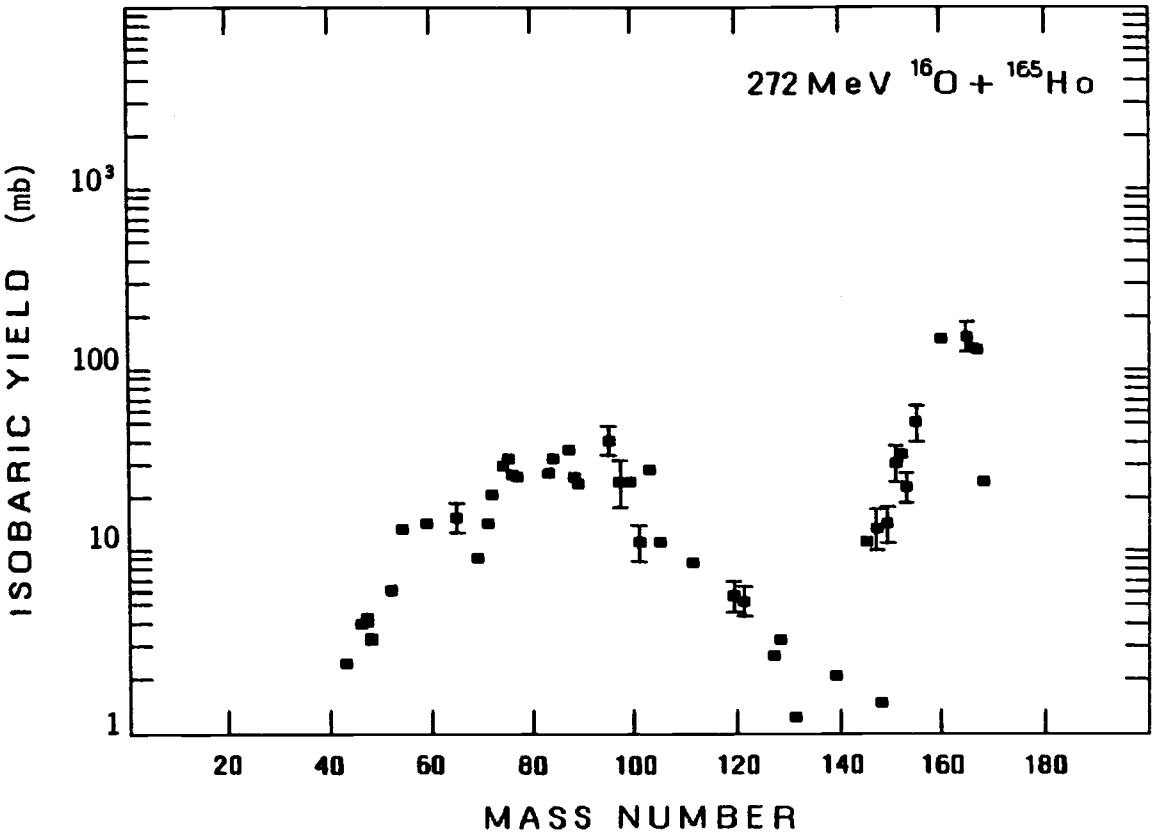

Fragment isobaric yield distribution for the reaction system 272 MeV $^{16}O + ^{165}Ho$.

Figure 8

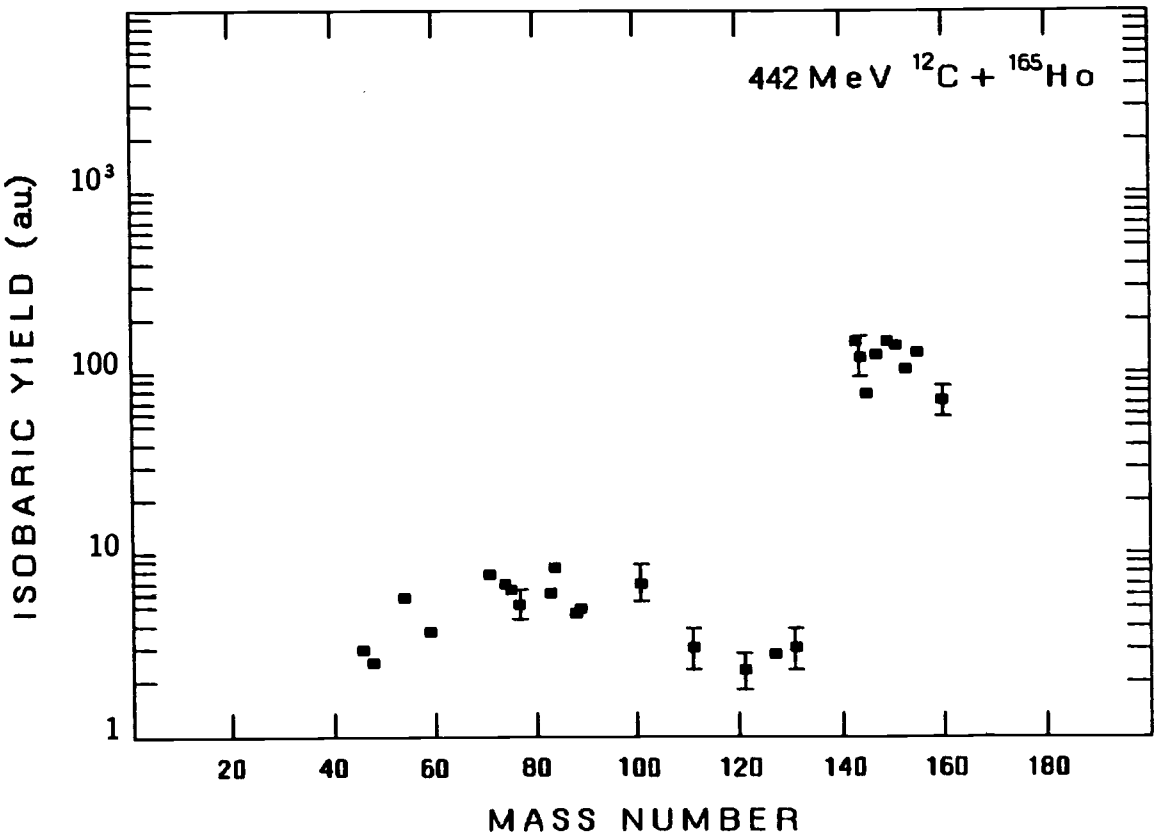

Fragment isobaric yield distribution for the reaction system 442 MeV ^{12}C + ^{165}Ho.

Figure 9

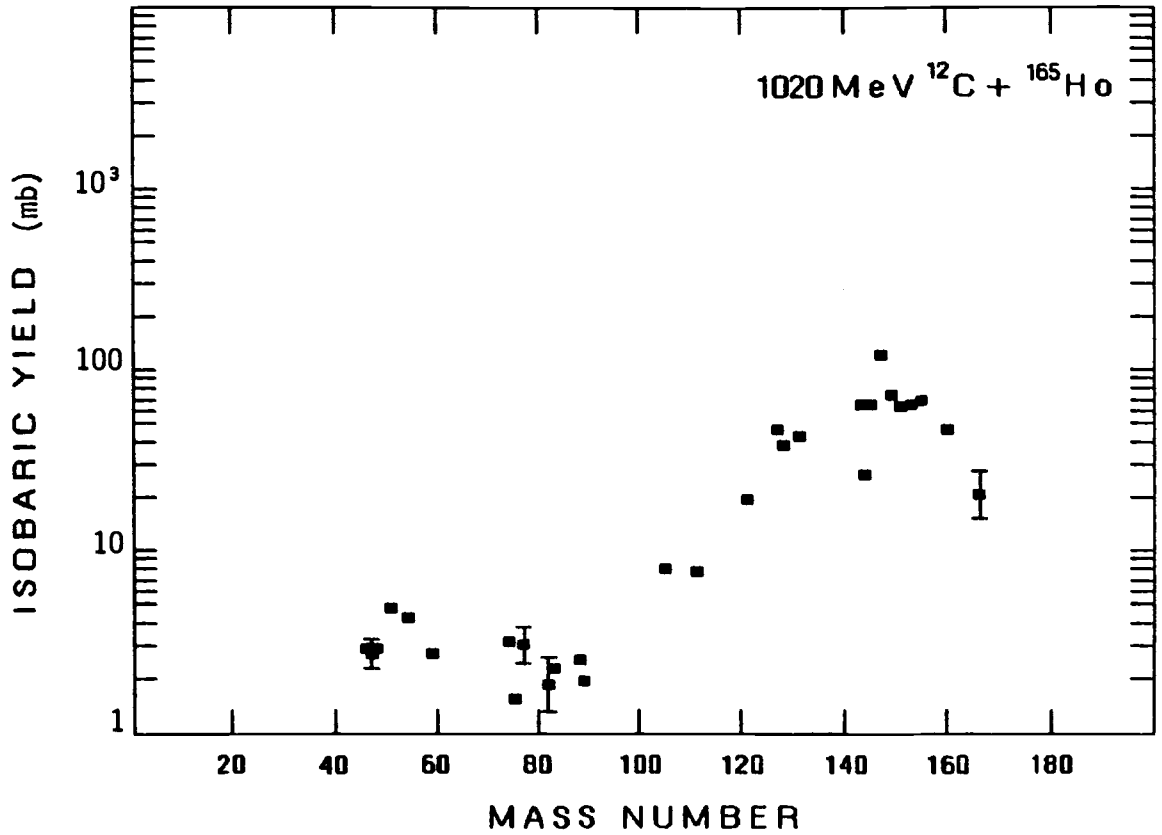

Fragment isobaric yield distribution for the reaction system 1020 MeV ^{12}C + ^{165}Ho.

Figure 10

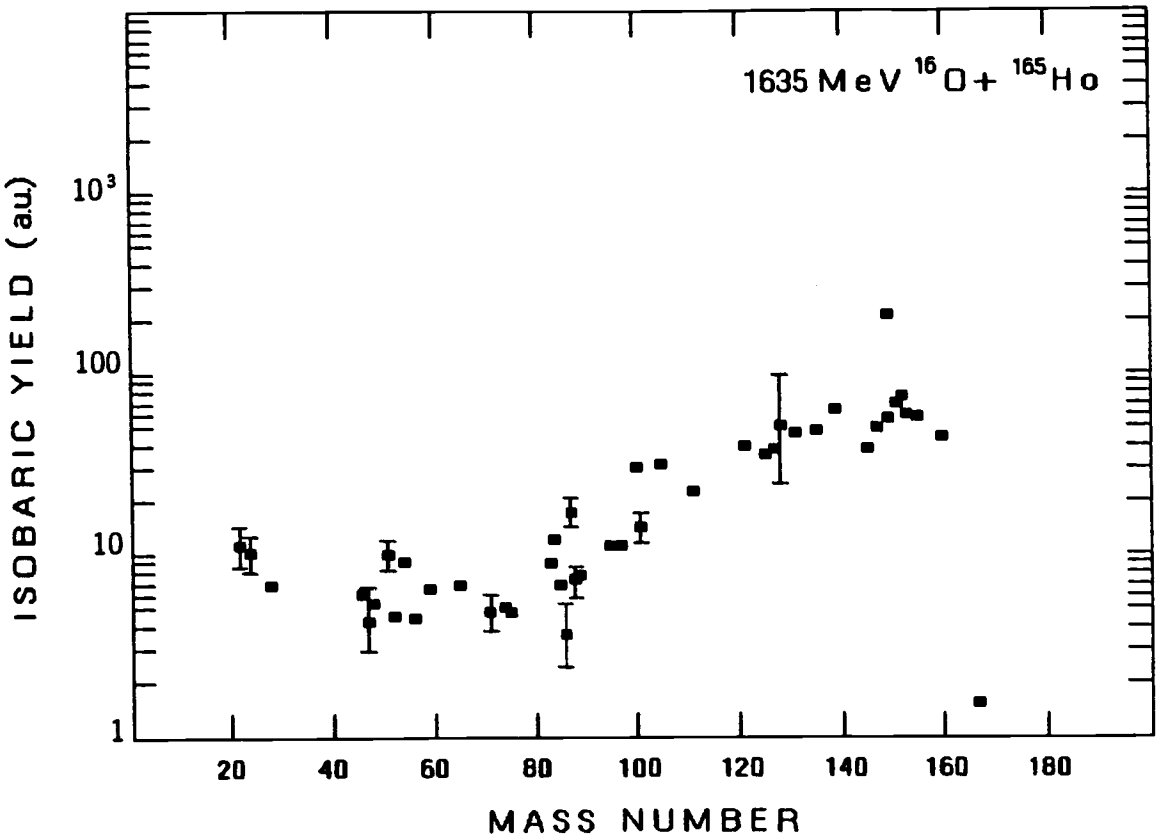

Fragment isobaric yield distribution for the reaction system 1635 MeV ^{16}O + ^{165}Ho.

Figure 11

parameters representing a smooth trend between the parameters used to fit data in neighboring mass regions.

The Z_p function results tabulated in tables D-1 to D-5 show several major discontinuities ($\leq$ 1 Z-unit). A discontinuity is observed between the mass numbers 120 and 140 in every set of Z_p functions. The discontinuities were found to occur very near closed proton or neutron shells. Two representative plots of the Z_p function results are plotted in figures 12 and 13 for the 272 MeV ^{16}O + ^{165}Ho and 1635 MeV ^{16}O + ^{165}Ho systems. The two nearly vertical lines with symbols represent nuclides along the Z=50 and N=82 closed shells illustrating the proximity of the closed shells to the discontinuities in the Z_p functions.

One explanation may be that the discontinuities are a result of the secondary stage (deexcitation) of the interaction which are most likely to be affected by shell closures. Energies in the primary stage are orders of magnitude greater than closed shell energies, effectively washing out any observable influence. The effect of the closed shells on the deexcitation chain was examined using the Monte Carlo method with simplistic particle emission probabilities taken from reference 53. Primary fragments predicted by the firestreak code (see appendix B) were used to compare the calculated effects of the closed shells on the deexcitation paths. No net effect was observed ($\leq$ 0.4 Z-units) between deexcited nuclei which passed through a closed shell and those that did not.

A possible explanation which can not be examined with these calculations is the influence of the closed shell near the end of a deexcitation chain (low excitation energy) where any effect will be

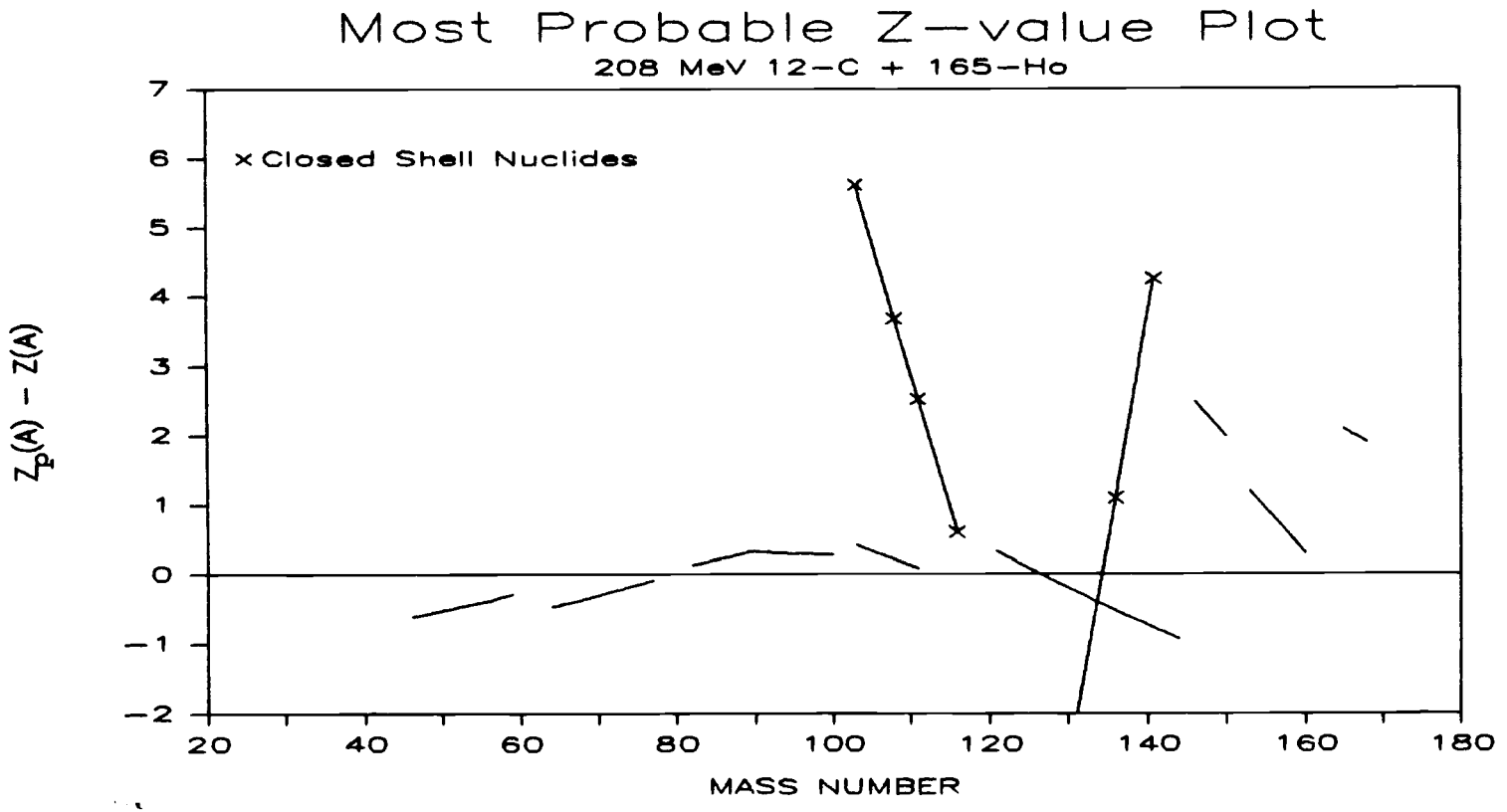

Plot of most probable X-value (from charge dispersion fit) relative to valley of beta stability. Z(A) is the most stable Z calculated at a given A (formula 2-35 in reference 109). Closed Shell nuclei are represented by "x" points.

Figure 12

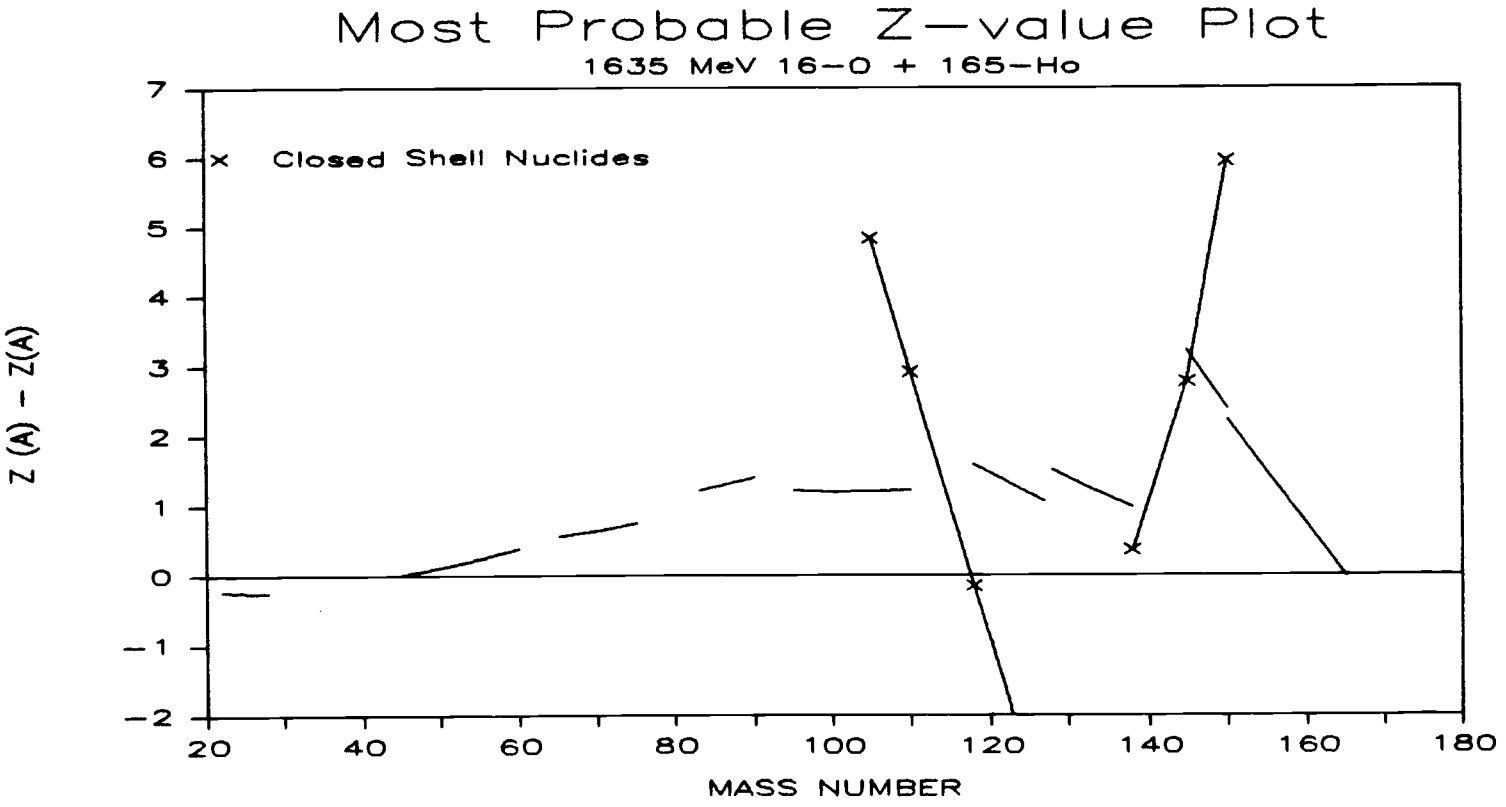

Plot of most probable X-value (from charge dispersion fit) relative to valley of beta stability. Z(A) is the most stable Z calculated at a given A (formula 2-35 in reference 109). Closed shell nuclei are represented by "x" points.

Figure 13

maximized. The emission of the last few nucleons from a nucleus with low excitation energy will be extremely sensitive to the specific level densities of the resultant nuclei. These cases are not correctly simulated by the Fermi gas level densities used in our calculations.

Another discontinuity is observed in the Z_p functions for the 208 MeV ^{12}C + ^{165}Ho and 272 MeV ^{16}O + ^{165}Ho reaction systems in the mass region between 160 and 165. There is no clear explanation for these breaks, however, two possible causes may be that the breaks occur between trans-target products and products lighter than the target, and the yield surface is changing very rapidly in this mass region. A mechanism for how these observations may effect the Z_p functions is not known.

The uncertainties in each point in figures D-1 to D-5 represent the fractional uncertainty in the measured isotopic cross section leading to that point and not any systematic uncertainty introduced by the charge dispersion analysis. The magnitude of the systematic uncertainty depends on the fit of each independent radionuclide yield by the Gaussian charge distributions, the position of the measured radionuclide Z relative to Z_p (those points farthest from Z_p have the largest uncertainties), uncertainties in $S_Z(A)$ and $Z_p(A)$, and the extent to which the mass yield curve is a slow, smoothly varying function of A whose magnitude and shape are to be determined. Morrissey, et al. [27] have suggested that by using a propagation of errors treatment one can estimate that on the average, individual points on the mass yield curve have a systematic uncertainty of approximately ±30%

which would be added to the uncertainty in the measured value. The average mass yield within each small A-bin used in the charge dispersion analysis, however, is known to ±15% assuming a constant or slowly varying value of the mass yield over the region of the A-bin [27,54,55]. This analysis breaks down for regions (usually near the target mass) where the mass yield is varying rapidly with product mass.

Effects of secondary particle induced reactions on the measured cross sections must be examined in order to determine the reliability of the values which are attributed to primary interactions. Secondary particles of concern are those particles and fragments produced in the primary interaction with sufficient kinetic energy to induce an interaction in a second target nucleus. Several observations of high energy light ion emissions, capable of inducing secondary reactions, have been reported in the literature from both relativistic heavy ion (RHI) [39,56,57] and intermediate energy heavy ion [58] induced interactions. The cross sections of light ions are generally found to decrease rapidly as mass and charge increase (with the apparent exception of ^{4}He [39]). The most abundant emissions are π^{+}, π^{-}, p, n, d, t, ^{3}He, and ^{4}He.

The effects of secondary particle induced reactions on measured target fragmentation cross sections at intermediate energies is not generally known. One can obtain some information by examining the data from RHI induced interactions where the extent of secondary reactions has been widely studied. Secondary particle induced reactions are expected to be more extensive at the higher energies due to larger secondary particle multiplicities.

Cumming, et al. [59,60] reported a study of secondary reaction contributions to product nuclide cross sections from the reactions of 28 GeV protons and 25 GeV ^{12}C ions with copper. They reported finding insignificant secondary contributions for nuclides more than 11 mass units below the target mass. The contribution of secondary reactions to the cross section of nuclides 4 mass units below the target increased to between 1.9% and 2.6% per 100 mg/cm^2 of target thickness. Large secondary effects were only reported for very near-target nuclides (less than 3 mass units away from the target). The largest contribution of secondaries reported was 30% per 100 mg/cm^2 for nuclides from the 28 GeV proton + Cu experiment. Porile et al. [62] have studied the interaction of 25 GeV ^{12}C with a 100 mg/cm^2 Ag target and calculated an average 2.5% per 100 mg/cm^2 secondary particle induced contributions to the target fragment cross sections. Secondary effects were reported to rise sharply for nuclides less than 14 mass units from the target. The measured contribution was approximately 15% per 100 mg/cm^2 for A=100 and 25% per 100 mg/cm^2 for A=106 nuclides. Morrissey, et al. [27] have carefully studied secondary effects in the interaction of 8 GeV ^{20}Ne with ^{197}Au. Comparisons of a large number of nuclidic cross sections for products with mass between 40 and 196 from targets of 49.3 mg/cm^2 and 242.0 mg/cm^2 were made. It was found that the data was consistent with the assumption that there was no measurable effect from secondary particle induced reactions for any of the observed nuclides.

The above analyses, although predominantly from high energy interactions, indicate that secondary particle induced contributions to the measured cross sections are well below experimental uncertainties (≈10%) for all but the very near target nuclides (i.e. ^{160}Er). The most significant secondary particle induced contributions are observed for product nuclides near the target. ^{160}Er is the nearest target isotope (5 mass units below the target) observed and the most likely to be affected by secondary contributions. ^{160}Er is a trans-target nuclide (only 1 Z-unit above the target) observed with relatively large cross sections in all systems studied at all projectile energies indicating possible contributions from secondary reactions. Light ion multiplicities measured for RHI induced reactions are extremely large suggesting the observed effects of secondaries discussed above are generally greater than at intermediate energies. Based upon consistently small secondary effects over a target mass range which brackets A=165 (holmium) it is assumed that secondary particle induced reactions have negligible effect on the observables measured in this work (with the possible exception of ^{160}Er).

III. RESULTS AND DISCUSSION

A. YIELDS

1. Experimental Production Cross Sections

The measured nuclidic production cross sections are presented in table 3. Trans-target nuclides (nuclides with $Z > Z_{target}$) were identified for all interactions studied. The measured nuclidic production cross sections for observed trans-target nuclides are re-tabulated in table 9 for each interaction studied. Nuclides with 4 Z-units above the target were observed for 208 MeV ^{12}C and 272 MeV ^{16}O induced interactions, with 3 Z-units above the target for 442 MeV ^{12}C and 1020 MeV ^{12}C induced interactions, and with 2 Z-units above the target for 1635 MeV ^{16}O induced interactions. The observation of trans-target species at 17.0 MeV/A and 17.3 MeV/A are in exceptionally good agreement with the results of Aleklett, et al. with 4 Z-units above the target were identified for the interaction of 19 MeV/A ^{16}O + ^{154}Sm. Trans-target species have been previously reported at approximately 85 MeV/A, for nuclides with 1 Z-unit [63], 2 Z-units [38,63,65], and in one case, 3 Z-units above the target [66].

The unexpected observation of ^{166}Yb formed by the interaction of 1020 MeV ^{12}C with ^{165}Ho prompted a careful review of the specifics for the identification of this nuclide. Five gamma-ray lines (184.7, 705.3, 778.4, 1273.4, 2052.9 keV [67]) were identified with a 56.7 hour component. The 778.4 keV line was a poor quality identification

TRANS-TARGET NUCLIDIC CROSS SECTONS

MEASURED YIELDS

NUCLIDE	TPKE(MeV) 208 (mb)	272 (mb)	442 (a.u.)	1020 (mb)	1635 (a.u.)
^{160}Er	186. ± 19.	97. ± 10.	97. ± 10.	32. ± 3.	27. ± 3.
^{165}Tm	431. ± 43.	149. ± 23.	5. ± 2.		
^{167}Tm	124. ± 12.	116. ± 12.	3.1 ± 0.3		0.83 ± 0.08
^{168}Tm	0.90 ± 0.09	0.55 ± 0.06			
^{166}Yb	214. ± 21.	82. ± 8.	--	1.3 ± 0.4	
^{169}Yb	6.6 ± 0.7	13. ± 1.	1.0 ± 0.2		
^{169}Lu	3.5 ± 0.6	10. ± 1.			
^{170}Lu	--	4.5 ± 0.5			
^{171}Lu	--	1.6 ± 0.2			

A tabulation of the measured trans-target nuclidic yields. The values reported for 442 MeV ^{12}C + ^{165}Ho and 1635 MeV ^{16}O + ^{165}Ho reaction systems are relative values. Uncertainties reported are with respect to the measured value, the uncertainty with respect to the absolute cross section is s 50%.

Table 9

due to the presence of at least two other components. The 184.7 keV line was identified by a two component growth (^{166}Yb - ^{166}Tm) and decay fit. The 1273.4 and 2052.9 keV lines were both fit by single component ^{166}Yb identifications, with no other known identifications possible. The set of ^{166}Yb nuclidic cross sections calculated independently from each photopeak area (except the 778.4 keV line) agreed well with one another. Each individual cross section was within the experimental uncertainty of the weighted average for the set.

One may argue that the 1.6 millibarn cross section measured for the ^{165}Ho(1020 MeV ^{12}C, X)^{166}Yb interaction was the result of ^{12}C reacting with impurities in the target heavier than Ho. Assuming that the 0.01% contaminant (experimental chapter) is exclusively ^{168}Yb or ^{170}Yb the production cross section for ^{166}Yb would have to be 16000 millibarns (16 barns). The two assumptions necessary to produce the observed yield of ^{166}Yb via contaminant reactions are exceedingly unlikely, thus, we conclude that this nuclide is produced by an incomplete fusion mechanism.

The observation of ^{167}Tm in the 1635 MeV ^{16}O + ^{165}Ho interaction is slightly less defensible. The identification is based on the 41.0% abundant 207.8 keV gamma-ray. The next most abundant gamma-ray (1.6%, 531.5 keV) is more than a factor of 20 weaker than the 207.8 keV line. The 207.8 keV gamma was observed in 12 consecutive spectra spanning a period of 47 days. The decay consisted of a single 9.2 day component assigned to ^{167}Tm.

The yields of several Er, Tm and Yb isotopes are plotted as a function of total projectile kinetic energy (TPKE) in figure 14. The yields measured for the 442 MeV ^{12}C + ^{165}Ho and 1635 MeV ^{16}O + ^{165}Ho systems are plotted as bars representing 100% uncertainty in the absolute value of the cross sections (not the uncertainty of the measured value). A trend of decreasing nuclidic yield as a function of increasing projectile energy is clearly evident for ^{166}Yb where all cross sections plotted are absolute. The decreasing yield is evident, even for nuclides with the large 100% uncertainty plotted data. (The increase in ^{169}Yb and ^{169}Lu yields between 208 MeV and 272 MeV may be attributed to the heavier primary system formed by the ^{16}O projectile, however, it is curious that the same effect is not observed for ^{166}Yb.)

Aleklett, et al. [64] and Gavron, et al. [68] have determined that the bulk of observed nuclides are formed by complete fusion or incomplete fusion mechanisms. Aleklett reports that 93% of the interactions at 8.5 MeV/A proceed by a complete fusion mechanism. This quantity decreases to 35% at 19 MeV/A and <5% at 35 MeV/A. The yield of trans-target nuclides and the mass of the heaviest trans-target species reported in this work (table 9) both decrease with increasing projectile energy, in agreement with the results reported by Aleklett. Although the yields and masses of trans-target nuclides are decreasing over the projectile energy range studied, it is clear that at least some amount of projectile mass is transferred to the target even at 100 MeV/A.

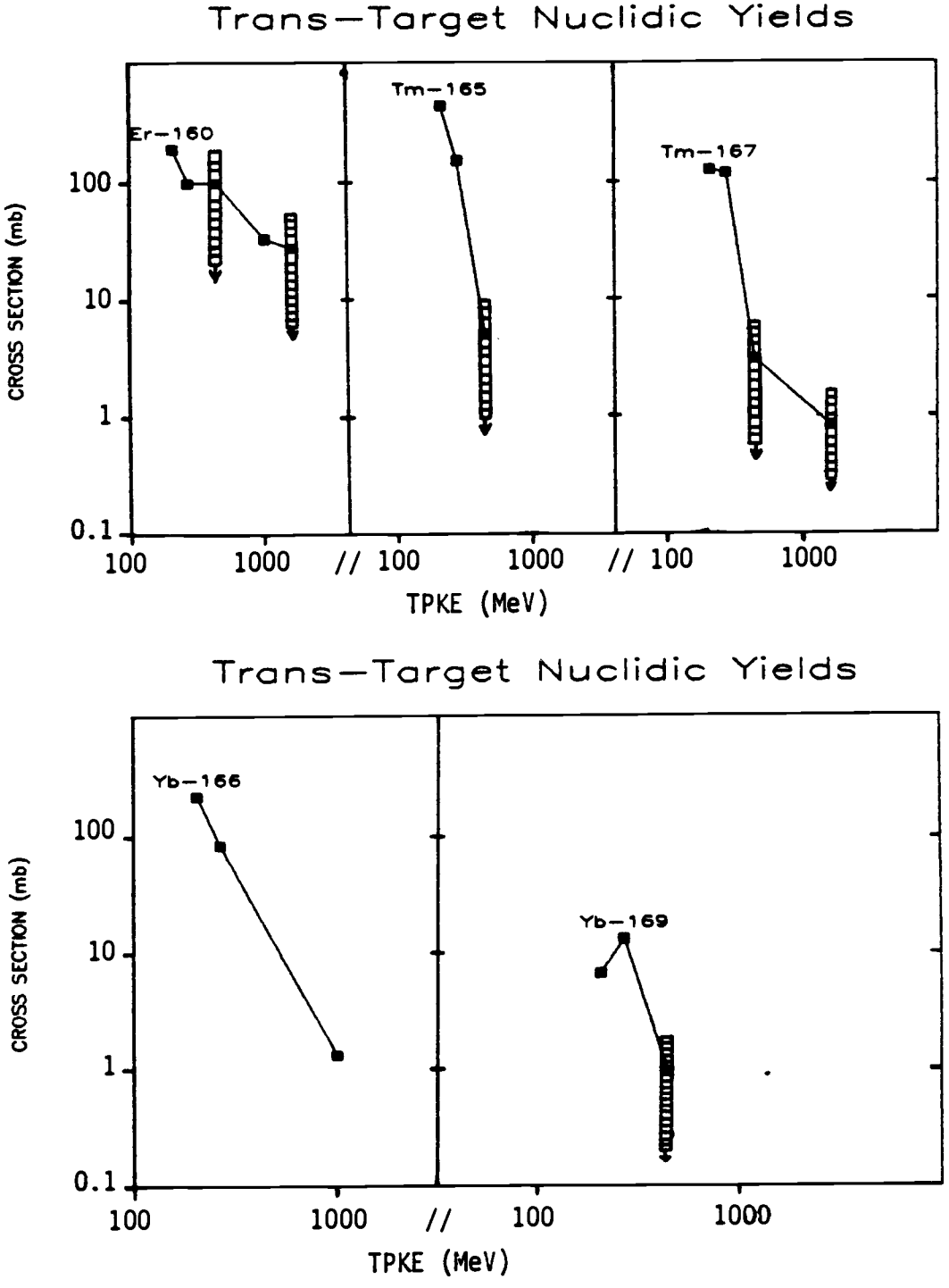

Trans-target nuclidic production cross sections plotted as a function of total projectile kinetic energy (TPKE).

Figure 14

The masses of the trans-target nuclides observed for reactions induced by 442 MeV or 1020 MeV ^{12}C, or 1635 MeV ^{16}O indicate these products could not have been the result of completely fused systems. The excitation energies for such a fused system would have caused the evaporation chain to end significantly below the target mass. These observations are in agreement with the work of Aleklett, et al. [64] and Gavron, et al. [68]. They measured velocity spectra which were interpreted to indicate that the trans-target nuclides were produced by a combination of complete fusion and incomplete fusion mechanisms at projectile energies of 15 to 20 MeV/A. The contribution of complete fusion decreases drastically by 35 MeV/A, and the heaviest species produced by 85 MeV/A projectiles were the result of very gentle (low momentum transfer) interactions. (Note that contributions from secondary reactions may be significant for the ^{160}Er nuclide--it is almost universally observed for interactions induced in holmium targets, see appendix C).

Calculated heavy fragment distributions were found to agree with the general conclusion that a significant fraction of the observed trans-target yield resulting from 208 MeV ^{12}C and 272 MeV ^{16}O induced interactions (17.3 MeV/A and 17.0 MeV/A, respectively) are from completely fused systems [64,68]. The probable origin of these heavy fragments is discussed further in section C2, below.

2. Experimental Mass Yields

The isobaric yield distributions, mass yields, for the systems studied are shown in figures 7-11. A composite of these distributions is presented in figure 15 to more easily discern qualitative changes and trends in the mass yield curves as the projectile energy increases. In figure 15, one observes an asymmetric peak occurring in the heavy fragregion ($A \geq 120$) of the plot for all systems studied. This "heavy fragment" yield is sharply peaked at approximately the target mass number for the lowest projectile energies (208 and 265 MeV). The mass number at which the yield reaches a maxima decreases and the distribution broadens as the energy of the projectile is increased. A broad peak in the mass region $50 \leq A \leq 110$ is also observed for interactions induced by 208 MeV ^{12}C, 272 MeV ^{16}O, and 442 MeV ^{12}C projectiles. Recent work by Gavron, et al. [68] has identified significant fission cross sections for similar reaction systems. The nuclides in this intermediate mass region are also associated with a generally increasing Z_p trend (becoming more neutron deficient) at fixed mass number, A, with projectile energy, illustrated in figure 16. One possible explanation for this observation is that the primary fragment excitation energy is increasing with increasing projectile energy. The mass yields are discussed in more detail, below.

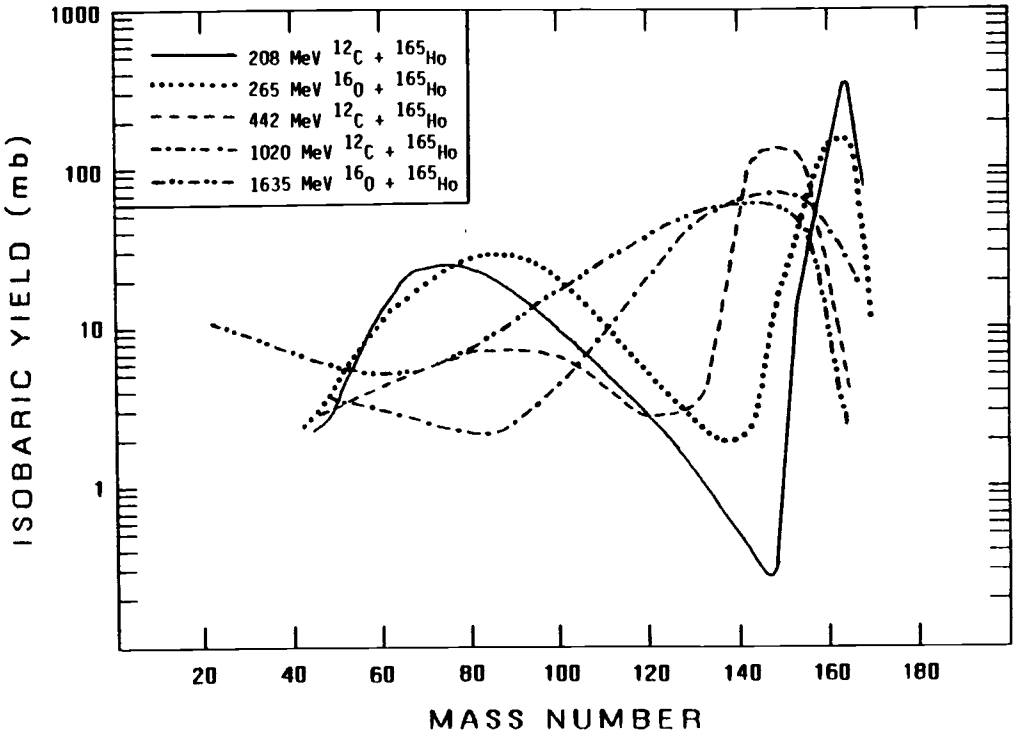

Combined isobaric yield distributions for all five systems studied. Curves plotted for 442 MeV and 1635 MeV data represent relative cross sections.

Figure 15

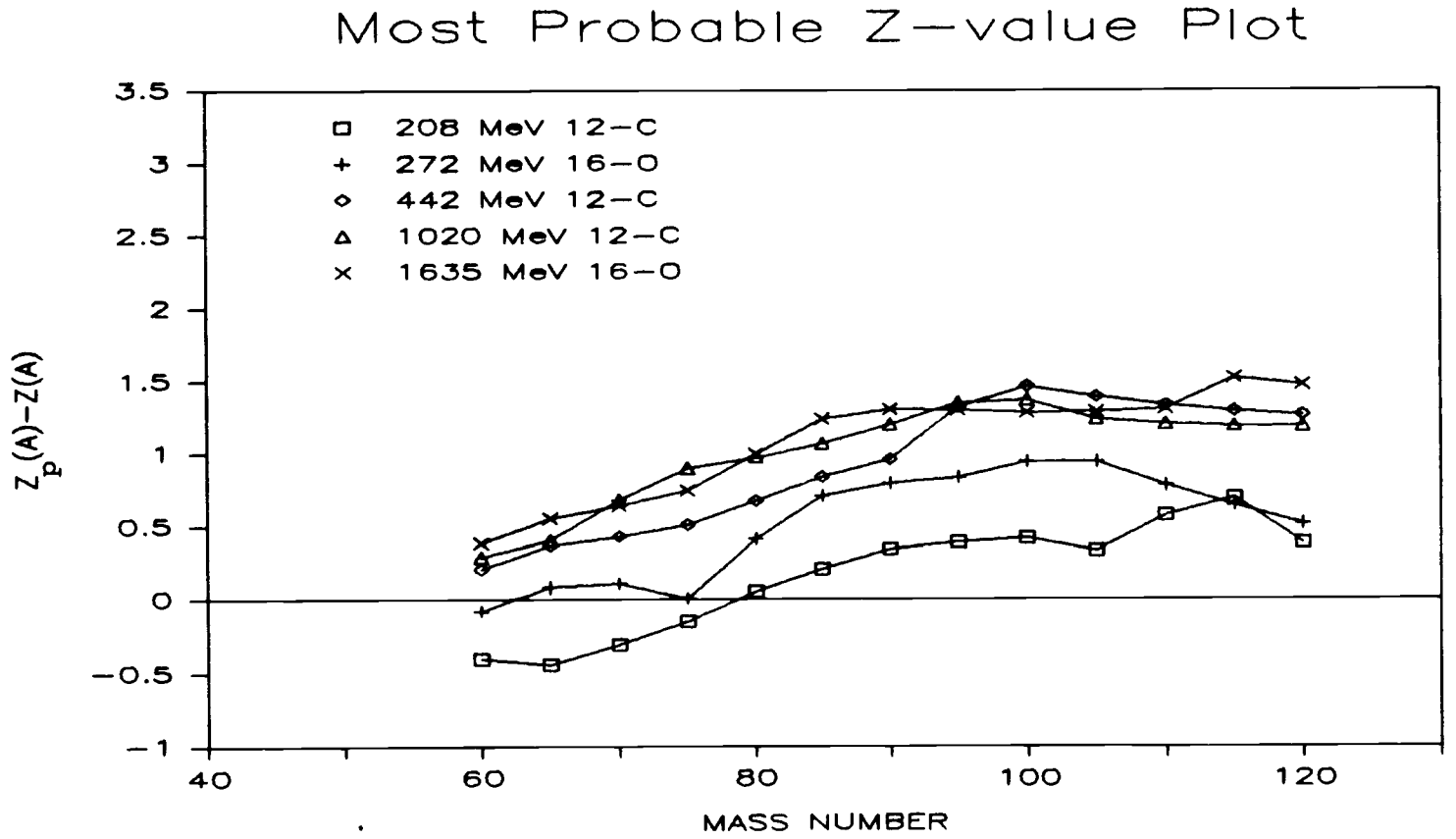

Plot of the most probable Z-value (from charge dispersion fits) relative to valley of beta stability, for the fission fragment mass region of all systems studied. Z(A) is the most stable Z calculated at a given A (from reference 109). The most probable Z regions have been smoothly connected to facilitate viewing the trends.

Figure 16

2a. Heavy Fragment Yields

Focusing attention on the mass region above A≥120 in figure 15 we find a major peak in the mass yield curve of all five systems studied. This peak in the yield distribution is predicted by firestreak and sum-rule model calculations to be the result of variously excited fragments relatively near the target mass which undergo deexcitation by particle emission (and fast β-decay, for which corrections have been made) forming the observed nuclides. There are two obvious trends which are observed for this region. First, the mass number at which the heavy mass distribution reaches a maxima decreases from A≈165 for the lowest total projectile kinetic energies, TPKE's, (208 MeV ^{12}C and 272 MeV ^{16}O) to A≈150 for the highest TPKE (1635 MeV ^{16}O). The decrease in mass number of the distribution maxima is accompanied with an increase in the overall width and a more pronounced asymmetry with a "spallation-like" tail towards lower masses. The increase in width and asymmetry implies a decrease in slope of the spallation-like tail of the distritoward lower masses (figure 15).

The slopes of the heavy fragment mass yield distribuhave been associated with the nuclear temperature, a smaller slope corresponding to larger average deposition of energy in the target (higher temperature) [59]. Campi, et al. [69] have proposed the relationship:

$$\langle E/A_T \rangle = \frac{10}{(S * A_T)} \quad \text{MeV/A}$$

where S is the inverse logarithmic derivative of $\sigma(A_F)$. The mass yield data presented in figure 15 shows a distinct trend of decreasing slope for the heavy fragment distribution as the total projectile kinetic energy (TPKE) increases from 208 MeV to 1635 MeV. This trend continues to higher energies, seen in the isobaric yields presented in appendix C. The corresponding increase in $\langle E/A_T \rangle$ is from approximately 0.2 MeV/A for 208 MeV ^{12}C to 1.5 MeV/A for 1635 MeV ^{16}O. $\langle E/A_T \rangle$ increases to approximately 1.9 MeV/A for 2.9 GeV ^{12}C induced reactions. An upper limit of $\langle E/A_T \rangle$ = 2.3 MeV/A is observed for reactions induced by 7.7 GeV ^{20}Ne, 20.8 GeV ^{20}Ne, and 33.8 GeV ^{40}Ar. These results suggest that limiting fragmentation is not observed in the intermediate energy regime. (The concept of limiting fragmentation states that product distributions approach limiting forms as the bombarding energy increases.) The results of the firestreak code calculations indicate a trend of increasing excitation energies with increasing projectile energy, however, there is a parallel trend of increasingly broad primary fragment mass distributions which contribute to the broad (and subsequently the smaller slope) heavy fragment distributions for higher energy projectiles.

The decreasing mass number at which the mass yield maxima occurs as a function of increasing projectile energy is likely due, at least in part, to the increasing nuclear temperature. The results of the firestreak calculations predict the heaviest target fragment excitation energies increase from ≈200 MeV at the lowest projectile energies to 1000 MeV at the highest. The heaviest observed nuclides, however, have been attributed to the gentlest of collisions [64,66]

resulting from the smallest amount of transferred mass, not from large mass transfer and subsequent deexcitation.

The increasing width of the heavy fragment yield distributions is due to an increasing excitation energy which will broaden the distribution of deexcited products, and a broadening of the primary fragment distribution (as a result of a variety of mechanisms) which will be reflected in the observed product distribution. The distinctly asymmetric shape of a spallation-like heavy fragment distribution is seen for 1020 MeV ^{12}C and 1635 MeV ^{16}O induced interactions. The increased width of the heavy fragment distribution at 37 MeV/A may be partially attributable to spallation-like events, however, the expected asymmetric nature of the heavy fragment distribution (decreased slope of low-mass side of distribution) is not observed.

From the observed trends in the mass yield curves and previously reported observations [63,64,66], one can conclude that as projectile energy increases the mass of the most probable target fragments decrease from trans-target species, formed by complete and incomplete fusion processes, to primary fragments below the target mass. The fading of the transfer mechanism seems to be rather rapid, evidenced by figure 14, however, at least a small degree of mass transfer is evident in all reactions studied from ≈17 MeV/A to ≈102 MeV/A. The decreasing amount of mass transfer is accompanied by the onset of a high energy spallation-like mechanism (possibly occurring near 37 MeV/A) clearly evident above 85 MeV/A. As the energy of the projectile is increased, the excitation energy deposited into the heavy primary product appears to increase along with the decrease in

mass of the fragment. This study, however, is incapable of measuring the relative extent to which excitation energy and initial primary distributions effect the observed distributions. The heavy fragment distribution is formed by a complex combination of many mass transfer channels and the increasing probability of spallation-type interactions as the projectile energy increases above ≈35 MeV/A.

2b. Fission Yields

The broad peaks at intermediate mass in the mass yield distributions for 208 MeV ^{12}C, 272 MeV ^{16}O, and 442 MeV ^{12}C induced interactions have been previously attributed to fission fragments. Gavron, et al. [68] have recently published cross sections for fission induced in rare earth targets by ^{12}C and ^{16}O at energies similar to the 208 MeV ^{12}C and 272 MeV ^{16}O used in this study. They reported fission cross sections comparable to the values reported in this study, table 10, suggesting that most (or all) of the fragments observed in the intermediate mass peak are from fission events (see below for calculation).

A second identifying feature of the fission mass yield is the full-width at half-maximum (FWHM) of the peak. The FWHM values determined for the fission mass distributions reported in this study are included in table 10. These values are similar to the FWHM ≈ 40 mass units reported by Plasil, et al. for ^{186}Os compound nuclei with E^*=120 MeV [70]. The measured values reported in this study also agree with theoretical FWHM predictions of Nix [71] where FWHM = 41 ± 3 for nuclei with fissility parameters equivalent to ^{177}Ta and ^{181}Re at E^*=195 MeV and 240 MeV, respectively. These results are further evidence that the peaks in the mass yield curves in the mass region of 45 - 120 are mostly (or completely) the result of fission events.

Lower limit reaction cross sections and fission cross sections are presented in table 10. The lower limit of the reaction cross section of a given reaction system is calculated by integrating the area under the respective mass yield curve between the highest mass for which data exists and A=40. The fission cross section was

YIELD DISTRIBUTION SUMMARY TABLE

TPKE	CROSS SECTION (mb) (rxn)	(fis)	%(fis)	YIELD MAXIMA (A-units) Heavy Frag. MAX	FWHM	Fission Frag. CEN	FWHM
208	2680(270)	420(60)	13.3	163(2)	5.5(.3)	82(5)	35(7)
272	2570(260)	570(90)	17.4	165(2)	12(1)	85(5)	35(7)
442	2840(280)*	160(24)*	4.3	148(3)	17(1)	75(5)	46(8)
1020	2850(290)	0	--	150(5)	35(3)	--	--
1635	2970(300)*	0	--	150(5)	39(4)	--	--

A tabulation of heavy fragment and fission yields and parameters describing general aspects of the yield distributions. Uncertainties are noted in parenthesis. The yields for 442 and 1635 MeV data are arbitrary units, uncertainties are relative to the value, not absolute cross section. The %(fis) values represent the measured fission cross section divided by total reaction cross sections from reference 83. The cross sections for 442 MeV ^{12}C and 1635 MeV ^{16}O (marked with *) induced reactions are presented as arbitrary units.

Table 10

calculated by integrating the area under the mass yield curve between masses A=45 and A=120 for reactions induced by 208 MeV ^{12}C, 272 MeV ^{16}O, and 442 MeV ^{12}C. The fission contribution is also expressed as a fraction of the total reaction cross section to facilitate comparisons between the reaction systems. The total reaction cross section was taken from Wilcke, et al. [83] to reduce uncertainties from the methods of calculating isobaric yields and integrating the mass yield curves. There were no fission cross sections calculated for the 1020 MeV ^{12}C + ^{165}Ho and 1635 MeV ^{16}O + ^{165}Ho systems since a fission peak could not be resolved.

The qualitative trend most evident, as a function of projectile kinetic energy, in the data presented in table 10 is the decreasing fission yield for reactions induced by ^{12}C projectiles. (The magnitude of the fission cross section is extremely sensitive to the fissioning system angular momentum [63,68,72-74], therefore, direct comparisons can only be made between reaction systems with the same projectile.) The fraction of interactions resulting in fission decrease significantly between 17 MeV/A and 37 MeV/A (even assuming a 100% uncertainty in the absolute cross sections at 37 MeV/u) and continue to decrease to a small (or nonexistent) level by 85 MeV/A. Similarly for ^{16}O induced interactions, the fission cross section at 17 MeV/A is significant, while, at 102 MeV/A it is nearly (or completely) absent.

The scaling of experimental observables with a characteristic reaction quantity (such as total projectile energy) has been shown to be valid at high energies [76-78]. Many comparisons of intermediate energy reaction observables are compared in terms of relative

projectile velocity (MeV/A); however, this quantity cannot function as a scaling variable. This is evident when comparing the fission cross sections measured for 208 MeV ^{12}C and 272 MeV ^{16}O induced interactions. A greater fission cross section results from ^{16}O than ^{12}C even though the relative velocities of the projectiles are both 17 MeV/A. Many recent publications [79,80] have clearly linked this effect with the angular momentum carried by the projectile.

The fission yields measured in this work can be used to extend the data of Sikkeland [81] above ≈10 MeV/A. The yields measured for 208 MeV ^{12}C, 272 MeV ^{16}O, and 442 MeV ^{12}C induced fission of holmium targets are plotted in figure 17 along with the lower energy data of Sikkeland [81]. The abscissa in these plots is E_{CM}-V, where E_{CM} and V are the center-of-mass and Coulombic energies of the reaction system, respectively. Figure 17 shows the fission cross sections rising steeply after the threshold of sufficient angular momentum and excitation energy are reached. Above ≈10 MeV/A (laboratory frame) the fission yield gradually slows its rising trend and levels off around ≈15-20 MeV/A (laboratory frame) as has been observed elsewhere [68]. The data from this study extends the trend to higher energies where we find the fission yield, as a function of projectile energy, decreases rapidly above ≈40 MeV/A (laboratory frame).

The decrease of the cross section is a good indicator for where the angular momentum begins to decrease. Although excitation energy may be increasing, the effect of excitation energy on the fission probability is small when compared to angular momentum. Using formalisms taken from the JULIAN-PACE deexcitation computer code (see appendix B), the observation is illustrated by the change of the

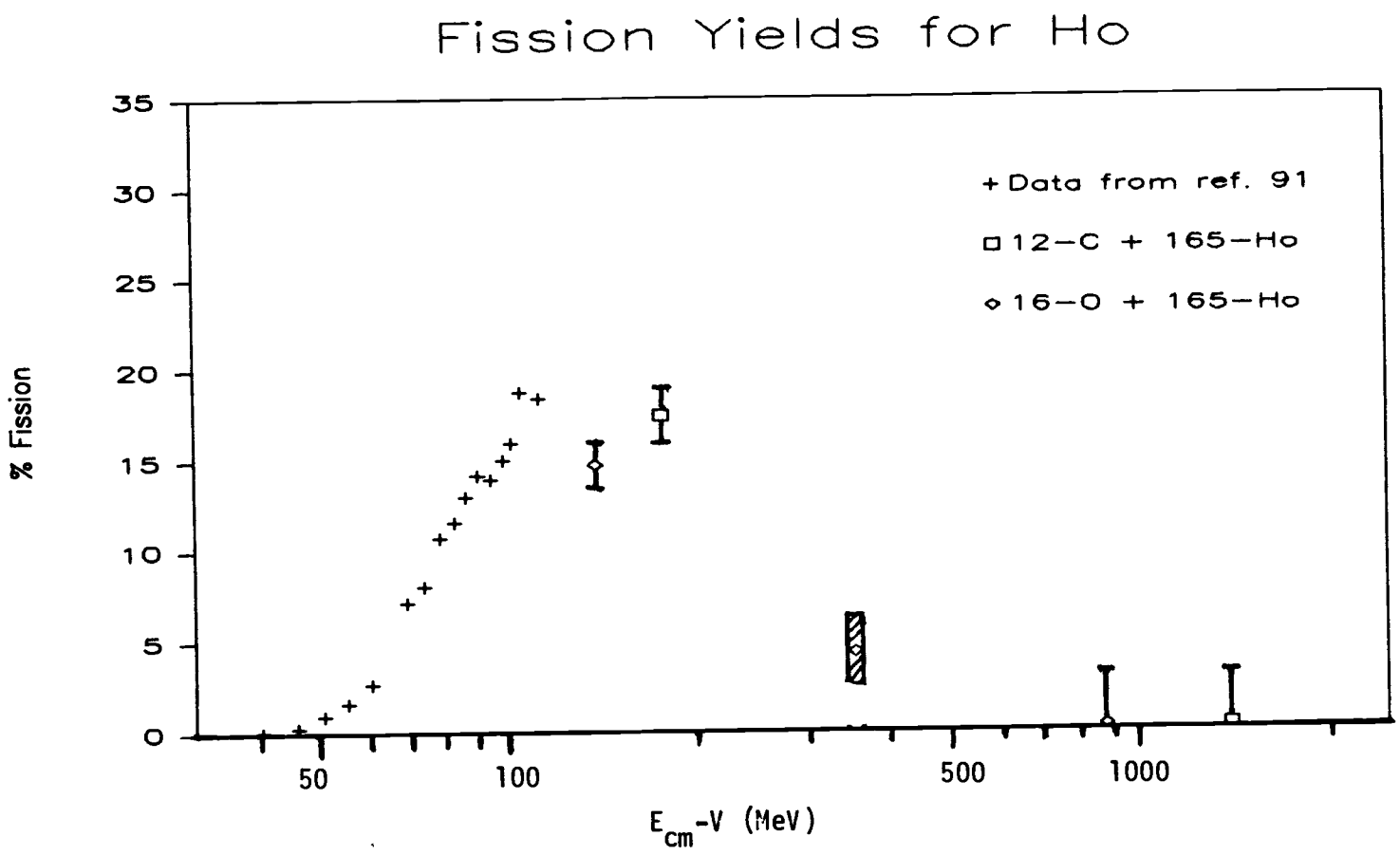

Fission yields plotted as a function of E_{cm}-V. E_{cm} is the center of mass kinetic energy and V the Coulombic energy of the given system. The shaded region represents the uncertainty due to the unknown absolute cross section.

Table 17

calculated fission probability, P(fis), as a function of excitation energy and angular momentum. For the ^{181}Re nucleus with 40 $\hbar$ of angular momentum, the probability of fission increases from about 0.8% for E^*=200 MeV to 2% at E^*=500 MeV. Assuming the same nucleus with 300 MeV excitation energy, the change of P(fis) with angular momentum is demonstrated by P(fis) = 1.2% at 40 $\hbar$, 3.8% at 50 $\hbar$, and 12% at 60 $\hbar$. These results are a good indication that the decreasing fission cross section observed in this study is due primarily to a decrease in angular momentum transferred to the (potentially) fissioning system.

One can approximate the angular momentum trend as a function of the projectile energy by making the assumption that the angular momentum transferred to the fissioning system scales roughly with the linear momentum [68,82]:

$$\frac{P_{par}}{P_{CN}} \propto \frac{\langle l_{sys} \rangle}{l_{crit}}$$

P_{par}/P_{CN} is the fractional longitudinal momentum transfer to the target, and $\langle l_{sys} \rangle$ and l_{crit} are the transferred and critical angular momenta for the given system. The linear momenta for observed fragments were obtained from the systematics of Viola, et al. [36]. These values represent average fractional linear momentum transfer values. The average fractional momentum transfers for the systems are shown in table 11. Included in table 11 is a column representing the $\langle l_{sys} \rangle$ value estimated by equation 5. The l_{crit} values used to determine $\langle l_{sys} \rangle$ values were calculated using values tabulated by

Wilcke, et al. [83] ($l_{crit}\{^{12}C+^{165}Ho\}=57\hbar$ and $l_{crit}\{^{16}O+^{165}Ho\}=68\hbar$). The Wilcke values were used since it has been shown that the Wilczynski sum-rule formalism underestimates calculated l_{crit} values [68,82]. The derived angular momentum limit corresponding to full linear momentum transfer (l_{crit}) reported in reference [82] is equal to the values tabulated by Wilcke.

The $\langle l_{sys} \rangle$ values in table 11 clearly demonstrate the reason no fission events are observed for 1020 MeV ^{12}C and 1635 MeV ^{16}O induced interactions. The probability for fission of a hypothetical nucleus A=180, E^*=500 MeV, and 20 $\hbar$ of angular momentum (resulting from the interaction of 1020 MeV ^{12}C or 1635 MeV ^{16}O with ^{165}Ho) is less than 0.005. The fission probabilities for $\langle l_{sys} \rangle$ = 50 and 60 $\hbar$ are 3% and 12%, respectively, for hypothetical fissioning systems with A=180 and E^*=200 MeV. Although the fission probabilities can not be used as quantitative comparisons to measured ratios of fission to reaction cross sections, the trends are clearly similar. Anticipated fission cross sections at 85 MeV/A or more would be quite small, while above 20 MeV/A one would expect appreciable fission cross sections (especially from high-l tails of realistic angular momentum distributions).

DEDUCED MOMENTUM TRANSFERS

TPKE (MeV)	208	272	442	1020	1635
P_{par}/P_{CN}	0.90(9)	0.9(1)	0.76(9)	0.43(7)	0.32(8)
$\langle l_{sys} \rangle$ ($\hbar$)	51	61	43	24	21
σ(fis)	13.3	17.4	4.3	--	--

A tabulation of the deduced fractional linear momentum transfer, P_{par}/P_{CN}, and angular momentum transfer, $\langle l_{sys} \rangle$, to the target nucleus for the interactions studied. Fission cross sections are included for comparison.

Table 11

B. PHENOMENOLOGICAL MODEL PREDICTIONS

Two phenomenological models of intermediate energy nucleus-nucleus collisions have been chosen to predict observables for comparison to measured values in an attempt to understand significant features of the data. The first of these models is the Wilczynski generalized sum-rule model [11,12]. The sum-rule model calculations were only used for the three lower energy systems. Gavron, et al. [68] and Loveland, et al. [84] found large discrepancies between experimental yield distributions and those calculated with the Wilczynski formalism for projectile energies above 45 MeV/A. Natowitz, et al. [39] report observing a projectile fragmentation mechanism for 43 MeV/A ^{20}Ne entirely analogous to that observed at relativistic energies. They report the onset of fragmentation occurs when the projectile velocity becomes comparable to the Fermi velocity in the projectile. Natowitz also reports particle emission not characteristic of either a fragmentation or compound nucleus source with similar systematics of non-equilibrium particle emissions reported by Awes, et al. [89,90]. The Wilczynski sum-rule model allows only complete and incomplete fusion reaction channels with projectile energy only affecting the incident channel wavelength. The Wilczynski model would not be applicable for reactions with significant participation of fragmentation-like interactions.

The data are also compared with the predictions of the nuclear firestreak model [30,91]. The firestreak calculation was used to predict primary target fragment distributions for all experimental

systems investigated. Unlike the sum-rule model, the firestreak model can duplicate fusion reactions (capture of the projectile or a fraction thereof) as well as spallation-like interactions. The details of the firestreak and Wilczynski sum-rule models and the specific implementations are discussed in appendix B.

The Wilczynski sum-rule and firestreak models are both interaction models which predict aspects of the primary fragment distributions. Two different formalisms were used to calculate the deexcitation path of the primary target fragments yielding predicted distributions which are compared to those measured in the laboratory. The first is a version of the DFF code [53], and the second is the JULIAN-PACE code [75]. The significant difference between these calculations is that the JULIAN-PACE code includes the effects of angular momentum, whereas, the DFF code does not. The JULIAN-PACE code could only be used to calculate the deexcitation for the three lower energy reaction systems due to limitations of the computer code implementation. The DFF code was used for all five systems. Further discussion and details about the deexcitation formalisms and specific implementations used are contained in appendix B. This remainder of section compares the results of the two reaction model calculations to the data and also discusses the effects of the two deexcitation codes.

1. Deexcitation Parameters and Procedures

The DFF code has been widely used to predict the deexcitation path of various calculated primary target fragment distributions for relativistic heavy ion and high energy proton induced interactions in

heavy mass targets [27,77,78,84]. This study involves primary fragment distributions with significantly different characteristics from those which the DFF code has been used. The average angular momentum transferred to the target fragment is expected to be as high as 68 hbar, and the tail of the angular momentum distributions are expected to exceed 80 hbar [12]. The fission barrier is predicted to vanish for nuclei near ^{165}Ho with $\geq$80 hbar angular momentum. Deexcitation calculations which do not correct barriers for the angular momentum are clearly unrealistic for nuclei with high angular momenta. Discussion of fission fragment distributions for 208 MeV ^{12}C, 272 MeV ^{16}O, and 442 MeV ^{12}C induced interactions, therefore, is generally limited to distributions for which the fragments resulting from interactions induced by >80 MeV/A where angular momentum transfer is expected to be relatively small (<20 hbar).

Prior to the deexcitation calculations the variable fission parameters, B_f (the fission barrier energy) and a_f/a_n (the ratio of saddle to equilibrium level density parameters), were determined. The parameters were determined by matching calculated fission cross sections to accurately measured values. The codes were used to calculate the fission yields of highly excited compound nuclei in the mass region specific to this study (A≈180). The parameters affecting fission were varied until the calculated and measured fission cross sections matched within experimental error. A common technique [70,88] for determining the fission parameters was to choose a constant multiplier, M, by which to multiply the C-P-S rotating liquid drop fission barrier [92] (B_{RLD}), then vary a_f/a_n until the

measured fission cross section equals the predicted value. Common values of M varied from 0.6 to 1.0 and a_f/a_n varied from 1.00 to 1.2.

Recent work has attempted to determine absolute fission barriers, the quantitative dependence on angular momentum, and realistic values for the ratio of level density parameters. The ratio of level density parameters, a_f/a_n at high excitation energies is generally expected to be close to 1.00±0.01 [72,73]. The values used in the calculations performed in this study were allowed to vary between 1.00 and 1.01. The fission barrier, B_f parameter, and its dependence on angular momentum, is the second major factor determining the calculated fission yield. A consistent description of the fission barrier was determined by empirically matching measured fission cross sections of well understood interaction systems with predicted fission cross sections calculated by the JULIAN-PACE code. The JULIAN-PACE code includes a Bass model subroutine [75] which was used to calculate the complete fusion cross section. Reaction system data and measured σ(fis), taken from references [72,81] are tabulated in table 12 with final values of B_f, a_f/a_n, and calculated σ(fis). The fission barrier is expressed as the Cohen-Plasil-Swiatecki rotating liquid drop barrier, B^{RLD}, multiplied by a scaling factor.

Recent attempts have been made to directly calculate absolute fission barriers by including the "finite range" corrections suggested by Krappe, Nix and Sierk [93]. The fission barriers, including finite range corrections scaled to angular momentum, calculated by Blann, et al. matched empirically determined fission barriers within ≈1 MeV [13]. The results of the calibration

FISSION BARRIER COMPARISONS

Reaction System	Meas. (fis)	Calc. (fis)	M	$B_f(0)$	a_f/a_n
100 MeV ^{12}C + ^{174}Yb	19.4	40.9	0.8	16.97	1.01
100 MeV ^{12}C + ^{174}Yb	19.4	29.2	0.85	18.03	1.01
100 MeV ^{12}C + ^{174}Yb	19.4	14.6	0.9	19.09	1.01
134 MeV ^{16}O + ^{165}Ho	263.	251.2	0.9	19.69	1.01
140 MeV ^{16}O + ^{170}Er	294.	456.4	0.8	16.97	1.01
140 MeV ^{16}O + ^{170}Er	294.	361.5	0.85	18.03	1.01
140 MeV ^{16}O + ^{170}Er	294.	278.7	0.9	19.09	1.01
166 MeV ^{16}O + ^{165}Ho	530.	463.7	0.9	19.69	1.01

Tabulation of calculated and measured fission yields as a function of fission barrier and level density parameters. The measured cross sections are taken from references 81 and 90. The JULIAN-PACE code was used to calculate fission yields with ground state fission barrier $B_f(0) = M*B_f$ and ratio of level densities parameter: a_f/a_n. Energies are expressed in the laboratory frame.

Table 12

procedure used in this study (table 12) indicate the best fission barrier is $0.90*B_{RLD}$ used with a ratio of level densities parameter $a_f/a_n=1.01$ The fission barrier generated by multiplying the C-P-S barrier by a constant factor, $B_f= 0.90*B_{RLD}$, is found to be within 1 MeV (the observed discrepancy for the finite range corrected barriers [13]) of recently calculated barriers including finite range corrections [13,94]. The deexcitation calculations for this work used the empirically determined parameters for two reasons: they agreed reasonably well with recent theoretical predictions and this combination of fission parameters fit the measured fission cross sections in the mass region around A=180 better than the Sierk barriers (which included finite range corrections [72,94] with a_f/a_n approximately 1.0.

The philosophy used in the deexcitation of the primary fragments produced by the firestreak and Wilczynski sum-rule codes was that one should use parameters which reproduced data for studies where the reaction was well understood. The fission parameters $B_f=0.90*B_{RLD}$ and $a_f/a_n=1.005\pm.005$ were used for all deexcitation calculations with both codes. Arbitrarily varying these parameters to fit the measured data of a poorly understood reaction system would only be an exercise in numerology and would not yield information about the validity of the models themselves.

2. Reaction Yield Comparison

A complete summary of calculated and measured yields are presented in table 13. The measured percent fission cross section represent the observed fission cross section divided by the total reaction cross section published in reference 83. The tabulated cross sections calculated by the firestreak and sum-rule codes represent only "transmutation" events (elastic scattering events have been omitted). The model calculated σ(tot) values represent, therefore, a lower limit of the reaction cross section causing the "percent fission" to be an upper limit value. This should be noted when comparing calculated and measured percent fission quantities.

Inspection of values tabulated in table 13 shows the reaction cross sections calculated by the sum-rule model are extremely small. This observation was expected since the sum-rule model is known to underestimate l_{crit} [82].

REACTION AND FISSION CROSS SECTIONS
SUMMARY AND COMPARISON

TPKE(MeV):		208	272	442	1020	1635
MODELS:						
FSTRK	σ(rxn):	3341	3480	3346	2989	3113
+	σ(fis):	4	67	45	--	--
DFF	%(fis):	0.1	1.1	1.3	--	--
WILCZ.	σ(rxn):	1808	2546	1041		
+	σ(fis):	2	64	13		
DFF	%(fis):	0.1	2.5	1.3		
FSTRK	σ(rxn):	3341	3480	3346		
+	σ(fis):	27	161	29		
J-P	%(fis):	0.8	4.6	0.9		
WILCZ.	σ(rxn):	1808	2546	1041		
+	σ(fis):	55	202	24		
J-P	%(fis):	3.0	7.9	2.2		
MEAS.	σ(fis):	420	570	160	--	--
	%(fis):	13.3	17.4	4.3	--	--

Comparison of measured and calculated yields. Measured cross sections for 442 MeV and 1635 MeV data are tabulated as arbitrary values. The %(fis) values were calculated by dividing the measured fission cross sections by total reaction cross sections from reference 83.

Table 13

3. Fission Yield Comparisons

The fission cross sections predicted for primary distributions deexcited by the DFF code are significantly lower than those predicted by the JULIAN-PACE calculation for all reaction systems. This dramatizes the importance of including the angular momentum in the calculation of fission yields (through the effect on the fission barrier height) for reactions induced in holmium by intermediate energy heavy ions.

The fission yields predicted by the firestreak model (deexcitation calculated by the JULIAN-PACE) are significantly less than the measured yields. The observed fraction of yield which fissions is 5 to 20 times greater than predicted by the firestreak model. The fission yields predicted by the sum-rule model are also substantially less than measured yields, however, they are also larger than (2 to 4 times) the values predicted by the firestreak model. The low fission yields predicted by the Wilczynski sum-rule model were expected based on the previous findings that the model underestimated the angular momenta transferred to primary fragments [68,82]. The results of Huizenga, et al. [82] indicate the l_{crit} values calculated in the sum-rule model are factor of ≈7/5 too small. Gavron, et al. [68] reported fission cross sections calculated by the sum-rule model underestimated measured values by a factor of 10 for 315 MeV ^{16}O + ^{142}Nd. Gavron attributed this observation to insufficient transfer of angular momentum in the initial interaction.

The magnitude of l_{crit} is extremely important but the shape of the angular momentum distribution was found to be the major factor determining the calculated fission yield for the reactions studied in

this work. Most calculated fission events occur for the primary fragments which make up the high-l tail of the angular momentum distribution for a given fragment. Two examples of the sum-rule generated angular momentum distributions for typical reaction channels are shown in figure 18. When the primary distributions predicted by the firestreak and sum-rule models are deexcited by the JULIAN-PACE code, substantial differences between fission cross sections are observed (table 13). Inspection of the primary fragment distributions indicate very similar excitation energies for all fragments and the average angular momentum transfer calculated by the two reaction models was similar. The firestreak code divides the calculation into impact parameter bins effectively generating a sharp cuating a sharp cut-off angular momentum distribution. The sum-rule code, on the other hand, smooths the angular momentum distribution cut-off by adding the "transmission coefficients", T_l [95]. The resulting high-l tail of the distribution represents primary fragment cross section having significantly enhanced fission probability. This tail is not reproduced by the firestreak calculation (i.e. for the (^{16}O,^{4}He) channel: l_{max}(sum-rule) = 62 $\hbar$, l_{max}(firestreak) = 55 $\hbar$, and $\langle l(\text{sum-rule})\rangle \simeq \langle l(\text{firestreak})\rangle \simeq 46\ \hbar$) and represents the increased sum-rule fission yields observed for these fragments. Thus, calculated fission yields can be greatly altered not only by increasing l_{crit} (and thereby $\langle l\rangle$), but also by changing the shape of the angular momentum distribution.

The trend of the measured fission yields for reactions induced by ^{12}C projectiles has been shown in section A, above, to reach a maximum value for ≈17 MeV/A and then decrease substantially (by a

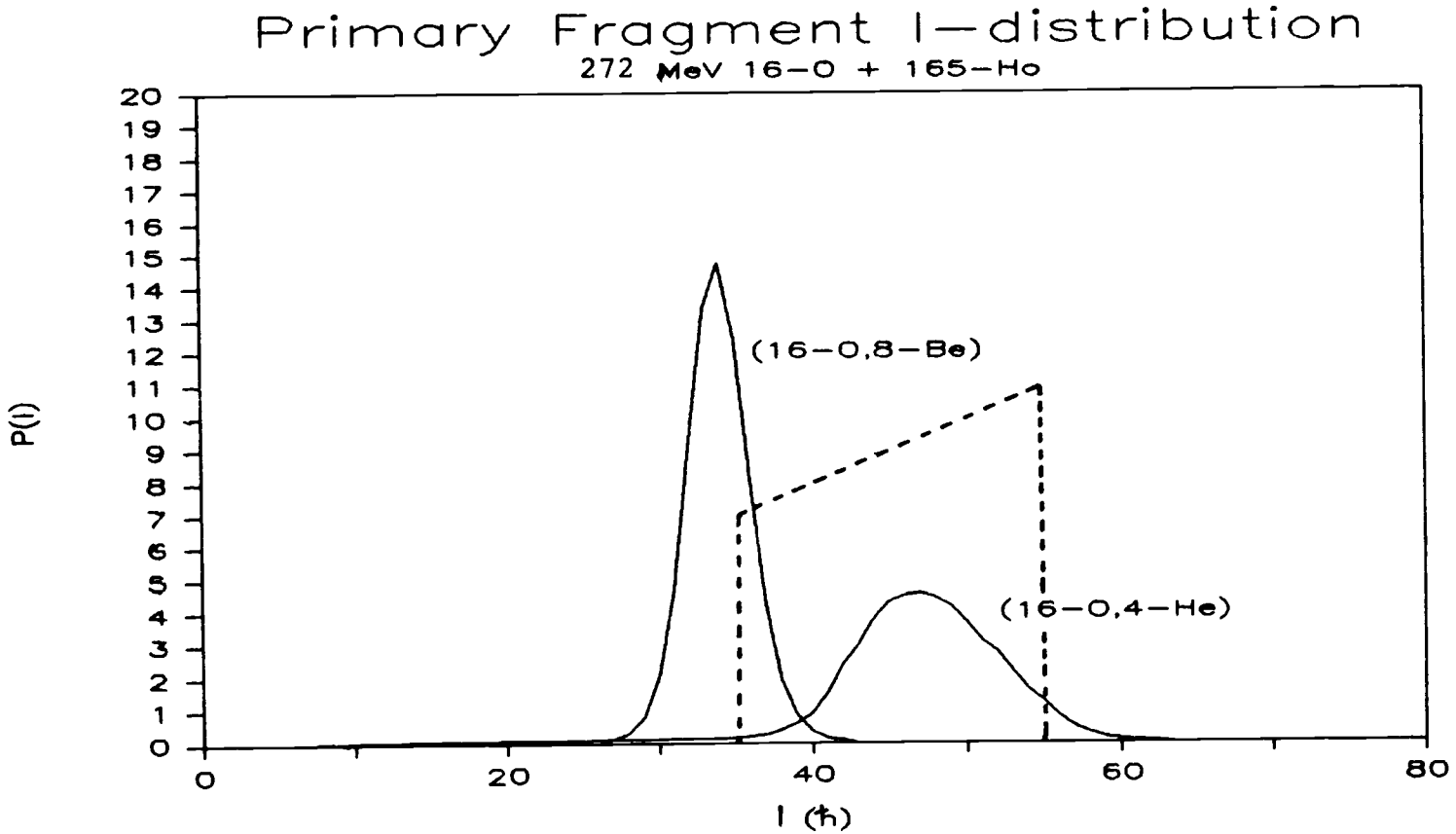

Angular momentum probability distribution for two typical primary products (^{177}Ta and ^{173}Lu) generated by the sum-rule code for the interaction of 272 MeV ^{16}O + ^{165}Ho. The distribution generated by the firestreak code for ^{177}Ta is also included for comparison (dashed line).

Figure 18

factor of between two and four, accounting for the 50% uncertainty in absolute cross sections) for 37 MeV/A ^{12}C. No fission cross section was observed for 85 MeV/A ^{12}C. The fission yield measured for the 272 MeV ^{16}O + ^{165}Ho system was at least 25% greater than for the 208 MeV ^{12}C induced reactions. This is attributable to the increased angular momentum and excitation energy available [68-70] and the increased fissility of the compound system [70,92]. The trend for the calculated fission yields decreases between 17 MeV/A and 37 MeV/A by less than 40% in the case of the sum-rule primary distribution. There is no apparent decrease in fission yield predicted by the firestreak model calculation.

The total calculated fission cross section was found to result from the fission of several channels. The major contribution from the sum-rule primaries came from the large complete fusion cross section which accounted for >90% of the calculated fission yield for 208 MeV ^{12}C and 272 MeV ^{16}O induced interactions, decreasing to ≈75% for 442 MeV ^{12}C induced fission. The remainder of the fission yield originated from the (HI,n), (HI,p), and (HI,α) channels. The sum-rule model is known to overestimate the complete fusion cross section [64] resulting in a overestimate of the fission cross section contribution from this reaction channel. The firestreak model yielded a more even distribution of primaries resulting in a wider variety of channels contributing to the fission yield. The major channels which led to fission were: complete fusion, (HI,n), (HI,p), (HI,np), (HI,p2n), and (HI,α). These channels accounted for ≥92% of the fission cross section for the three lowest energy systems. The completely fused system predicted by the firestreak model accounted

for 73%, 50%, and 33% of the fission yields for the 208 MeV ^{12}C, 272 MeV ^{16}O, and 442 MeV ^{12}C induced reactions, respectively. An increasing contribution to the fission from incomplete fusion primaries is suggested by the decreasing values of P_{par}/P_{CN} in previous observations [68,69].

All efforts, within the philosophy expressed above, to more accurately reproduce the observed fission yields from the calculated primary distributions failed. The measured fission cross section for the 208 MeV ^{12}C + ^{165}Ho and 272 MeV ^{16}O + ^{165}Ho (and possibly 442 MeV ^{12}C) systems are greater than any of the calculated fission yields. The Wilczynski sum-rule primary distributions deexcited by the JULIAN-PACE code yield the largest fission yields; however, still underestimate the measured values by factors between roughly 3 and 5. Numerological exercises were performed to force fit the data. All three of the observed fission cross sections can be independently fit by JULIAN-PACE deexcitation of primary fragment distributions given an allowable range of input fission parameters: B_f=0.75-0.90*B_{RLD} and a_f/a_n=1.05-1.10. This range of parameters has previously been used to reproduce data with calculated yields [70,91, 96]. Recently, strong arguments have been presented that for very high excitation energies, values of a_f/a_n>1.02 are unrealistic [72,73,75], suggesting that the primary angular momentum distributions are in error and not the deexcitation parameters or formalism.

Gavron, et al. [68] recently compared the results of predicted fission cross sections to measured values for reactions induced in several targets by ^{12}C and ^{16}O with energies up to 24 MeV/A. They report results of calculated fission cross sections which are greater

than measured values. The assumption was used that only the complete fusion channel contributed to the fission yield. The complete fusion cross section was given by the Bass cross section. The Bass model was shown to overestimate the complete fusion cross section by including partial waves which contributed to incomplete fusion channels. The results from calculated fission cross sections were in good agreement with the data for ^{238}U targets because the partially fused systems still had high fissility. The calculated fission cross sections for lighter targets, however, were overestimated since the partially fused systems were far less likely to fission. We have used the Bass model to calculate the complete fusion cross section for 17 MeV/A ^{16}O + ^{165}Ho. Assuming a simple (2l+1) angular momentum distribution, $a_f/a_n=1.01$, and $B_f(0)=0.9(B_f)$ the JULIAN-PACE deexcitation code predicts a fission cross section of 595 mb. This value is in generally good agreement with the measured value, overestimating it by only about 5%.

A brief summary of the above comparison between calculated and measured fission yields is that both the Wilczynski sum-rule and firestreak interaction models probably underestimate the angular momentum (or at least the tail of the distribution) transferred to the target fragment. The similarity in average transferred angular momentum and the extremely large differences between fission cross sections predicted by the sum-rule and firestreak models (especially for the 208 MeV ^{12}C + ^{165}Ho system) suggests that the shape of the calculated angular momentum distribution may be incorrect as predicted by the firestreak model.

4. Heavy Fragment Yield Comparisons

Calculated heavy fragment distributions were found to agree with the general conclusion that a significant fraction of the observed trans-target yield resulting from 208 MeV ^{12}C and 272 MeV ^{16}O induced interactions (17.3 MeV/A and 17.0 MeV/A, respectively) are from completely fused systems [64,68]. The Julian-Pace code was used to calculate the possible effects of deexcitation of ^{177}Ta (from 208 MeV ^{12}C + ^{165}Ho) and ^{181}Re (from 272 MeV ^{16}O + ^{165}Ho) excited nuclei. The results indicated significant production probability for deexcited trans-target nuclides with masses to A≈168 (14%) and A≈170 (15%) originating from ^{177}Ta (E^*=171 MeV) and ^{181}Re (E^*=200 MeV), respectively. Approximately 45% of the total calculated trans-target yield resulted from complete fusion events. Similar calculations were performed for 442 MeV ^{12}C, 1020 MeV ^{12}C, and 1635 MeV ^{16}O induced reactions with holmium targets. No trans-target nuclides were predicted to survive, regardless of initial origin. This observation disagrees with the experimental results. Although the heaviest predicted factions are the result of the "softest" collisions, too much excitation energy is transferred to allow the survival of any trans-target nuclides.

Although the complete fusion mechanism may be predominantly responsible for the production of the observed trans-target nuclides for interactions induced by projectiles between 15 and 20 MeV/A, the nuclides with $Z > Z_{target}$ observed for interactions induced by projectiles above 30 MeV/A are probably not primarily a result of complete fusion, rather of incomplete fusion processes. The incomplete fusion mechanism is responsible for the production of

observed trans-target nuclides throughout the intermediate energy region (17.0 MeV/A to 96 MeV/A). The role of incomplete fusion processes in this energy regime is also interpreted as a decreasing trend with increasing projectile energy, however, still evident at 100 MeV/A.

The heavy fragment yield distributions generated by the various model calculations discussed above were found to be identical for 208 MeV ^{12}C and 272 MeV ^{16}O induced reactions. The various calculated distributions for the 442 MeV ^{12}C + ^{165}Ho reaction system are presented in figure 19. The mass axis has been significantly expanded to emphasize differences in the various distributions. The smaller Wilczynski peak magnitudes are a result of the smaller total "reaction" cross sections, discussed previously in section 3a.

The heavy fragment yield distributions calculated for 442 MeV ^{12}C induced interactions are distinctly different. The final distributions calculated by the JULIAN-PACE code are significantly broader than those generated by the DFF code. This observation can be explained by the combined effect of angular momentum and excitation energy on the particle emission widths. Large fragment angular momenta and excitation energies are known to enhance the emission probability of particles heavier than neutrons [86,87], such as deuterons, tritons, and alphas. The heavier particles remove smaller amounts of energy per emitted nucleon than lighter ones resulting in a generally lower-mass final distribution of fragments.

The JULIAN-PACE deexcitation of ^{177}Ta, E^*=345 MeV, and $\langle l \rangle$=39.8 $\hbar$ is an example of this effect. The average calculated energy removed by the neutron was 16.9 MeV, and for the alpha was 30.5 MeV.

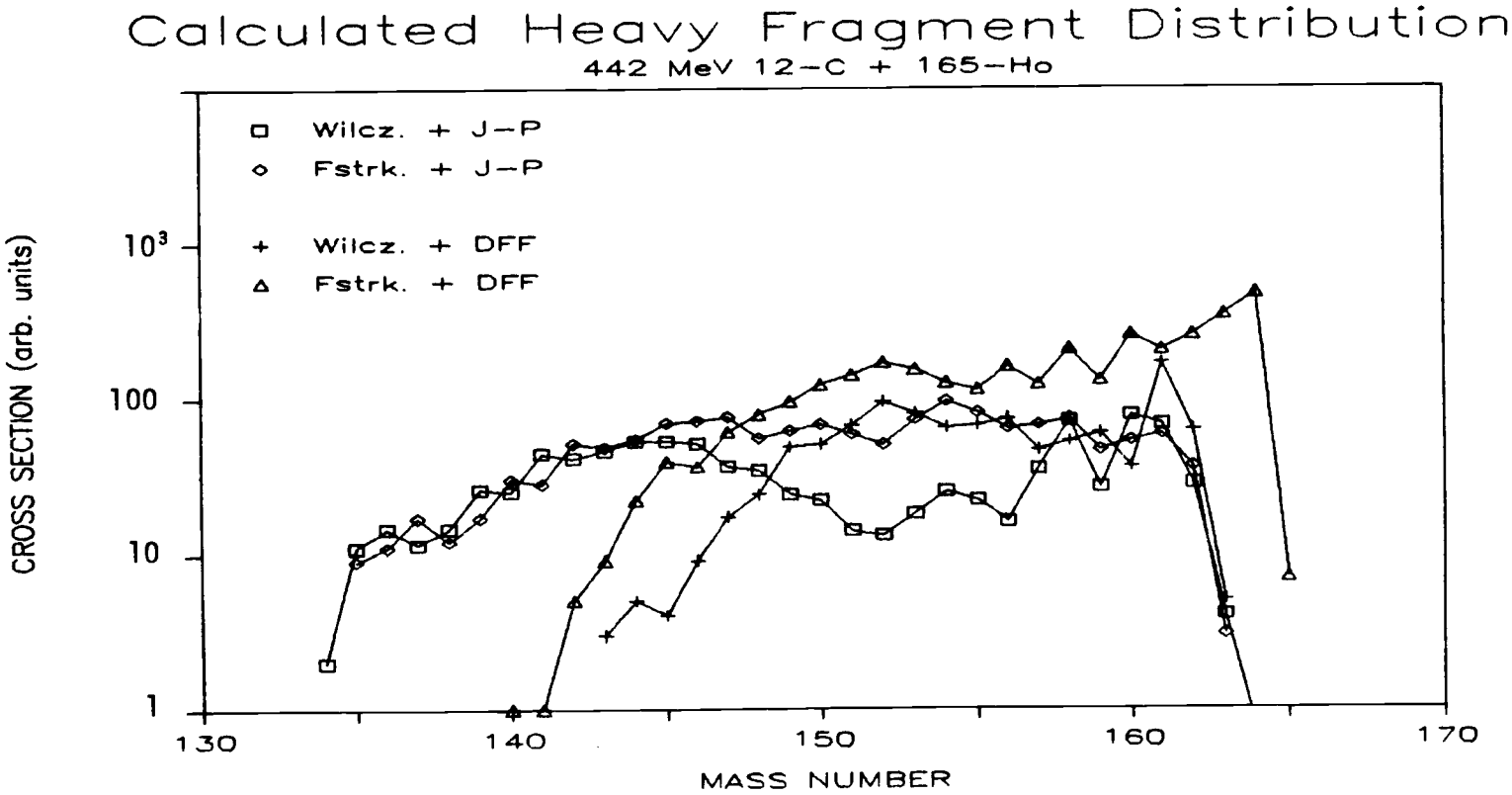

Heavy fragment isobaric yields calculated using various combinations of interaction and deexcitation codes for reactions induced by 442 MeV carbon.

Figure 19

The overall probability of emitting an alpha particle from the above excited ^{177}Ta nucleus is 38%; while for the same nucleus with E^*=182 MeV, and $\langle l \rangle$=44.2 $\hbar$ the probability is only 7.3%. Figure 20 shows the final product distribution resulting from the deexcitation of ^{177}Ta, E^*=345 MeV, and $\langle l \rangle$=39.8$\hbar$ calculated by both the JULIAN-PACE and DFF codes. The final product distribution calculated by the JULIAN-PACE code is broader (with a smaller slope on the low-mass side of the distribution) and peaks at a lower mass number than the distribution calculated with the DFF formalism. The widths may be approximated by fitting the distributions with a normal curve. The full-width at half-maximum (FWHM) are estimated to be 8.7 and 6.5 mass units for the final product distributions calculated by the JULIAN-PACE and DFF codes, respectively. The full-width at quarter-maximum (FWQM) for the same distributions are 12.5 and 9.4 mass units. The requirement of large angular momentum and high excitation energy for significant heavy particle emission is the reason heavy fragment distributions calculated by the JULIAN-PACE code for 208 MeV ^{12}C and 272 MeV ^{16}O induced reactions are not obviously broader than those calculated by the DFF code. This effect is illustrated in figure 20, where the final product distribution resulting from the deexcitation of ^{177}Ta, E^*=182 MeV, and $\langle l \rangle$=44.2$\hbar$ calculated by both the JULIAN-PACE and DFF codes are shown. For primary distributions with low to intermediate excitation energy or relatively low angular momentum, the DFF code would be expected to calculate heavy fragment distributions which are generally the same as the JULIAN-PACE code. These model calculations suggest that the width and the slope of the heavy fragment distribution are affected

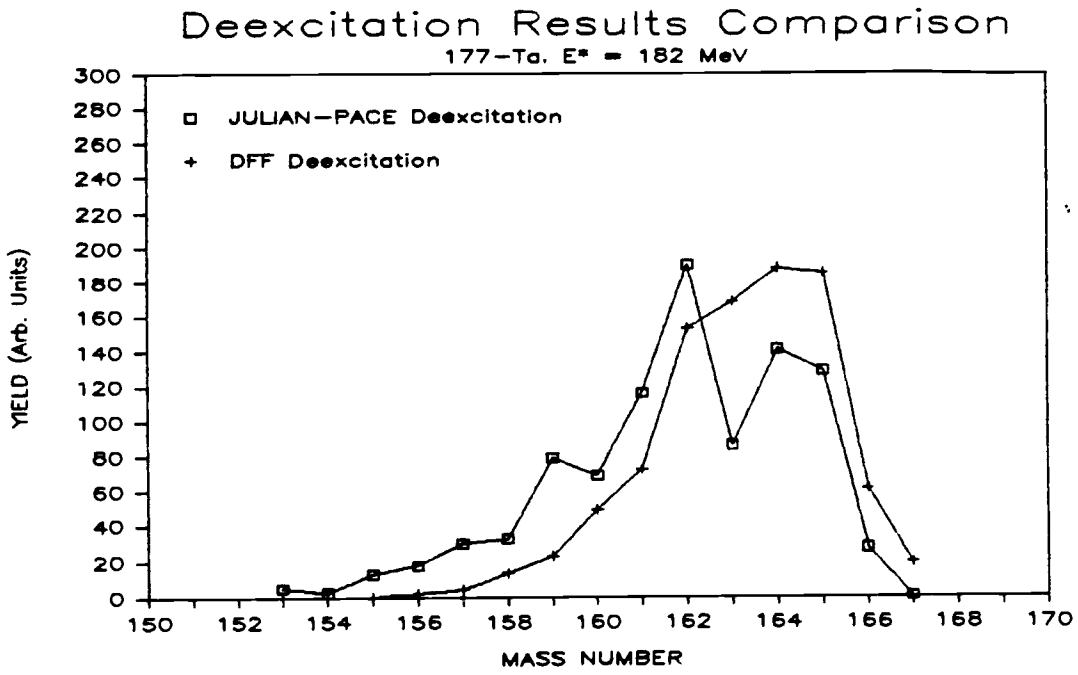

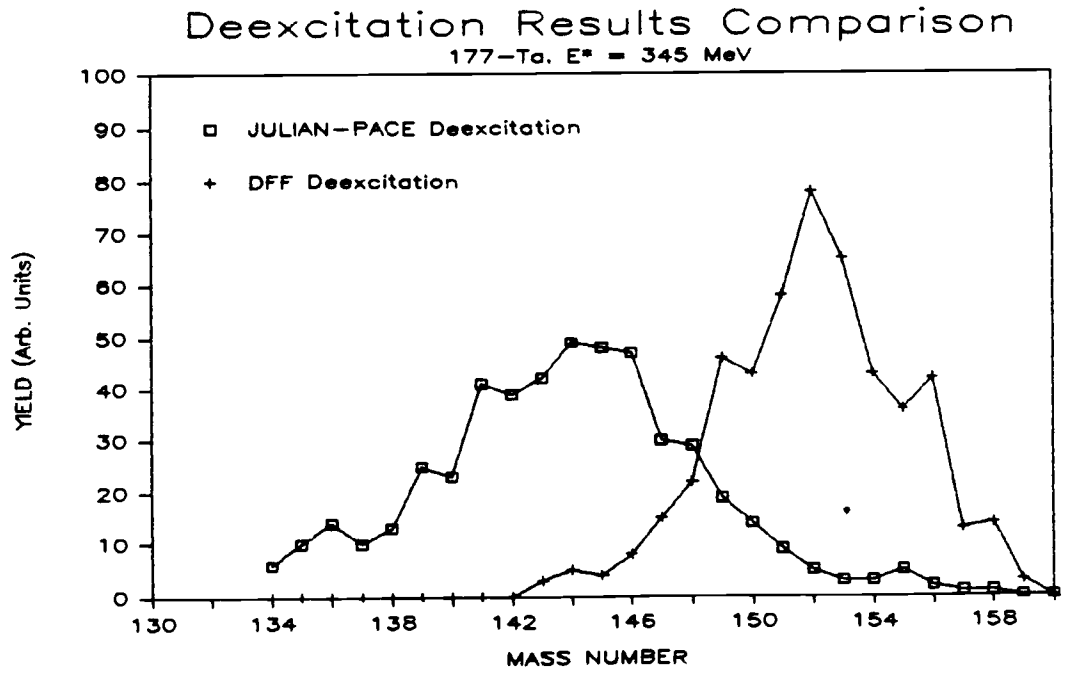

Comparitive deexcitation results of ^{177}Ta with 182 MeV excitation energy and <l> = 44$\hbar$ (upper frame) and with 345 MeV excitation energy and <l> = 40$\hbar$ (lower frame).

Figure 20

by a combination of the primary fragment excitation energy and angular momentum.

A great deal of attention was devoted to the differences between the calculated heavy fragment distributions in the preceding discussion; however, the outstanding feature is the similarity of these results. The following discussion compares measured heavy fragment distributions to the general features of the theoretical curves. The heavy fragment data are plotted with the model predictions in figures 21-25. The predicted distributions for the two lowest energies are represented by a single average distribution because of the general similarity of the different curves.

The observed heavy fragment distribution width increases and the slope of the low-mass side of the distribution decreases with increasing projectile kinetic energy. This general trend is duplicated by the calculated heavy fragment distributions. More specifically, the data are well represented by model calculations for interactions induced by 1020 MeV ^{12}C and 1635 MeV ^{16}O projectiles. The width of the measured heavy fragment distribution for the 208 MeV ^{12}C + ^{165}Ho is slightly underestimated, becoming more severe for the 272 MeV ^{16}O + ^{165}Ho system. The sumrule and firestreak models (deexcited by the JULIAN-PACE code) adequately predict the general heavy fragment distribution for 442 MeV ^{12}C induced interactions. The sum-rule model, however, predicts a significant valley near mass number 155 which is not observed. The final distributions resulting from the DFF deexcitation calculation are significantly narrower than the results measured for 442 MeV ^{12}C induced interactions. General features of the measured heavy fragment distribution at higher

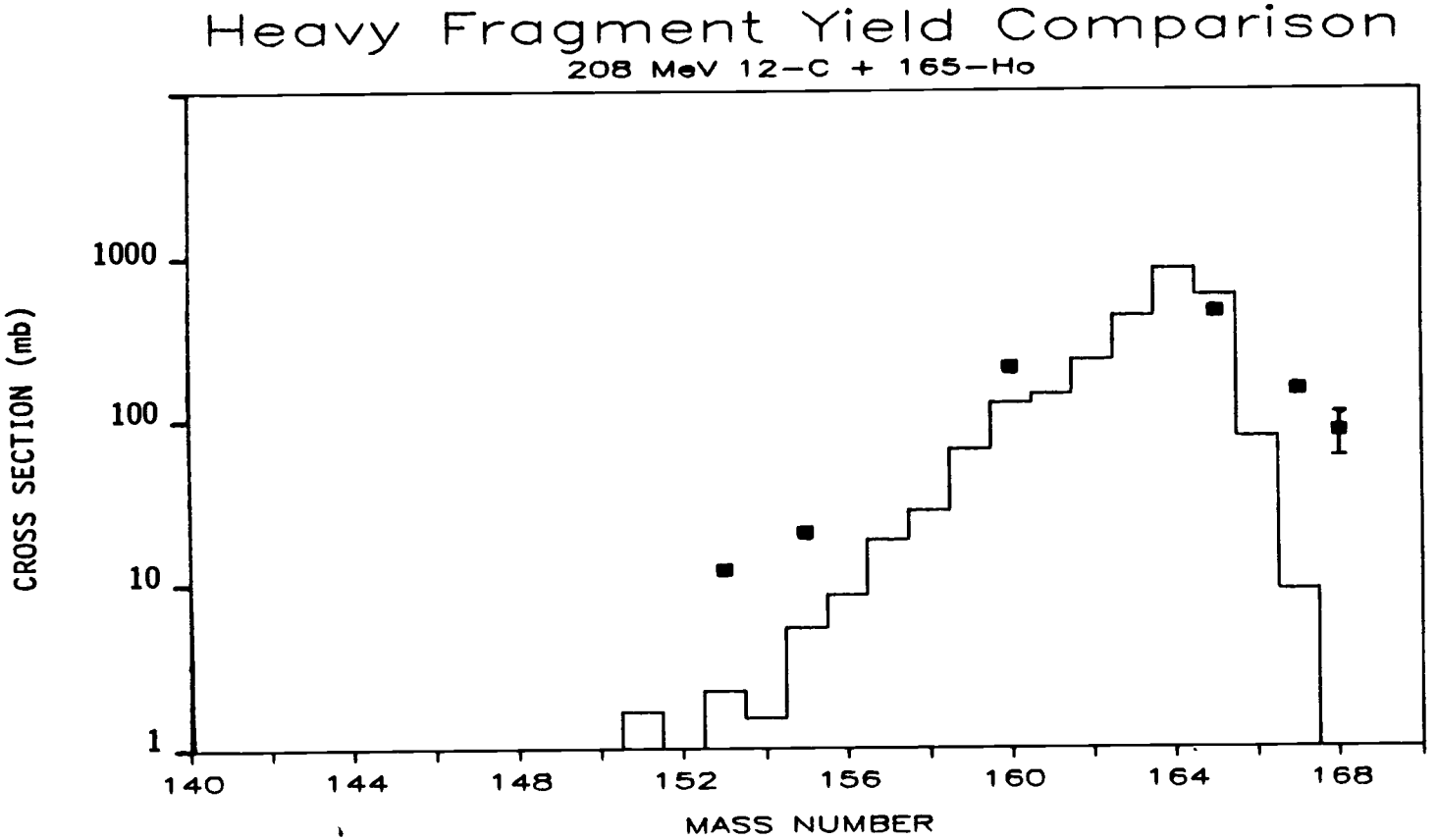

Comparison plot of measured heavy fragment isobaric yields (filled squares) and an average calculated heavy fragment distribution (step curve).

Figure 21

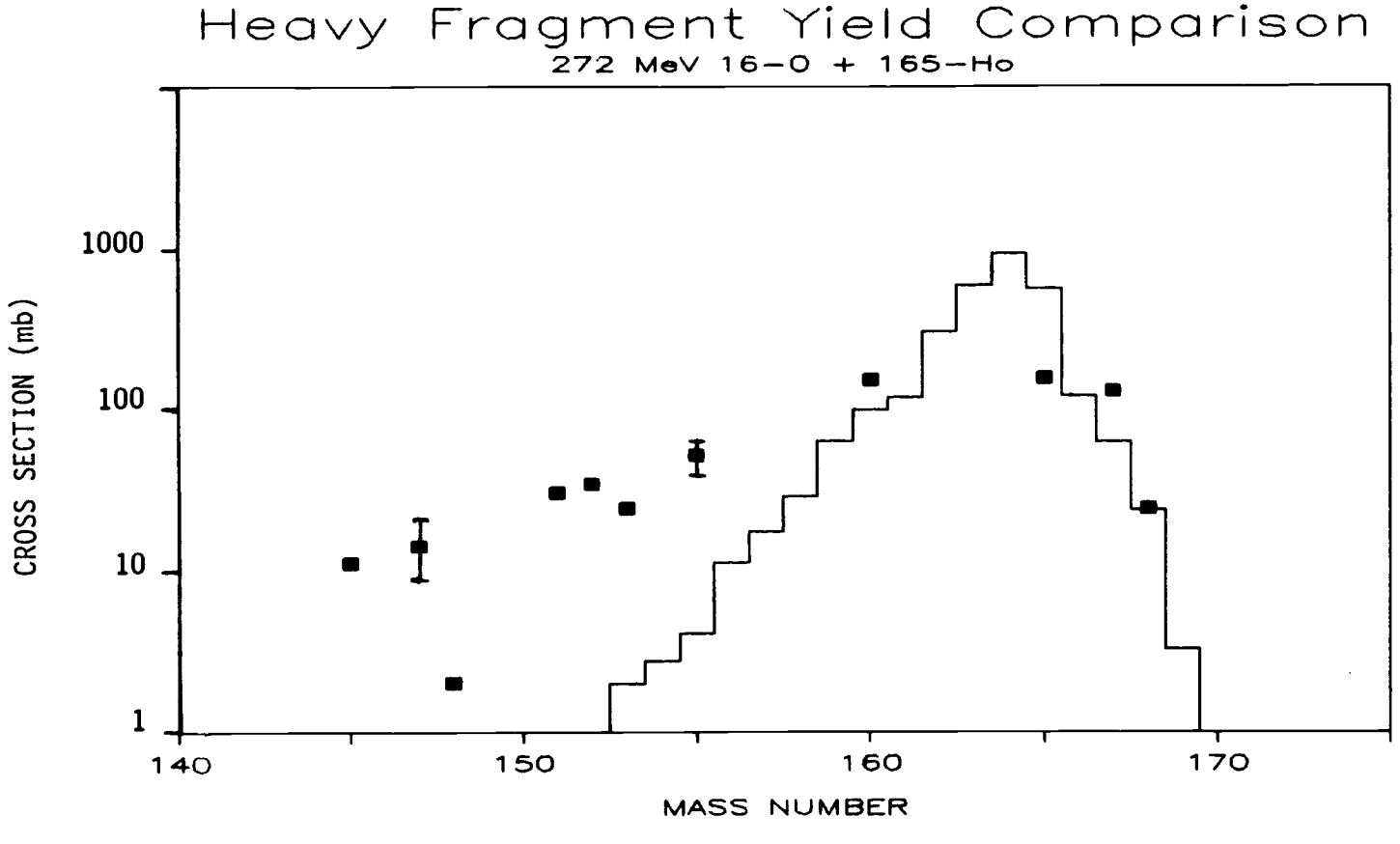

Comparison plot of measured heavy fragment isobaric yields (filled squares) and an average calculated heavy fragment distribution (step curve).

Figure 22

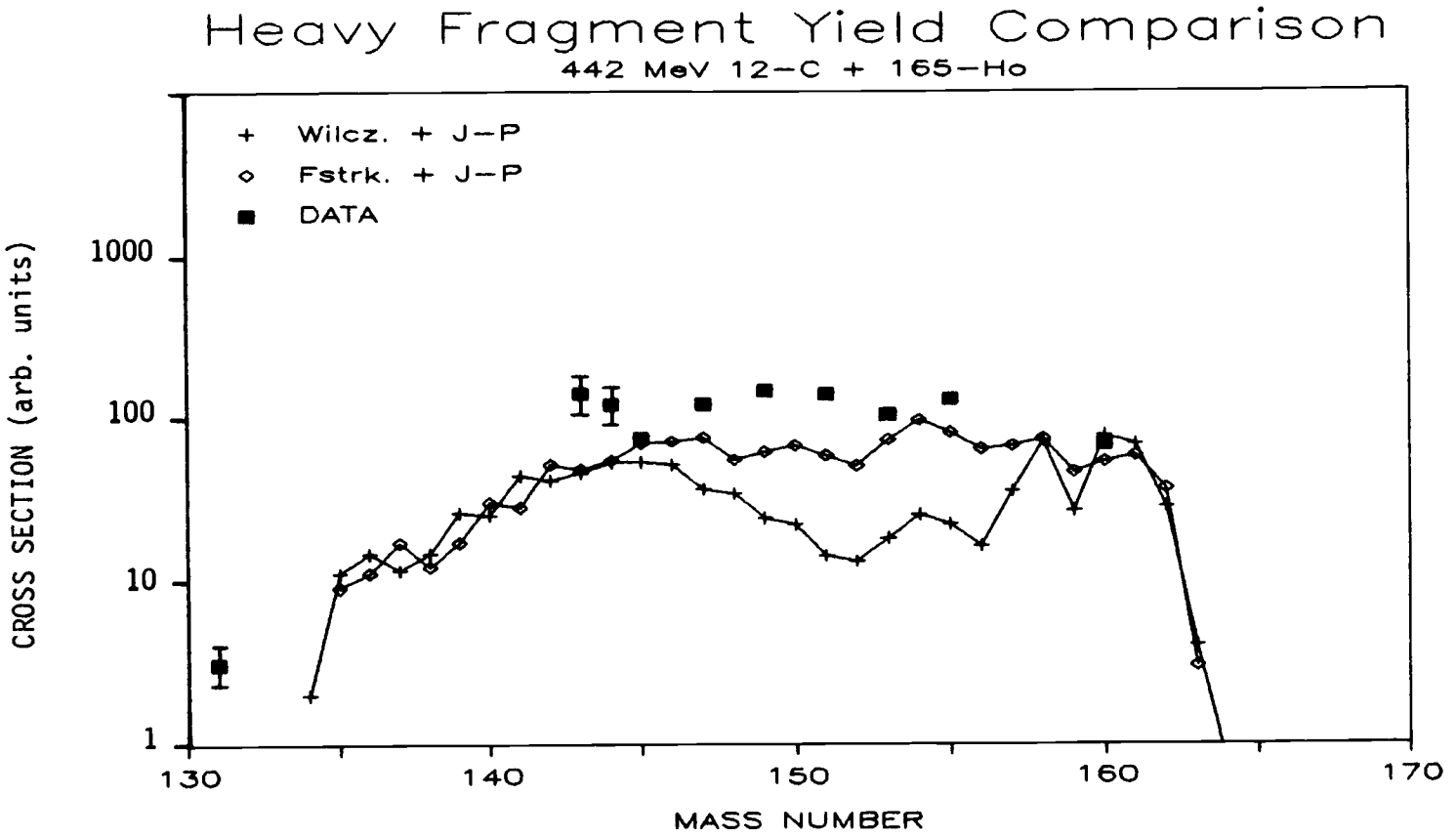

Comparison plot of measured heavy fragment isobaric yields (filled squares) and calculated heavy fragment yield distributions (pluses and diamonds). Calculated distributions generated by Wilczynski sum-rule and JULIAN-PACE computer codes (pluses) and firestreak and JULIAN-PACE codes (diamonds).

Figure 23

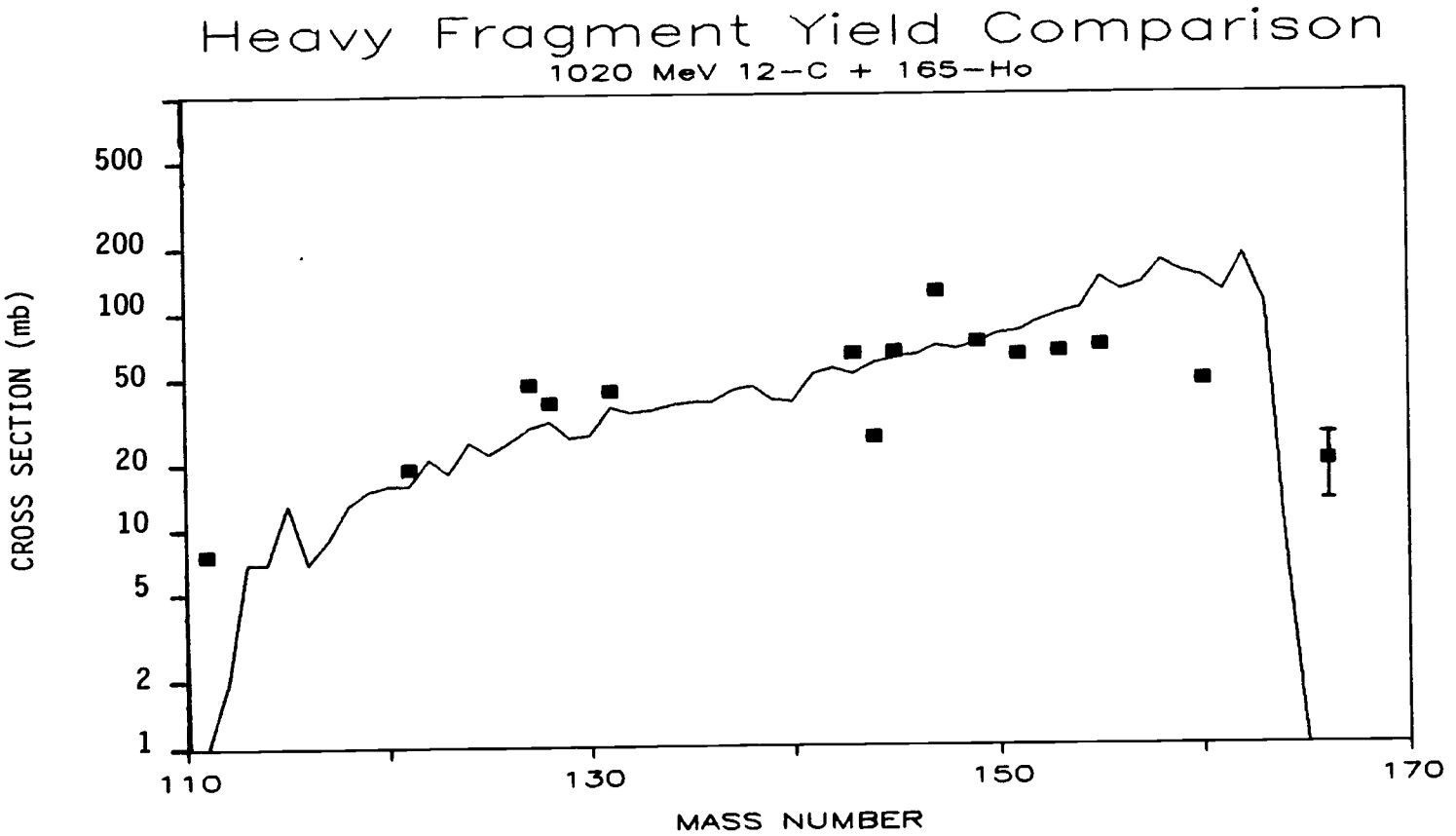

Comparison plot of measured heavy fragment isobaric yields (filled squares) and a calculated heavy fragment yield distribution (line). The calculated distribution was generated using the firestreak and DFF computer codes discussed in the text.

Figure 24

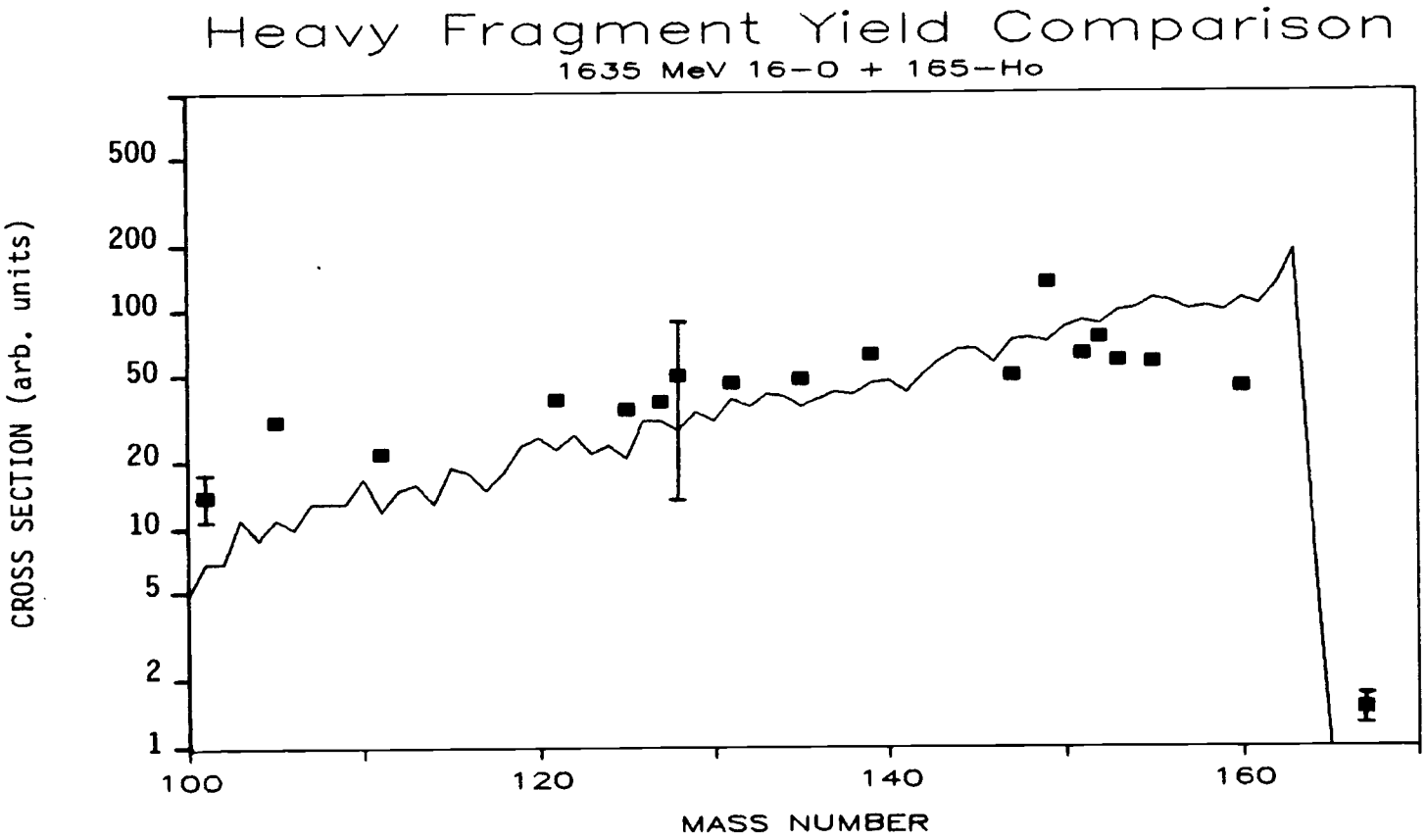

Comparison plot of measured heavy fragment isobaric yields (filled squares) and a calculated heavy fragment yield distribution (line). The calculated distribution was generated using the firestreak and DFF computer codes discussed in the text.

Figure 25

energies are reproduced by calculations based on the firestreak model and deexcitation by the DFF code, however, the yields for the high mass nuclides are significantly overestimated.

The observed heavy fragment distributions are, in general, accurately represented by the calculated distributions for projectile energies above 440 MeV. The results for the 442 MeV ^{12}C + ^{165}Ho reaction system demonstrate the necessity of including angular momentum effects in deexcitation calculations for this projectile energy regime. At higher energy the importance of angular momentum seems to decline since the general shape of the observed distributions are reasonably well reproduced by the DFF code. This may be due to the smaller momentum transfers occurring in the higher energy systems. All model calculations underestimate the heavy fragment distribution widths for 208 MeV ^{12}C and 272 MeV ^{16}O induced interactions. The cause of this discrepancy between observations and calculations is not known.

IV. SUMMARY AND CONCLUSIONS

This chapter reviews and highlights noteworthy aspects of the data and comparisons with phenomenological models. New revelations and topics of agreement or disagreement with previously reported work and theories are reviewed. Finally, ideas on the direction of future endeavors to answer questions raised by this study are presented. The "points of interest" are:

1. Trans-target nuclides are observed for all projectile energies studied. The charge, mass, and cross section of the trans-target species all decrease steadily as the energy of a given projectile is increased. The evolution of the heavy fragment yield with increasing projectile energy is generally characterized by a decreasing mass at which the yield maximum occurs and a significant decreasing slope of the low-mass side of the distribution. These observations may be indicative of a slowly decreasing contribution of complete and incomplete fusion events, an increasing excitation energy and angular momentum (up to 40 MeV/A) and the onset and increase of a spallation-like mechanism (above 30 MeV/A) as the projectile energy increases.

2. The firestreak and Wilczynski sum-rule models predict very similar heavy fragment distributions for 208 MeV ^{12}C and 272 MeV ^{16}O induced interactions. These calculated distributions are narrower than those observed. The firestreak model

(deexcitation calculated by the JULIAN-PACE code) accurately predicts the shape of the observed heavy fragment yield distribution for 442 MeV ^{12}C induced interactions. The sum-rule adequately predicts the width; however, the shape is poorly reproduced. Angular momentum effects are observed in the calculated heavy fragment yields of the 442 MeV ^{12}C + ^{165}Ho system. The DFF code (which omits angular momentum effects) predicts distributions narrower than those generated by the JULIAN-PACE code for 442 MeV ^{12}C. The firestreak model (deexcitation calculated by the DFF code) accurately predicts heavy fragment distributions for 1020 MeV ^{12}C and 1635 MeV ^{16}O induced interactions, however, overestimates high mass yields. One should note that these conclusions are affected to an unknown extent by the assumption that the charge dispersion of mass captured by the target is assumed to scale linearly with the A/Z ratio of the projectile.

3. Both the firestreak and Wilczynski sum-rule models significantly underestimate the fission yields for the systems in which fission is observed. Previous work has concluded that the angular momentum transferred to the target fragment, in at least a fraction of the events, is underestimated by the sum-rule model [68]. The firestreak model predicts similar average transferred angular momentum suggesting these quantities are unrealistically low. The firestreak model also predicts a narrower (sharp cut-off) angular momentum

distribution than the sum-rule model which may also be unrealistic.

4. The evolution of the fission yield with increasing projectile energy is characterized by a broad maximum near 200 MeV center-of-mass energy, an increasing Z_p of the fragments. The decrease in observed fission cross sections above 17 MeV/A projectile energy is found to correlate with a decrease in $\langle l_{sys} \rangle$, the deduced average system angular momentum.

The necessity of future research in this region of nuclear reactions is clear. The results of this study suggest the complicating influence of angular momentum and the overlap between fusion and spallation-like processes on the measured quantities reported. The need to characterize the contributions of these processes is necessary to understand the observed trends. The subsequent incorporation of these effects, and an accurate representation of angular momentum distributions in an interaction model is important to understand measured trends. Assessment of reaction model performance is dependent on the deexcitation code used to determine the final fragment distributions. The results reported in this work proved the necessity of including angular momentum effects in the deexcitation calculations for intermediate energy heavy ion induced interactions in low fissility targets. Effects of angular momentum were observed in fission yields (and for heavy fragment yields from 442 MeV ^{12}C) resulting from highly excited, rapidly rotating primaries.

The firestreak model is very useful over an extremely wide range of projectile energies. Modifications which are indicated by the data suggest a re-examination of the energy and angular momentum transfer mechanism, especially for the most peripheral collisions. The model clearly underestimates the angular momentum and probably predicts an unrealistic distri bution of values. A severe limitation at the lowest energies is the sudden geometrical cut-off. This allows the target nucleus to capture only that portion of the projectile volume which overlaps the target in a straight-line trajectory. A more accurate approach would be to simulate a more realistic trajectory and include a semiempirical characterization (to facilitate calculations) of nuclear forces to allow the capture of projectile nucleons whose trajectory may not directly overlap with the target.

The realm of intermediate energy nuclear reactions is a field rich with information about the interaction process between nuclei. The transition between low-energy and high energy mechanisms is complicated. Mechanisms identified with low-energy reactions overlap with high-energy processes. This work, and others like it, have given a broad panorama of the region and given scientists a general knowledge base with which to design future endeavors.

V. REFERENCES

1. J.P. Bondorf, J.R. Huizenga, M.I. Sobel, and D. Sperber, Phys. Rev. C11, 1265 (1975)

2. A. Fleury and J.M. Alexander, Ann. Rev. Nucl. Part. Sci., 24, 279 (1974)

3. L. Kowalski, J.M. Miller, and J.C. Jodogne, Phys. Rev. 169, 894 (1968)

4. M. Lefort, Institut de Physique Nucleaire Report No. IN2P3, (1975)

5. J.S. Blair, Lectures in Theoretical Physics, (ed. P.D. Kunz and W.E. Brittain), v. 8C, (University of Colorodo Press, Boulder, CO, 1966)

6. C. Mahaux and H.A. Weidenmuller, Ann. Rev. Nucl. Part. Sci., 29, 1 (1979)

7. W. Norenberg, J. Phys. (Paris), 37, C5-141 (1976)

8. W.U. Schroder and H.R. Huizenga, Ann. Rev. Nucl. Part. Sci., 27, 465 (1977)

9. D.K. Scott, Progress in Particle and Nuclear Physics Proc. of the Intl. School of Nucl. Phys., Erice, D. Wilkinson, Ed., Pergamon Press (1979)

10. J. Wilczynski, Phys. Lett. B47, 484 (1973)

11. K. Siwek-Wilczynska, E.H. du Marchie van Voorthuysen, J. van Popta, R.H. Siemssen, and J. Wilczynski, Phys. Rev. Lett. 42, 1599 (1979)

12. J. Wilczynski, K. Siwek-Wilczynska, J. van Driel, S. Gonggrijp, D.C.J. Hageman, R.V.F. Janssens, J. Lukasiak, and R.H. Siemssen, Phys. Rev. Lett. 45, 606 (1980)

13. M. Blann, D. Akers, T.A. Komoto, F.S. Dietrich, L.F. Hansen, J.G. Woodsworth, W. Scobel, J. Bisplinghoff, F. Plasil, and R.L. Ferguson, Phys. Rev. C26, 1471 (1982)

14. N.F. Mott, Proc. R. Soc. A, 126, 259 (1930)

15. P.E. Hodgson, Nuclear Heavy-Ion Reactions (Clarendon Press, 1978), p. 30, 491

16. J.A. Kuehner, E. Almquist, and D.A. Bromley,
Phys. Rev. 131, 1254 (1963)

17. C.K. Gelbke, R. Bock, and A. Richter,
Phys. Rev. C9, 852 (1974)

18. J.P. Bondorf, J.R. Huizenga, M.I. Sobel and D. Sperber
Phys. Rev. C11, 1265 (1975)

19. J.R. Huizenga, Com. Nucl. Part. Phys., 7, 17 (1976)

20. M. Lefort, Nukleonika, 21, 111 (1976)

21. L.G. Moretto and J.S. Sventek,
Phys. Lett. B58, 26 (1975)

22. R.P. Schmitt, P. Russo, R. Babinet, R. Jared, and
L.G. Moretto, Nucl. Phys. A279, 141 (1977)

23. A. Poskanzer, Nature 278, 17 (1979)

24. A.S. Goldhaber and H.H. Heckman,
Ann. Rev. Nucl. Part. Sci., 28, 161 (1978)

25. W.G. Meyer, H.H. Gutbrod, Ch. Lukner, and A. Sandoval,
Phys. Rev. C22, 179 (1980)

26. A.I. Warwick, H.H. Wieman, H.H. Gutbrod, M.R. Maier,
J. Peter, H.G. Ritter, H. Stelzer, F. Weik,
M. Freedman, D.J. Henderson, S.B. Kaufman, E.P. Steinberg,
and B.D. Wilkins, Phys. Rev. C27, 1083 (1983)

27. D.J. Morrissey, W. Loveland, M. de Saint Simon, and
G.T. Seaborg, Phys. Rev. C21, 1783 (1980)

28. J.D. Bowman, W.J. Swiatecki, and C.F. Tsang,
Lawrence Berkeley Laboratory Report, LBL-2908 (1973)

29. G.D. Westfall, J. Gosset, P.J. Johansen,
A.M. Poskanzer, W.G. Meyer, H.H. Gutbrod, A. Sandoval,
and R. Stock, Phys. Rev. Lett. 37, 1202 (1976)

30. W.D. Myers, Nucl. Phys. A296, 177 (1978)

31. S.T. Butler and C.A. Pearson, Phys. Rev. Lett. 7, 69
(1961) and Phys. Rev. 129, 836 (1963)

32. A.M. Poskanzer, R.G. Sextro, A.M. Zebelman,
H.H. Gutbrod, A. Sandoval, and R. Stock,
Phys. Rev. Lett. 35, 1701 (1975)

33. M. Gyulassy, Lawrence Berkeley Laboratory Report,
LBL-6594, (1977), unpublished

34. V.E. Viola, Jr., B.B. Back, K.L. Wolf, T.C. Awes, C.K. Gelbke, and H. Breuer, Phys. Rev. C26, 178 (1982)

35. R.C. Stokstad, Y. Chan, M. Murphy, I. Tserruya, S. Wald, and A. Budzanowski, Lawrence Berkeley Laboratory Report, LBL-15874 (1983)

36. V.E. Viola, Jr., R.G. Clark, W.G. Meyer, A.M. Zebelman, and R.G. Sextro, Nucl. Phys. A261, 174 (1976)

37. Y. Chan, M. Murphy, R.G. Stokstad, I. Tserruya, S. Wald, and A. Budzanowski, Phys. Rev. C27, 447 (1983)

38. J. Blachot, J. Crancon, H. Nifenecker, A. Lleres, A. Gizon, and J. Genevey, Z. Phys. A303, 85 (1981)

39. J.B. Natowitz, M.N. Namboodiri, L. Adler, R.P. Schmitt, R.L. Watson, S. Simon, M. Berlanger, and R. Choudhury, Phys. Rev. Lett. 47, 1114 (1981)

40. U. Lynen, H. Ho, W. Kuhn, D. Pelte, U. Winkler, W.F.H. Moller, Y.T. Chu, P. Doll, A. Gobbi, K. Hildenbrand, A. Olmi, H. Stelzer, R. Bock, H. Lohner, R. Glasow, and R. Santo, Nucl. Phys. A387, 129c (1982)

41. D.K. Scott, Michigan State University Cyclotron Laboratory Report, MSUCL-359 (1981), unpublished

42. R.H. Kraus, Jr, W. Loveland, K. Aleklett, P.L. McGaughey, T.T. Sugihara, G.T. Seaborg, T. Lund, Y. Morita, E. Hagebo, and I.R. Haldorsen, Nucl. Phys. A432, 525 (1985)

43. E. Hagebo, Private communication, 1985.

44. W.D. Loveland and K. Aleklett, Private communication, 1985.

45. F. Hubert, A. Fleury, R. Bimbot, and D. Gardes Ann. Phys. (Paris) 5S, 1-214 (1980)

46. D.J. Morrissey, D. Lee, R.J. Otto, and G.T. Seaborg Nucl. Inst. Meth. 158, 499 (1978)

47. M.J. Koskelo, P.A. Aarnio, J.T. Routti, Helsinki University of Technology Report TKK-F-A426 (1980)

48. P.A. Aarnio, M.J. Koskelo, P. Zombori, Nucl. Inst. Meth. 184, 487 (1981)

49. U. Reus and W. Westmeier, At. Data Nucl. Data Tables, 29, 1 (1983), ibid., 29, 193 (1983)

50. I. Binder, R.H. Kraus, Jr., R. Klein, D. Lee, and M.M. Fowler, Lawrence Berkeley Laboratory Report, LBL-6515 (1977), unpublished

51. A.C. Wahl, Proceedings of the Symposium on the Physics and Chemistry of Fission, Salzburg, 1965, Vol. I, p317.

52. D.J. Morrissey, W.R. Marsh, R.J. Otto, W. Loveland, and G.T. Seabors, Phys. Rev. C18, 1267 (1978)

53. I. Dostrovsky, Z. Fraenkel, and G. Friedlander, Phys. Rev. 116, 683 (1959)

54. R.J. Otto, M.M. Fowler, D. Lee, and G.T. Seaborg, Phys. Rev. Lett. 36, 1356 (1976)

55. D.J. Morrissey, Lawrence Berkeley Laboratory Report, LBL-7713 (1978), Ph.D. Thesis, unpublished

56. A.S. Goldhaber and H.H. Heckman, Ann. Rev. Nucl. Part. Sci., 28, 161 (1978)
H.J. Crawford, P.B. Price, J. Stevenson, and L.W. Wilson, Phys. Rev. Lett. 34, 329 (1975)
J. Gosset, H.H. Gutbrod, W.G. Meyer, A.M. Poskanzer, A. Sandoval, G.D. Westfall, Phys. Rev. C16, 629 (1977)

57. J. Hudis, I. Dostrovsky, G. Friedlander, J.R. Grover, N.T. Porile, L.P. Remsberg, R.W. Stoenner, and S. Tanaka, Phys. Rev. 129, 434 (1963)

58. T.C. Awes, S. Saini, B. Poggi, C.K. Gelbke, D. Cha, R. Legrain, and G.D. Westfall, Phys. Rev. C25, 2361 (1982)
T.J.M. Symons, P. Doll, M. Bini, D.L. Hendrie, J. Mahoney, G. Mantzouranis, D.K. Scott, K. van Bibber, Y.P. Viyogi, H.H. Wieman, and C.K. Gelbke, Phys. Lett. 94B, 131 (1980)

59. J.B. Cumming, R.W. Stoenner, and P.E. Haustein, Phys. Rev. C14, 1554 (1976)

60. J.B. Cumming, P.E. Haustein, and R.W. Stoenner, Phys. Rev. C10, 739 (1974)

61. J.B. Cumming, P.E. Haustein, T.J. Ruth, and G.J. Virtes Phys. Rev. C17, 1632 (1978)

62. N.T. Porile, G.D. Cole, C.R. Rudy Phys. Rev. C19, 2288 (1979)

63. T. Lund, D. Molzahn, R. Brandt, B. Bergersen, D. Eriksen, E. Hagebo, I.R. Haldersen, T. Bjornstad, and C. Richard-Serre, Phys. Lett., 102B, 239 (1981)

64. K. Aleklett, W. Loveland, T.T. Sugihara, D.J. Morrissey, Li Wenxin, W. Kot, and G.T. Seaborg, Lawrence Berkeley Laboratory Report, LBL-17887 (1984) Proceedings of the 5th Nordic Meeting on Nuclear Physics, Jyvaskyla, Finland, 1984

65. J. Blachot, J. Crancon, J. Genevey, Agizon, and A. Lleres, Z. Phys. A301, 91 (1981)

66. J.P. Dufour, H. Delagrange, R. Del Moral, A. Fleury, F. Hubert, Y. Llabador, M.B. Mauhourat, K. Schmidt, and A. Lleres, Nucl. Phys. A387, 157c (1982)

67. The gamma-ray lines assigned to the 56.7 hour ^{166}Yb are emitted by the 7.7 hour ^{166}Yb, however, in most cases the equilibrium had been attained before measurements began. The only gamma ray emitted directly by the ^{166}Yb nuclide is at 82.4 keV, below our lower level energy threshold.

68. A. Gavron, J. Boissevain, H.C. Britt, K. Eskola, P. Eskola, M.M. Fowler, H. Ohm, J.B. Wilhelmy, T.C. Awes, R.L. Ferguson, F.E. Obenshain, F. Plasil, and C.R. Young, Phys Rev. C30, 1550 (1984)

69. X. Campi, J. Desbois, and E. Lipparini, Nuc. Phys. A428, 327c (1984)

70. F. Plasil, 4th International Conference on Reactions Between Complex Nuclei, Nashville, TN (1974), p. 107

71. J.R. Nix, Nucl. Phys. A130, 241 (1969)

72. J. van der Plicht, H.C. Britt, M.M. Fowler, Z. Fraenkel, A. Gavron, J.B. Wilhelmy, F. Plasil, T.C. Awes, and G.R. Young, Phys. Rev., C28, 2022 (1983)

73. M. Blann and T.T. Komoto, Phys. Rev. C26, 472 (1982)

74. A.M. Zebelman, L. Kowalski, J. Miller, K. Beg, Y. Eyal, G. Jaffe, A. Kandil, and D. Logan, Phys. Rev., C10, 200 (1974)

75. A. Gavron, Phys. Rev. C21, 230 (1980)

76. D.J. Morrissey, W. Loveland, G.T. Seaborg, Z. Phys., A289, 123 (1978)

77. S.B. Kaufman, E.P. Steinberg, and B.D. Wilkins, Phys. Rev. Lett., 41, 1359 (1978)

78. W. Loveland, Cheng Luo, P.L. McGaughey, D.J. Morrissey, and G.T. Seaborg, Phys. Rev. C24, 464 (1981) and Proc. Int'l. Conf. Nucl. Phys., p. 523 (1980)

79. M. Blann, Nucl. Phys. 80, 223 (1965)

80. J. Galin, B. Gatty, D. Guerreau, and Z. Tarrago, Phys. Rev. C10, 638 (1974)

81. T. Sikkeland, Phys. Rev., 135, B669, (1964)

82. J.R. Huizenga, J.R. Birkelund, L.E. Tubbs, D. Hilscher, U. Jahnke, H. Rossner, B. Gebauer, and H. Lettau, Phys. Rev. C28, 1853 (1983)

83. J.R. Birkelund, L.E. Tubbs, J.R. Huizenga, J.N. De, and D. Sperber, Phys. Rep. 56, 107 (1979) The results of the calculation are tabulated in: W.W. Wilcke, J.R. Birkelund, H.J. Wollersheim, A.D. Hoover, J.R. Huizenga, W.U. Schroder, and L.E. Tubbs, Atomic Data Nuclear Data Tables, 25, 389 (1980)

84. W. Loveland, K. Aleklett, P.L. McGaughey, K.J. Moody, R.M. McFarland, R.H. Kraus, Jr., and G.T. Seaborg, Lawrence Berkeley Laboratory Report LBL-16280 (1983), submitted to Phys. Rev. C

85. R.H. Kraus, Jr. and W. Loveland, Oregon State University Annual Report DOE/ER70035-1 (August, 1980) R.H. Kraus, Jr., K. Aleklett, P.L. McGaughey, and W. Loveland, Oregon State University Annual Report DOE/ER/70035-2 (July, 1981)

86. J. Galin, H. Oeschler, S. Song, B. Borderie, M.F. Rivet, I. Forest, R. Bimbot, D. Gardes, B. Gatty, H. Guillemot, M. Lefort, B. Tamain, and X. Tarrago, Phys. Rev. Lett. 48, 1787 (1982)

87. M.F. Rivet, B. Borderie, S. Song, D. Guerreau, H. Oeschler, R. Bimbot, I. Forest, J. Galin, D. Gardes, B. Gatty, M. Lefort, B. Tamain, and X. Tarrago, Nucl. Phys. A387, 143C (1982)

88. F. Plasil, D.S. Burnett, H.C. Britt, and S.G. Thompson, Phys. Rev. 142, 696 (1966)

89. T.C. Awes, C.K. Gelbke, B.B. Back, A.C. Mignerey, K.L. Wolf, P. Dyer, H. Breuer, and V.E. Viola, Phys. Lett. 87B, 43, (1979)

90. T.C. Awes, G. Poggi, S. Saini, C.K. Gelbke, R. Legrain, and G.D. Westfall, Phys. Lett. 103B, 417 (1981)

91. P.L. McGaughey, Lawrence Berkeley Laboratory Report LBL-15325 (1982) Ph.D. Thesis, unpublished
P.L. McGaughey, W. Loveland, D.J. Morrissey, K. Aleklett, and G.T. Seaborg, Phys. Rev. C31, 896 (1985)

92. S. Cohen, F. Plasil, and W.J. Swiatecki, Ann. Phys. 82, 557 (1974)

93. H.J. Krappe, J.R. Nix, and A. Sierk, Phys. Rev. C20, 992 (1979)

94. A. Sierk, Subroutine BARFIT, private communication (1984)

95. J.P. Bondorf, F. Dickmann, D.H.E. Gross, and P.J. Siemens, J. Phys. (Paris), 32, C6-C145 (1971)

96. F. Plasil, R.L. Ferguson, R.L. Hahn, F.E. Obenshain, F. Pleasonton, and G.R. Young, Phys. Rev. Lett. 45, 333 (1980)

97. J.T. Routti and S.G. Prussin, Nucl. Inst. Meth. 72, 125 (1969)
J.T Routti, University of California Radiation Laboratory Report, UCRL-19452 (1969), unpublished

98. J. Gosset, J.I. Kapusta, and G.D. Westfall, Phys. Rev. C18, 844, (1978)

99. G. Cecil, S. Das Gupta, and W.D. Myers, Phys. Rev. C22, 2018, (1980)

100. L.F. Oliveira, R. Donangelo, and J.O. Rasmussen, Phys. Rev. C19, 826 (1979)

101. M. Goldhaber and E. Teller, Phys. Rev. 74, 1046 (1948)

102. W.D. Myers, W.J. Swiatecki, T. Kodama, L.J. El-Jaick, and E.R. Hilf, Phys. Rev. C15, 2032 (1977)

103. J. Wilczynski and K. Siwek-Wilczynska, Phys. Lett. 55B, 270 (1975)

104. C. Toepffer, Z. Phys. 253, 78 (1972)

105. K.A. Geoffroy, D.G. Sarantites, M.L. Halbert, D.C. Hensley, R.A. Dayras, and J.H. Barker, Phys. Rev. Lett., 43, 1303 (1979)

106. R. Vandenbosch and J.R. Huizenga,
Nuclear Fission (Academic Press, N. Y., 1973) p. 233

107. A. Gilbert and A.G.W. Cameron,
Can. J. Phys. 43, 1446 (1965)

108. M.H. Salamon, Lawrence Berkeley Laboratory Report,
LBL-10446 (1980), unpublished.

109. P. Marmier and E. Sheldon, Physics of Nuclei and
Particles, Academic Press, (1969) p. 36

110. L.F. Oliveira, Lawrence Berkeley Laboratory Report,
LBL-8561 (1978), Ph.D. thesis, unpublished

111. L. Winsberg, Nucl. Inst. Meth., 150, 465 (1978)

112. F. Hubert, H. Delagrange, and A. Fleury,
Nucl. Phys. A228, 415 (1974)

VI. A P P E N D I C E S

A. SAMPO-80

The gamma-ray spectral analysis program, SAMPO [97], was originally introduced for use on large mainframe computers. SAMPO-80 [47,48] is an adaptation (updated and somewhat abbreviated) of the original code for batch use on a 16-bit minicomputer. SAMPO-80 functions as a two-part code enabling it to run on minicomputers with limited memory and program size. Part I (SAMPOCAL) calculates peak shape parameters from calibration spectra. The peak shape parameters are used by Part II (SAMPOFIT), along with energy and efficiency calibrations, which identifies peaks and calculates peak area, energies, intensities, and associated errors. A flowchart of the procedure used to determine the various calibration parameters is given in the experimental chapter (figure 4).

Adaptation of SAMPO-80 to the Nuclear Data 6660 (ND-6660) system at OSU and to our specific needs required significant revision of the code including greater interactive capability, expanded analysis capabilities, and various I/O options. The implementation was written in standard FORTRAN-77. Only the I/O routines required library programs not available in ANSII standard FORTRAN. Several desirable user options not included in the original code were added. Segments of the code were rewritten to optimize memory allocation and runtime and properly interface with the file structure used in our system. Program segments executing input of control information for the program, spectral data, and output of the results table for subsequent use have been rewritten to allow the user complete interactive control of file definitions.

The peak identification segment of SAMPOFIT was replaced with a more efficient logic sequence, however, the basic algorithm was unchanged. A significant modification in the implementation of the peak finding routine was made to identify multiplets more reliably in the low-energy quarter of the spectrum (≈80-500 keV) and avoid errant elimination of multiplet peaks in the high-energy quarter of the spectrum (≥1500 keV). The interpolation subroutine was rewritten and minor changes in program logic throughout the codes were made to optimize runtime under FORTRAN-77 compilation. Common area usage to pass variables was greatly expanded resulting in significant optimization of runtime and a small overall reduction of memory requirements.

SAMPOFIT supports five output modes to display the peak fit results. The first format is unalterable by the user since it is matched to the requirements of TAU1 [46]. The remaining four modes are user selectable for line printer output. The default output mode is a short summary table listing the peak channel number, energy, area, intensity, and associated errors. Included with each peak listing is the fit interval and number of peaks fit together in a multiplet. The user may select a detailed analysis including complete listings of least squares fit parameters, peak shape parameters, error analysis results, and all of the information included in the summary table. A user selectable option to display a line printer plot of spectral data, background and peak fits for each fitting interval may be added to either of the above tabular listings.

SAMPOFIT may be run in a completely interactive mode or job streams may be created for automated batch style analysis enabling overnight processing of data. The most time intensive part of the analysis is the output of data to a dot-matrix printer. Table A-1 compares SAMPOFIT run times for the shortest and longest output modes. It is clear that the program is printer bound for the system configuration used at OSU. The actual analysis time (cpu processing time) is approximated by disposing the output to hard disk (the fastest output device available). The processing time is found to be exceptionally fast at approximately 2 seconds per peak. The computer code is available upon request from the author. Minimum hardware requirements are 256k-bytes of internal memory, an hardcopy output device, and a mass storage medium.

SAMPOFIT Runtimes for Various Output Formats

Output Mode	Output Device	Analysis Time	# Peaks Fit	Sec/Peak
Summary Table	Printer	471 sec.	130	3.0 sec.
Longest Output	Printer	3132 sec.	127	24.7 sec.
Summary Table	Disk	290 sec.	130	2.2 sec.
Longest Output	Disk	620 sec.	130	4.8 sec.

A tabulation of the analysis time of the SAMPO-80 computer code implemented on the OSU ND-6660. The analysis times of shortest and longest output formats are compared for standard dot matrix printer and disk file output.

Table A-1

B. THEORETICAL MODELS

1. INTRODUCTION

This appendix describes the models and the implementations used to generate the various calculated quantities for comparison to the data. This work was not designed to be a comprehensive discussion of all current models used to predict the various observables of a reaction. Instead, two popular reaction models, the firestreak [30] model as implemented by Morrissey and McGaughey [91] and the Wilczynski generalized sum-rule model [11,12] have been chosen. Two deexcitation calculations were also used. These methods, a version of the Dostrovsky-FraenkelFriedlander (DFF) deexcitation code [53] and the PACE modification of the JULIAN code [75], are conceptually similar with the exception that the JULIAN-PACE code explicitly includes angular momentum and the DFF code does not.

2. FIRESTREAK MODEL

The firestreak model was originally proposed by Myers [30] to aid understanding of fragmentation in relativistic heavy-ion (RHI) reactions. Gosset, et al. [98] have used this model to predict light particle spectra produced in RHI induced collisions. Cecil et al. [99] later formulated analytic expressions for the collision model to include nuclear diffuseness in the calculation of experimental observables. This model was implemented by Morrissey and McGaughey [91] to follow the target fragmentation process and include a nuclear transparency function. The firestreak model is unique in the capability to describe both high energy fragmentation processes and the capture of projectile fragments at lower energies.

The firestreak model has its conceptual origins in the purely geometric abrasion-ablation model of Bowman, et al. [28]. The abrasion-ablation model envisioned a relativistic projectile colliding with a target nucleus in such a way that the entire overlapping region of the two nuclei would be sheared away in a "clean-cut" fashion (see figure B-1). The remaining piece of the target, the target spectator, would gain an excitation energy due only to the increased surface area of the nucleus. The collision is assumed to be "clean-cut", therefore, no momentum or frictional energy are transferred to the target. The projectile, similarly, would gain an excitation energy due to the nuclear deformation and would continue at the beam velocity in the forward direction (at 0 degrees, β_{inc} in figure B-1). The overlapping region would travel independently of the projectile and target spectators (at an

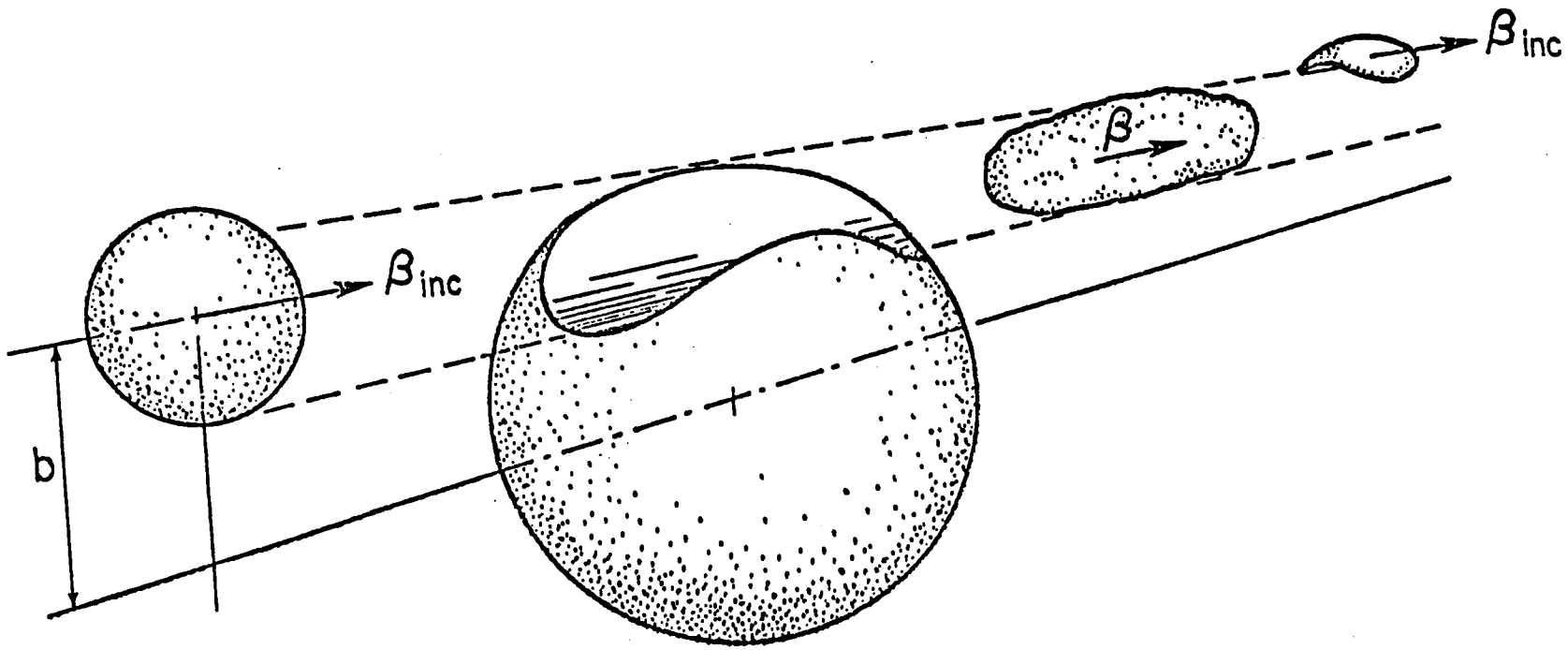

A simple schematic representation of an high energy peripheral nuclear interaction.
This figure is borrowed from reference 29.

Figure B-1

intermediate velocity, β in figure B-1) and could be described by a thermal model such as the fireball proposed by Westfall, et al. [29].

The abrasion-ablation model has been found to be somewhat unrealistic. The predicted excitation energies due to surface deformations significantly underestimate observed results [100]. Further, the "clean-cut" concept assumes that no momentum is transferred to the target spectator which has been experimentally shown to be incorrect [9,84]. The firestreak model is an enhancement of this concept and attempts to treat the collision in a more realistic manner.

The firestreak model simulates the collision of a high-energy heavy-ion with a target nucleus as a totally inelastic process in the overlap region. The overlap geometry is identical to the abrasion-ablation model, but the nuclei are assumed to have diffuse surfaces which are generated by folding a surface described by a Yukawa function into a conventional sharp-sphere density distribution. During the instant of the collision process, the interaction is assumed to be confined to the geometric overlap region with straight line trajectories. The colliding regions of the projectile and target are divided into "infinitesimal" colinear tubes of nuclear matter which undergo inelastic collisions (figure B-2). A "transparency function" was included to prevent collisions from occurring between tubes containing an insufficient density of nucleons. The transparency function included a variable parameter allowing a measure of control over the total reaction cross section.

FIRESTREAK

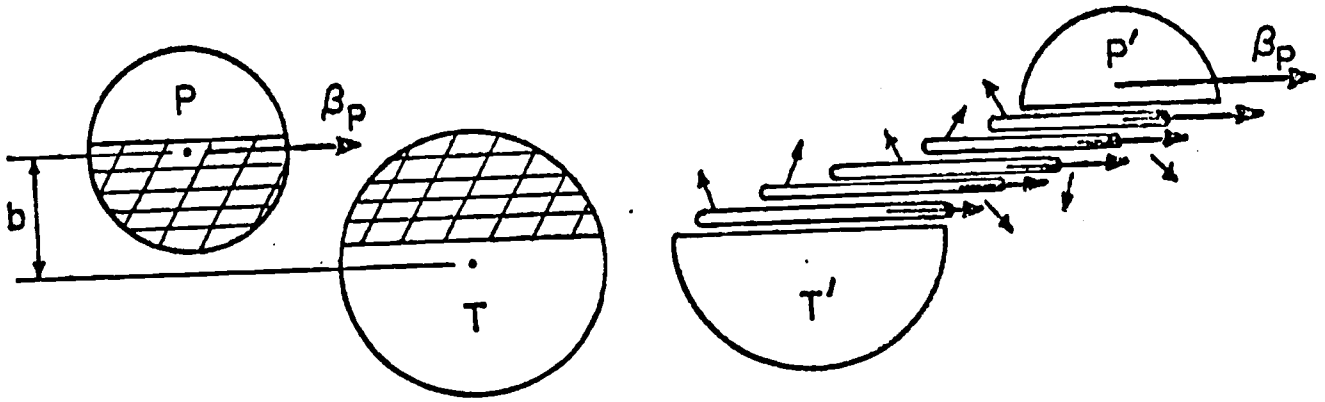

Schematic representation of colliding tubes concept used in the firestreak model. Incident projectile, P, collides with target, T, with overlap b. After the interaction tubes captured by the target contribute to final fragment mass and excitation energy. This figure is borrowed from reference 110.

Figure B-2

Upon collision of two tubes, it is assumed that the tubes fused and the kinetic and thermal energies equilibrated. The kinetic energy of each tube will determine its final disposition: whether it remains as part of the target fragment or is ejected. If the resulting kinetic energy of a given fused tube is less than its binding energy to the target remnant, the tube remains a part of the fragment and contributes its mass, linear and angular momenta, kinetic and thermal energies to the fragment. The angular momentum for each tube is assumed to be equal to the linear momentum times the radial distance of the tube from the center of the target nucleus. The momenta and energies of the captured tubes are summed to determine the resultant values transferred to the target fragment. After determining the final status of all the tubes, a final excitation energy is added to the target fragment based upon the deformation resulting from tubes which have escaped from the target remnant. No deformation energy is added if a net mass is captured by the target fragment.

The charge dispersions (or dispersion of the number of neutrons and protons in the residues) in the primary distributions of fragments with net mass less than the target were calculated by the GDR model of Morrissey, et al. [52]. This calculation is based upon the concept that the fluctuation in the number of neutrons and protons swept away from the target residue can be described by the zero point vibrations of the giant dipole resonance (GDR) of the target nucleus. The GDR has been described as an out-of-phase vibration of the neutrons against the protons [102]. Myers, et al. [103] have treated the GDR in terms of harmonic oscillator (HO)

potential to describe the motion of the neutrons against the protons. This results in a Gaussian distribution in the number of protons removed from the target which is centered about the target Z_T/A_T and with a width proportional to the HO classical turning point displacement. The charge of heavy primary fragments with a net mass greater than the target was calculated assuming the mass transferred to the target had the same mass to charge ratio as the projectile.

3. SUM-RULE MODEL

The Wilczynski sum-rule model originates from the concept that incomplete fusion and complete fusion (compound nucleus formation) are directly linked with the angular momentum of the reaction system [10]. It is believed that if the projectile is to fuse with the target, the angular momentum of the system must be between 0h and the critical angular momentum, l_{cr}, which defines the limiting angular momentum for the complete fusion channel [4]. The natural extension to this concept is used to explain the relationship between angular momentum and incomplete fusion. Any given fragment of the projectile may fuse with the target provided the angular momentum of the reaction system is less than the $l_{cr}(f)$ value for that particular fragment, f. The reaction l-space is thus broken into windows, each window corresponding to a reaction channel representing transfer of the heaviest fragment allowable by the angular momentum constraints. Windows with successively higher angular momenta will correspond to reaction channels where the projectile fragment that fuses with the target becomes smaller.

Siwek-Wilczynska, et al. [11], in their first paper on the generalized concept of critical angular momentum, incorporated the above concepts in the model to describe incomplete fusion reactions between light heavy-ions and rare earth element targets. Using this model, one can calculate critical angular momenta for the fusion of the projectile and various projectile fragments with the target nucleus from the balance of Coulomb, centrifugal and nuclear forces. A sharp cutoff approximation is used to determine the fraction of the

total cross section which results in a given reaction channel. The $^{12}C + ^{160}Gd$ reaction is used to demonstrate the model:

$$\sigma_R = \frac{h^2}{8\pi\mu E} \sum_{l=0}^{l=l_{hg}} (2l + 1) \qquad [B-1]$$

$l=0$ is the reaction cross section, where l_{hg} is the hard-grazing angular momentum characterized by the distance of closest approach equal to the sum of the nuclear half-density radii. The sharp cutoff approximation divides the reaction cross section into the following l-windows:

$$0 < l < l_{cr(C+Gd)}; \text{ complete fusion} \qquad [B-2]$$

$$l_{cr(C+Gd)} < l < (12/8)l_{cr(Be+Gd)}; \ ^{8}Be \text{ capture}$$

$$l_{cr(Be+Gd)} < l < (12/4)l_{cr(\alpha+Gd)}; \ \alpha \text{ capture}$$

where $l_{cr(C+Gd)}$, $l_{cr(Be+Gd)}$, and $l_{cr(\alpha+Gd)}$ are the critical angular momenta for $^{12}C + ^{160}Gd$, $^{8}Be + ^{160}Gd$, and $\alpha + ^{160}Gd$ systems.

The sum-rule model incorporates two major refinements of the sharp cutoff model discussed above. These are 1) each reaction channel is assigned a statistical probability [95], and 2) an angular momentum "transmission coefficient" is used to smooth the l-cutoff.

The probability factor was developed by Bondorf, et al. to explain the exponential dependence of the cross section on the ground state Q-value, Q_{gg}:

$$p(i) = C \exp\{[Q_{gg}(i)-Q_c(i)]/T\} \qquad [B-3]$$

where T is the effective temperature and Q_c is the change of the coulomb interaction energy due to the transfer of charge in the interaction. The smooth cutoff l "transmission coefficient", T_l, is given by:

$$T_l = \{1 + \exp[(l - l_{lim}(i))/\delta]\}^{-1} \qquad [B-4]$$

where, $$l_{lim}(i) = \frac{A_p}{A_{cf}} \; l_{cr}(\text{target} + \text{cf})$$

and A_p is the projectile mass, A_{cf} is the captured fragment mass, and l_{cr} is obtained from the balance of forces. The final expression for the cross section for a given reaction channel is:

$$\sigma(i) = \frac{\hbar^2}{8\pi\mu E} \sum_{l=0}^{l_{max}} (2l+1)N_l T_l(i) \exp\{[Q_{gg}(i)-Q_c(i)]/T\} \qquad [B-5]$$

where N_l is a normalization factor and l_{max} is the maximum l for which the colliding system gets in to the region where the total nucleus-nucleus potential is attractive [103].

The excitation energy for a given transfer product generated by the sum-rule model was calculated using the optimum excitation energy formalism of Hubert et al. [112], where:

$$E(opt)^* = Q_{gg} - Q_{opt} \qquad [B-6]$$

$$Q_{opt} = E(f)_{cm} - E(i)_{cm}$$

where $E(i)_{cm}$ and $E(f)_{cm}$ are the entrance and exit channel kinetic energies, respectively. $E(f)_{cm}$ is the optimal kinetic energy of a system taken from the semiclassical DWBA analysis of Toepffer [104] for transfer reactions. Hubert et al. [112] included recoil effects to arrive at the following relation:

$$E(f)_{cm} = E(i)_{cm} \frac{Z_A, Z_B,}{Z_A Z_B} \frac{1 - (m_x R_A,/m_A R_{min})}{(m_B/m_B,) + (m_x R_A,/m_B, R_{min})}$$

In this expression, m_X, m_A, and m_B are the masses of the transferred fragment, the incident particle and the target, respectively. R_A, and R_{min} are the radius of the projectile fragment and distance of closest approach, respectively.

The angular momentum of the target fragments is given by a distribution in l-values. Geoffroy, et al. [105] found that the average angular momentum transferred to the target by the capture of a given projectile fragment increases linearly with the mass of the captured fragment. One can calculate the distribution of angular momentum transferred to the target, l_{frag}, by scaling the distribution of projectile angular momenta resulting in a given reaction channel by the fraction of the projectile mass captured by the target:

$$P(l_{frag}) = (A_{PF}/A_P)\ \{(2l+1)N_l T_l(i)\}; \qquad 0 \leq l \leq l_{max} \qquad [B\text{-}8]$$

for values of projectile angular momentum between $l=0$ and $l=l_{max}$. (A_{PF}/A_P) is the fraction of the projectile mass captured by the target. The expression in brackets, taken over the range $0 \leq l \leq l_{max}$ represents the distribution of angular momenta which contribute to the reaction channel "i" (taken at any one l-value, it represents the probability for that given l-value contributing to reaction channel i). The distribution in angular momentum of each primary fragment serve as input parameters for the Julian-Pace deexcitation code.

4. DEEXCITATION

The firestreak and Wilczynski sum-rule models discussed above are used to predict the "primary product" distributions resulting from the direct interaction of projectile and target nuclei. The computer code implementations of these models calculate "primary products" which are nuclei with varying amounts of excitation energy, angular momentum, and recoil energy. The calculated primary products must be deexcited in accordance with some formalism to yield a product distribution which can be compared to experimental observations.

The DFF formalism of Dostrovsky, et al. [53] is the first of two used in this work. The DFF formalism treats the deexcitation of nuclei by particle emission and fission as a Monte-Carlo process. The formalism allows proton, neutron, deuteron, triton, ^{3}He, and ^{4}He particle emission. One should note that in calculating all emission widths (including fission), no angular momentum corrections were considered. A modified version of the original DFF code [91] was used. This implementation includes a more realistic treatment of fission as outlined in Vandenbosch and Huizenga [106]. The probability of fission is estimated by Γ_f/Γ_n, and is determined at each step of the evaporation chain composed of the excited primary fragment and the various successive deexcitation daughter nuclei. The expression used for Γ_f/Γ_n is (equation [B-9]):

$$\Gamma_f/\Gamma_n = \frac{K^o a_n\{[4a_f(E-E_f)]^{1/2} - 1\}}{4A^{2/3}a_f(E-B_n)\ \exp\{[4a_n(E-B_n)]^{1/2} - [4a_f(E-E_f)]^{1/2}]\}}$$

$K^o=h^2/8\pi^2mr^2$, a_f/a_n is the ratio of saddle point to equilibrium deformation level density parameters, E is the excitation energy, E_f is the fission barrier energy and B_n is the neutron binding energy. The fission barrier heights in the implementation used were modified from those used in reference 91 to reflect the more recent liquid drop parameters. The Cohen-Plasil-Swiatecki (CPS) nonrotating liquid drop fission barriers were used and are defined as follows:

For $0 \leq x \leq 0.75$:

$$B^{LD} = 444.89[0.2829 - 0.3475x - 0.0016x^2 + 0.0501x^3] \qquad [B\text{-}10]$$

For $0.75 \leq x \leq 1.0$:

$$B^{LD} = 444.89[1.4(1-x)^2 - 4.5560(1-x)^3 + 6.7443(1-x)^4]$$

and $$x = \frac{E_C}{2E_S} = (Z^2/A)\ [50.883(1-1.7826I^2)]^{-1}$$

where x is the fissility parameter, and $I=(N-Z)/A$ is the relative neutron excess. A variable parameter, M, is incorporated into the EVA code to allow scaling of the fission barrier according to $B_f=M*B^{LD}$. This parameter is discussed further in the Results and

Discussion chapter. One should note that this treatment is for a nonrotating liquid drop and does not include the CPS rotating liquid drop formalism for angular momentum. The resultant fission fragments are deexcited as necessary until the fragment excitation energy is less than 10 MeV.

The JULIAN-PACE deexcitation code [75] is generally similar to the DFF formalism discussed above. The deexcitation process is followed by a Monte Carlo procedure, and fission competition is allowed at each stage of the deexcitation chain. JULIAN-PACE, however, includes angular momentum throughout the calculation. The total emission width is used in determining the probability of fission:

$$\frac{\Gamma_f(J)}{\Gamma_{tot}(J)} = N \{ N + 2 \sum_{v} \int_{0}^{E'} g_v \sigma_v(\varepsilon) \mu \varepsilon_p(E'-\varepsilon,J)\, d\varepsilon \}^{-1} \qquad [B-11]$$

where the sum is taken over the allowed decay modes (neutron, proton, deuteron, etc.). μ is the reduced mass; g_v is a statistical factor for particle emission; $\sigma_v(\varepsilon)$ is the inverse cross section; and B_v is the binding energy of the evaporating particle. Also,

$$N = [\frac{h^2}{4\pi}] \int_{}^{E''} \rho(E''-\eta)d\eta \qquad [B-12]$$

$$E' = E-E_{min}(j)-B_v$$

$$E'' = E-E_{sp}(J)$$

and

$$\rho(E,J) = \rho_o(U)(2J+1)\ \exp\{2[a(U-E_{rot}(J))]^{1/2}\}$$

In the above expressions, E is the excitation energy of the fissioning nucleus and $\rho(E,J)$ is the level density at excitation energy E. U=E-P where P is the pairing energy; $E_{rot}(J)$ is the rotating liquid drop energy obtained using the CPS formalism [92]; $\rho_o(U)$ is taken from the Gilbert and Cameron formalism [107]. After each stage of the deexcitation chain the fission barrier is reevaluated to reflect the loss of angular momentum and excitation energy in the previous step. The user-defined parameters used in JULIAN-PACE are: a_f/a_n, the ratio of level density parameters at the saddle point and ground state deformations; and B_f, the fission barrier. Angular momentum is included in the fission barrier calculation using the CPS formalism, however, input parameters allow the user to effectively represent other barrier values.

The two deexcitation formalisms used are conceptually similar with the major exception that angular momentum effects are included in JULIAN-PACE but not in the DFF formalism. The comparison of calculated results to measured quantities may give an indication of the importance of angular momentum in the deexcitation processes for the fragments produced in the reactions studied in this work.

C. HIGH ENERGY DATA

I. INTRODUCTION

The data presented in this appendix have been reported, in part, in reference 86. The data are included with this work without comment (except for instances noted previously). The purpose of including the data with this work is to gather together in one place all data resulting from the study of interactions induced in holmium targets by intermediate and high energy projectiles.

The data are presented in tabular form using the same format as within the main body of this work. The procedure of data acquisition and analysis is identical to the procedures outlined in the Experimental chapter. Unique aspects of beam flux measurement at the LBL Bevalac are discussed in reference 91.

The data are presented for the interaction systems tabulated in table C-1 along with the irradiation information. The accelerator used was the Bevalac at the Lawrence Berkeley Laboratory. The typical experiment at the Bevalac involved irradiating several target/catcher stacks simultaneously to maximize the use of beam time. A tabulation of materials preceeding the holmium target stack is presented in table C-2. The Salamon formalism [108] was used to calculate the center-of-target projectile energy, $E_{proj}(COT)$. The observed gamma-rays necessary to identify a nuclide are tabulated in table C-3. Measured production cross sections and calculated independent and isobaric yields are tabulated in tables C-4 to C-11. The isobaric yields are plotted as a function of the nuclidic mass

number in figures C-1 to C-8 (these are all placed immediately after table C-11). The Z_p functional forms used to determine independent and mass yields are presented in tables C-12 to C-19. The measured kinematical result (F/B and 2W(F+B) values) are tabulated in tables C-20 to C-22; and the deduced kinematical quantities (β_{par}, P_{par}, <V> and <T>) are compiled in tables C-23 to C-25. Kinematical quantities were not obtained for the other experiments because catcher foils were not counted separately from the target.

The data for the 12.5 GeV ^{12}C + ^{165}Ho system are anomalous. There is no consistency between yields of determined for this experiment and those of experiments with lower or higher energies. No explanation for this phenomenon is available, however, a possible answer may be that the target may have contained a gross impurity (such as uranium). The data should be viewed with this in mind.

IRRADIATION INFORMATION

ION	PROJECTILE ENERGY INIT. (GeV)	-COT- (GeV)	(GeV/A)	TOTAL FLUX (IONS)	IRRAD. LENGTH (MIN)	Ho TARGET THICKNESS (mg/cm^2)	CATCHER THICKNESS (mg/cm^2)	TAEI to COUNTING (hours)	ACCEL.
$^{12}C^{6+}$	3.0	2.9	0.24	8.39×10^{13}	1605.	225.0	35.8	15.0	Bevalac
$^{20}Ne^{10+}$	8.0	7.7	0.38	3.74×10^{13}	1073.	220.0	35.4	3.5	Bevalac
$^{12}C^{6+}$	12.6	12.5	1.04	9.07×10^{12}	750.	(Ho) 224.	35.8	14.5	Bevalac
		12.5	1.04			(^{144}Sm) 15.1	17.5	14.8	
		12.5	1.04			(^{152}Sm) 22.1	17.5	15.0	
$^{20}Ne^{10+}$	21.0	20.8	1.04	1.07×10^{13}	859.	(Ho) 223.	17.5	4.0	Bevalac
		20.8	1.04			(Ce) 77.	17.5	4.3	
$^{40}Ar^{18+}$	35.9	33.8	0.85	2.51×10^{12}	1243.	1650.	20.3	4.0	Bevalac

The above is a tabulation of irradiation conditions and targetry data for the indicated experiments. Projectile energies are tabulated for the extracted beam and at the center-of-target. The TAEI to counting column shows approximate lapsed times between the end-of-irradiation and the first gamma spectroscopic measurement for each experiment. Mylar was used for all catchers in the above experiments.

Table C-1

MATERIALS IN BEAM (mg/cm^2)

Projectile	Mylar	Al	Ta	Bi	Au	U
3 GeV ^{12}C	216.	10.	59.	244.	1.0	155.
8 GeV ^{20}Ne	432.	-	588.	148.	-	50.6
12.6 GeV ^{12}C	34.4	80.	-	-	-	233.4
21 GeV ^{20}Ne	142.	-	175.	-	1.0	237.4
35.9 GeV ^{40}Ar	980.	29.	363.	-	510.	410.

A tabulation of the total thickness of targets, catchers and monitor foils which preceded the target assemblies discussed in this work.

Table C-2

NUCLIDE IDENTIFICATION GAMMA-RAYS

NUCLIDE	(ENERGY (keV)--BRANCHING RATIO (%))		
^{22}Na	1274.6-- 99.9		
^{24}Na	1368.5--100.		
^{28}Mg	400.6-- 35.9	1342.2-- 54.0	1778.9--100.
^{42}K	1524.2-- 18.4		
^{43}K	372.8-- 88.3	617.5-- 78.7	
^{44g}Sc	1157.0-- 99.9		
^{44m}Sc	271.2-- 77.8	1157.0--108.3	
^{46g}Sc	889.2--100.	1120.5--100.	
^{47}Ca	1297.1-- 74.9		
^{47}Sc	159.4-- 68.0		
^{48}Sc	983.5--100.	1037.5-- 97.5	1312.1--100.
^{48}V	983.5--100.	1312.1-- 97.5	
^{51}Cr	320.1-- 9.83		
^{52g}Mn	744.2-- 90.0	935.5-- 94.5	1434.1--100.
^{54}Mn	834.8--100.		
^{56}Mn	846.7-- 98.9		
^{56}Co	846.8-- 99.9	1238.3-- 67.0	
^{57}Co	122.1-- 85.6		
^{58g}Co	810.8-- 99.4		
^{59}Fe	1099.3-- 56.5	1291.6-- 43.2	
^{65}Zn	1115.5-- 50.7		
^{69}Ge	1106.4-- 36.0		
^{69m}Zn	438.6-- 94.8		
^{71}As	174.9-- 83.6		
^{72}Ga	629.9-- 25.2	834.0-- 95.6	
^{72}As	834.0-- 80.1		
^{72}Se	834.0-- 91.3		
^{73g}Se	361.2-- 97.		
^{74}As	595.8-- 60.3		
^{75}Se	136.0-- 55.6	264.6-- 58.2	
^{75}Br	286.5-- 92.0		
^{76}As	559.1-- 44.7		
^{76g}Br	559.1-- 72.3		
^{76}Kr	270.2-- 21.0	315.7-- 40.	406.5-- 12.
^{77g}Br	239.0-- 23.1	520.7-- 22.4	
^{79g}Kr	261.3-- 12.7		
^{82}Sr	776.5-- 13.4		
^{82m}Rb	554.3-- 62.8	776.5-- 84.5	
^{83g}Sr	381.6-- 17.3	762.7-- 29.7	
^{83}Rb	520.4-- 46.1	529.5-- 30.0	
^{84g}Rb	881.6-- 67.8		

Table C-3

NUCLIDE	(ENERGY (keV)--BRANCHING RATIO (%))		
^{85g}Sr	514.0--100.		
^{86g}Rb	1076.6-- 8.78		
^{86g}Y	627.7-- 32.6	777.4-- 22.4	1076.6-- 82.5
	1153.0-- 30.5		
^{86}Zr	243.0-- 95.8	1076.7-- 82.5	
^{87g}Y	388.4-- 85.3	484.8-- 92.2	
^{87m}Y	381.1-- 78.5		
^{88}Y	898.0-- 94.0	1836.0-- 99.4	
^{88}Zr	392.9-- 97.3	898.0-- 94.0	1836.0-- 99.4
^{89g}Zr	909.2-- 99.9		
^{90m}Y	202.5-- 96.9	479.5-- 90.6	
^{90g}Nb	141.2-- 69.0	1129.1-- 92.0	
^{90}Mo	257.3-- 77.6		
^{93m}Mo	684.7-- 99.7	1477.1-- 99.1	
^{93g}Tc	1363.0-- 65.8	1520.3-- 23.8	
^{94g}Tc	702.7-- 99.8	849.7-- 97.7	871.0--100.
^{95g}Nb	765.8-- 99.9		
^{95g}Tc	765.8-- 93.9		
^{95m}Tc	765.8-- 93.9		
^{96g}Tc	778.2--100.	849.9-- 97.8	
^{96}Nb	568.9-- 55.7	778.2-- 96.9	1091.3-- 49.5
^{97}Ru	215.7-- 85.8		
^{99}Mo	140.5-- 90.7		
^{99m}Rh	340.6-- 69.1		
^{100g}Rh	539.6-- 78.4	1553.4-- 20.5	
^{100}Pd	539.6--103.0	822.5-- 26.5	1107.1-- 17.4
	1553.4-- 27.0		
^{101g}Rh	127.2-- 73.0	198.0-- 70.8	
^{101m}Rh	306.8-- 86.8		
^{101}Pd	296.3-- 19.2		
^{102g}Rh	475.1-- 94.0	631.3-- 55.5	
^{103g}Ag	118.7-- 31.3	148.2-- 28.4	1273.8-- 9.4
^{104g}Ag	555.8-- 92.8	767.6-- 65.9	
^{105g}Rh	318.9-- 19.2		
^{105g}Ag	280.4-- 31.0	344.5-- 41.6	
^{106m}Ag	406.2-- 13.5	451.0-- 28.4	717.3-- 29.1
	748.4-- 20.7	1045.8-- 29.7	
^{108m}In	242.9-- 37.0	875.6-- 93.0	1056.8-- 30.5
^{110m}In	657.7-- 97.0	884.7-- 91.7	
^{110m}Ag	657.9-- 94.7	884.7-- 72.9	
^{111}In	171.3-- 90.3	245.4-- 94.0	
^{116}Te	93.7-- 31.2	931.8-- 27.7	1293.5-- 95.0

Table C-3 (cont.)

NUCLIDE	(ENERGY (keV)--BRANCHING RATIO (%))			
^{117}Te	719.7-- 64.7			
^{119g}Te	644.0-- 84.4			
^{119m}Te	153.6-- 66.7	1212.7-- 67.0		
^{120}I	560.4-- 73.0			
^{121g}Te	573.1-- 79.7			
^{121m}Te	212.2-- 82.6	573.1-- 79.5		
^{121}I	212.5-- 85.0			
^{121}Xe	252.7-- 17.6	445.2-- 10.8		
^{122}Xe	350.2-- 7.74	564.1-- 17.7		
^{123}I	159.0-- 83.2			
^{123m}Te	159.0-- 84.0			
^{123}Xe	148.9-- 48.6			
^{124}I	602.7-- 61.0			
^{125g}Xe	188.4-- 54.9			
^{126}I	388.6-- 32.2	666.3-- 31.3		
^{126}Ba	233.6-- 20.4	388.6-- 42.3		
^{127g}Xe	202.8-- 68.3			
^{127}Cs	124.7-- 15.8	411.9-- 59.0		
^{128}Ba	273.4-- 14.5	442.9-- 25.8		
^{129}Cs	371.9-- 31.1	411.5-- 22.7		
^{131g}Ba	123.8-- 29.2	216.1-- 19.9	496.3-- 47.1	
^{131}La	108.5-- 23.1	365.8-- 16.0	418.4-- 18.2	
^{132}Cs	667.5-- 97.4			
^{132}La	464.5-- 77.0			
^{132}Ce	182.1-- 79.0			
^{133}Ba	356.0-- 62.3			
^{134g}Cs	604.7-- 97.6	795.8-- 85.4		
^{135g}Ce	265.6-- 42.4	606.8-- 19.5		
^{139g}Ce	165.8-- 78.9			
^{141}Ce	145.4-- 48.4			
^{143}Pm	742.0-- 38.3			
^{144}Ce	133.5-- 11.1			
^{144}Pm	618.0-- 98.6	696.5-- 99.5		
^{145}Eu	653.6-- 15.3	893.8-- 65.8		
^{146}Pm	453.8-- 62.3	747.4-- 35.9		
^{146}Eu	633.2-- 43.0	747.2-- 98.0		
^{146}Gd	154.6-- 46.5	747.2--108.0	1058.7-- 7.4	
	1534.2-- 6.80			
^{147}Nd	91.1-- 27.9			
^{147}Eu	121.3-- 22.7	197.3-- 25.8		
^{147}Gd	229.2-- 64.4	396.5-- 34.1	928.9-- 18.8	
^{148g}Pm	550.2-- 22.0	915.3-- 11.5		
^{148m}Pm	550.2-- 95.6	630.0-- 89.1		

Table C-3 (cont.)

NUCLIDE	(ENERGY (keV)--BRANCHING RATIO (%))		
^{148}Eu	550.3-- 99.0	611.3-- 19.3	629.9-- 70.9
	725.7-- 13.0		
^{149}Gd	149.6-- 41.7	298.5-- 22.6	
^{151}Pm	167.7-- 7.8	275.2-- 6.6	340.1-- 22.4
	717.6-- 4.0		
^{151}Gd	153.6-- 5.10	243.2-- 4.59	
^{151g}Tb	108.3-- 25.0	251.7-- 26.0	287.0-- 25.0
^{152}Dy	256.8-- 97.5		
^{152g}Tb	344.3-- 57.0		
^{153}Gd	97.4-- 30.1	103.2-- 21.8	
^{153}Tb	211.9-- 32.5		
^{154g}Tb	123.1-- 28.0		
^{155}Tb	105.3-- 23.0	180.1-- 6.83	262.3-- 4.8
^{155}Dy	227.0-- 68.8		
^{156g}Tb	199.2-- 40.2	534.3-- 67.0	1222.4-- 31.2
^{157}Dy	326.2-- 93.2		
^{160}Tb	298.6-- 27.4	879.4-- 30.0	966.2-- 25.2
^{160m}Ho	728.1-- 30.0		
^{160}Er	728.1-- 36.	879.1-- 23.	961.9-- 21.
	965.8-- 21.		

A tabulation of observed gamma-ray photopeak energies and associated branching ratios required to identify a given nuclide. This tabulation represents the fewest gamma-rays observed for a given nuclide (other characteristic gamma-rays may have been observed for various nuclides).

Table C-3 (cont.)

2.9 GeV ^{12}C + ^{165}Ho
MASS YIELD TABLE (mb)

NUCLIDE	MEASURED YIELD	CALCULATED INDEPENDENT YIELD	MASS YIELD	YIELD TYPE
^{24}Na	10. ± 1.	8.1 ± 0.8	12. ± 1.	C
^{28}Mg	2.0 ± 0.2	2.0 ± 0.2	10. ± 1.	C
^{46g}Sc	4.0 ± 0.4	4.0 ± 0.4	7.4 ± 0.7	I
^{47}Sc	1.6 ± 0.6	1.5 ± 0.6	5. ± 2.	C
^{48}Sc	1.1 ± 0.1	1.1 ± 0.1	9. ± 2.	I
^{48}V	1.4 ± 0.1	1.4 ± 0.1	4.9 ± 0.5	C
^{51}Cr	5.3 ± 0.6	4.7 ± 0.6	10. ± 2.	C
^{54}Mn	4.6 ± 0.7	4.6 ± 0.7	8. ± 1.	I
^{59}Fe	1.2 ± 0.1	1.2 ± 0.1	8.2 ± 0.8	C
^{65}Zn	4.7 ± 0.5	3.1 ± 0.3	8.4 ± 0.8	C
^{69}Ge	4.5 ± 0.5	3.0 ± 0.3	8.5 ± 0.9	C
^{71}As	2.7 ± 0.3	1.9 ± 0.2	5.6 ± 0.6	C
^{72}As	3. ± 1.	2. ± 1.	7. ± 3.	C
^{74}As	2.4 ± 0.2	2.4 ± 0.2	8.7 ± 0.9	I
^{75}Se	4.9 ± 0.5	2.7 ± 0.3	7.3 ± 0.7	C
^{76}Kr	1.7 ± 0.3	1.4 ± 0.3	8. ± 1.	C
^{77g}Br	4.2 ± 0.4	2.4 ± 0.2	6.3 ± 0.6	C
^{82}Sr	2.3 ± 0.7	2.2 ± 0.6	8. ± 2.	C
^{83g}Sr	5.2 ± 0.7	4.5 ± 0.6	9. ± 1.	C
^{83}Rb	8.5 ± 0.9	3.8 ± 0.4	10. ± 1.	C
^{84g}Rb	1.8 ± 0.2	1.8 ± 0.2	11. ± 1.	I
^{85g}Sr	7.8 ± 0.8	3.7 ± 0.4	8.6 ± 0.9	C
^{86g}Y	6.9 ± 0.7	5.0 ± 0.5	8.5 ± 0.9	C
^{86}Zr	2.3 ± 0.3	2.3 ± 0.3	12. ± 2.	C
^{87g}Y	9.0 ± 0.9	4.8 ± 0.5	22. ± 2.	C
^{87m}Y	11. ± 1.	5.6 ± 0.6	-	C
^{88}Y	5.3 ± 0.5	5.2 ± 0.5	20. ± 2.	C
^{88}Zr	11. ± 1.	8.6 ± 0.9	15. ± 2.	C
^{89g}Zr	7.9 ± 0.8	4.7 ± 0.5	8.8 ± 0.9	C
^{90}Nb	7.4 ± 0.7	5.8 ± 0.6	10. ± 1.	C
^{95g}Nb	0.51 ± 0.07	0.51 ± 0.07	16. ± 2.	C
^{97}Ru	6.1 ± 0.6	5.9 ± 0.6	17. ± 2.	C
^{99m}Rh	2. ± 1.	-	-	C
^{100g}Rh	4.3 ± 0.4	1.2 ± 0.4	7.5 ± 0.8	C
^{101m}Rh	5. ± 1.	-	-	C
^{105g}Ag	11. ± 1.	10. ± 1.	15. ± 2.	C
^{111g}In	12. ± 1.	6.2 ± 0.6	12. ± 1.	C

Table C-4

2.9 GeV ^{12}C + ^{165}Ho
YIELD TABLE (cont)

NUCLIDE	MEASURED YIELD	CALCULATED INDEPENDENT YIELD	MASS YIELD	YIELD TYPE
^{121g}Te	18. ± 2.	5.5 ± 0.6	32. ± 3.	C
^{121m}Te	0.98 ± 0.01	1.0 ± 0.1	-	I
^{122}Xe	15. ± 2.	12. ± 1.	35. ± 4.	C
^{123}I	26. ± 3.	10. ± 1.	30. ± 3.	C
^{125g}Xe	29. ± 3.	15. ± 2.	37. ± 4.	C
^{127g}Xe	21. ± 2.	5.9 ± 0.6	33. ± 3.	C
^{127}Cs	29. ± 5.	17. ± 3.	37. ± 7.	C
^{128}Ba	16. ± 2.	12. ± 1.	30. ± 3.	C
^{129}Cs	27. ± 3.	9.1 ± 0.9	35. ± 4.	C
^{131g}Ba	24. ± 2.	11. ± 1.	31. ± 3.	C
^{134g}Cs	25. ± 3.	-	-	C
^{135g}Cs	26. ± 3.	16. ± 2.	35. ± 4.	C
^{145}Eu	24. ± 2.	11. ± 1.	26. ± 3.	C
^{146}Eu	8.4 ± 0.8	-	-	C
^{146}Gd	25. ± 3.	-	-	C
^{147}Eu	42. ± 4.	22. ± 2.	92. ± 9.	C
^{147}Gd	25. ± 3.	17. ± 2.	29. ± 4.	C
^{148}Eu	6.7 ± 0.7	6.7 ± 0.7	43. ± 4.	I
^{149}Gd	30. ± 3.	16. ± 2.	35. ± 4.	C
^{151}Gd	23. ± 2.	10. ± 1.	37. ± 4.	C
^{151g}Tb	18. ± 2.	16. ± 2.	38. ± 4.	C
^{152g}Tb	35. ± 4.	28. ± 3.	52. ± 5.	C
^{153}Gd	36. ± 4.	10. ± 1.	59. ± 6.	C
^{153}Tb	33. ± 3.	24. ± 2.	41. ± 4.	C
^{155}Tb	42. ± 4.	18. ± 2.	46. ± 5.	C
^{155}Dy	35. ± 4.	31. ± 3.	52. ± 5.	C
^{156g}Tb	10. ± 1.	-	-	C
^{157}Dy	44. ± 4.	29. ± 3.	47. ± 5.	C
^{160}Er	11. ± 1.	10. ± 1.	46. ± 5.	C

A tabulation of measured nuclidic yields and calculated independent and mass yields. The Yield Type column indicates whether yields are independent or cumulative yields.

Table C-4 (cont.)

7.7 GeV ^{20}Ne + ^{165}Ho
MASS YIELD TABLE (mb)

NUCLIDE	MEASURED YIELD	CALCULATED INDEPENDENT YIELD	MASS YIELD	YIELD TYPE
^{28}Mg	2.4 ± 0.2	2.3 ± 0.2	13. ± 1.	C
^{44g}Sc	2.6 ± 0.7	2.6 ± 0.7	15. ± 3.	C
^{44m}Sc	3.0 ± 0.4	3.0 ± 0.4	-	I
^{46g}Sc	8.4 ± 0.8	8.4 ± 0.8	15. ± 2.	I
^{47}Sc	3.6 ± 0.4	3.6 ± 0.4	10. ± 1.	C
^{48}Sc	2.5 ± 0.2	2.5 ± 0.2	16. ± 2.	I
^{48}V	2.9 ± 0.3	2.8 ± 0.3	11. ± 1.	C
^{52g}Mn	1.5 ± 0.2	1.4 ± 0.1	8.8 ± 0.9	C
^{56}Co	1.1 ± 0.1	1.1 ± 0.1	11. ± 2.	C
^{58g}Co	6.3 ± 0.6	-	-	I
^{59}Fe	2.0 ± 0.2	2.0 ± 0.2	12. ± 1.	C
^{69}Ge	6. ± 1.	4. ± 1.	10. ± 2.	C
^{72}As	6.5 ± 0.9	6.4 ± 0.9	14. ± 2.	C
^{73g}Se	4.2 ± 0.4	3.5 ± 0.3	9.1 ± 0.9	C
^{74}As	3.1 ± 0.3	3.1 ± 0.3	11. ± 1.	I
^{75}Se	7.0 ± 0.7	4.0 ± 0.4	9.1 ± 0.9	C
^{82m}Rb	5.3 ± 0.6	-	-	I
^{83}Rb	11. ± 1.	5.1 ± 0.5	14. ± 1.	C
^{86g}Y	8. ± 2.	5. ± 1.	12. ± 3.	C
^{87g}Y	9. ± 2.	6. ± 1.	24. ± 4.	C
^{87m}Y	14. ± 2.	7.2 ± 0.8	-	C
^{89g}Zr	11. ± 1.	6.8 ± 0.7	15. ± 2.	C
^{90g}Nb	9.4 ± 0.9	7.8 ± 0.8	19. ± 2.	C
^{93m}Mo	4.5 ± 0.5	-	-	I
^{95g}Nb	1.0 ± 0.1	1.0 ± 0.1	14. ± 1.	C
^{95g}Tc	9.4 ± 0.9	7.0 ± 0.7	42. ± 12.	C
^{95m}Tc	13. ± 6.	13. ± 6.	-	C
^{97}Ru	7.6 ± 0.8	6.1 ± 0.6	16. ± 2.	C
^{101m}Rh	7. ± 1.	-	-	C
^{105g}Rh	5.0 ± 0.9	4.5 ± 0.9	50. ± 9.	C
^{105g}Ag	17. ± 4.	10. ± 2.	27. ± 7.	C
^{106m}Ag	3.0 ± 0.3	-	-	I
^{110m}In	8. ± 3.	-	-	C
^{111g}In	14. ± 1.	7.8 ± 0.8	21. ± 2.	C
^{116}Te	16. ± 3.	13. ± 2.	44. ± 7.	C
^{117}Te	20. ± 3.	14. ± 2.	38. ± 5.	C
^{119m}Te	2.9 ± 0.4	-	-	I

Table C-5

7.7 GeV ^{20}Ne + ^{165}Ho
YIELD TABLE (cont)

NUCLIDE	MEASURED YIELD	CALCULATED INDEPENDENT YIELD	MASS YIELD	YIELD TYPE
^{121g}Te	18. ± 2.	-	-	I
^{121}I	29. ± 5.	16. ± 2.	38. ± 6.	C
^{123}I	23. ± 4.	8. ± 1.	29. ± 5.	C
^{125g}Xe	21. ± 2.	10. ± 1.	28. ± 3.	C
^{126}Ba	14. ± 6.	11. ± 4.	38. ± 16.	C
^{127g}Xe	21. ± 2.	5.8 ± 0.6	39. ± 4.	C
^{128}Ba	31. ± 4.	19. ± 2.	46. ± 6.	C
^{129}Cs	30. ± 3.	8.7 ± 0.9	55. ± 6.	C
^{131g}Ba	40. ± 4.	13. ± 1.	62. ± 6.	C
^{132}Ce	23. ± 2.	17. ± 2.	46. ± 5.	C
^{135g}Ce	36. ± 5.	16. ± 3.	49. ± 6.	C
^{139g}Ce	29. ± 3.	2.8 ± 0.3	110. ± 30.	C
^{143}Pm	39. ± 4.	15. ± 2.	52. ± 5.	C
^{145}Eu	41. ± 4.	32. ± 3.	81. ± 8.	C
^{146}Gd	28. ± 20.	-	-	C
^{147}Eu	47. ± 5.	28. ± 3.	62. ± 6.	C
^{147}Gd	27. ± 3.	22. ± 3.	74. ± 7.	C
^{148m}Pm	6. ± 1.	-	-	I
^{149}Gd	40. ± 4.	28. ± 3.	60. ± 6.	C
^{151g}Tb	60. ± 18.	47. ± 14.	115. ± 35.	C
^{152g}Tb	47. ± 13.	32. ± 9.	69. ± 19.	C
^{152}Dy	21. ± 4.	18. ± 3.	92. ± 18.	C
^{153}Gd	35. ± 4.	9.4 ± 0.9	57. ± 6.	C
^{155}Tb	33. ± 14.	13. ± 5.	47. ± 21.	C
^{155}Dy	56. ± 11.	37. ± 7.	80. ± 15.	C
^{156g}Tb	11. ± 1.	-	-	C
^{157}Dy	68. ± 7.	31. ± 3.	85. ± 9.	C
^{160}Tb	6. ± 1.	6. ± 1.	43. ± 9.	I

A tabulation of measured nuclidic yields and calculated independent and mass yields. The Yield Type column indicates whether yields are independent or cumulative yields.

Table C-5 (cont.)

12.5 GeV ^{12}C + ^{165}Ho
MASS YIELD TABLE

NUCLIDE	MEASURED YIELD	CALCULATED INDEPENDENT YIELD	MASS YIELD	YIELD TYPE
^{22}Na	19. ± 2.	18. ± 2.	44. ± 5.	C
^{24}Na	30. ± 3.	26. ± 3.	47. ± 5.	C
^{28}Mg	5. ± 1.	5. ± 1.	40. ± 8.	C
^{43}K	6. ± 1.	6. ± 1.	24. ± 6.	C
^{44m}Sc	5. ± 1.	-	-	I
^{46g}Sc	20. ± 2.	20. ± 2.	30. ± 3.	I
^{47}Sc	6.2 ± 0.6	6.2 ± 0.6	17. ± 2.	C
^{48g}Sc	2.0 ± 0.2	2.0 ± 0.2	18. ± 2.	I
^{48}V	3.5 ± 0.3	3.5 ± 0.3	16. ± 2.	C
^{51}Cr	13. ± 1.	13. ± 1.	28. ± 3.	C
^{52g}Mn	1.7 ± 0.2	1.7 ± 0.2	15. ± 2.	C
^{54}Mn	19. ± 2.	19. ± 2.	29. ± 3.	C
^{56}Mn	9. ± 3.	8. ± 3.	21. ± 8.	C
^{56}Co	1.9 ± 0.2	1.9 ± 0.2	18. ± 2.	C
^{58g}Co	16. ± 2.	-	-	C
^{59}Fe	3.8 ± 0.4	3.6 ± 0.4	16. ± 2.	C
^{69}Ge	4.4 ± 0.5	4.3 ± 0.5	29. ± 3.	C
^{71}As	3.9 ± 0.4	3.8 ± 0.4	38. ± 4.	C
^{74}As	31. ± 3.	31. ± 3.	52. ± 5.	I
^{75}Se	20. ± 3.	18. ± 3.	40. ± 5.	C
^{76}As	9.0 ± 0.9	9.0 ± 0.9	36. ± 4.	I
^{77g}Br	15. ± 1.	14. ± 1.	39. ± 4.	C
^{82}Sr	1.8 ± 0.2	1.7 ± 0.2	31. ± 4.	C
^{83}Rb	26. ± 3.	23. ± 2.	37. ± 4.	C
^{85}Sr	29. ± 3.	25. ± 2.	41. ± 4.	C
^{86}Zr	0.6 ± 0.3	0.3 ± 0.3	31. ± 18.	C
^{86g}Y	8.7 ± 0.9	8.4 ± 0.8	26. ± 3.	C
^{87m}Y	18. ± 2.	-	-	C
^{88}Zr	8.8 ± 0.9	8.5 ± 0.9	35. ± 4.	C
^{88}Y	23. ± 2.	23. ± 2.	39. ± 4.	C
^{89g}Zr	13. ± 1.	12. ± 1.	25. ± 3.	C
^{90g}Nb	6.8 ± 0.7	6.6 ± 0.7	37. ± 4.	C
^{90m}Y	11. ± 1.	-	-	I
^{93m}Mo	2.5 ± 0.5	-	-	I
^{95g}Nb	1.5 ± 0.3	1.5 ± 0.3	22. ± 4.	C
^{95g}Tc	11. ± 4.	9. ± 3.	21. ± 8.	C
^{96g}Tc	4.2 ± 0.4	-	-	C
^{97}Ru	10. ± 2.	8. ± 1.	25. ± 4.	C
^{99m}Rh	7. ± 2.	-	-	C

Table C-6

12.5 GeV ^{12}C + ^{165}Ho
YIELD TABLE (cont)

NUCLIDE	MEASURED YIELD	CALCULATED INDEPENDENT YIELD	MASS YIELD	YIELD TYPE
^{100g}Rh	10. ± 3.	9. ± 3.	22. ± 6.	C
^{100}Pd	2.7 ± 0.3	2.6 ± 0.3	27. ± 3.	C
^{101m}Rh	19. ± 2.	-	-	C
^{102g}Rh	13. ± 5.	-	-	C
^{105g}Ag	10. ± 1.	10. ± 1.	30. ± 3.	C
^{105g}Rh	4.3 ± 0.8	4.3 ± 0.8	40. ± 7.	C
^{106m}Ag	3.1 ± 0.4	-	-	I
^{110m}Ag	8. ± 3.	-	-	I
^{111g}In	27. ± 3.	23. ± 2.	43. ± 4.	C
^{114m}In	1.4 ± 0.1	-	-	I
^{119g}Te	13. ± 2.	7. ± 1.	23. ± 3.	C
^{119m}Te	4. ± 1.	2.2 ± 0.4	-	C
^{120b}Sb	0.25 ± 0.03	-	-	C
^{121g}Te	22. ± 2.	6.3 ± 0.6	34. ± 3.	C
^{121m}Te	5.8 ± 0.6	-	-	I
^{122}Xe	11. ± 2.	9. ± 2.	22. ± 5.	C
^{123m}Te	0.8 ± 0.4	-	-	I
^{123}I	20. ± 3.	6.5 ± 0.9	25. ± 4.	C
^{125g}Xe	20. ± 4.	8. ± 2.	25. ± 5.	C
^{127}Xe	14. ± 2.	2.9 ± 0.4	27. ± 4.	C
^{128}Ba	20. ± 2.	16. ± 2.	31. ± 3.	C
^{131g}Ba	29. ± 3.	10. ± 1.	37. ± 4.	C
^{132}La	42. ± 7.	17. ± 3.	34. ± 6.	C
^{135g}Ce	24. ± 5.	13. ± 3.	29. ± 6.	C
^{145}Eu	27. ± 3.	19. ± 2.	42. ± 4.	C
^{146}Eu	26. ± 3.	-	-	C
^{146}Gd	15. ± 2.	-	-	C
^{147}Eu	37. ± 10.	18. ± 5.	47. ± 12.	C
^{147}Gd	18. ± 2.	15. ± 2.	37. ± 4.	C
^{148m}Pm	15. ± 2.	-	-	I
^{148}Eu	15. ± 2.	15. ± 1.	53. ± 5.	C
^{149}Gd	30. ± 3.	18. ± 2.	39. ± 4.	C

A tabulation of measured nuclidic yields and calculated independent and mass yields. The Yield Type column indicates whether yields are independent or cumulative yields.

Table C-6 (cont.)

12.5 GeV ^{12}C + ^{152}Sm
MASS YIELD TABLE (mb)

NUCLIDE	MEASURED YIELD	CALCULATED INDEPENDENT YIELD	MASS YIELD	YIELD TYPE
^{22}Na	11. ± 1.	10. ± 1.	23. ± 2.	C
^{24}Na	17. ± 2.	15. ± 2.	29. ± 3.	C
^{28}Mg	2.8 ± 0.3	2.8 ± 0.3	21. ± 2.	C
^{42}K	5. ± 2.	5. ± 2.	10. ± 5.	C
^{43}K	2.2 ± 0.4	2.2 ± 0.4	9. ± 1.	C
^{44m}Sc	1.9 ± 0.2	-	-	I
^{46g}Sc	5.4 ± 0.5	5.4 ± 0.5	9.5 ± 0.9	I
^{47}Sc	3.9 ± 0.5	3.9 ± 0.5	11. ± 1.	C
^{48}Sc	0.9 ± 0.1	0.9 ± 0.1	6.0 ± 0.7	I
^{48}V	2.2 ± 0.2	2.2 ± 0.2	9.1 ± 0.9	C
^{52g}Mn	1.3 ± 0.1	1.2 ± 0.1	9.0 ± 0.9	C
^{54}Mn	6.0 ± 0.6	6.0 ± 0.6	11. ± 1.	I
^{56}Mn	3. ± 2.	3. ± 2.	7. ± 4.	C
^{56}Co	0.8 ± 0.1	0.8 ± 0.1	11. ± 2.	C
^{58g}Co	8.8 ± 0.9	-	-	C
^{59}Fe	1.5 ± 0.2	1.5 ± 0.2	6.5 ± 0.6	C
^{65}Zn	5.7 ± 0.6	4.4 ± 0.4	7.5 ± 0.7	C
^{69m}Zn	0.4 ± 0.1	-	-	I
^{71}As	2.8 ± 0.3	2.6 ± 0.3	6.9 ± 0.7	C
^{72}As	3.5 ± 0.4	3.5 ± 0.3	6.1 ± 0.6	C
^{72}Se	0.5 ± 0.1	0.5 ± 0.1	6. ± 2.	C
^{74}As	2.1 ± 0.2	2.1 ± 0.2	4.9 ± 0.5	I
^{75}Se	5.7 ± 0.6	4.4 ± 0.4	7.3 ± 0.7	C
^{76}As	1.1 ± 0.6	1.1 ± 0.6	14. ± 8.	I
^{76g}Br	2.4 ± 0.5	2.2 ± 0.5	6. ± 1.	C
^{77g}Br	5.4 ± 0.5	4.5 ± 0.5	8.0 ± 0.8	C
^{79g}Kr	4. ± 2.	4. ± 2.	8. ± 3.	C
^{82m}Rb	2.8 ± 0.4	-	-	I
^{83}Rb	4.3 ± 0.4	3.4 ± 0.3	5.8 ± 0.6	C
^{84g}Rb	6.6 ± 0.7	6.6 ± 0.7	12. ± 1.	C
^{85g}Sr	8.1 ± 0.9	3.1 ± 0.4	9. ± 1.	C
^{86}Zr	1.3 ± 0.4	1.3 ± 0.4	5. ± 2.	C
^{86g}Y	16. ± 2.	5.8 ± 0.8	10. ± 1.	C
^{87g}Y	5.8 ± 0.6	3.4 ± 0.3	16. ± 2.	C
^{87m}Y	9. ± 2.	4.4 ± 0.4	-	C
^{88}Zr	9. ± 1.	7. ± 1.	11. ± 2.	C
^{88}Y	2.5 ± 0.2	2.0 ± 0.2	9.0 ± 0.9	C
^{89g}Zr	8.1 ± 0.8	4.6 ± 0.5	8.7 ± 0.9	C
^{90m}Y	10. ± 1.	-	-	I

Table C-7

12.5 GeV ^{12}C + ^{152}Sm
YIELD TABLE (cont)

NUCLIDE	MEASURED YIELD	INDEPENDENT YIELD	MASS YIELD	YIELD TYPE
^{90}Mo	0.9 ± 0.5	0.9 ± 0.5	9. ± 5.	C
^{90g}Nb	4.8 ± 0.5	3.8 ± 0.4	6.9 ± 0.7	C
^{93m}Mo	2.3 ± 0.2	-	-	I
^{95g}Nb	0.5 ± 0.1	0.5 ± 0.1	7. ± 2.	C
^{95g}Tc	6.5 ± 0.7	4.8 ± 0.5	22. ± 2.	C
^{95m}Tc	6.0 ± 3.0	6. ± 3.	-	C
^{96}Nb	1.4 ± 0.4	0.9 ± 0.3	19. ± 7.	C
^{97}Ru	6.6 ± 0.7	5.3 ± 0.5	13. ± 1.	C
^{99}Mo	0.13 ± 0.07	0.13 ± 0.07	11. ± 5.	C
^{100g}Rh	8.1 ± 0.8	7.2 ± 0.7	16. ± 2.	C
^{100}Pd	2.8 ± 0.3	2.6 ± 0.3	18. ± 2.	C
^{101}Pd	4. ± 1.	4. ± 1.	13. ± 5.	C
^{101g}Rh	1.8 ± 0.6	1.8 ± 0.6	16. ± 2.	C
^{101m}Rh	8.7 ± 2.5	5.5 ± 0.6	-	C
^{105g}Ag	9.4 ± 0.9	7.0 ± 0.7	16. ± 2.	C
^{105g}Rh	2.3 ± 0.5	2.2 ± 0.5	18. ± 8.	C
^{106m}Ag	2.5 ± 0.4	-	-	I
^{111g}In	10 ± 1.	6.1 ± 0.6	13. ± 1.	C
^{114m}In	18. ± 6.	-	-	I
^{119g}Te	6. ± 3.	3. ± 1.	15. ± 3.	C
^{119m}Te	3. ± 1.	3. ± 1.	-	I
^{121g}Te	14. ± 1.	4.1 ± 0.4	27. ± 3.	C
^{121m}Te	1.4 ± 0.2	1.4 ± 0.2	-	I
^{121}I	16. ± 3.	8. ± 1.	18. ± 3.	C
^{122}Xe	10. ± 1.	8.0 ± 0.8	20. ± 2.	C
^{123m}Te	0.8 ± 0.2	-	-	I
^{123}I	18. ± 3.	6.0 ± 0.9	22. ± 3.	C
^{124}I	3.8 ± 0.9	3.8 ± 0.9	23. ± 6.	I
^{125g}Xe	17. ± 2.	7.6 ± 0.8	21. ± 2.	C
^{127g}Xe	14. ± 1.	3.3 ± 0.3	25. ± 2.	C
^{127}Cs	17. ± 7.	9. ± 4.	21. ± 8.	C
^{128}Ba	14. ± 1.	11. ± 1.	24. ± 2.	C
^{131g}Ba	17. ± 2.	5.4 ± 0.6	29. ± 3.	C
^{132}Cs	0.4 ± 0.1	0.4 ± 0.1	34. ± 11.	I
^{132g}La	30. ± 3.	8.7 ± 0.9	25. ± 2.	C
^{132}Ce	18. ± 3.	14. ± 2.	36. ± 5.	C
^{133g}Ba	12. ± 1.	-	-	C

Table C-7 (cont.)

12.5 GeV ^{12}C + ^{152}Sm
YIELD TABLE (cont)

NUCLIDE	MEASURED YIELD	CALCULATED INDEPENDENT YIELD	MASS YIELD	YIELD TYPE
^{135g}Ce	18. ± 2.	8.3 ± 0.8	24. ± 2.	C
^{139g}Ce	15. ± 2.	2.0 ± 0.2	47. ± 5.	C
^{143}Pm	18. ± 2.	15. ± 1.	60. ± 6.	C
^{144}Pm	22. ± 2.	22. ± 2.	65. ± 7.	C
^{145}Eu	1.3 ± 0.1	1.3 ± 0.1	55. ± 12.	C
^{146}Eu	2.4 ± 0.3	-	-	C
^{147}Nd	9. ± 1.	8. ± 1.	61. ± 10.	C
^{147}Eu	5. ± 2.	5. ± 2.	46. ± 17.	C
^{148g}Pm	10. ± 1.	10. ± 1.	63. ± 6.	I
^{148m}Pm	11. ± 1.	11. ± 1.	-	I
^{151}Pm	5.0 ± 0.5	4.7 ± 0.5	70. ± 7.	C
^{151}Tb	1.8 ± 0.9	1.7 ± 0.9	59. ± 30.	C
^{152g}Tb	0.5 ± 0.1	0.4 ± 0.1	7. ± 2.	C

A tabulation of measured nuclidic yields and calculated independent and mass yields. The Yield Type column indicates whether yields are independent or cumulative yields.

Table C-7 (cont.)

12.5 GeV ^{12}C + ^{144}Sm
MASS YIELD TABLE (mb)

NUCLIDE	MEASURED YIELD	CALCULATED INDEPENDENT YIELD	MASS YIELD	YIELD TYPE
^{28}Mg	2.4 ± 0.2	2.4 ± 0.2	26. ± 3.	C
^{42}K	4. ± 2.	4. ± 2.	12. ± 5.	C
^{44m}Sc	3.4 ± 0.7	-	-	I
^{46g}Sc	6.0 ± 0.6	6.0 ± 0.6	12. ± 1.	I
^{47}Sc	3.5 ± 0.4	3.5 ± 0.4	14. ± 1.	C
^{48}Sc	0.76 ± 0.08	0.76 ± 0.08	9.0 ± 0.9	I
^{48}V	4.0 ± 0.4	3.8 ± 0.4	11. ± 1.	C
^{51}Cr	9.1 ± 0.9	8.0 ± 0.8	15. ± 2.	C
^{52g}Mn	2.3 ± 0.2	2.2 ± 0.2	9.3 ± 0.9	C
^{54}Mn	8. ± 1.	8. ± 1.	14. ± 2.	I
^{56}Co	1.6 ± 0.6	1.5 ± 0.6	11. ± 5.	C
^{57}Co	5.3 ± 0.5	4.9 ± 0.5	15. ± 1.	C
^{58g}Co	13. ± 2.	-	-	C
^{59}Fe	0.9 ± 0.1	0.9 ± 0.1	7. ± 1.	C
^{65}Zn	8.9 ± 0.9	6.9 ± 0.7	14. ± 1.	C
^{69m}Zn	0.4 ± 0.3	-	-	I
^{69}Ge	4.3 ± 0.7	3.9 ± 0.6	10. ± 2.	C
^{71}As	5.5 ± 0.6	5.0 ± 0.5	17. ± 2.	C
^{72}As	5.1 ± 0.5	5.0 ± 0.5	10. ± 1.	C
^{72}Se	1.2 ± 0.3	1.1 ± 0.3	12. ± 3.	C
^{74}As	6.6 ± 0.7	6.6 ± 0.7	14. ± 1.	I
^{75}Se	9.0 ± 0.9	7.0 ± 0.7	14. ± 1.	C
^{76}As	2.7 ± 0.3	2.7 ± 0.3	18. ± 3.	I
^{76g}Br	3.8 ± 0.9	3.5 ± 0.9	11. ± 3.	C
^{77g}Br	7.7 ± 0.8	6.4 ± 0.6	14. ± 1.	C
^{79g}Kr	7.8 ± 0.8	6.7 ± 0.7	17. ± 2.	C
^{82}Sr	7. ± 2.	6. ± 2.	21. ± 5.	C
^{82m}Rb	4. ± 1.	-	-	I
^{83g}Sr	8.3 ± 0.9	6.4 ± 0.7	16. ± 2.	C
^{83}Rb	13. ± 1.	8.5 ± 0.9	23. ± 2.	C
^{84g}Rb	11. ± 2.	5.7 ± 0.9	24. ± 4.	I
^{85g}Sr	13. ± 1.	6.8 ± 0.7	17. ± 2.	C
^{86}Rb	1.4 ± 0.5	1.4 ± 0.5	31. ± 10.	I
^{86}Zr	4.3 ± 0.4	3.9 ± 0.4	21. ± 2.	C
^{86g}Y	15. ± 2.	11. ± 1.	23. ± 2.	C
^{87g}Y	9. ± 2.	4.0 ± 0.9	30. ± 5.	C
^{87m}Y	14. ± 1.	7.8 ± 0.8	-	C

Table C-8

12.5 GeV ^{12}C + ^{144}Sm
YIELD TABLE (cont)

NUCLIDE	MEASURED YIELD	CALCULATED INDEPENDENT YIELD	MASS YIELD	YIELD TYPE
^{88}Y	1.8 ± 0.5	1.6 ± 0.4	5. ± 1.	C
^{88}Zr	15. ± 2.	11. ± 1.	26. ± 3.	C
^{89g}Zr	13. ± 1.	7.9 ± 0.8	17. ± 2.	C
^{90m}Y	2.1 ± 0.2	-	-	I
^{90g}Nb	10. ± 1.	7.7 ± 0.8	19. ± 2.	C
^{90}Mo	2.2 ± 0.7	2.1 ± 0.7	20. ± 6.	C
^{93m}Mo	3.0 ± 0.3	-	-	I
^{95g}Tc	21. ± 2.	15. ± 2.	35. ± 4.	C
^{95m}Tc	10. ± 3.	10. ± 3.	-	C
^{96g}Tc	3.0 ± 0.3	-	-	I
^{97}Ru	13. ± 1.	9.2 ± 0.9	20. ± 2.	C
^{99g}Rh	0.7 ± 0.3	0.7 ± 0.3	23. ± 5.	C
^{99m}Rh	11. ± 2.	9. ± 2.	-	C
^{100g}Rh	16. ± 2.	12. ± 1.	26. ± 3.	C
^{100}Pd	7.2 ± 0.7	6.5 ± 0.7	32. ± 3.	C
^{101g}Rh	3.3 ± 0.8	3.3 ± 0.8	27. ± 3.	C
^{101m}Rh	15. ± 2.	9.4 ± 0.9	-	C
^{105g}Rh	1.6 ± 0.6	1.6 ± 0.6	21. ± 2.	C
^{105g}Ag	17. ± 2.	13. ± 1.	28. ± 3.	C
^{106m}Ag	1.9 ± 0.2	-	-	I
^{111g}In	17. ± 2.	11. ± 1.	23. ± 2.	C
^{119g}Te	21. ± 2.	11. ± 1.	31. ± 4.	C
^{119m}Te	1.8 ± 0.2	1.8 ± 0.2	-	I
^{121g}Te	23. ± 2.	6.9 ± 0.7	37. ± 4.	C
^{121m}Te	0.6 ± 0.2	0.6 ± 0.2	-	I
^{121}I	28. ± 6.	21. ± 4.	52. ± 11.	C
^{122}Xe	11. ± 1.	10. ± 1.	51. ± 5.	C
^{123m}Te	0.4 ± 0.1	-	-	I
^{123}I	31. ± 3.	16. ± 2.	37. ± 4.	C
^{125g}Xe	27. ± 3.	18. ± 2.	38. ± 4.	C
^{127g}Xe	29. ± 3.	11. ± 1.	38. ± 4.	C
^{127}Cs	25. ± 6.	17. ± 4.	38. ± 10.	C
^{128}Ba	19. ± 2.	16. ± 2.	52. ± 5.	C
^{129}Cs	34. ± 3.	15. ± 2.	42. ± 4.	C
^{131g}Ba	30. ± 3.	16. ± 2.	38. ± 4.	C
^{132g}La	40. ± 4.	22. ± 2.	49. ± 5.	C
^{133}Ba	18. ± 2.	-	-	C

Table C-8 (cont.)

12.5 GeV ^{12}C + ^{144}Sm
YIELD TABLE (cont)

NUCLIDE	MEASURED YIELD	CALCULATED INDEPENDENT YIELD	MASS YIELD	YIELD TYPE
^{135g}Ce	37. ± 4.	25. ± 3.	53. ± 5.	C
$^{141}Ce_*$	2.2 ± 0.2	1.9 ± 0.2	5.0 ± 0.5	C
$^{144}Ce_*$	4. ± 1.	4. ± 1.	57. ± 20.	C
$^{144}Pm^*$	1.4 ± 0.3	1.4 ± 0.3	18. ± 3.	I

A tabulation of measured nuclidic yields and calculated independent and mass yields. The Yield Type column indicates whether yields are independent or cumulative yields. Significant secondary contributions are expected for very near target nuclides (flagged with "*").

Table C-8 (cont.)

20.8 GeV ^{20}Ne + ^{165}Ho
MASS YIELD TABLE (mb)

NUCLIDE	MEASURED YIELD	CALCULATED INDEPENDENT YIELD	MASS YIELD	YIELD TYPE
^{28}Mg	6.1 ± 0.6	5.9 ± 0.6	33. ± 3.	C
^{44g}Sc	2.0 ± 0.4	2.0 ± 0.4	18. ± 3.	C
^{44m}Sc	4.2 ± 0.7	4.2 ± 0.7	-	I
^{46}Sc	11. ± 1.	11. ± 1.	19. ± 2.	I
^{47}Sc	7.3 ± 0.7	7.2 ± 0.7	19. ± 2.	C
^{48}Sc	2.8 ± 0.3	2.8 ± 0.3	18. ± 2.	I
^{48}V	4.4 ± 0.4	4.3 ± 0.4	18. ± 2.	C
^{51}Cr	13. ± 1.	12. ± 1.	27. ± 3.	C
^{52g}Mn	2.2 ± 0.2	2.1 ± 0.2	13. ± 1.	C
^{69}Ge	9. ± 1.	6. ± 1.	16. ± 2.	C
^{71}As	6.1 ± 0.6	4.6 ± 0.5	13. ± 1.	C
^{72}As	6. ± 1.	6. ± 1.	13. ± 3.	C
^{74}As	4.1 ± 0.4	4.1 ± 0.4	13. ± 1.	I
^{77g}Br	7.2 ± 0.7	4.5 ± 0.5	11. ± 1.	C
^{86g}Y	10. ± 3.	8. ± 2.	18. ± 5.	C
^{87g}Y	17. ± 2.	10. ± 1.	20. ± 2.	C
^{87m}Y	18. ± 2.	10. ± 1.	-	C
^{88}Y	5.9 ± 0.6	5.6 ± 0.6	17. ± 2.	C
^{94g}Tc	5.5 ± 0.6	4.5 ± 0.4	15. ± 1.	C
^{100g}Rh	9.0 ± 0.9	8.8 ± 0.9	24. ± 2.	C
^{101m}Rh	1. ± 2.	-	-	C
^{110m}In	9. ± 2.	-	-	C
^{111g}In	18. ± 2.	11. ± 1.	28. ± 3.	C
^{117}Te	17. ± 3.	13. ± 3.	37. ± 7.	C
^{121g}Te	21. ± 2.	7.7 ± 0.8	30. ± 3.	C
^{121}Xe	8.2 ± 0.8	7.3 ± 0.7	34. ± 4.	C
^{122}Xe	16. ± 2.	16. ± 2.	37. ± 4.	C
^{123}I	29. ± 3.	13. ± 1.	38. ± 4.	C
^{123}Xe	19. ± 2.	14. ± 1.	33. ± 3.	C
^{125g}Xe	26. ± 6.	13. ± 3.	32. ± 7.	C
^{127g}Xe	24. ± 2.	7.9 ± 0.8	40. ± 4.	C
^{127}Cs	28. ± 3.	16. ± 2.	39. ± 4.	C
^{128}Ba	25. ± 3.	18. ± 2.	48. ± 6.	C
^{129}Cs	34. ± 3.	13. ± 1.	50. ± 5.	C
^{131g}Ba	30. ± 2.	14. ± 1.	40. ± 4.	C
^{131}La	26. ± 3.	18. ± 2.	46. ± 6.	C
^{135g}Ce	30. ± 3.	19. ± 2.	44. ± 5.	C

Table C-9

20.8 GeV ^{20}Ne + ^{165}Ho
YIELD TABLE (cont)

NUCLIDE	MEASURED YIELD	CALCULATED INDEPENDENT YIELD	MASS YIELD	YIELD TYPE
^{145}Eu	27. ± 3.	25. ± 3.	106. ± 11.	C
^{147}Gd	26. ± 5.	24. ± 5.	94. ± 18.	C
^{149}Gd	32. ± 3.	27. ± 3.	67. ± 7.	C
^{151}Tb	23. ± 8.	21. ± 7.	72. ± 24.	C
^{152g}Tb	59. ± 13.	49. ± 11.	113. ± 25.	C
^{155}Tb	41. ± 7.	19. ± 3.	49. ± 8.	C
^{155}Dy	49. ± 5.	40. ± 4.	89. ± 9.	C
^{156g}Tb	16. ± 2.	-	-	C
^{157}Dy	70. ± 6.	40. ± 4.	84. ± 8.	C

A tabulation of measured nuclidic yields and calculated independent and mass yields. The Yield Type column indicates whether yields are independent or cumulative yields.

Table C-9 (cont.)

20.8 GeV ^{20}Ne + ^{nat}Ce
MASS YIELD TABLE (mb)

NUCLIDE	MEASURED YIELD	CALCULATED INDEPENDENT YIELD	MASS YIELD	YIELD TYPE
^{28}Mg	4.1 ± 0.4	4.1 ± 0.4	34. ± 3.	C
^{44g}Sc	1.4 ± 0.5	1.4 ± 0.5	14. ± 2.	C
^{44m}Sc	3.5 ± 0.4	3.5 ± 0.4	-	I
^{48}Sc	1.4 ± 0.1	1.4 ± 0.1	13. ± 1.	I
^{48}V	3.7 ± 0.4	3.6 ± 0.4	11. ± 1.	C
^{52g}Mn	2.2 ± 0.2	2.2 ± 0.2	11. ± 1.	C
^{59}Fe	1.6 ± 0.2	1.5 ± 0.2	11. ± 1.	C
^{69}Ge	7. ± 4.	6. ± 4.	9. ± 5.	C
^{72}As	11. ± 1.	11. ± 1.	14. ± 1.	C
^{73g}Se	4.8 ± 0.5	4.8 ± 0.5	11. ± 1.	C
^{75}Se	10. ± 8.	7. ± 6.	12. ± 9.	C
^{75}Br	4.6 ± 0.5	4.6 ± 0.5	13. ± 1.	C
^{76}As	1.1 ± 0.8	1.1 ± 0.8	28. ± 21.	I
^{83}Rb	17. ± 2.	6.4 ± 0.6	22. ± 2.	C
^{86g}Y	13. ± 1.	7.2 ± 0.7	16. ± 2.	C
^{87g}Y	23. ± 2.	13. ± 1.	30. ± 4.	C
^{87m}Y	20. ± 2.	11. ± 1.	-	C
^{88}Y	5.8 ± 0.9	5.3 ± 0.8	20. ± 3.	C
^{89g}Zr	17. ± 2.	9. ± 1.	22. ± 2.	C
^{90g}Nb	12. ± 1.	9.2 ± 0.9	21. ± 2.	C
^{93g}Tc	6. ± 1.	5. ± 1.	24. ± 7.	C
^{93m}Mo	5.2 ± 0.5	-	-	I
^{94g}Tc	7.2 ± 0.7	-	-	C
^{96g}Tc	6.2 ± 0.7	-	-	I
^{97}Ru	13. ± 1.	10. ± 1.	24. ± 2.	C
^{101m}Rh	19. ± 2.	-	-	C
^{103}Ag	6.9 ± 0.7	6.5 ± 0.7	34. ± 3.	C
^{104}Ag	13. ± 1.	11. ± 1.	30. ± 5.	C
^{105g}Ag	20. ± 2.	16. ± 2.	31. ± 3.	C
^{106m}Ag	6.2 ± 0.6	-	-	I
^{108m}In	7. ± 4.	-	-	C
^{110m}In	10. ± 2.	-	-	C
^{111g}In	25. ± 3.	15. ± 2.	30. ± 3.	C
^{119m}Te	10. ± 1.	-	-	I
^{120}I	24. ± 4.	23. ± 4.	44. ± 7.	C
^{121g}Te	34. ± 3.	11. ± 1.	44. ± 4.	C
^{121}I	40. ± 5.	37. ± 5.	59. ± 6.	C

Table C-10

20.8 GeV ^{20}Ne + ^{nat}Ce
YIELD TABLE (cont)

NUCLIDE	MEASURED YIELD	CALCULATED INDEPENDENT YIELD	MASS YIELD	YIELD TYPE
^{122}Xe	22. ± 2.	18. ± 2.	41. ± 4.	C
^{123}I	59. ± 6.	22. ± 2.	65. ± 7.	C
^{123}Xe	38. ± 4.	27. ± 3.	40. ± 4.	C
^{124}I	5.7 ± 0.6	5.7 ± 0.6	41. ± 4.	I
^{125g}Xe	54. ± 5.	27. ± 3.	43. ± 4.	C
^{125}Cs	35. ± 7.	27. ± 6.	93. ± 21.	C
^{127g}Xe	53. ± 5.	15. ± 2.	70. ± 11.	C
^{127}Cs	27. ± 10.	16. ± 6.	49. ± 18.	C
^{129}Cs	33. ± 3.	11. ± 1.	44. ± 4.	C
^{131g}Ba	60. ± 6.	27. ± 3.	66. ± 7.	C
^{131}La	32. ± 8.	23. ± 6.	63. ± 17.	C
^{132g}La	43. ± 5.	24. ± 3.	60. ± 9.	C
^{132m}La*	26. ± 6.	26 ± 6.	-	I
^{132}Ce*	15. ± 2.	13. ± 1.	87. ± 10.	C
^{133g}Ce*	9. ± 5.	8. ± 4.	18. ± 10.	C
^{135g}Ce	44. ± 4.	28. ± 3.	61. ± 6.	C

A tabulation of measured nuclidic yields and calculated independent and mass yields. The Yield Type column indicates whether yields are independent or cumulative yields. Significant secondary contributions may be present for very near target nuclides (flagged with "*").

Table C-10 (cont.)

33.8 GeV ^{40}Ar + ^{165}Ho
MASS YIELD TABLE (mb)

NUCLIDE	MEASURED YIELD	CALCULATED INDEPENDENT YIELD	MASS YIELD	YIELD TYPE
^{24}Na	36. ± 4.	31. ± 3.	57. ± 6.	C
^{28}Mg	7.2 ± 0.7	7.1 ± 0.7	45. ± 4.	C
^{42}K	8. ± 2.	8. ± 2.	17. ± 4.	C
^{44g}Sc	3.0 ± 0.7	3.0 ± 0.7	20. ± 3.	C
^{44m}Sc	4.5 ± 0.5	4.5 ± 0.5	-	I
^{46g}Sc	10. ± 1.	10. ± 1.	19. ± 2.	I
^{47}Sc	5. ± 2.	5. ± 2.	15. ± 5.	C
^{48}Sc	2.6 ± 0.3	2.6 ± 0.3	19. ± 2.	I
^{48}V	3.8 ± 0.4	3.8 ± 0.4	14. ± 1.	C
^{51}Cr	11. ± 1.	10. ± 1.	19. ± 2.	C
^{54}Mn	11. ± 1.	11. ± 1.	18. ± 2.	I
^{59}Fe	2.4 ± 0.2	2.3 ± 0.2	15. ± 1.	C
^{65}Zn	11. ± 1.	8.6 ± 0.9	15. ± 1.	C
^{69}Ge	6. ± 1.	6. ± 1.	11. ± 2.	C
^{71}As	5.4 ± 0.5	4.9 ± 0.5	11. ± 1.	C
^{72}As	7.1 ± 0.7	7.1 ± 0.7	12. ± 1.	C
^{72}Se	1.2 ± 0.2	1.1 ± 0.1	8. ± 1.	C
^{74}As	3.5 ± 0.4	3.5 ± 0.4	10. ± 1.	I
^{75}Se	9. ± 2.	7. ± 1.	11. ± 2.	C
^{76}As	1.1 ± 0.3	1.1 ± 0.3	28. ± 9.	I
^{77g}Br	16. ± 3.	12. ± 2.	20. ± 4.	C
^{83}Rb	11. ± 2.	3.2 ± 0.6	13. ± 3.	C
^{86}Zr	4. ± 2.	4. ± 2.	16. ± 9.	C
^{86g}Y	14. ± 1.	11. ± 1.	19. ± 2.	C
^{87g}Y	15. ± 2.	8.4 ± 0.8	28. ± 4.	C
^{87m}Y	17. ± 2.	8.6 ± 0.9	-	C
^{88}Zr	15. ± 2.	12. ± 1.	20. ± 2.	C
^{88}Y	4. ± 2.	4. ± 2.	14. ± 6.	C
^{89g}Zr	11. ± 1.	7.1 ± 0.7	13. ± 1.	C
^{90m}Y	10. ± 1.	-	-	I
^{93g}Tc	5.5 ± 0.9	5.2 ± 0.8	27. ± 5.	C
^{93m}Mo	5.3 ± 0.5	-	-	I
^{94g}Tc	7.0 ± 0.7	-	-	C
^{95g}Nb	1.1 ± 0.2	1.1 ± 0.2	22. ± 4.	C
^{95g}Tc	14. ± 3.	11. ± 3.	24. ± 6.	C
^{96g}Tc	4.4 ± 0.5	-	-	C
^{97}Ru	8.8 ± 0.9	7.8 ± 0.8	21. ± 2.	C

Table C-11

33.8 GeV ^{40}Ar + ^{165}Ho
YIELD TABLE (cont)

NUCLIDE	MEASURED YIELD	CALCULATED INDEPENDENT YIELD	MASS YIELD	YIELD TYPE
^{100g}Rh	8.2 ± 0.8	7.8 ± 0.8	16. ± 2.	C
^{100}Pd	3.2 ± 0.3	3.0 ± 0.3	21. ± 2.	C
^{101m}Rh	11. ± 1.	-	-	C
^{105g}Ag	12. ± 2.	10. ± 2.	21. ± 3.	C
^{106m}Ag	3.8 ± 0.4	-	-	I
^{110m}In	7.4 ± 0.7	-	-	C
^{111g}In	14. ± 1.	10. ± 1.	20. ± 2.	C
^{119g}Te	19. ± 2.	12. ± 1.	30. ± 4.	C
^{119m}Te	3.7 ± 0.7	3.7 ± 0.7	-	I
^{121g}Te	19. ± 2.	-	-	I
^{121}I	37. ± 5.	25. ± 4.	48. ± 7.	C
^{122}Xe	11. ± 4.	10. ± 3.	32. ± 11.	C
^{123m}Te	22. ± 9.	-	-	I
^{125g}Xe	21. ± 2.	13. ± 1.	25. ± 3.	C
^{126}I	2.9 ± 0.3	2.9 ± 0.3	52. ± 5.	I
^{127g}Xe	21. ± 2.	6.8 ± 0.7	28. ± 3.	C
^{127}Cs	34. ± 6.	25. ± 4.	47. ± 8.	C
^{128}Ba	21. ± 2.	19. ± 2.	56. ± 6.	C
^{129}Cs	35. ± 4.	16. ± 2.	43. ± 5.	C
^{131g}Ba	22. ± 5.	13. ± 3.	27. ± 6.	C
^{132g}La	39. ± 12.	28. ± 9.	60. ± 19.	C
^{133}Ba	24. ± 7.	-	-	C
^{135g}Ce	28. ± 3.	23. ± 3.	47. ± 6.	C
^{139g}Ce	31. ± 4.	9. ± 1.	42. ± 6.	C
^{139m}Nd	10. ± 2.	-	-	I
^{143}Pm	62. ± 8.	29. ± 4.	79. ± 11.	C
^{145}Eu	35. ± 4.	29. ± 3.	83. ± 8.	C
^{146}Eu	39. ± 4.	-	-	C
^{146}Gd	12. ± 1.	-	-	C
^{147}Eu	49. ± 14.	31. ± 9.	67. ± 19.	C
^{147}Gd	15. ± 3.	13. ± 3.	25. ± 5.	C
^{148}Eu	10. ± 1.	10. ± 1.	25. ± 3.	I
^{149}Gd	49. ± 10.	35. ± 7.	77. ± 16.	C
^{151g}Tb	22. ± 10.	17. ± 8.	42. ± 20.	C
^{152g}Tb	52. ± 5.	36. ± 4.	76. ± 8.	C
^{153}Gd	37. ± 6.	9. ± 2.	58. ± 9.	C
^{153}Tb	69. ± 7.	56. ± 7.	70. ± 7.	C

Table C-11 (cont.)

33.8 GeV ^{40}Ar + ^{165}Ho
YIELD TABLE (cont)

NUCLIDE	MEASURED YIELD	INDEPENDENT YIELD	MASS YIELD	YIELD TYPE
^{155}Tb	54. ± 5.	17. ± 2.	73. ± 7.	C
^{156g}Tb	31. ± 3.	-	-	C
^{160m}Ho	44. ± 7.	-	-	I
^{160}Tb	14. ± 2.	-	-	C

A tabulation of measured nuclidic yields and calculated independent and mass yields. The Yield Type column indicates whether yields are independent or cumulative yields.

Table C-11 (cont.)

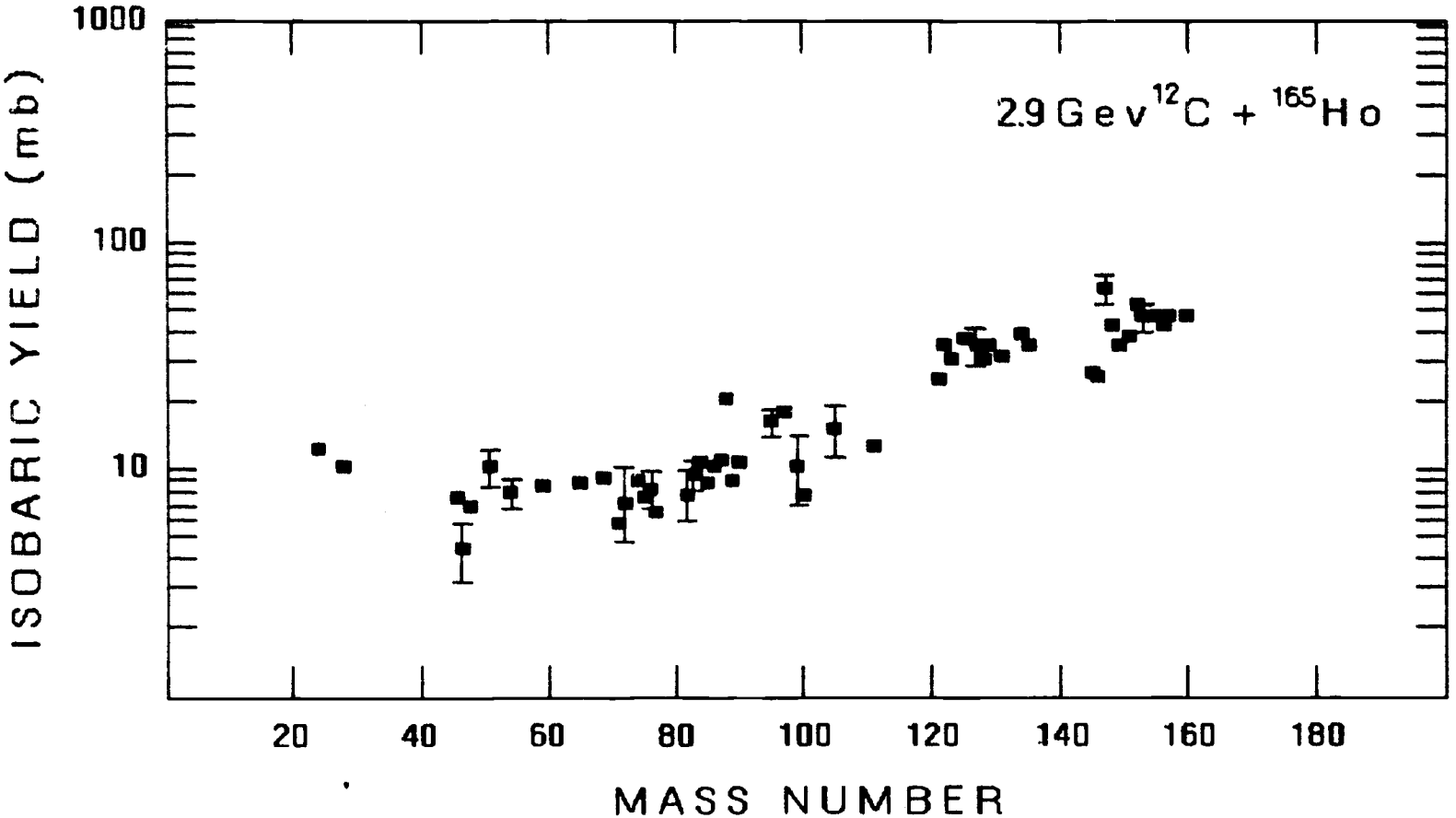

Fragment isobaric yield distribution for the reaction system 2.9 GeV ^{12}C + ^{165}Ho.

Figure C-1

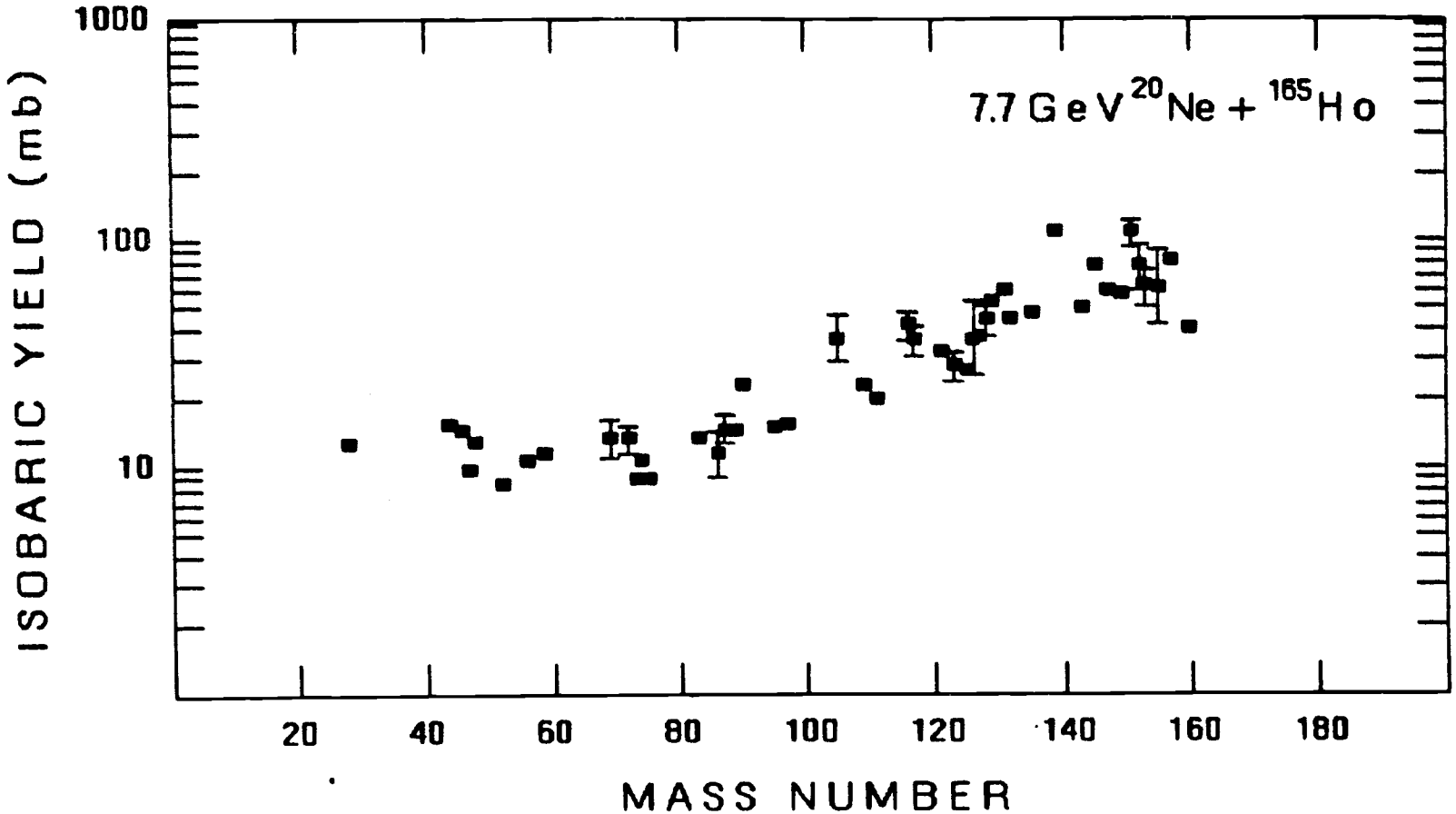

Fragment isobaric yield distribution for the reaction system 7.7 GeV ^{20}Ne + ^{165}Ho.

Figure C-2

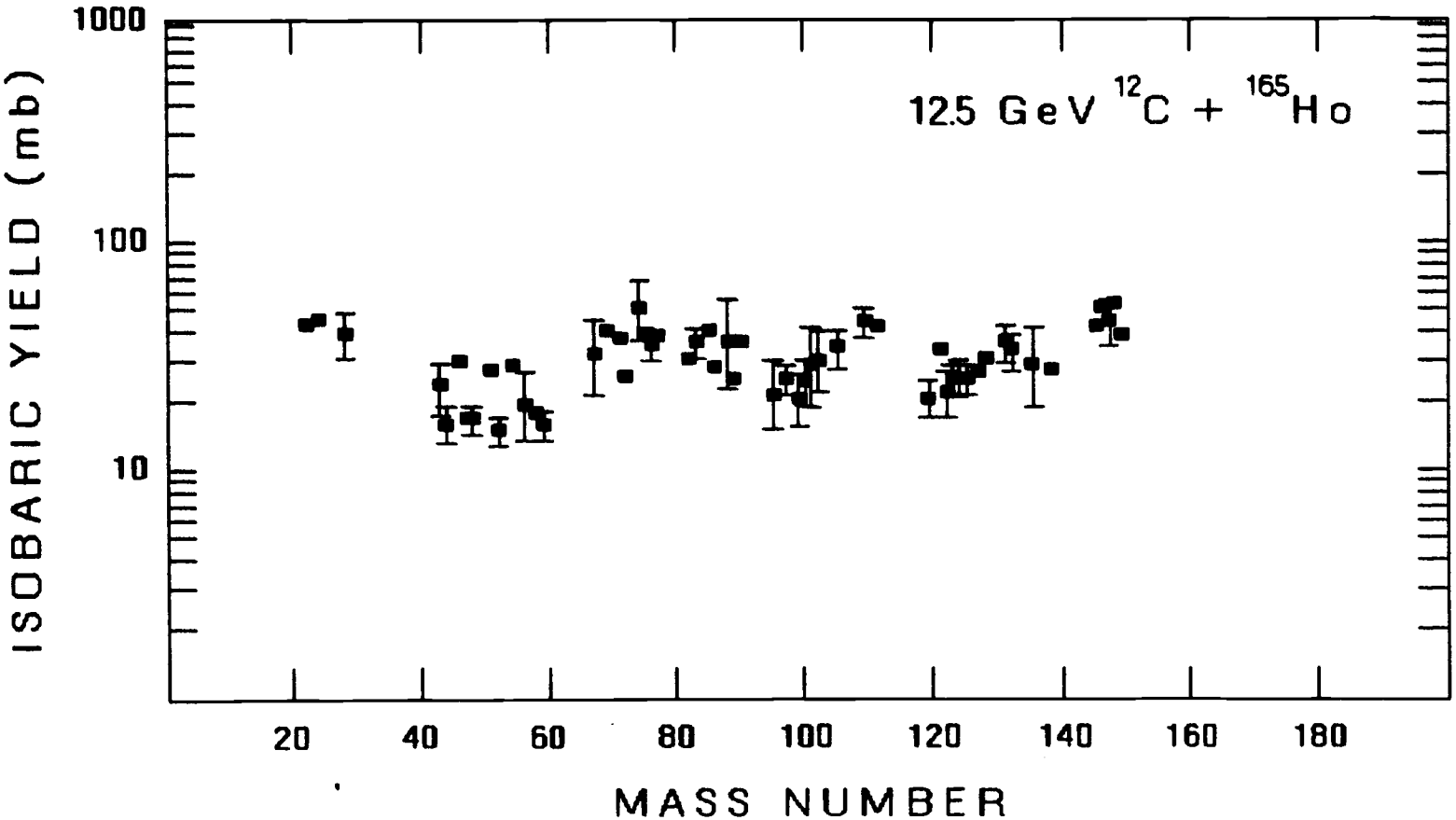

Fragment isobaric yield distribution for the reaction system 12.5 GeV ^{12}C + ^{165}Ho.

Figure C-3

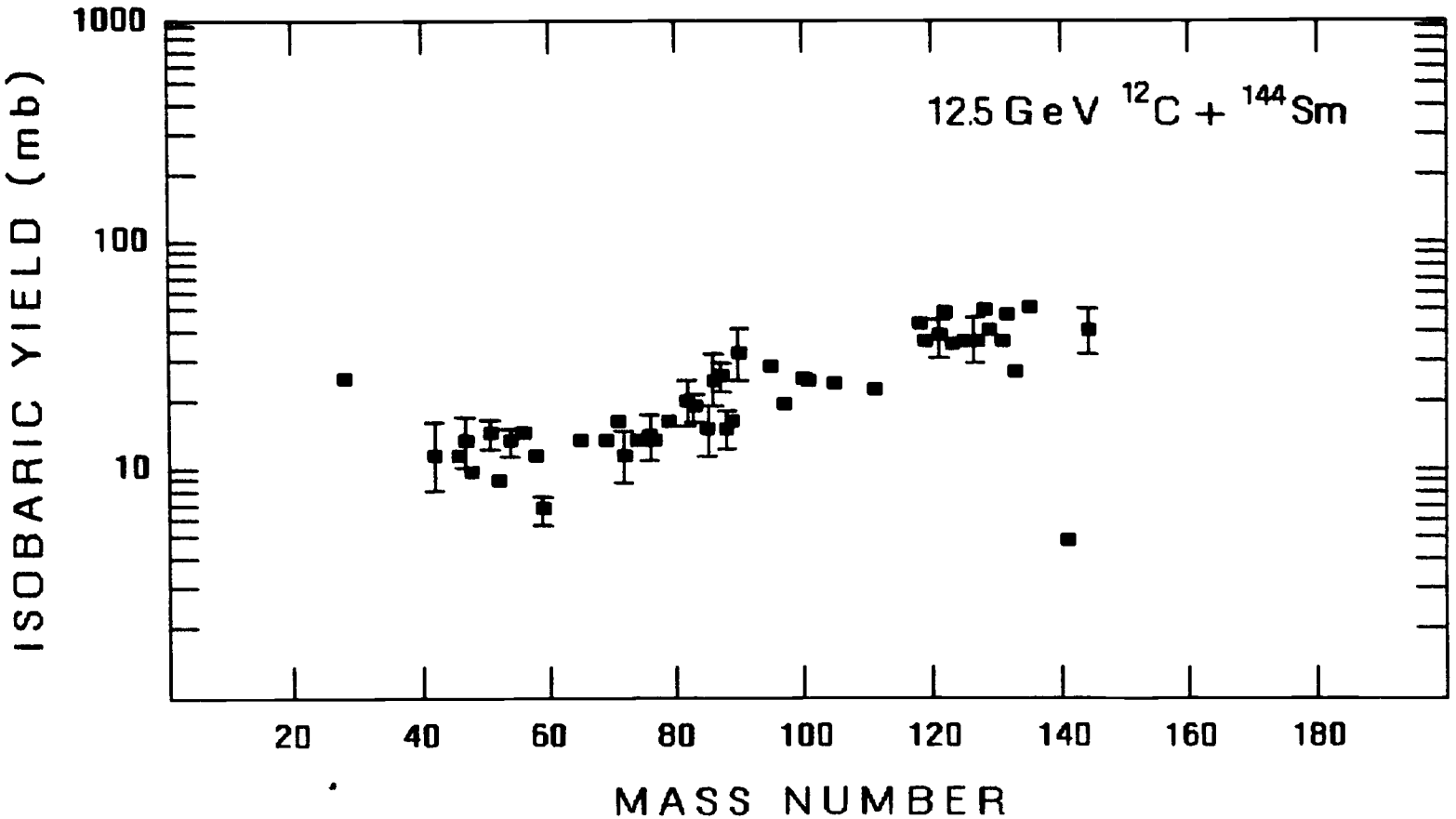

Fragment isobaric yield distribution for the reaction system 12.5 GeV ^{12}C + ^{144}Sm.

Figure C-4

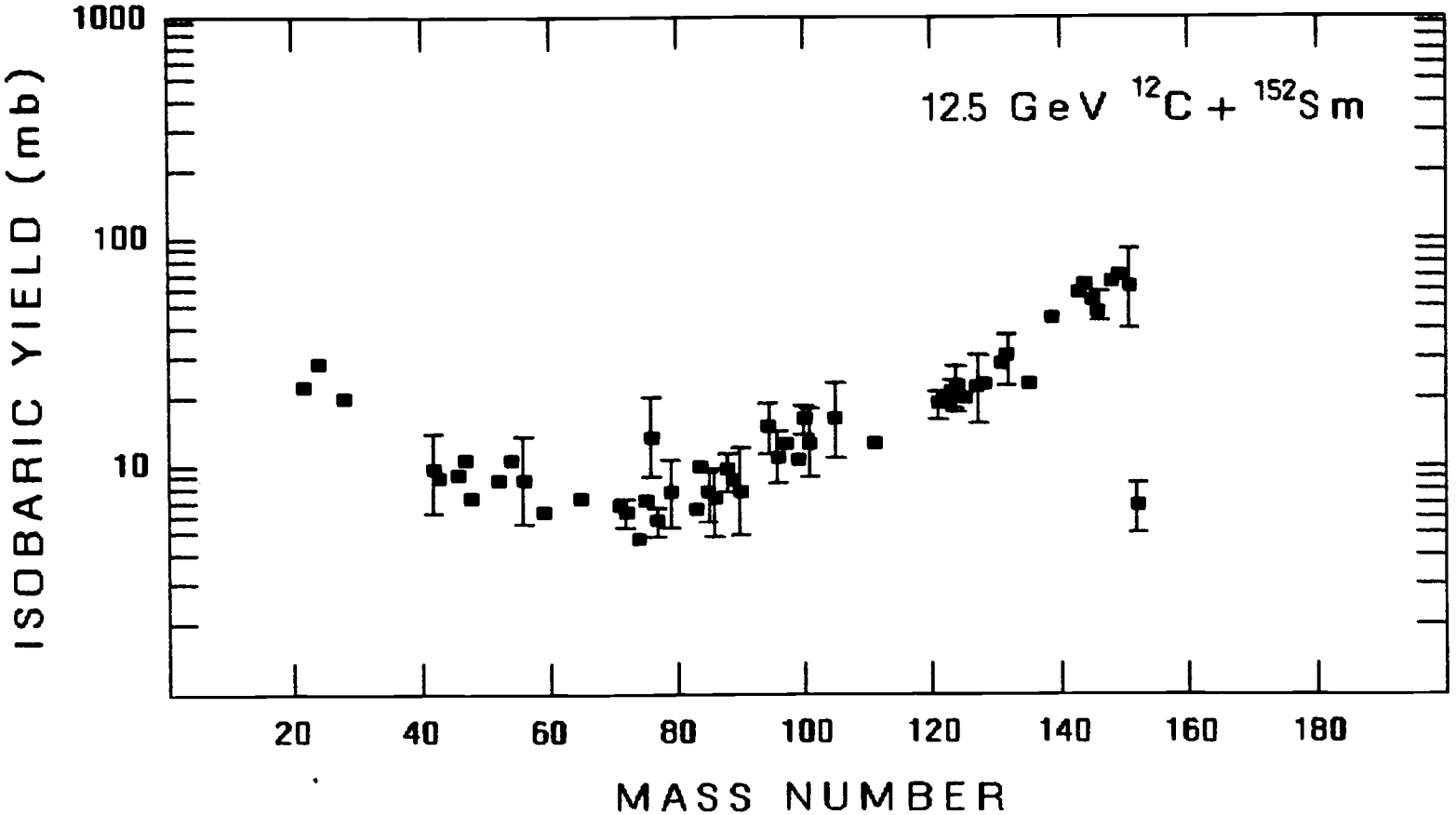

Fragment isobaric yield distribution for the reaction system 12.5 GeV ^{12}C + ^{152}Sm.

Figure C-5

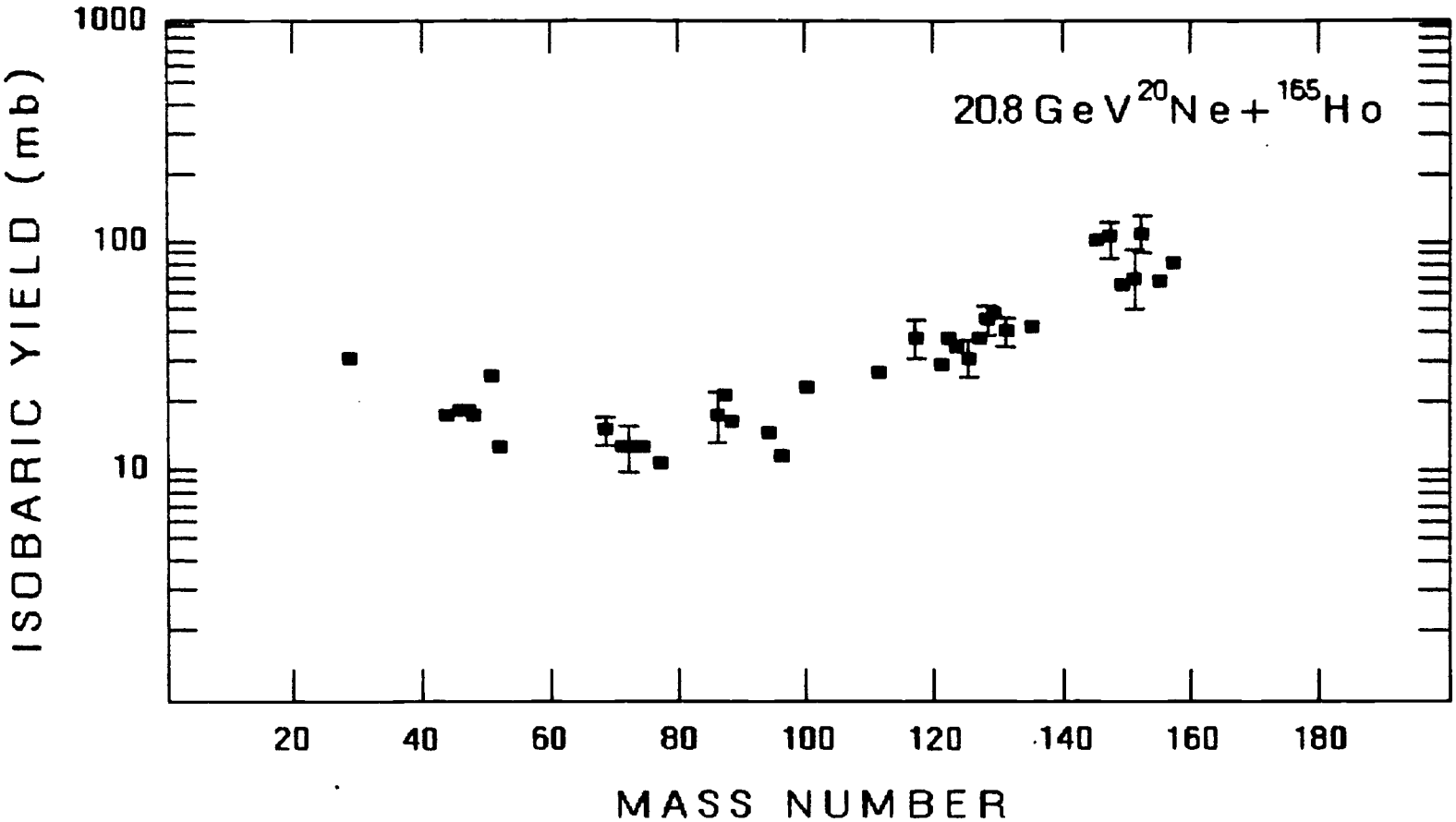

Fragment isobaric yield distribution for the reaction system 20.8 GeV ^{20}Ne + ^{165}Ho.

Figure C-6

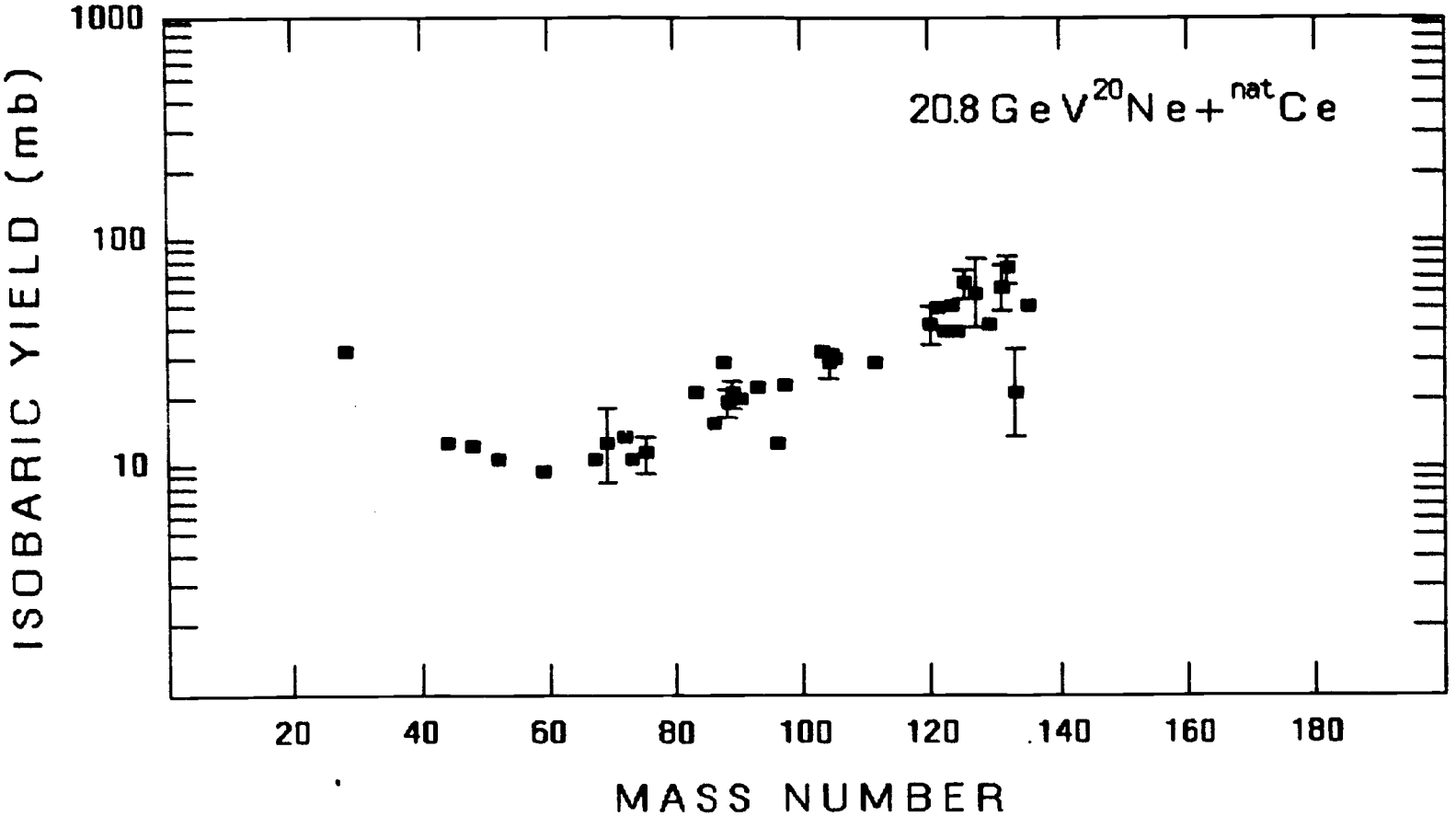

Fragment isobaric yield distribution for the reaction system 20.8 GeV ^{20}Ne + ^{nat}Ce.

Figure C-7

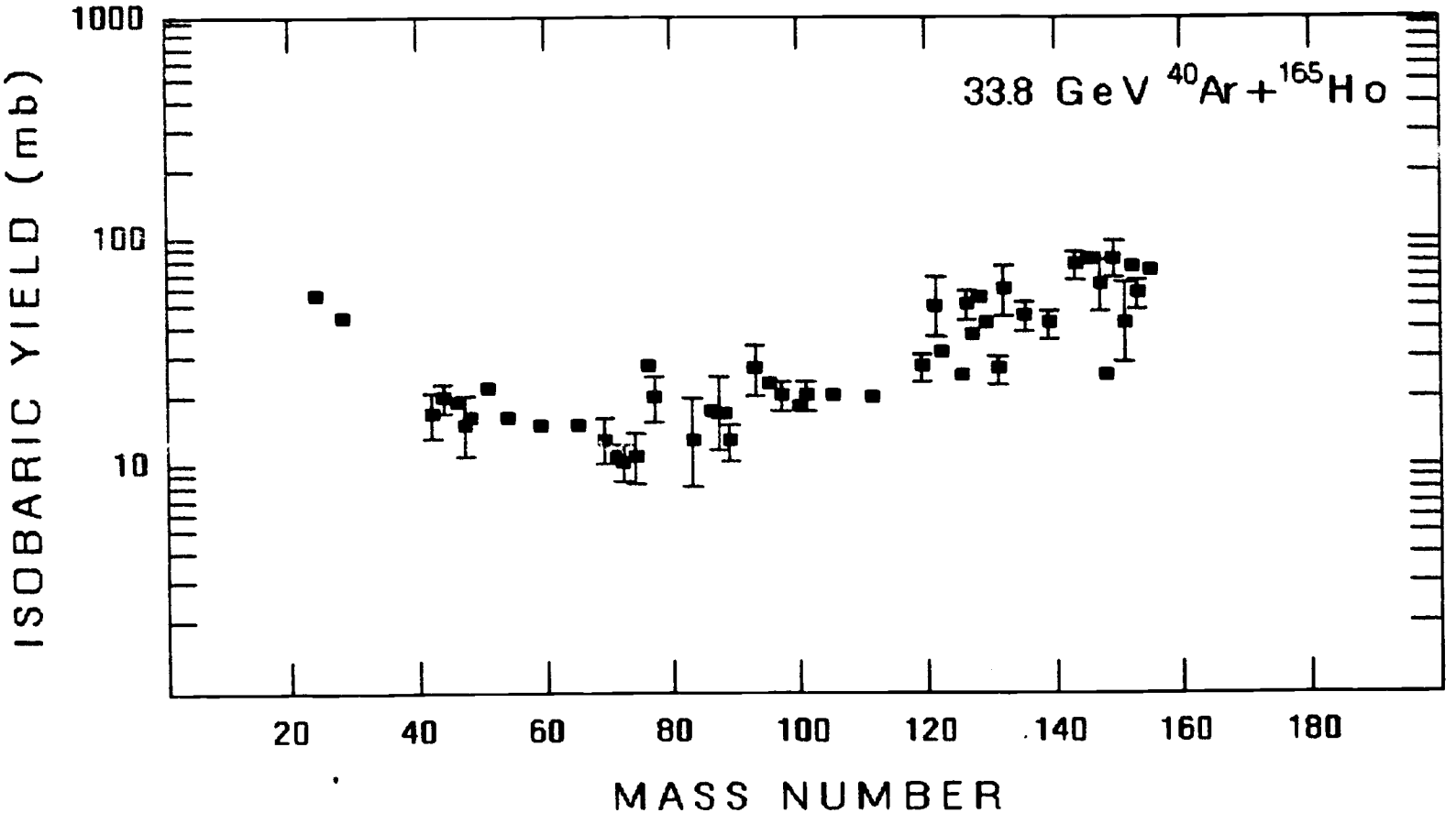

Fragment isobaric yield distribution for the reaction system 33.8 GeV ^{40}Ar + ^{165}Ho.

Figure C-8

2.9 GeV ^{12}C + ^{165}Ho
MASSY Z_p FUNCTION PARAMETERS

MASS REGION	Z_p FUNCTION	WIDTH
24 - 28	0.46 A + 0.05	0.5
46 - 59	0.45 A + 0.59	0.6
65 - 77	0.45 A + 0.52	1.0
82 - 90	0.445A + 0.72	0.6
95 - 111	0.44 A + 0.63	0.5
121 - 135	0.37 A + 8.27	0.6
143 - 151	$0.382A + 18.69 - 5.E\text{-}4A^2$	0.7
153 - 160	$0.36 A + 15.86 - 2.5E\text{-}4A^2$	0.6

A tabulation of the Z_p function and Gaussian width parameters of the respective mass regions used for calculation of independent and mass yields.

Table C-12

7.7 GeV $^{20}Ne + ^{165}Ho$
MASSY Z_p FUNCTION PARAMETERS

MASS REGION	Z_p FUNCTION	WIDTH
28 - 59	0.453 A + 0.37	0.6
69 - 75	0.439 A + 1.29	0.8
82 - 97	0.418 A + 2.93	0.8
105 - 113	0.394 A + 5.41	1.0
116 - 127	0.382 A + 6.86	0.9
128 - 139	0.39 A + 5.64	0.9
143 - 160	0.34 A + 13.37	0.8

A tabulation of the Z_p function and Gaussian width parameters of the respective mass regions used for calculation of independent and mass yields.

Table C-13

12.5 GeV ^{12}C + ^{165}Ho
MASSY Z_p FUNCTION PARAMETERS

MASS REGION	Z_p FUNCTION	WIDTH
22 - 28	0.46 A + 0.24	0.6
43 - 54	0.45 A + 0.51	0.5
56 - 59	0.45 A + 0.45	0.7
67 - 77	0.43 A + 1.21	0.6
82 - 90	0.425 A + 1.71	0.6
95 - 102	0.415 A + 3.11	0.7
105 - 111	0.41 A + 3.19	0.6
119 - 127	0.385 A + 6.58	0.8
128 - 138	0.37 A + 8.42	0.7
145 - 149	0.365 A + 9.85	0.8

A tabulation of the Z_p function and Gaussian width parameters of the respective mass regions used for calculation of independent and mass yields.

Table C-14

12.5 GeV ^{12}C + ^{152}Sm
MASSY Z_p FUNCTION PARAMETERS

MASS REGION	Z_p FUNCTION	WIDTH
22 - 28	0.45 A + 0.56	0.6
42 - 59	0.44 A + 0.98	0.6
65 - 79	0.415 A + 2.88	0.6
83 - 90	0.408 A + 4.03	0.6
95 - 111	0.401 A + 4.61	0.8
118 - 128	0.371 A + 8.24	0.8
131 - 139	0.35 A + 11.37	0.9
143 - 152	0.349 A + 10.04	0.9

A tabulation of the Z_p function and Gaussian width parameters of the respective mass regions used for calculation of independent and mass yields.

Table C-15

12.5 GeV ^{12}C + ^{144}Sm
MASSY Z_p FUNCTION PARAMETERS

MASS REGION	Z_p FUNCTION	WIDTH
28 - 59	0.44 A + 1.21	0.6
65 - 79	0.412 A + 2.84	0.7
82 - 90	0.408 A + 3.69	0.8
95 - 111	0.378 A + 7.11	0.8
118 - 135	0.388 A + 5.77	0.8
141 - 144	0.388 A + 5.88	0.7

A tabulation of the Z_p function and Gaussian width parameters of the respective mass regions used for calculation of independent and mass yields.

Table C-16

20.8 GeV ^{20}Ne + ^{165}Ho
MASSY Z_p FUNCTION PARAMETERS

MASS REGION	Z_p FUNCTION	WIDTH
28 - 52	0.453 A + 0.36	0.6
69 - 77	0.437 A + 1.39	0.9
86 - 97	0.418 A + 2.93	0.8
100 - 111	0.398 A + 4.87	0.9
117 - 125	0.382 A + 6.71	0.8
127 - 136	0.365 A + 8.86	0.9
145 - 157	0.355 A + 10.57	0.7

A tabulation of the Z_p function and Gaussian width parameters of the respective mass regions used for calculation of independent and mass yields.

Table C-17

20.8 GeV ^{20}Ne + ^{nat}Ce
MASSY Z_p FUNCTION PARAMETERS

MASS REGION	Z_p FUNCTION	WIDTH
28 - 59	0.45 A + 0.60	0.6
67 - 76	0.44 A + 1.30	0.5
83 - 97	0.41 A + 3.80	0.8
101 - 111	0.415 A + 3.18	0.7
119 - 124	0.38 A + 7.05 (Iodine)	0.5
121 - 131	0.365 A + 8.85	0.8
131 - 135	0.355 A + 10.14	0.8

A tabulation of the Z_p function and Gaussian width parameters of the respective mass regions used for calculation of independent and mass yields.

Table C-18

33.8 GeV ^{40}Ar + ^{165}Ho
MASSY Z_p FUNCTION PARAMETERS

MASS REGION	Z_p FUNCTION	WIDTH
28 - 59	0.45 A + 0.55	0.6
65 - 77	0.42 A + 2.64	0.6
83 - 89	0.39 A + 5.54	0.6
93 - 97	0.37 A + 7.49	0.7
100 - 111	0.37 A + 7.79	0.7
119 - 139	0.34 A + 11.77	0.7
143 - 156	0.365 A + 9.42	0.8

A tabulation of the Z_p function and Gaussian width parameters of the respective mass regions used for calculation of independent and mass yields.

Table C-19

2.9 GeV ^{12}C + ^{165}Ho
MEASURED KINEMATICAL QUANTITIES

NUCLIDE	F/B	2W(F±B) (mg/cm^2 Ho)	k	N
^{24}Na	4.2 ± 0.5	17. ± 2.	0.369	1.88
^{47}Sc	4.6 ± 0.5	13. ± 2.	0.769	1.29
^{71}As	6.5 ± 0.7	5.2 ± 0.6	0.911	1.12
^{77g}Br	6.3 ± 0.6	4.4 ± 0.5	0.791	1.21
^{87g}Y	3.7 ± 0.4	2.4 ± 0.2	0.610	1.38
^{87m}Y	14. ± 4.	3.4 ± 1.0	0.637	1.35
^{89g}Zr	8.3 ± 0.8	4.4 ± 0.5	0.725	1.24
^{97}Ru	13. ± 5.0	5. ± 2.	0.698	1.23
^{101m}Rh	18. ± 1.	3.6 ± 0.4	0.626	1.31
^{111g}In	13. ± 2.	3.6 ± 0.5	0.521	1.40
^{123}I	24. ± 7.	1.5 ± 0.4	0.282	1.89
^{129}Cs	10. ± 3.	2.3 ± 0.5	0.308	1.76

A tabulation of the measured kinematical quantities, the forward-to-backward ratio (F/B) and the "pseudo-range" (2W[F+B]), for nuclides identified in the target and both catcher foils. Also tabulated for each nuclide are the range-energy formula fit parameters, k and N (see text).

Table C-20

12.5 GeV ^{12}C + ^{165}Ho
MEASURED KINEMATICAL QUANTITIES

NUCLIDE	F/B	2W(F+B) (mg/cm^2 Ho)	k	N
^{24}Na	2.7 ± 0.4	10. ± 2.	0.588	1.61
^{28}Mg	2.5 ± 0.3	11. ± 1.	0.576	1.57
^{43}K	2.0 ± 0.2	5.4 ± 0.5	0.791	1.28
^{44m}Sc	1.4 ± 0.6	4.2 ± 0.5	0.783	1.28
^{46}Sc	1.4 ± 0.5	4. ± 1.	0.824	1.24
^{47}Sc	1.8 ± 0.2	6.1 ± 0.6	0.982	1.11
^{48}Sc	1.5 ± 0.2	4.8 ± 0.5	0.817	1.23
^{48}V	1.2 ± 0.1	6.2 ± 0.6	0.997	1.10
^{71}As	2.3 ± 0.6	5. ± 1.	0.817	1.18
^{74}As	2. ± 1.	5. ± 2.	0.825	1.16
^{77g}Br	1.9 ± 0.2	3.2 ± 0.4	0.649	1.32
^{83}Rb	1.4 ± 0.4	1.7 ± 0.4	0.538	1.70
^{87g}Y	3.3 ± 0.3	3.2 ± 0.3	0.646	1.31
^{88}Y	1.6 ± 0.2	1.5 ± 0.2	0.309	1.69
^{88}Zr	1.9 ± 0.6	1.1 ± 0.4	0.431	1.72
^{89g}Zr	4.0 ± 0.9	2.5 ± 0.5	0.560	1.37
^{90g}Nb	3.4 ± 0.6	2.9 ± 0.5	0.555	1.38
^{96g}Tc	2.8 ± 0.6	3.0 ± 0.7	0.590	1.33
^{97}Ru	4. ± 1.	2.6 ± 0.6	0.568	1.34
^{100g}Rh	2. ± 1.	2. ± 1.	0.539	1.39
^{101m}Rh	4.2 ± 0.6	2.4 ± 0.4	0.514	1.41
^{111g}In	8. ± 4.	2. ± 1.	0.373	1.61
^{128}Ba	2.8 ± 0.8	1.5 ± 0.4	0.260	1.88
^{131g}Ba	2.3 ± 0.2	0.9 ± 0.1	0.219	1.97

A tabulation of the measured kinematical quantities, the forward-to-backward ratio (F/B) and the "pseudo-range" (2W[F+B]), for nuclides identified in the target and both catcher foils. Also tabulated for each nuclide are the range-energy formula fit parameters, k and N (see text).

Table C-21

33.8 GeV ^{40}Ar + ^{165}Ho
MEASURED KINEMATICAL QUANTITIES

NUCLIDE	F/B	2W(F+B) (mg/cm^2 Ho)	k	N
^{24}Na	2.4 ± 0.2	9.2 ± 0.9	0.656	1.54
^{28}Mg	2.1 ± 0.4	8. ± 2.	0.707	1.45
^{44m}Sc	1.7 ± 0.2	6.7 ± 0.7	0.799	1.24
^{47}Sc	1.8 ± 0.3	7. ± 1.	0.760	1.26
^{48}Sc	0.7 ± 0.4	9. ± 4.	0.840	1.19
^{71}As	2.0 ± 0.2	3.1 ± 0.4	0.844	1.16
^{87g}Y	3.6 ± 0.4	2.5 ± 0.3	0.588	1.36
^{87m}Y	2.9 ± 0.4	2.2 ± 0.4	0.569	1.39
^{97}Ru	6. ± 2.	3. ± 1.	0.628	1.27
^{100g}Rh	3.1 ± 0.9	2.6 ± 0.7	0.570	1.35
^{101m}Rh	3.5 ± 0.4	2.7 ± 0.3	0.577	1.34
^{111g}In	4.8 ± 0.6	1.9 ± 0.3	0.416	1.51

A tabulation of the measured kinematical quantities, the forward-to-backward ratio (F/B) and the "pseudo-range" (2W[F+B]), for nuclides identified in the target and both catcher foils. Also tabulated for each nuclide are the range-energy formula fit parameters, k and N (see text).

Table C-22

2.9 GeV ^{12}C + ^{165}Ho
DEDUCED KINEMATICAL QUANTITIES

NUCLIDE	β_{par}	P_{par} (MeV/c)	<V> ($\sqrt{[MeV/A]}$)	<T> (MeV)
^{71}As	0.0094	620.	0.64	17.
^{77g}Br	0.0077	549.	0.54	13.
^{87g}Y	0.0035	287.	0.36	6.4
^{87m}Y *	0.0072	585.	0.37	6.7
^{89g}Zr	0.0081	670.	0.50	13.
^{97}Ru *	0.0092	833.	0.48	13.
^{101m}Rh	0.0077	721.	0.35	7.2
^{111g}In	0.0073	759.	0.38	9.3
^{123}I *	0.0045	520.	0.21	3.1
^{129}Cs	0.0048	578.	0.30	6.5

A tabulation of kinematical quantities deduced following the two-step interaction formalism as implemented by Winsberg [111]. These quantites are only tabulated for nuclides for which the quantities are thought to be valid. Uncertainties are estimated to be <25%, nuclides for which the uncertainty is between 25% and 50% are flagged with a "*" (see text).

Table C-23

12.5 GeV ^{12}C + ^{165}Ho
DEDUCED KINEMATICAL QUANTITIES

NUCLIDE	β_{par}	P_{par} (MeV/c)	$\langle V \rangle$ ($\sqrt{[MeV/A]}$)	$\langle T \rangle$ (MeV)
^{71}As *	0.0073	482.	1.1	23.
^{74}As *	0.0077	530.	1.2	30.
^{77g}Br	0.0038	270.	0.78	13.
^{83}Rb *	0.0011	86.	0.45	4.7
^{87g}Y	0.0066	532.	0.70	12.
^{88}Y	0.0015	119.	0.40	4.0
^{88}Zr *	0.0015	126.	0.33	2.7
^{89g}Zr	0.0059	491.	0.56	7.8
^{90g}Nb	0.0059	496.	0.63	10.
^{96g}Tc *	0.0053	478.	0.66	12.
^{97}Ru *	0.0062	559.	0.56	8.7
^{100g}Rh *	0.0031	290.	0.56	8.9
^{101m}Rh	0.0068	636.	0.65	12.
^{111g}In *	0.0057	584.	0.38	4.6
^{128}Ba *	0.0028	333.	0.38	5.1
^{131g}Ba	0.0016	199.	0.29	3.1

A tabulation of kinematical quantities deduced following the two-step interaction formalism as implemented by Winsberg [111]. These quantites are only tabulated for nuclides for which the quantities are thought to be valid. Uncertainties are estimated to be <25%, nuclides for which the uncertainty is between 25% and 50% are flagged with a "*" (see text).

Table C-24

33.8 GeV ^{40}Ar + ^{165}Ho
DEDUCED KINEMATICAL QUANTITIES

NUCLIDE	β_{par}	P_{par} (MeV/c)	<V> ($\sqrt{[MeV/A]}$)	<T> (MeV)
^{47}Sc	0.0081	352.	1.7	79.
^{48}Sc *	0.0005	23.	1.7	82.
^{71}As	0.0042	275.	0.77	24.
^{87g}Y	0.0055	448.	0.56	16.
^{87m}Y	0.0042	340.	0.52	13.
^{97}Ru *	0.0081	730.	0.58	18.
^{100g}Rh *	0.0050	461.	0.58	19.
^{101m}Rh	0.0055	518.	0.58	19.
^{111g}In	0.0050	511.	0.43	12.

A tabulation of kinematical quantities deduced following the two-step interaction formalism as implemented by Winsberg [111]. These quantites are only tabulated for nuclides for which the quantities are thought to be valid. Uncertainties are estimated to be <25%, nuclides for which the uncertainty is between 25% and 50% are flagged with a "*" (see text).

Table C-25

D. CHARGE DISPERSIONS

The charge dispersions generated by the fitting procedure described in chapter II, section C-2 are shown in figures D-1 to D-5 for the reaction systems indicated. The abscissa is labeled with Z-Z(mp) which is the distance a given nuclide lies away from the most probable Z-value for the respective mass bin. The Z_{mp} for a nuclide is calculated using the Z_p function for the given mass region. The Z_p function parameters and Gaussian width parameters resulting from the fitting procedure (chapter II, section C-2) are presented in tables D-1 through D-5.

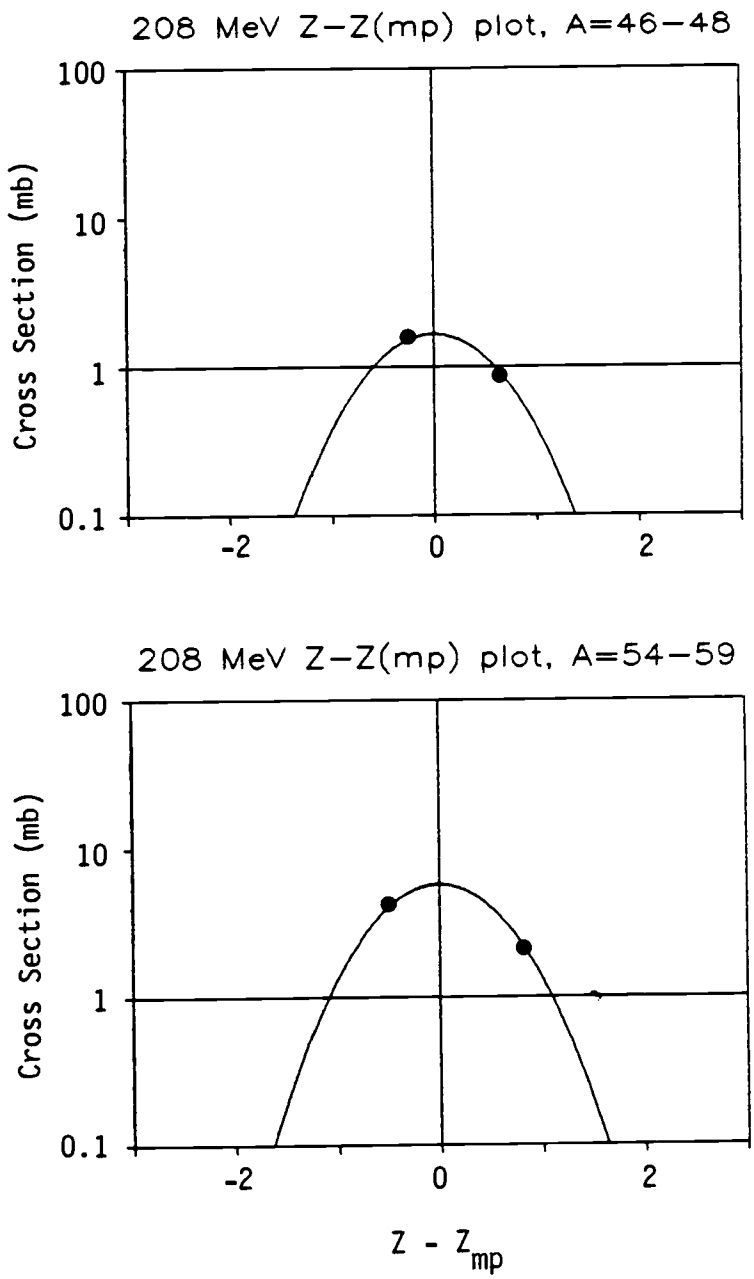
208 MeV Z−Z(mp) plot, A=46−48
Cross Section (mb)
100
10
1
0.1
-2
0
2
208 MeV Z−Z(mp) plot, A=54−59
Cross Section (mb)
100
10
1
0.1
-2
0
2
Z - Z_mp

Figure D-1

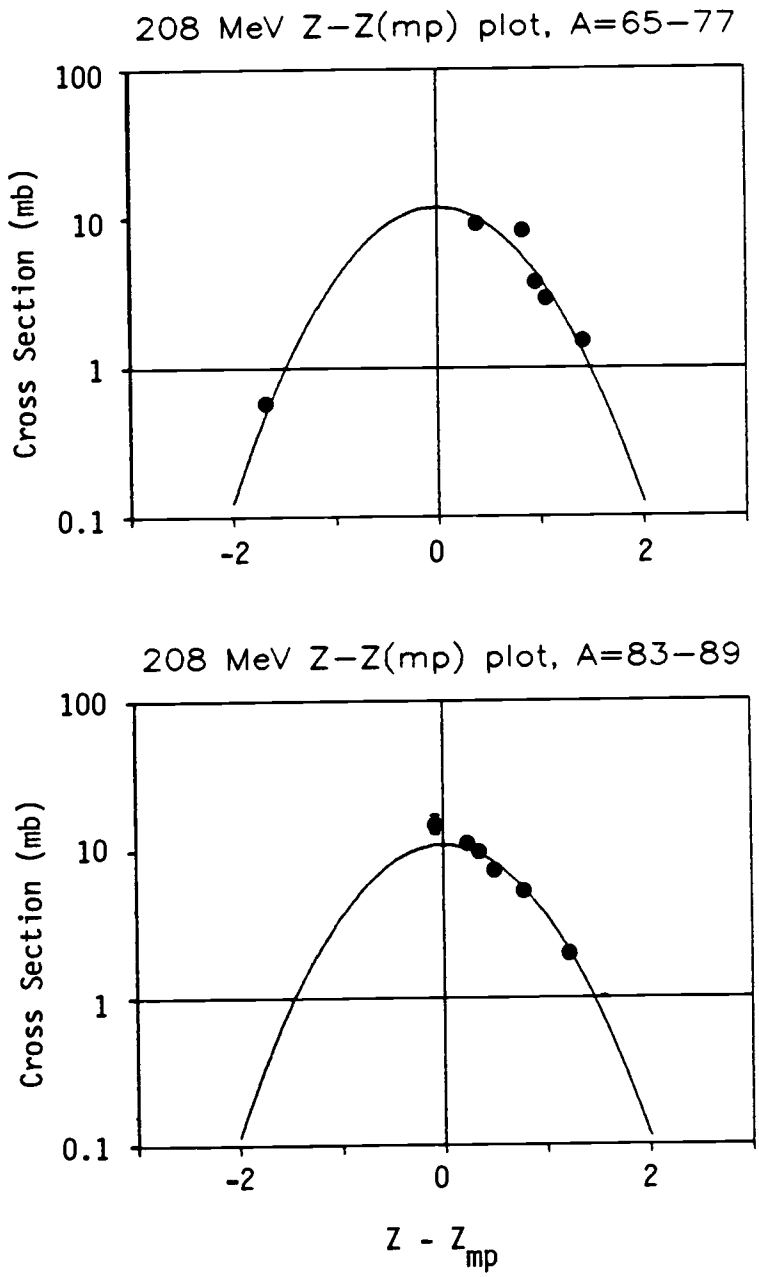

Figure D-1(cont.)

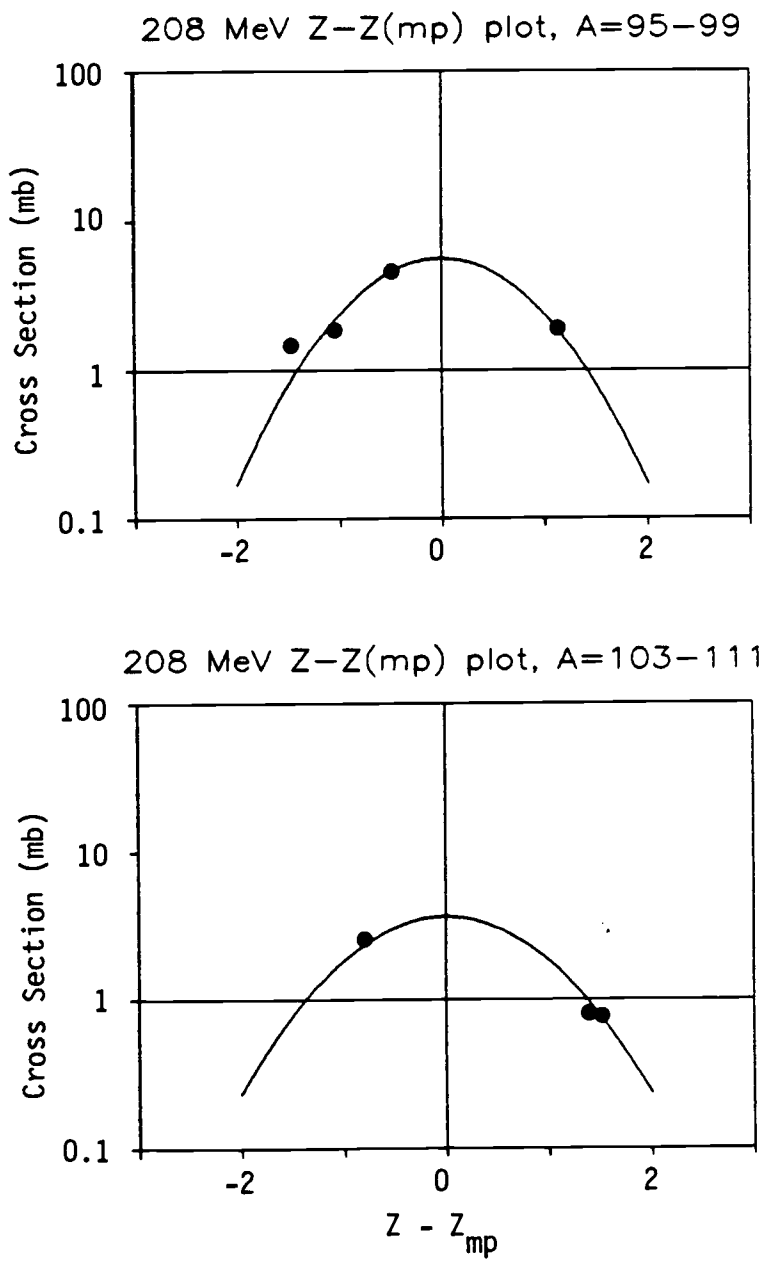

Figure D-1(cont.)

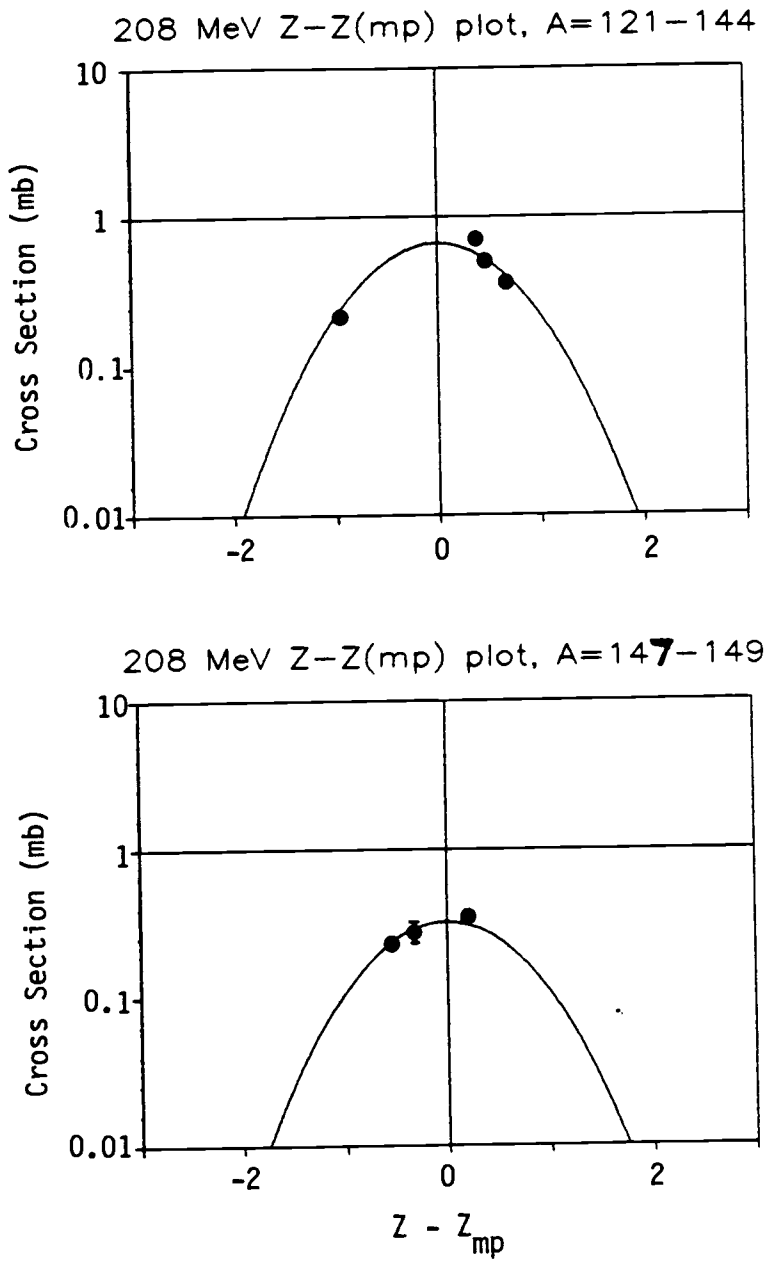

Figure D-1(cont.)

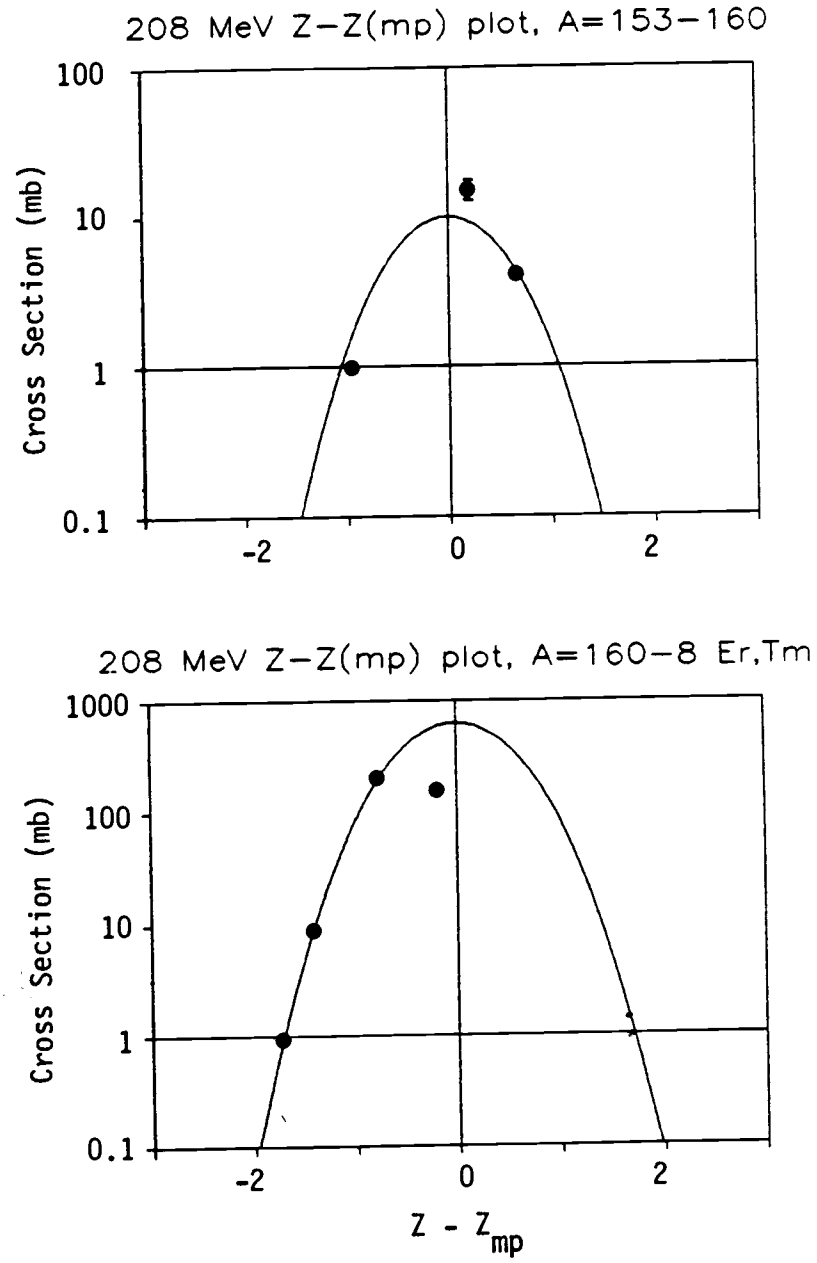

Calculated fragment charge dispersion plots for the reaction system 208 MeV ^{12}C + ^{165}Ho.

Figure D-1 (cont.)

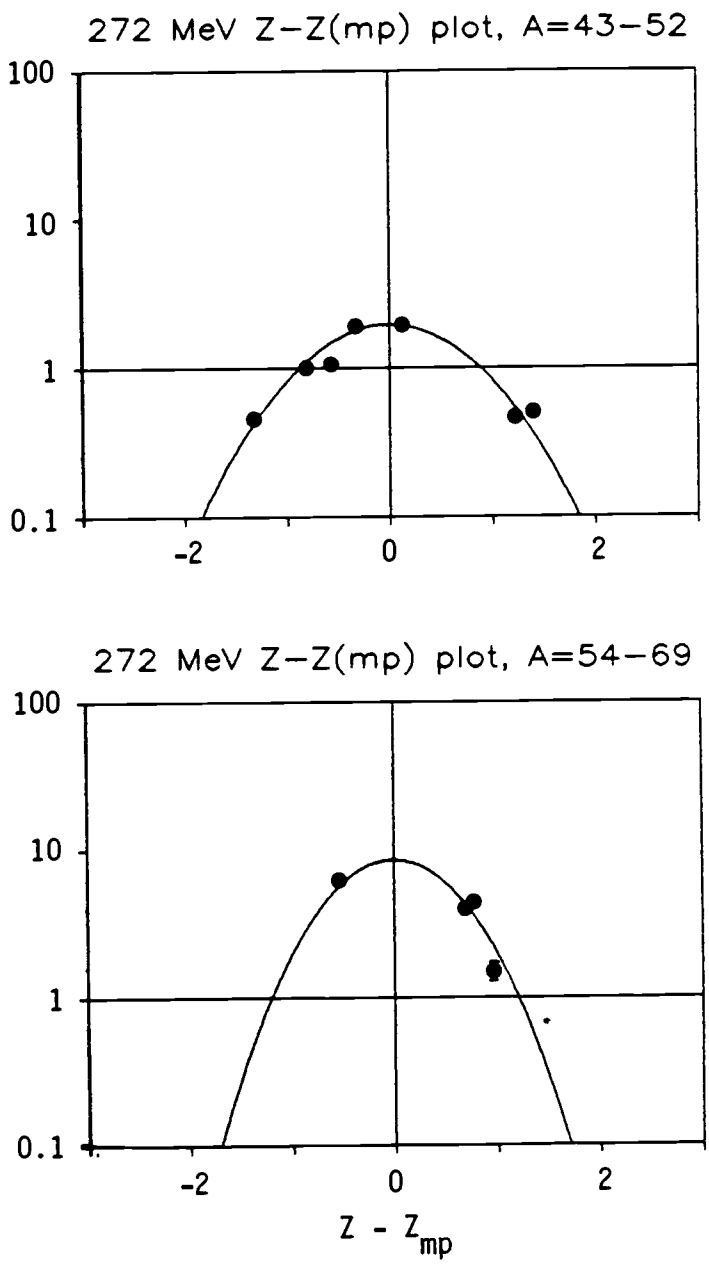
272 MeV Z−Z(mp) plot, A=43−52
100
10
1
0.1
-2
0
2
272 MeV Z−Z(mp) plot, A=54−69
100
10
1
0.1
-2
0
2
Z - Z mp

Figure D-2

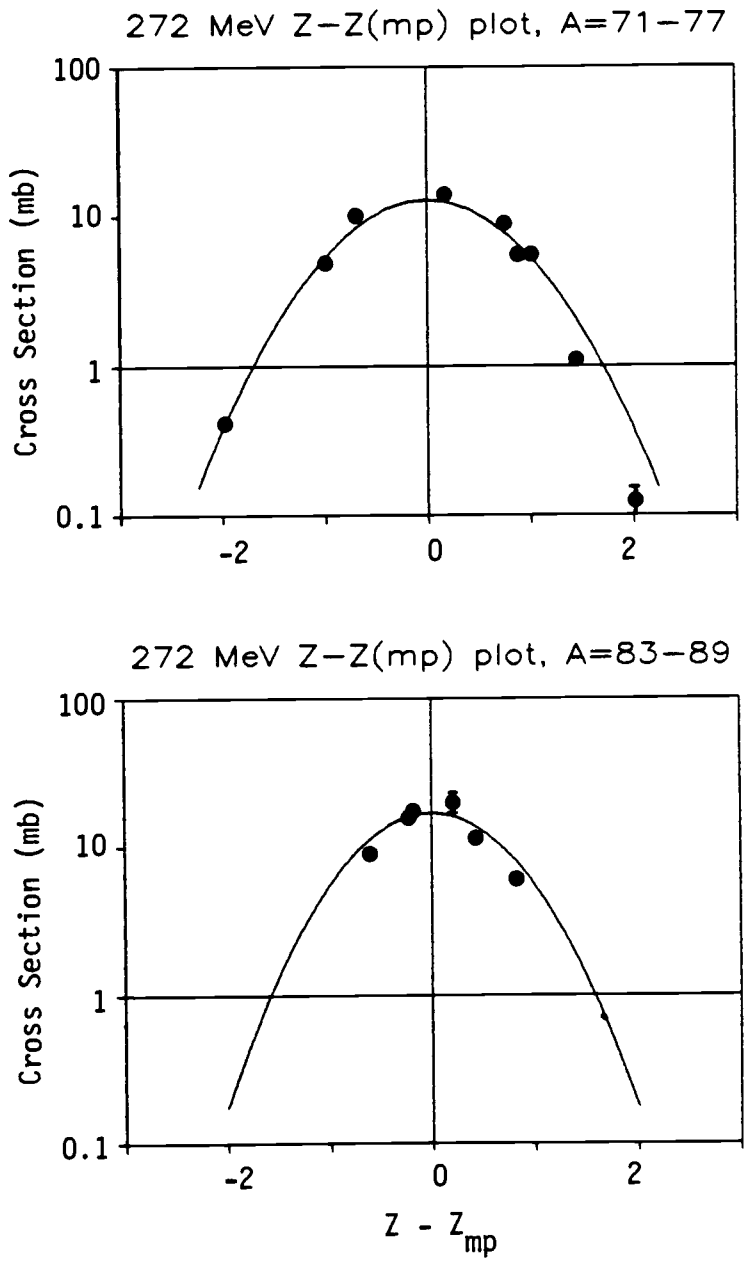

Figure D-2(cont.)

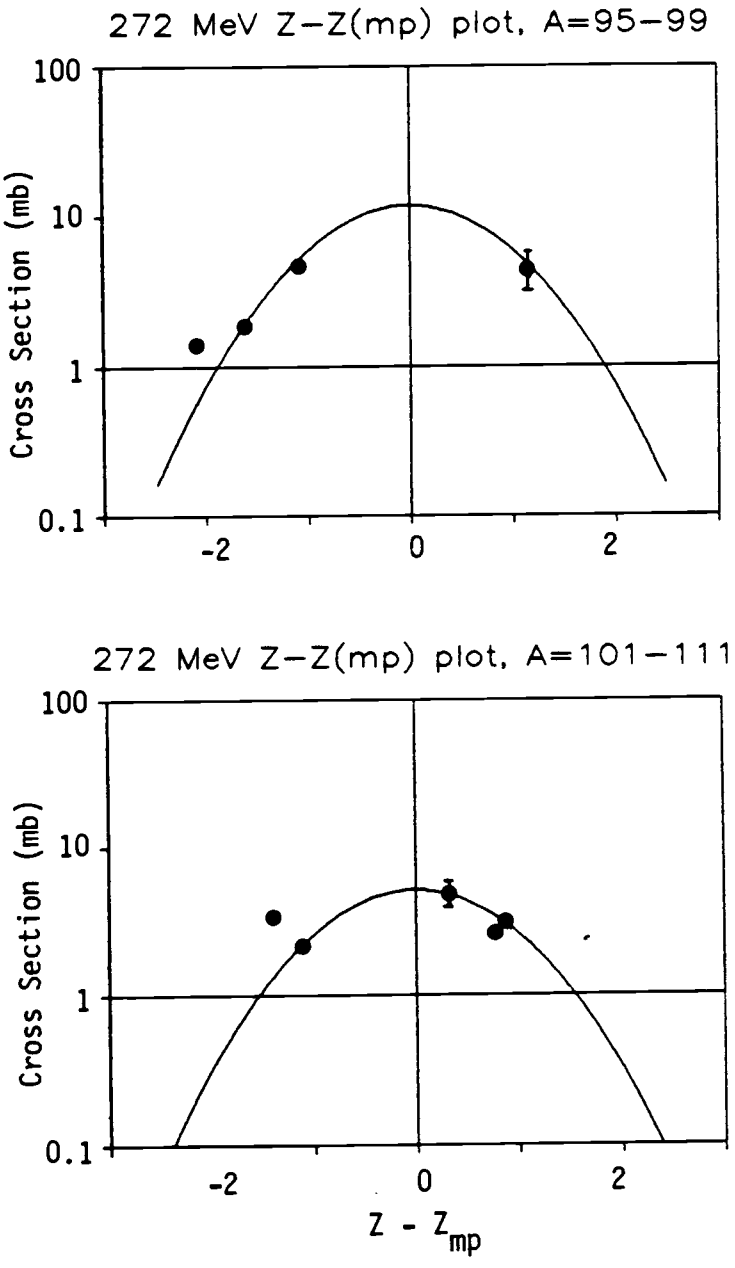

Figure D-2(cont.)

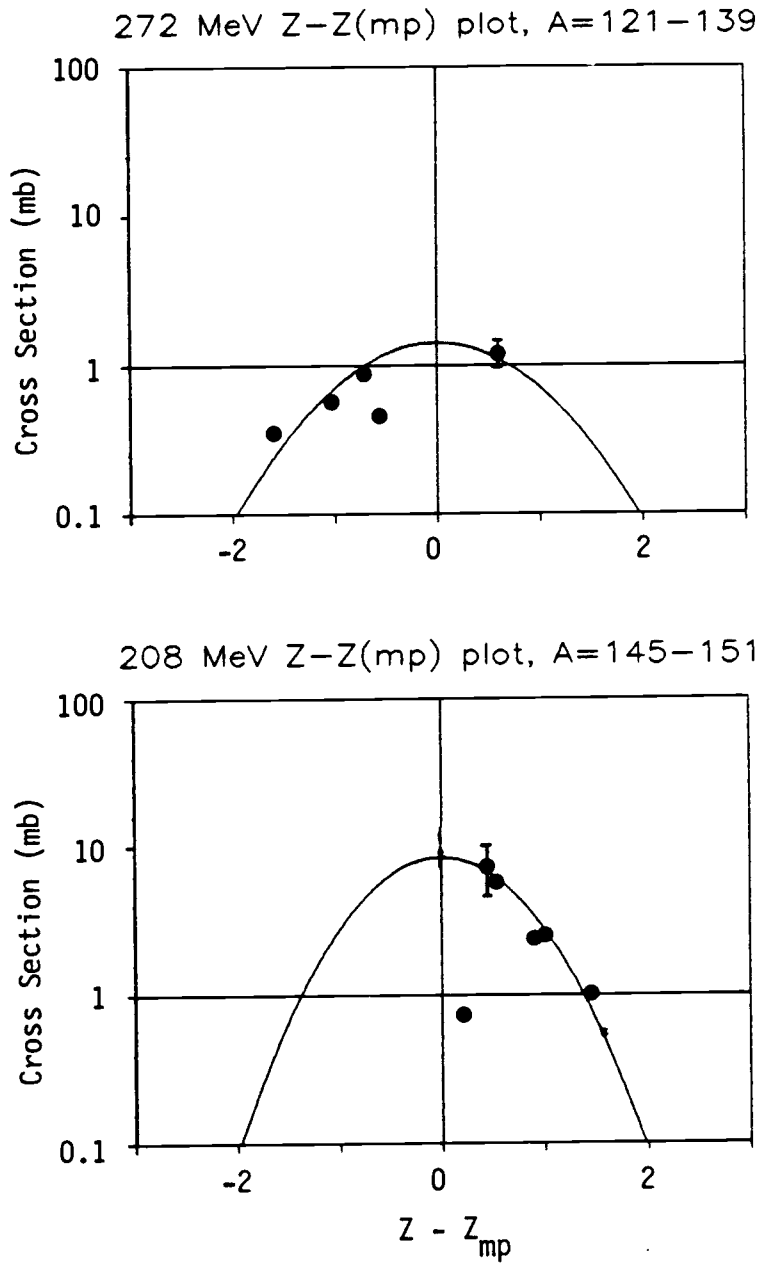

Figure D-2(cont.)

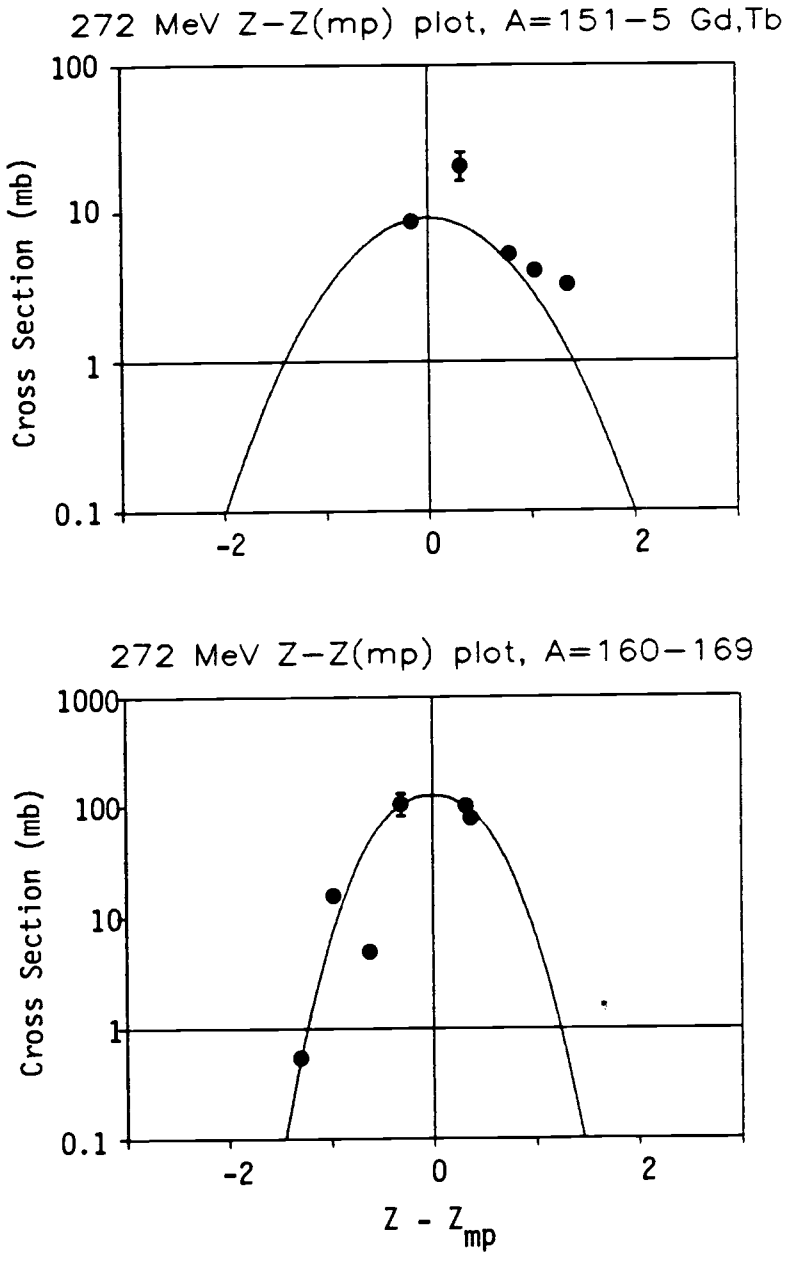

Calculated fragment charge dispersion plots for the reaction system 265 MeV ^{16}O + ^{165}Ho.

Figure D-2 (cont.)

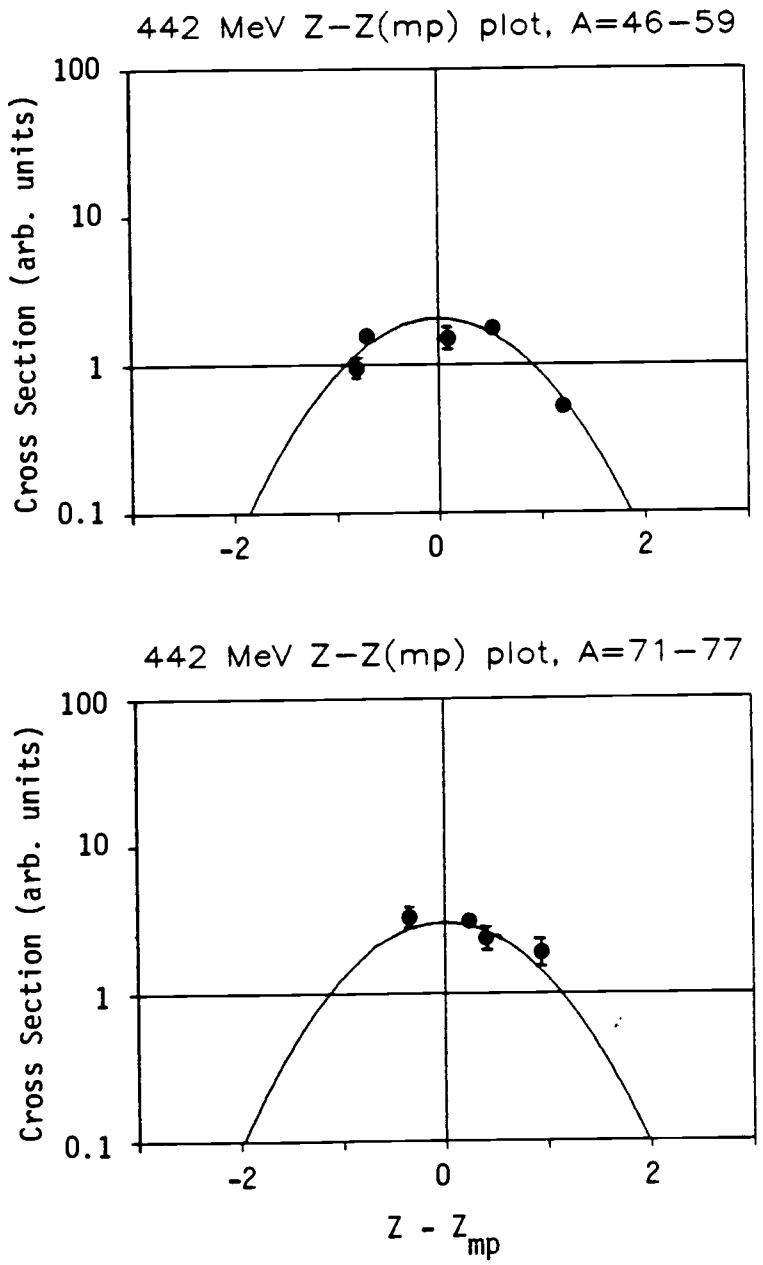
442 MeV Z−Z(mp) plot, A=46−59
Cross Section (arb. units)
100
10
1
0.1
-2
0
2
442 MeV Z−Z(mp) plot, A=71−77
Cross Section (arb. units)
100
10
1
0.1
-2
0
2
Z - Z mp

Figure D-3

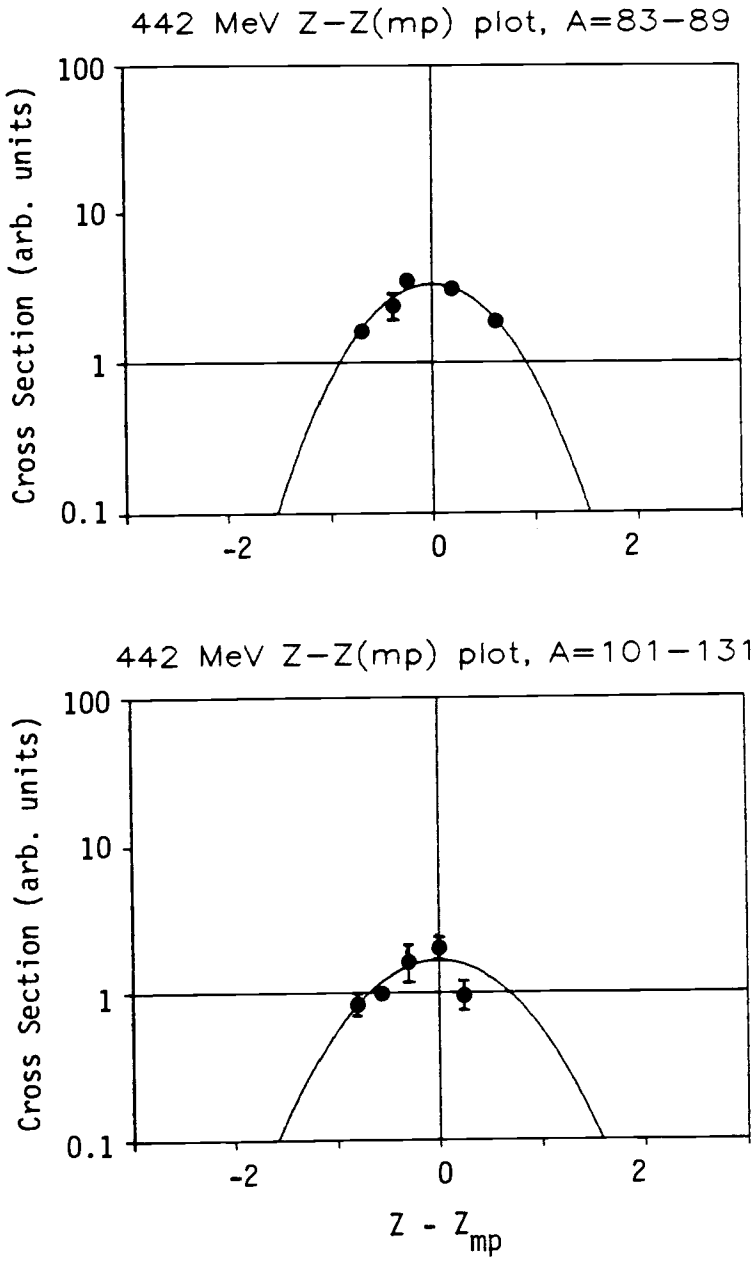

Figure D-3 (cont.)

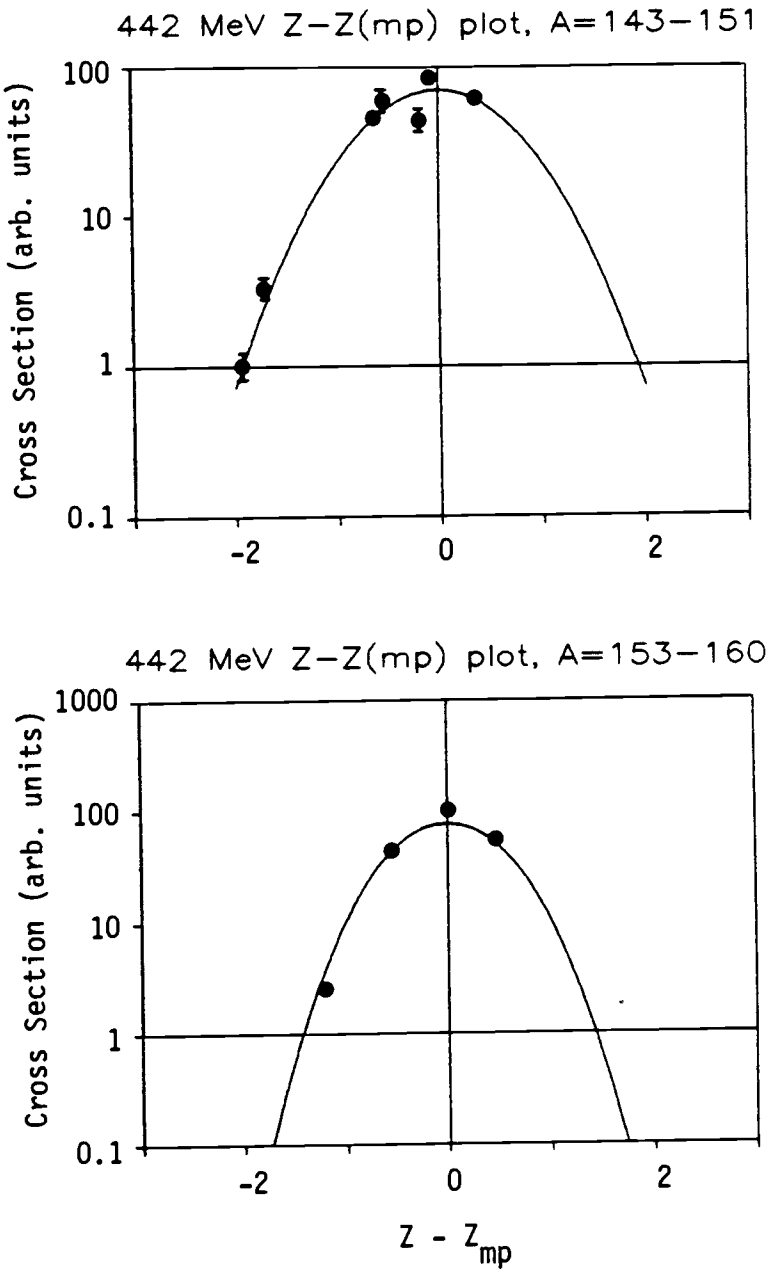

Calculated fragment charge dispersion plots for the reaction system 442 MeV ^{12}C + ^{165}Ho.

Figure D-3(cont.)

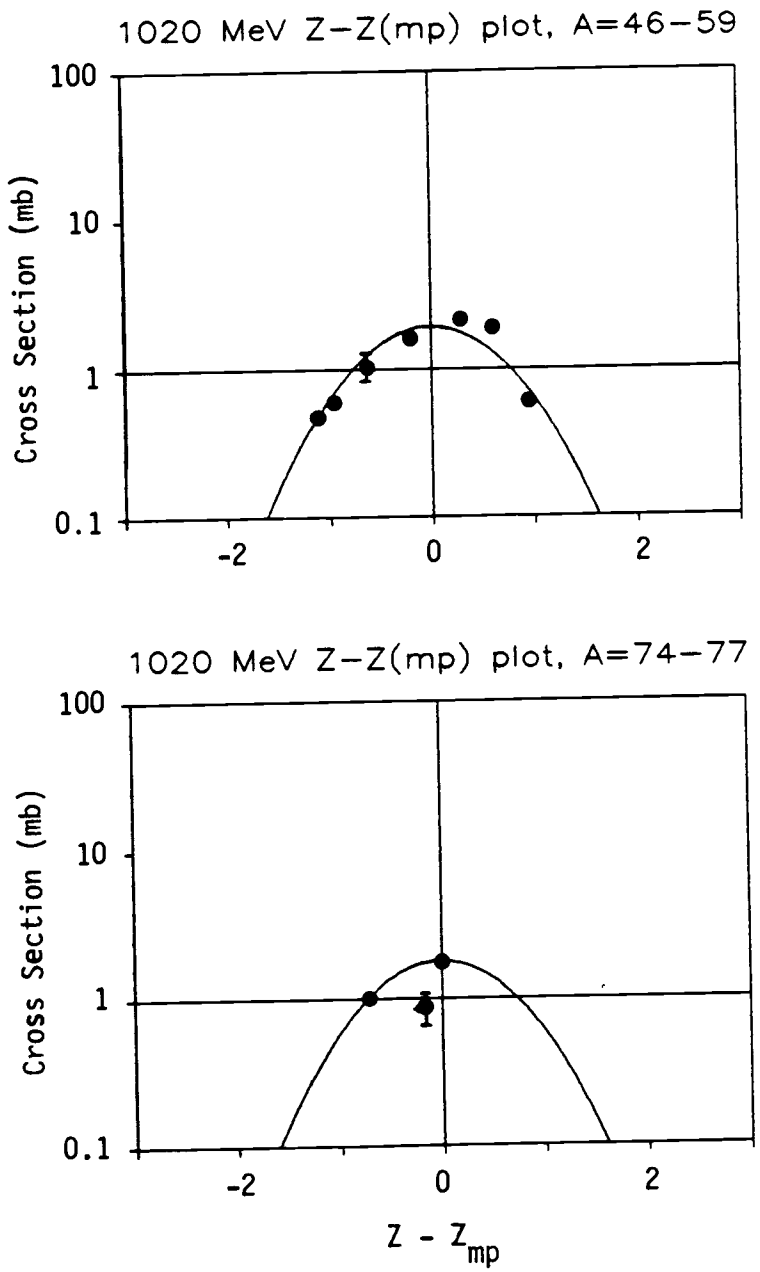
1020 MeV Z−Z(mp) plot, A=46−59
Cross Section (mb)
100
10
1
0.1
-2
0
2
1020 MeV Z−Z(mp) plot, A=74−77
Cross Section (mb)
100
10
1
0.1
-2
0
2
Z - Z_mp

Figure D-4

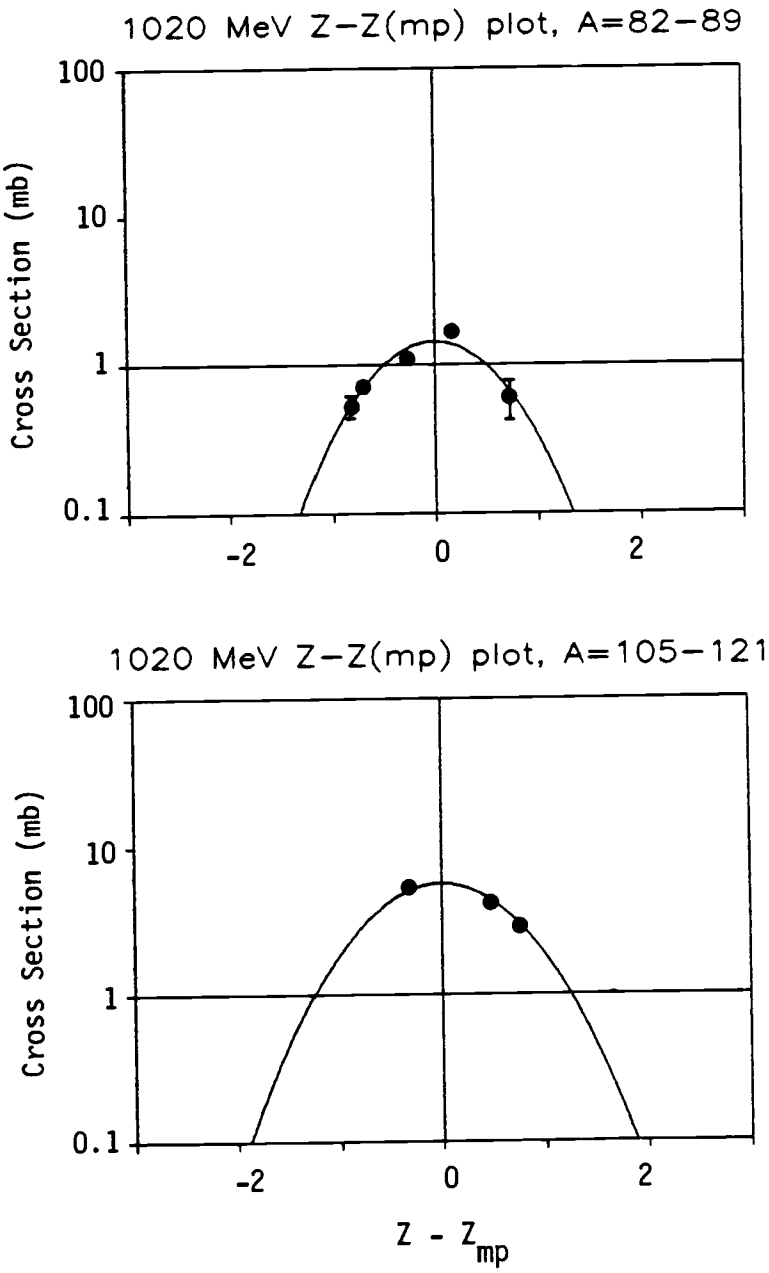

Figure D-4(cont.)

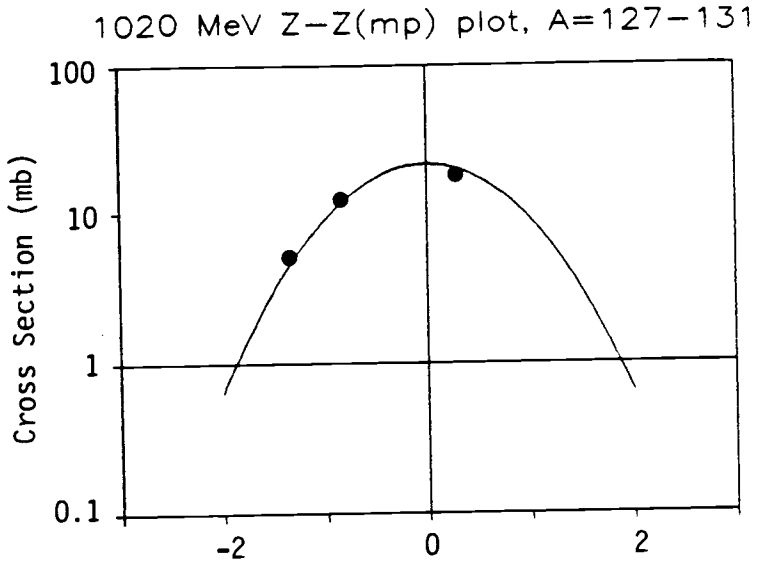

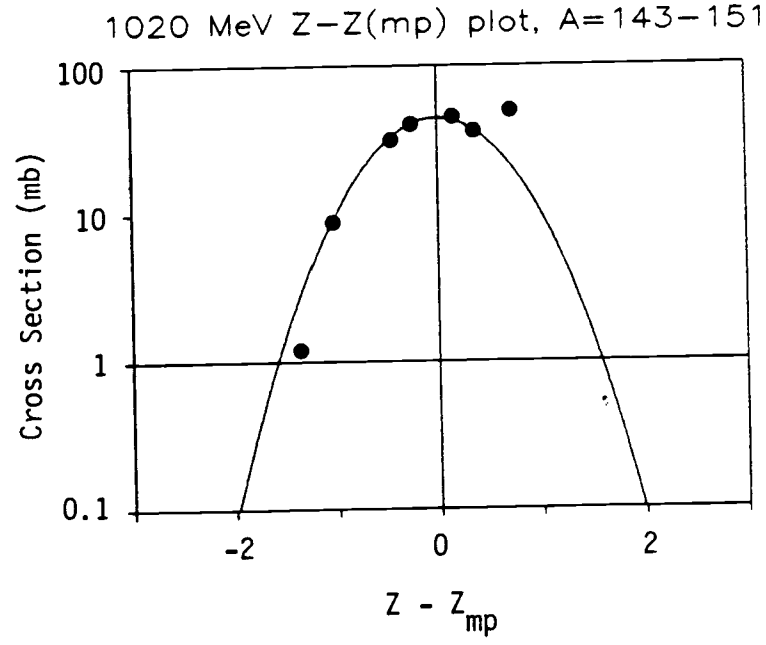

Figure D-4(cont.)

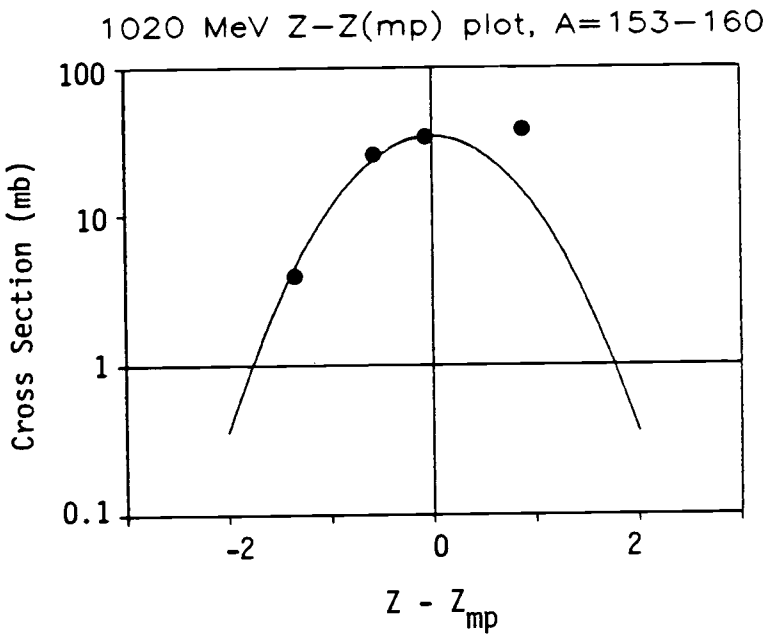

Calculated fragment charge dispersion plots for the reaction system 1020 MeV ^{12}C + ^{165}Ho.

Figure D-4 (cont.)

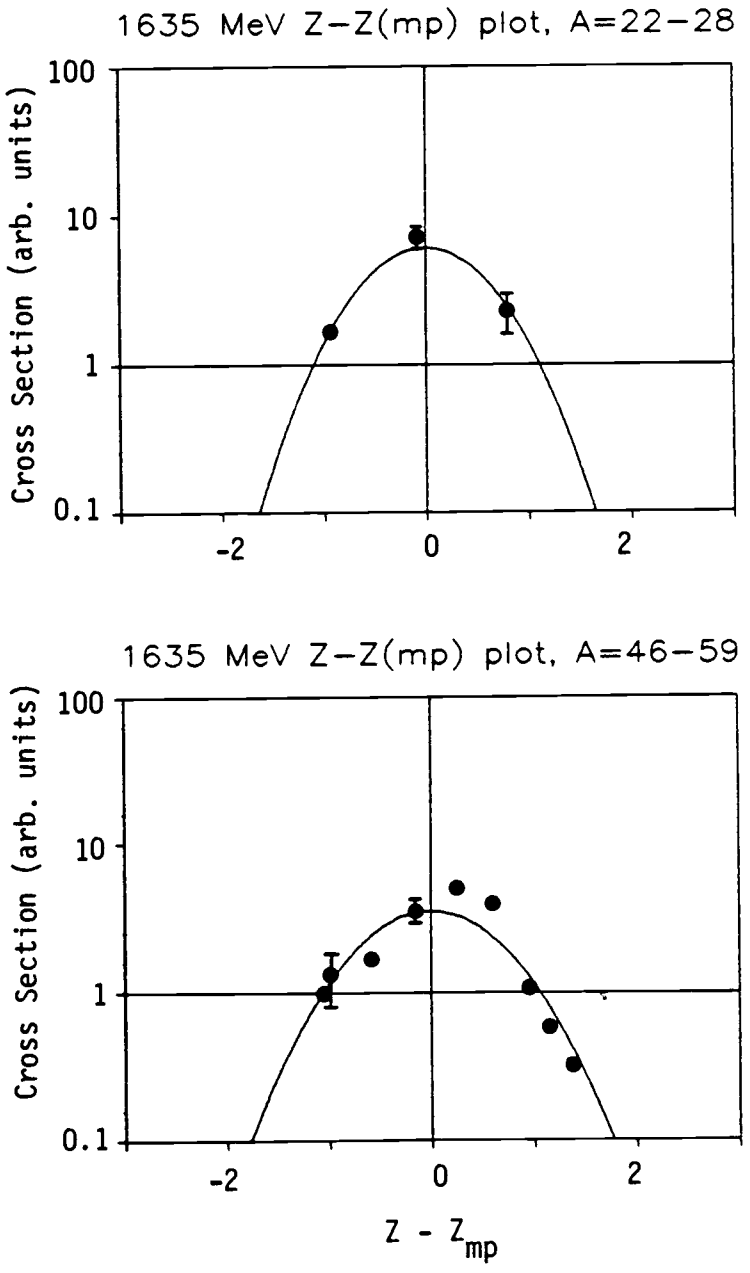
1635 MeV Z−Z(mp) plot, A=22−28
Cross Section (arb. units)
100
10
1
0.1
-2
0
2
1635 MeV Z−Z(mp) plot, A=46−59
Cross Section (arb. units)
100
10
1
0.1
-2
0
2
Z - Z_mp

Figure D-5

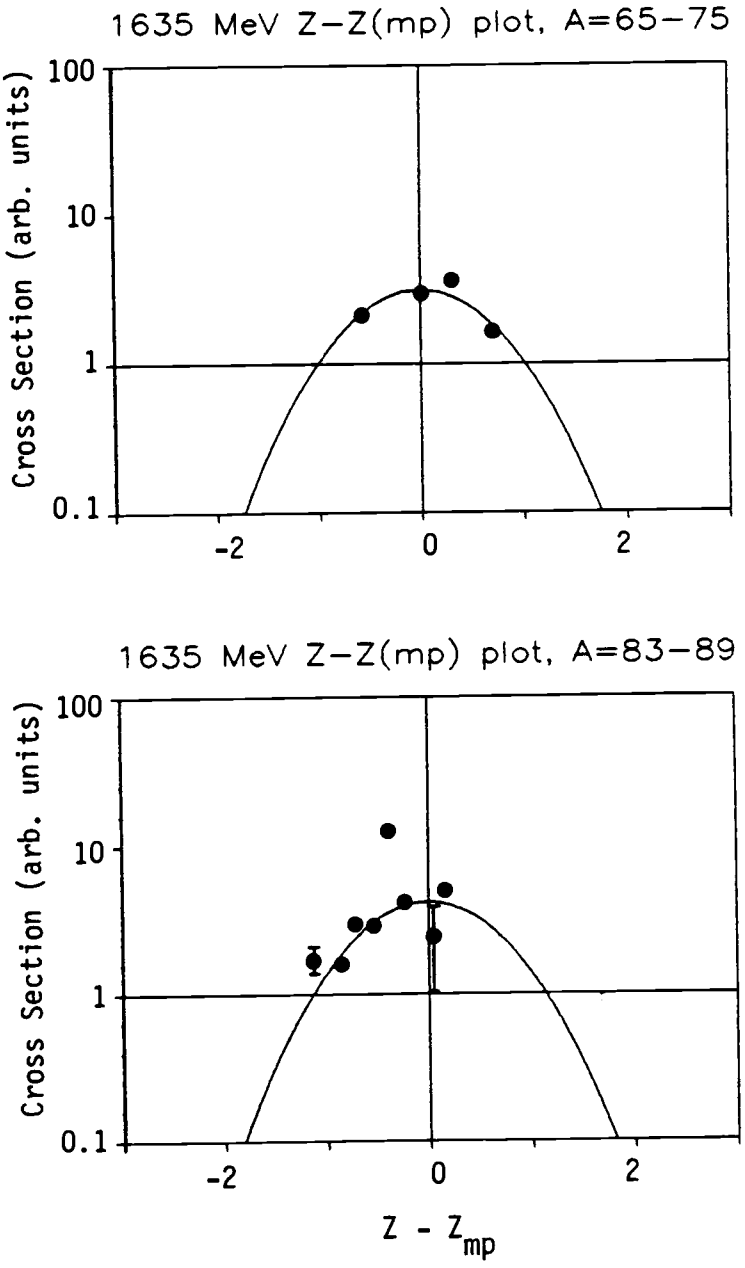

Figure D-5 (cont.)

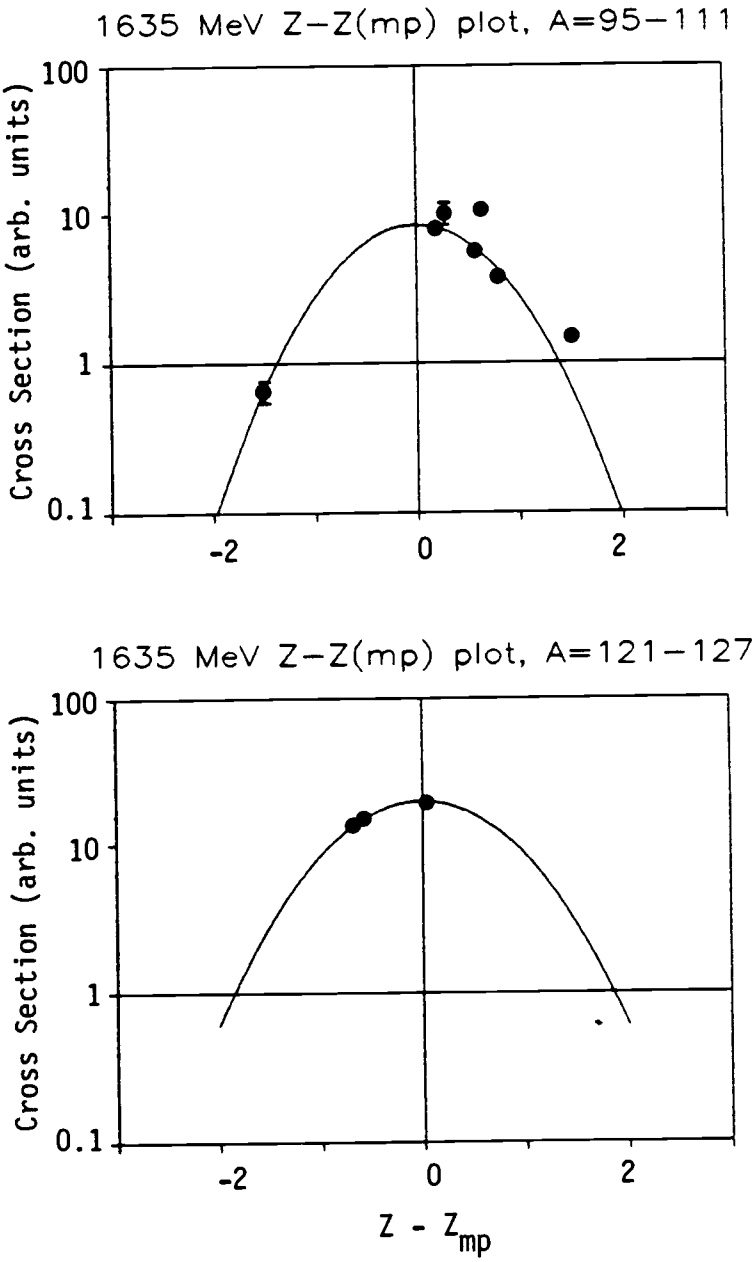

Figure D-5(cont.)

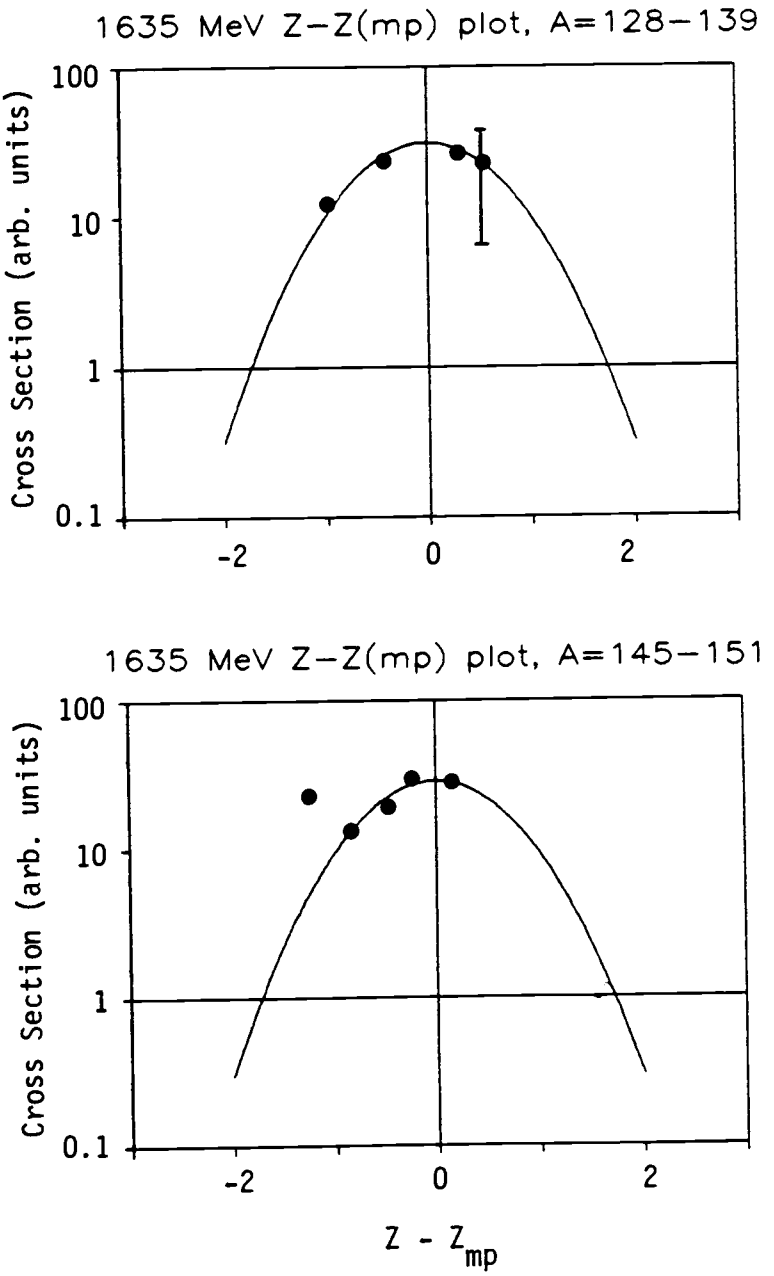

Figure D-5(cont.)

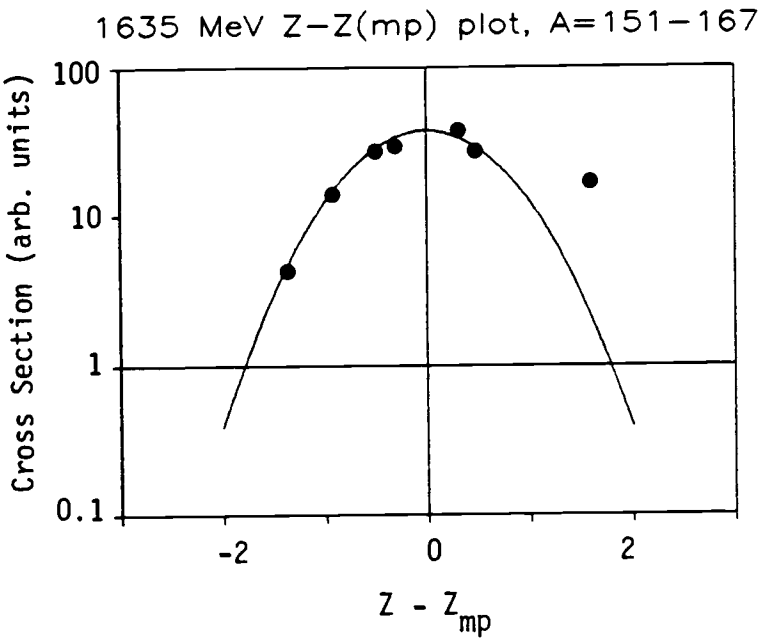

Calculated fragment charge dispersion plots for the reaction system 1635 MeV ^{16}O + ^{165}Ho.

Figure D-5(cont.)

208 MeV ^{12}C + ^{165}Ho
MASSY Z_p FUNCTION PARAMETERS

MASS REGION	Z_p FUNCTION	WIDTH
46 - 59	0.45 A - 0.	0.5
65 - 77	0.445A - 0.319	0.6
83 - 89	0.425A + 1.373	0.6
95 - 99	0.39 A + 4.43	0.7
103 - 111	0.345A + 9.275	0.8
121 - 144	0.318A + 13.14	0.6
146 - 149	0.24 A + 28.03	0.6
153 - 160	$0.295A + 23.88 - 0.0002A^2$	0.4
160 - 168	0.292A + 21.36	0.4

A tabulation of the Z_p function and Gaussian width parameters of the respective mass regions used for calculation of independent and mass yields.

Table D-1

272 MeV ^{12}C + ^{165}Ho
MASSY Z_p FUNCTION PARAMETERS

MASS REGION	Z_p FUNCTION	WIDTH
43 - 52	0.45 A + 0.18	0.7
54 - 69	0.45 A - 0.02	0.5
71 - 77	0.422A + 1.61	0.7
83 - 89	0.395A + 4.42	0.6
95 - 99	0.38 A + 5.99	0.8
101 - 111	0.355A + 8.83	0.8
121 - 139	0.385A + 6.13	0.8
145 - 151	0.23 A + 28.74	0.7
151 - 155	0.26 A + 24.4	0.6
160 - 169	0.33 A + 14.86	0.3

A tabulation of the Z_p function and Gaussian width parameters of the respective mass regions used for calculation of independent and mass yields.

Table D-2

442 MeV ^{12}C + ^{165}Ho
MASSY Z_p FUNCTION PARAMETERS

MASS REGION	Z_p FUNCTION	WIDTH
48 - 59	0.445A + 0.44	0.7
71 - 77	0.425A + 1.89	0.7
83 - 89	0.422A + 2.258	0.5
101 - 131	0.375A + 7.175	0.6
143 - 151	0.23 A + 29.82	0.6
153 - 160	0.225A + 30.11	0.4

A tabulation of the Z_p function and Gaussian width parameters of the respective mass regions used for calculation of independent and mass yields.

Table D-3

1020 MeV ^{12}C + ^{165}Ho
MASSY Z_p FUNCTION PARAMETERS

MASS REGION	Z_p FUNCTION	WIDTH
46 - 59	0.44 A + 0.95	0.6
74 - 77	0.425A + 2.275	0.6
82 - 89	0.425A + 2.43	0.5
105 - 121	0.38 A + 6.34	0.6
127 - 131	0.375A + 7.715	0.7
143 - 151	0.30 A + 19.15	0.5
153 - 160	0.25 A + 26.34	0.6
160 - 166	0.20 A + 35.70	0.4

A tabulation of the Z_p function and Gaussian width parameters of the respective mass regions used for calculation of independent and mass yields.

Table D-4

1635 MeV ^{12}C + ^{165}Ho
MASSY Z_p FUNCTION PARAMETERS

MASS REGION	Z_p FUNCTION	WIDTH
22 - 28	0.45 A + 0.32	0.5
46 - 59	0.45 A + 0.445	0.6
65 - 75	0.43 A + 1.75	0.6
83 - 89	0.425A + 2.43	0.6
95 - 111	0.39 A + 5.419	0.6
118 - 127	0.319A + 14.07	0.7
128 - 139	0.319A + 14.63	0.6
145 - 149	0.20 A + 34.44	0.6
151 - 167	0.21 A + 32.78	0.6

A tabulation of the Z_p function and Gaussian width parameters of the respective mass regions used for calculation of independent and mass yields.

Table D-5